Thèse n° 7654

Hydraulic stimulation of pre-existing discontinuities in tight rocks

Présentée le 28 février 2020

à la Faculté de l’environnement naturel, architectural et construit
Laboratoire de géo-énergie - Chaire Gaznat en géo-énergie
Programme doctoral en mécanique

pour l’obtention du grade de Docteur ès Sciences

par

Federico CIARDO

Acceptée sur proposition du jury

Prof. M. E. S. Violay, présidente du jury
Prof. B. T. A. Lecampion, directeur de thèse
Prof. H. S. Bhat, rapporteur
Dr G. Siddiqi, rapporteur
Prof. J.-F. Molinari, rapporteur

École
polytechnique
fédérale
de Lausanne

2020

> The science of mathematics presents the most brilliant example of
> the extension of the sphere of pure reason without the aid of experience.
> — Immanuel Kant

To:
my parents - Mario & Beatrice -
my brother - Francesco -
and Ana . . .

Abstract

Hydraulic stimulation is an engineering technique whose aim is to enhance the permeability of fractured rock masses at depths ranging from one to five kilometers. It consists in the injection of fluid at sufficiently high pressure in order to shear pre-existing fractures and/or to create new fractures. The local reduction of effective stresses can indeed result into localized inelastic deformations along pre-existing discontinuities which upon dilation increase the overall permeability of the rock mass. Although this technique is used to extract deep geothermal energy from crystalline rocks, some fundamental hydro-mechanical mechanisms are not yet fully understood, especially in regards to the transition between aseismic and seismic slip.

In this context, the present thesis investigates the interplay between pore pressure diffusion within pre-existing discontinuities and induced deformations including the possible nucleation of a dynamic rupture. This is achieved via the development of specific numerical algorithms that are extensively verified against existing analytical and semi-analytical solutions of fracture growth. Thanks to the use of a boundary integral representation for elasticity, fluid driven deformations localized on pre-existing discontinuities can be efficiently modelled, without involving an intensive discretization of the whole domain.

We first present an in-depth study on the effect of dilatancy on the propagation of a fluid driven crack along a frictional weakening planar fault. The numerical results reveal that shear-induced dilatancy can effectively stabilize an otherwise unstable fault with respect to the nucleation of an unabated dynamic rupture. Although counter-intuitive, this is valid only for sufficiently large injection over-pressure. This important result is confirmed theoretically using linear elastic fracture mechanics (LEFM) under small-scale yielding approximation. The simulations further show that this stabilization still holds even for large increase of fault permeability associated with shear deformations. In a second part of this manuscript, a new boundary element solver for localized inelastic deformations along a large set of pre-existing planes is proposed and described. Upon validation against several analytical and semi-analytical solutions, a series of problems are addressed in order to illustrate the capabilities, accuracy and performance of this algorithm. It is then used to model hydraulic stimulation of fractured rock masses in the extreme cases of critically stressed and marginally pressurized conditions.

Keywords: Hydraulic stimulation, Deep geothermal energy, Induced seismicity, Friction, Dilatancy, Faults, Fractures, Shear bands, Localized phenomena, Boundary element method.

Sommario

La stimulazione idraulica è una tecnica ingegneristica che ha come scopo quello di aumentare la permeabilità di rocce fratturate a profondità che variano da uno a cinque chilometri. Nello specifico, la stimulazione idraulica consiste nell'iniezione di fluido ad alta pressione con lo scopo di rompere a taglio pre-esistenti fratture in profondità e/o di creare nuove fratture. La riduzione locale delle tensioni normali efficaci, infatti, può portare a deformazioni inelastiche localizzate su pre-esistenti discontinuità le quali aumentano la permeabilità della roccia a seguito del processo di dilatanza. Sebbene questa tecnica è utilizzata per estrarre energia geotermica di profondità da basamenti granitici, alcuni meccanismi fondamentali che controllano i processi idro-meccanici non sono stati ancora del tutto capiti, specialmente riguardo alla transizione di deformazioni a taglio sismiche e non sismiche.

In questo contesto, la presente tesi approfondisce l'interazione tra diffusione del fluido all'interno di pre-esistenti discontinuità e deformazioni indotte, tenendo in conto del possibile avvenimento di rotture dinamiche. Questo obbiettivo è raggiunto attraverso lo sviluppo di specifici algoritmi numerici che sono stati verificati in maniera estesa attraverso la comparazione dei risultati con soluzioni analitiche e semi-analitiche di propagazione della frattura. Grazie a l'utilizzo di una rappresentazione integrale del contorno per l'elasticità, le deformazioni indotte dal fluido e localizzate su pre-esistenti discontinuità possono essere modellate efficientemente, senza coinvolgere una intensiva discretizzazione dell'intero dominio.

In primo luogo, presentiamo una studio profondo su l'effetto della dilatanza sulla propagazione di una frattura spinta dal fluido su una faglia piana caratterizzata da indebolimento di attrito. I risultati numerici rivelano che la dilatanza indotta a taglio può effettivamente stabilizzare una altrimenti instabile faglia dall'avvenimento di una incontrollata rottura dinamica. Sebbene non intuitivo, questo è valido soltanto per pressioni di iniezione del fluido sufficientemente grandi. Questo importante risultato è confermato teoreticamente usando la teoria elastica della meccanica della frattura sotto l'approssimazione di snervamento a piccola scala. Le simulazioni inoltre mostrano che questa stabilizzazione è ancora valida anche quando la permeabilità della faglia aumenta considerevolmente con le deformazioni a taglio. In una seconda parte di questa tesi, un nuovo risolutore agli elementi di contorno adatto per deformazioni inelastiche locali è proposto e descritto. Dopo una validazione usando varie soluzioni analitiche e semi-analitiche, problemi di diversa natura sono stati risolti in maniera da mostrare le capacità, la accuratezza e le performances del risolutore sviluppato. Quest'ultimo è poi utilizzato per studiare la stimulazione idraulica di rocce fratturate in condizioni estreme di criticità tensionale e pressurizzazione marginale.

Parole chiavi: Stimulazione idraulica, Energia geotermica di profondità, Sismicità indotta, Attrito, Dilatanza, Faglie, Fratture, Bande a taglio, Fenomeni localizzati, Metodo degli elementi di contorno.

Acknowledgements

In a nutshell, I would like to express my deep and sincere gratitude to my thesis director Prof. B. Lecampion for offering me the opportunity to pursue a PhD at EPFL. Surely, these four years of collaboration have enriched my knowledge as well as my person. I am very thankful for his valuable advices and his guidance.

I want to thank my dissertation committee members, Professors J.-F. Molinari, H. Bhat, M. Violay and Dr. G. Siddiqi for their precious time and interesting comments on my research work. A special thanks goes to Dr. G. Siddiqi for introducing me to several people in order to spread out my research work and extend my contact network.

During my stay at GEL laboratory, I had amazing colleagues that helped keeping my daily humor up. Notably, I want to sincerely thank my office mate Fatima and Dong for all the conversations we had during the lunches on campus. Although sometimes not relevant in terms of contents, they were efficient medicine for my humor. A final thanks goes also to the new colleagues, Dimitry, Alexis and Carlo for bringing lightness to the laboratory.

I give special thanks to my friends Andrea, Enrico, Matteo and Claire for the amazing time spent together in Lausanne. The night life was much better with you and I am sure our friendship will never end.

Now I want to spend few words for a person that really left a mark on me during my PhD. Thanks a million D. Nikolskyi (Dima). Thanks for helping me moving from one house to another, for our road trips with Alfetta, for our mountain hikes and - more importantly - for your help on my PhD work. Your mind is brilliant and your advices helped me a lot. I will never forget all this.

A big thanks to my parents, Mario and Beatrice, who sacrificed part of their life to give me financial (and emotional) support. If I am here now, it is mostly because of you. You will always have my thanks.

Last but not least, I want to thank the two most important persons for me: my twin Francesco and my lovely half Ana. You always encouraged me, especially during my

personal difficulties. I feel very lucky to have you always by my side. I can not thank you all enough for what you have done for me.

Lausanne, February 11, 2020. F. Ciardo

Acknowledgement of Support

I gratefully acknowledge the support received during the period of this doctoral work – Feb. 2016 / Jan. 2020. Particularly, I would like to thank the Swiss Federal Office of Energy (SFOE) for supporting my studies through the Stim-Design project (SI/50135401), as well as the Swiss National Science Foundation (grant 160577).

Lausanne, February 11, 2020. F. Ciardo

Contents

Abstract (English) v

Abstract (Italiano) vii

Acknowledgements ix

Acknowledgement of Support xi

List of Figures xvi

List of Tables xxviii

1 Introduction 1
- 1.1 Preamble 1
- 1.2 Motivations 2
  - 1.2.1 Geothermal energy extraction 2
    - 1.2.1.1 Hydraulic stimulation mechanisms in EGS 4
    - 1.2.1.2 Injection-induced seismicity 5
  - 1.2.2 A short review of existing numerical simulators for hydraulic stimulation of fractured rock masses 6
- 1.3 Organisation of this manuscipt 7

2 Boundary integral equation for fracture problems 9
- 2.1 Conventions and notations 9
- 2.2 Conservation of momentuum 10
- 2.3 Kinematics and compatibility 12
- 2.4 Link between equilibrium and compatibility 14
- 2.5 Constitutive law 14
- 2.6 Maxwell-Betti reciprocity theorem 15
- 2.7 Kelvin fundamental solution 16
- 2.8 Boundary integral representation 17
- 2.9 Displacement discontinuity method for fractures 18
  - 2.9.1 Displacement boundary integral representation 20
    - 2.9.1.1 Fundamental edge dislocation solution 22

2.9.1.2 Fundamental solution of plane dislocation dipoles 24
2.10 Numerical discretization, collocation and regularization after integration . 25
2.10.1 Fracture discretization 25
2.10.2 Shape functions and collocation of elasticity equations 26
2.10.3 Analytical integration over a reference element 27
2.10.4 Assembly of the final elastic system 28
2.10.5 Extension to quasi-dynamic approximation 31
2.11 Conclusions 33

3 Fluid flow in fractures 35
3.1 Governing equations of fluid dynamics 36
3.1.1 Lubrication approximation and width averaging 38
3.2 Flow in rough fractures 40
3.3 Finite volume method for fluid flow inside hydraulically conductive fractures 41
3.3.1 Discretization of fluid mass conservation equation 41
3.4 Conclusions 44

4 Effect of shear-induced dilatancy on the transition from aseismic to seismic slip along a pressurized fault 47
4.1 Introduction 48
4.2 Problem formulation 49
4.2.1 Equilibrium, activation and dilatancy of slip-weakening fault . . . 49
4.2.1.1 Activation and plasticity 51
4.2.1.2 Slip weakening and nucleation length-scale 53
4.2.2 Fluid flow 54
4.2.3 Initial and injection conditions 56
4.3 Activation and transition between aseismic and seismic slip 57
4.3.1 Case of a non-dilatant fault 57
4.3.2 Effect of dilatancy 59
4.3.2.1 Undrained fault response 59
4.3.2.2 Small scale yielding & stability condition 60
4.4 Numerical scheme description 62
4.4.1 Characteristic scales for dimensionless governing problem 64
4.5 Dilatant hardening effect on a fault characterized by constant permeability 65
4.5.1 Case of unstable fault without dilatancy $\tau_o > \tau_r$ 65
4.5.2 Case of an ultimately stable fault even without dilatancy ($\tau_o < \tau_r$) 71
4.6 Effect of shear-induced permeability changes 72
4.7 Conclusions 76
4.8 Supporting Information 80
4.8.1 Fully implicit hydro-mechanical solver for frictional planar fault: algorithm description 80
4.8.2 Verification of the numerical scheme: benchmark for the non-dilatant case 84

4.8.3 Mesh convergence study . . . 86
4.8.4 Case of otherwise unstable fault $\tau_o > \tau_r$ - Nucleation and Arrest . 87
4.8.5 Approximated solution for quasi-static growth assuming $a \propto \sqrt{4\alpha t}$ 88
4.8.6 Dilatancy effect on purely aseismic crack propagation . . . 93
4.8.7 Effect of shear-induced permeability changes: case of effective stress-dependent permeability . . . 93

5 A boundary element based solver for localized inelastic deformations 97

5.1 Introduction . . . 97
5.2 Problem formulation . . . 99
  5.2.1 Elastic medium with displacement discontinuities . . . 99
  5.2.2 Constitutive relations for displacement discontinuities segments . . 100
    5.2.2.1 Shear failure . . . 101
    5.2.2.2 Tensile failure . . . 102
  5.2.3 Initial and boundary conditions . . . 103
5.3 Numerical scheme . . . 104
  5.3.1 Boundary element method for elasto-static using a hierarchical matrix appriximation . . . 104
  5.3.2 An implicit time-stepping scheme . . . 106
    5.3.2.1 Outer yielding loop . . . 106
    5.3.2.2 Solution of the equilibrium under constraints . . . 106
    5.3.2.3 Solution of the tangent system for the trial active sets . . 108
5.4 Illustrative examples . . . 111
  5.4.1 A branched frictional fault system . . . 111
  5.4.2 Tensile wellbore failure . . . 112
  5.4.3 Shear-banding in uniaxial compression . . . 116
  5.4.4 Active Earth pressure against a rigid retaining wall . . . 120
  5.4.5 Fluid injection into a frictional weakening planar fault . . . 122
5.5 Conclusions . . . 124
5.6 Supporting Information . . . 125
  5.6.1 Verification tests . . . 125
    5.6.1.1 A planar fracture with homogenous friction properties subjected to compressive far-field stress . . . 125
    5.6.1.2 Arc crack under remote tension . . . 127
    5.6.1.3 A stair-like fracture subjected to remote compressive stress 128
  5.6.2 Other illustrative example . . . 129
    5.6.2.1 Mechanical opening and closure of a single planar fracture 129

6 Fluid induced aseismic slip in fractured rock masses: marginally pressurized vs critically stressed conditions 133

6.1 Introduction . . . 133
6.2 Fluid driven aseismic slip along a planar fault with neutral frictional properties . . . 135

6.3 Fluid injection into a Discrete Fracture Network . . . 138
6.3.1 Scaling & dimensionless governing parameters . . . 139
6.3.2 Critically stressed condition . . . 142
6.3.3 Marginally pressurized condition . . . 144
6.4 Discussion and conclusions . . . 146

7 Conclusions 149

A Stress kernels of boundary integral equations for plane elasticity 153

B Accelerated boundary element method via hierarchical matrix 157
B.1 Overview & general idea . . . 158
B.2 $\mathcal{H}$-matrix and Adaptive Cross Approximation . . . 160
B.2.1 Clustering and admissibility condition . . . 161
B.2.2 Low-rank approximation using ACA . . . 164

C HFPx2D: an open-source code for 2D fluid driven crack(s) propagation 167
C.1 Conception and current capabilities . . . 168
C.2 External dependencies . . . 170
C.3 Code architecture . . . 171

Bibliography 191

Curriculum Vitae 193

List of Figures

1.1 Different existing geothermal systems used to extract thermal energy from sub-surface. Taken from Shao et al. (2016). 2

1.2 Total installed capacity from worldwide geothermal power plants. Taken from Bertani (2015). 3

2.1 Traction vector definition from virtual splitting of an elastic deformable body subjected to a generalised system of forces. 11

2.2 Displacement field of an elastic body subjected to generalised system of forces. 13

2.3 Pre-existing crack in an infinite, linear elastic, isotropic and homogenous medium. This crack lies along the boundary Γ, which has been ideally divided in upper and lower part in order to differentiate respectively the upper and the lower surface of the fracture. 19

2.4 Effects in terms of normalized stress components $\frac{\pi(\kappa+1)}{2G}s_{ijk}$ of a unit edge dislocation located at the origin of an infinite, linear elastic, isotropic and homogenous medium. These components are derived analytically by solving the corresponding well-posed elastic boundary value problem. . . . 23

2.5 Example of a discretized planar fracture embedded in a 2-dimensional, infinite medium. Piecewise linear shape functions are used to discretize the displacement jumps across the fracture plane Γ. Therefore, there are four primary unknowns per element. 26

2.6 Reference displacement discontinuity element. The normal $d_n = u_n^- - u_n^+$ and shear displacement discontinuity $d_s = u_s^- - u_s^+$ are linearly evolving within an element. The boundary integral equation is enforced at the collocation points (orange points), located at $\pm 1/\sqrt{2}$ within the element. The unknown displacement discontinuities are located at the nodes $(-1, 1)$. 27

2.7 Influence of displacement discontinuity on source element e over receiver element k. A change of coordinates is performed in order to make the source element e coincide the unit reference element. The stress field is then computed at a collocation point of element k. 29

2.8 Final elastic boundary element matrix for a planar fracture with unit half-length, discretized with 24 linear elements. This fracture is embedded in an infinite, linear elastic, isotropic and homogenous medium, whose plane strain modulus is $E_p = 1$. Note that shear and normal degrees of freedom are uncoupled and $K^{el}_{sn} = K^{el}_{ns} = 0$ (white spots in the matrix plot). 31

3.1 Idealization of mechanically open versus mechanically closed fractures. In this picture, taken from Witherspoon (1980), ϵ denotes the asperity size, while $2b$ the fracture width. 36

3.2 Sketch of displacement discontinuities and fluid pressure variation along three mesh elements converging in one generic node i. The former vary linearly and discontinuously between different elements, whereas the latter is continuous at mesh node i. The control volume for finite volume scheme is centred at pressure node i inside which fluid is conserved. Note that this numerical scheme can be easily extended to the case where more than three mesh elements intersect at node i (and obviously to the case where only two elements converge at each pressure node, which is the case of the planar fracture of Figure 2.5). 42

4.1 Model of frictional weakening dilatant fault & loading conditions. Zoom represents schematically the dilatant process that occur during shear fracture propagation. 50

4.2 The Mohr-Coulomb plot (top) illustrates the evolution of the yielding surface $F(\tau, \sigma')$ with weakening of friction coefficient as well as the evolution of plastic displacement discontinuity vector $\dot{d}_j$ with slip after shear fracture activation due to fluid over-pressure ΔP. The linear evolution of friction coefficient $f = \tan(\phi)$ (left) and dilatancy angle $\tan(\psi)$ (right) with slip δ are displayed in the bottom plots. 51

4.3 Phase diagram of Garagash & Germanovich (2012) that describes the different regimes of propagation for a non-dilatant fault, as a function of the dimensionless fluid over-pressure $\Delta P/\sigma'_o$ and stress criticality τ_o/τ_p. Region 1 corresponds to the trivial case of an injection without fault re-activation. Regions $4a$, b, c corresponds to the unstable fault case for which an unabated dynamic rupture occurs as the residual shear strength (defined at ambient conditions) is lower than the in-situ shear stress ($\tau_r < \tau_o$). Regions 2 and 3 corresponds to the case of ultimately stable faults ($\tau_r > \tau_o$) for which most of the crack growth is aseismic although transient seismic slip may occur (region 2). 58

4.4 Time evolution of normalized half crack length a/a_w (top-left) and normalized peak slip δ/δ_w at the middle of the fault (top-right), i.e. at $x = 0$, for an otherwise unstable fault ($\tau_o/\tau_p = 0.75$), subjected to moderate over-pressure $\Delta P/\sigma'_o = 0.5$. The friction weakening ratio considered here is $f_r/f_p = 0.6$. The corresponding time evolution of normalized crack velocity va_w/α is showed in the plot at the bottom. We vary the dimensionless dilatancy parameter $\frac{\epsilon_d}{\beta\sigma'_o}$ below and above the critical stabilizing value-which is $\epsilon_{d,c}/(\beta\sigma'_o) = 0.25$ in this particular case. Red dots point the onset of unabated dynamic ruptures (color online). 66

4.5 Spatial profile of a) dimensionless pore pressure, b) friction coefficient, c) slip, d) effective normal stress for a critically stressed dilatant fault ($\tau_o/\tau_p = 0.75$), subjected to a moderate overpressure $\Delta p/\sigma'_o = 0.5$, at different (normalized) time snapshots. Sub-figures (e) show the evolution of normalized shear strength with slip, at the same time snapshots. Results for two dimensionless dilatancy parameters are reported: left) ultimately unstable fault for which $\epsilon_d/\beta\sigma'_o$ is lower than the critical stabilizing value for that particular set of parameter ($\epsilon_{d,c}/\beta\sigma'_o = 0.25$), right) ultimately stable for a dimensionless dilatancy above the stabilizing value. Red curves (color online) denote the numerical results at nucleation time for the unstable case (left). 67

4.6 Effect of dimensionless overpressure $\Delta P/\sigma'_o$ on a critically stressed dilatant fault ($\tau_o/\tau_p = 0.75$), in terms of time evolution of dimensionless half crack length a/a_w and dimensionless peak slip $\delta/\delta_{|x=0}$. The dimensionless dilatancy parameter equals the critical value for such configuration: $\epsilon_{d,c}/(\beta\sigma'_o) = 0.25$. 68

4.7 Time evolution of normalized half crack length and peak slip under quasi-static (QS) and quasi-dynamic (QD) approximation of elastic equilibrium. The latter is obtained by adding a seismic radiation damping term proportional to slip rate to elasticity equations in order to take into account energy dissipation through seismic waves orthogonal to fault plane during high slip rate (Rice 1993). The radiation damping term in normalized form reads $\frac{G\delta_w 4\alpha}{2c_s\tau_p a_w^2}$, being c_s the shear wave speed and G the shear modulus. We use here a very large value of 40 for such a dimensionless damping term, therefore over-damping the dynamic rupture. 69

4.8 Numerical estimation of the minimum amount of over-pressure required to activate the full benefit of dilatant hardening and stabilize an otherwise unstable fault ($\tau_r < \tau_o$) for different stress criticality between the ultimately stable limit ($\tau_r/\tau_p = f_r/f_p = 0.6$ in that case) and the undrained dilatant residual strength ($\tau_r^u/\tau_p = 1.25\tau_r/\tau_p = 0.75$ in that case). The black filled circle denotes the maximum value of over-pressure below which a finite dynamic event always nucleate (for over-pressure above the slip activation limit), while the empty circle corresponds to the minimum normalized over-pressure required to stabilize such a fault (aseismic slip only for larger over-pressure). The minimum over-pressure required for slip activation ($\Delta P/\sigma_o' = 1 - \tau_o/\tau_p$) is also displayed as empty square/continuous line. Stress criticality τ_o/τ_p larger than τ_r^u/τ_p always result in the nucleation of unrestricted dynamic rupture for any value of over-pressure larger than the activation limit. 70

4.9 Time evolution of normalized half crack length a/a_w and normalized peak slip δ/δ_w at the middle of the fault, i.e. at $x = 0$, for an ultimately stable fault ($\tau_o/\tau_p = 0.55$ and $\tau_o < \tau_r$, for $f_r/f_p = 0.6$), subjected to moderate over-pressure $\Delta P/\sigma_o' = 0.5$. We span several dilatancy cases by varying the dimensionless dilatancy parameter $\epsilon_d/(\beta\sigma_o')$. Red dots denote the onset of dynamic event, which is always characterized by a nucleation followed by an arrest (red arrow). The run-out distance increases with increase values of dimensionless dilatancy parameter $\epsilon_d/\beta\sigma_o'$. 72

4.10 Spatial profiles of dimensionless pore pressure (a), friction coefficient (b), slip (c) and effective normal stress (d) at different (normalized) time snapshots, for an otherwise ultimately stable fault ($\tau_o/\tau_p = 0.55$ - $f_r/f_p = 0.6$), subjected to a moderate over-pressure $\dfrac{\Delta P}{\sigma_o'} = 0.5$. Two dimensionless dilatancy parameters are considered: $\dfrac{\epsilon_d}{\beta\sigma_o'} = 0.1$ and $\dfrac{\epsilon_d}{\beta\sigma_o'} = 0.3$. Red lines refer to numerical results at nucleation time of a dynamic rupture. Since the background shear stress τ_o is lower than the residual fault strength τ_r at ambient conditions, the dynamic event is always followed by an arrest. 73

4.11 Effect of permeability increase on a critically stressed ($\tau_o/\tau_p = 0.75$, $f_r/f_p = 0.6$) dilatant fault under moderate over-pressure ($\Delta P/\sigma_o' = 0.5$): time evolution of normalized half crack length a/a_w and corresponding peak slip $\delta_{|x=0}/\delta_w$. The dimensionless dilatancy parameter $\epsilon_d/(\beta\sigma_o')$ is set to the corresponding critical stabilizing value (4.27), equal here to 0.25. The effect of permeability evolution following the slip dependent law (4.31) is investigated for five different values of the parameters (a, b) spanning small and large permeability increase from 1.5 to $\sim$ 60 times the initial fault permeability. 75

4.12 Spatial profiles of dimensionless pore pressure, friction coefficient, slip, effective normal stress and fault longitudinal permeability (in linear-log scale) at a given normalized time snapshot $\sqrt{4\alpha t}/a_w = 0.27$, for unstable fault ($\tau_o/\tau_p = 0.75$ - $f_r/f_p = 0.6$), subjected to a moderate over-pressure $\frac{\Delta P}{\sigma'_o} = 0.5$ and a dimensionless dilatancy parameter equal to the critical value, i.e. $\frac{\epsilon_{d,c}}{\beta \sigma'_o} = 0.25$. The different numerical results are obtained with different fault permeability evolution laws: i) constant permeability $k_f = \frac{\omega_o^2}{12}$, ii) slip-dependent permeability law $k_f = \frac{\omega_o^2}{12}\left(1 + a\frac{w(\delta)}{\omega_o}\right)^b$, with $a = 1 \& b = 2$ (cubic law for fault transmissivity) and $a = 2 \& b = 3, 5, 8, 10$. 77

4.13 Benchmark of numerical results against semi-analytical ones of Garagash & Germanovich (2012) in terms of time evolution of normalized half crack length a/a_w and normalized peak slip δ/δ_w at $x = 0$, for a non-dilatant fault subjected to moderate overpressure $\Delta P/\sigma'_o = 0.5$ and three initial stress conditions: i) $\tau_o/\tau_p = 0.75$ (unstable fault), ii) $\tau_o/\tau_p = 0.55$ (ultimately stable fault) and iii) $\tau_o/\tau_p = 0.51$ (ultimately stable fault). The friction weakening ratio is $\frac{f_r}{f_p} = 0.6$, so that $\frac{\delta_r}{\delta_w} = 0.4$. The red dots denote the nucleation/onset of an unabated dynamic rupture, whereas the red arrows denote the nucleation of dynamic event followed by an arrest. 84

4.14 Benchmark of numerical results against semi-analytical ones of Garagash & Germanovich (2012) in terms of normalized slip δ/δ_w and shear stress τ/τ_p profiles, for a non-dilatant ultimately stable fault subjected to moderate over-pressure $\Delta P/\sigma'_o = 0.5$. The stress criticality is $\tau_o/\tau_p = 0.55$ and the friction weakening ratio is $f_r/f_p = 0.6$. 85

4.15 Evolution of relative error in terms of normalized peak slip $\delta_{|x=0}/\delta_w$ at normalized time $\sqrt{4\alpha t}/a_w = 2$, as a function of number of elements within the nucleation length scale a_w. The test case investigated is a non-dilatant ultimately stable fault ($\tau_o/\tau_p = 0.55$ and $f_r/f_p = 0.6$), subjected to moderate overpressure $\frac{\Delta P}{\sigma'_o} = 0.5$. Semi-analytical results of Garagash & Germanovich (2012) in terms of normalized half crack length and peak slip at the fault center are available, allowing to calculate the relative error. . . 86

4.16 Evolution of normalized half crack length a/a_w and normalized peak slip $\delta_{|x=0}/\delta_w$ with normalized time $\sqrt{4\alpha t}/a_w$ for a frictional weakening dilatant fault. The fault is subjected to an initial uniform background shear stress $\tau_o/\tau_p = 0.65$ (unstable fault in the non-dilatant case for a friction weakening ratio of $f_r/f_p = 0.6$ - with relative low stress criticality though) and a moderate constant over-pressure $\dfrac{\Delta P}{\sigma'_o} = 0.5$ applied in the middle of the fault. Two dimensionless dilatancy parameters are considered: $\dfrac{\epsilon_d}{\beta\sigma'_o} = 0.05 < \dfrac{\tau_o}{\tau_r} - 1 = \dfrac{\epsilon_{d,c}}{\beta\sigma'_o}$ and $\dfrac{\epsilon_d}{\beta\sigma'_o} = 0.1 > \dfrac{\tau_o}{\tau_r} - 1 = \dfrac{\epsilon_{d,c}}{\beta\sigma'_o}$. Grey dotted lines denote semi-analytical results of Garagash & Germanovich (2012), whereas red dots denote nucleation of dynamic rupture. 88

4.17 Spatial profiles of dimensionless pore pressure (a), friction coefficient (b), slip (c) and effective normal stress (d) at different (normalized) time snapshots, for an otherwise unstable fault ($\tau_o/\tau_p = 0.65$ - relative low stress criticality for $f_r/f_p = 0.6$), subjected to a moderate over-pressure $\dfrac{\Delta P}{\sigma'_o} = 0.5$. Two dimensionless dilatancy parameters are considered: $\dfrac{\epsilon_d}{\beta\sigma'_o} = 0.05 < \dfrac{\tau_o}{\tau_r} - 1 = \dfrac{\epsilon_{d,c}}{\beta\sigma'_o}$ and $\dfrac{\epsilon_d}{\beta\sigma'_o} = 0.1 > \dfrac{\tau_o}{\tau_r} - 1 = \dfrac{\epsilon_{d,c}}{\beta\sigma'_o}$. Red lines refer to numerical results at nucleation time of an unabated dynamic rupture. . . 89

4.18 Comparison between numerical results and results associated with approximated solution for quasi-static crack growth ($a \propto \sqrt{4\alpha t}$) in terms of time evolution of normalized half-crack length a/a_w. The case investigated is a critically stressed fault ($\tau_o/\tau_p = 0.75$), subjected to moderate over-pressure $\Delta P/\sigma'_o = 0.5$ and two values of dimensionless dilatancy parameter $\dfrac{\epsilon_d}{\beta\sigma'_o} = 0.25 - 0.3$. 91

4.19 Comparison between numerical results and results associated with approximated solution for quasi-static crack growth ($a \propto \sqrt{4\alpha t}$) in terms of pore pressure profiles. The case investigated is a critically stressed fault ($\tau_o/\tau_p = 0.75$), subjected to moderate over-pressure $\Delta P/\sigma'_o = 0.5$ and a dimensionless dilatancy parameter $\dfrac{\epsilon_d}{\beta\sigma'_o} = 0.3$. The relative (and constant) position between crack tip and fluid front ($\gamma = \dfrac{a}{\ell_d(t)}$) is 2.48 and 3, which correspond to a dimensionless time of $\sqrt{4\alpha t}/a_w = 1$ and $\sqrt{4\alpha t}/a_w = 2$, respectively. 92

4.20 Dilatancy effect on normalized crack length a/a_w and peak slip δ/δ_w at $x = 0$ for a frictional weakening fault subjected to large overpressure $\Delta P/\sigma'_o = 0.75$. The fault is ultimately stable in the hypothetical absence of dilatancy as the uniform background shear stress $\tau_o = 0.55 \cdot \tau_p$ is lower than the fault residual strength at ambient conditions τ_r, for a friction weakening ratio of $f_r/f_p = 0.6$. Under such stress criticality and large over-pressure, the fault always exhibits seismic crack propagation (zone 3 of Figure 4.3). However, the crack velocity slows down for increasing values of dimensionless dilatancy parameters. 93

4.21 Effect of permeability increase on a critically stressed ($\tau_o/\tau_p = 0.75$, $f_r/f_p = 0.6$) dilatant fault in terms of time evolution of normalized half crack length a/a_w and peak slip $\delta_{|x=0}/\delta_w$. The dimensionless dilatancy parameter $\epsilon_d/(\beta\sigma'_o)$ is taken here equal to the critical stabilizing value 0.25. Under such conditions a fault with constant fault permeability $k_f = \omega^2/12$, subjected to moderate overpressure $\Delta P/\sigma'_o = 0.5$, never exhibit seismic slip. An effective stress-dependent permeability law has been considered ($k_f = k_* e^{(-\sigma'/\sigma_*)}$), with four different ratios of σ'_o/σ_* spanning low and large permeability increase. 94

4.22 Spatial profiles of dimensionless pore pressure, friction coefficient, slip, effective normal stress and fault longitudinal permeability (in linear-log scale) at a given normalized time snapshot $\sqrt{4\alpha t}/a_w = 0.4$, for unstable fault ($\tau_o/\tau_p = 0.75$ - $f_r/f_p = 0.6$), subjected to a moderate over-pressure $\dfrac{\Delta P}{\sigma'_o} = 0.5$ and a dimensionless dilatancy parameter equal to the critical value, i.e. $\dfrac{\epsilon_{d,c}}{\beta\sigma'_o} = 0.25$. The different numerical results are obtained with different fault permeability evolution laws: i) constant permeability $k_f = \dfrac{\omega_o^2}{12}$, ii) effective stress-dependent permeability law $k_f = k_* \cdot e^{(-\sigma'/\sigma_*)}$, with $\sigma'_o/\sigma_* = 1 - 2 - 5 - 8$. 95

5.1 A linearly isotropic elastic medium Ω containing a set of pre-existing potential fractures and slip planes whose mid-plane are denoted by Γ. Boundary regions with prescribed displacements or effective traction are denoted respectively as Γ_{u_i} and $\Gamma_{t'_i}$. 99

5.2 Composite yielding surface for displacement discontinuity segments combining a Mohr-Coulomb (region 2) with a tensile cut-off (region 1) - left panel. Softening of tensile strength, cohesion as well as friction is possible ultimately resulting in a purely frictional behavior at complete softening - right panel. A non-associated flow rule for the frictional response limit plastic dilatancy and result in critical state flow at complete softening (right). 101

5.3 Examples of eigenvalues distribution along the complex plane for the matrix $\mathbf{A}$ that arises from final system of equations (5.25) prior (a) and after (b) application of preconditioning matrix $\mathbf{P}_{up}$. Case of a planar fracture in an infinite domain discretized with 100 equal-sized segments with six element active in shear. The spectral radius of the original matrix $\mathbf{A}$ is $\rho(\mathbf{A}) \simeq 56.3$, while the one of the preconditioned matrix is $\rho(\mathbf{A}_p) \simeq 1.64$. 109

5.4 Sketch of branched frictional fault system subjected to a remote compressive load. All the material and geometrical parameters are reported in the figure. 112

5.5 Comparison between the numerical results obtained with the developed solver and the ones of Maerten et al. (2010) in terms of slip and tractions distribution along the main fault branch (left panel) of length $4a$ and along the secondary branch of length $2a$ (right panel). 113

5.6 Sketch of plane strain pressurized wellbore & far field loading conditions. The elasticity matrix is compressed using : $\eta = 5$, $\epsilon_{ACA} = 10^{-6}$, $n_{leaf} = 32$ resulting in a compression ratio $c_r = 0.113$. 114

5.7 Spatial profiles of normalized opening displacement discontinuity $\frac{d_n E_p}{R\sigma_{c,p}}$ (top-left), normal traction $t_n/\sigma_{c,p}$ (top-right) and tensile strength $\sigma_c/\sigma_{c,p}$ (bottom) along the horizontal direction (i.e. $\theta = 0$), at different normalized wellbore pressure $p_b/\sigma_{c,p}$ - $\mathcal{I}_2 = 1$ case. The light grey lines represent the Kirsch analytical solution valid in the elastic range (prior to crack nucleation). 115

5.8 Left: evolution of normalized opening displacement discontinuity at the wellbore $\frac{d_{n_{r=R}} E_p}{R\sigma_{c,p}}$ along the horizontal direction (i.e. $\theta = 0$), as function of normalized borehole pressurization $p_b/\sigma_{c,p}$, for different values of Irwin number $\mathcal{I}$. The dashed horizontal black line represents the theoretical value of normalized borehole pressure estimated from a pure strength criterion. Right: Normalized crack length as function of the normalized wellbore pressure for different Irwin number $\mathcal{I}$. 116

5.9 A rectangular bar subjected to uni-axial compression. Only one quarter of the bar is modelled due to symmetry. A set of structured (S) or unstructured (US) potential segments of failures are tested to investigate the corresponding mesh dependency. A defect (segment with lower strength) is introduced near the bottom-left corner (red segment). 117

5.10 Load-displacement curves for both structured (S) and unstructured (US) mesh, for different intensity values of in-homogeneity ϵ (center plot). The horizontal dashed black line represents the (normalized) traction value at $z = 0$ for plasticity nucleation that one would get if an homogeneous bar with only a pre-meshed slip line at 45° is considered (from the bottom-left corner of the bar to the tractions free lateral side). Evolution of normalized plastic shear deformations $|d_s/d_{s,max}|$ along pre-existing potential failure segments (structured and unstructured mesh) is displayed at different moment along the stress-strain curve. The color and the thickness of each pre-existing segment is proportional to the corresponding shear displacement discontinuity accumulated. 119

5.11 Softening case - Load-displacement curves for a bar subjected to uni-axial compression, discretized with a structured mesh (S) with an initial defect of intensity $\epsilon = 0.5$. Effect of the mesh size h as function with respect to the softening material length scale $l_{pz} = \dfrac{E_p \kappa_c}{c_p}$. 120

5.12 Top: sketch of a retaining wall & boundary conditions adopted. Bottom: evolution of normalized plastic shear deformations $|d_s/d_{s,max}|$ along the pre-existing potential failure segments (unstructured mesh) as a function of normalized translation of the rigid wall $\left|d_{n_{|x=-10}}\right|/H$. 121

5.13 Vertical profile of normalized horizontal stress distribution along the retaining wall (i.e. at $x = -10$) in corresponding of an active limit state. The blue solid line corresponds to the theoretical solution from Rankine theory $\left(K_a = \dfrac{1-\sin(\phi)}{1+\sin(\phi)}\right)$. 122

5.14 Time evolution of the normalized half-crack length a/a_w (left) and normalized peak slip δ/δ_w at the middle of the fault (right), i.e. at $x = 0$, for an ultimately stable fault ($\tau_o/\tau_p = 0.55$), subjected to a moderate over-pressure $\Delta P/\sigma'_o = 0.5$. a_w and δ_w are the characteristic patch length and slip weakening scale, respectively (see Garagash & Germanovich (2012) for details). The friction weakening ratio considered is taken here as $f_r/f_p = 0.6$. 123

5.15 Sketch of a planar fracture with homogeneous frictional properties, embedded in an infinite elastic medium, and subjected to a compressive remote stress $\sigma > 0$. 125

5.16 Benchmark between our numerical results and the analytical solution of Phan et al. (2003) in terms of slip and tractions distribution. The relative error in terms of slip distribution (bottom) shows a good accuracy of the numerical results. 126

5.17 Sketch of an arc crack subjected to a unitary tensile remote stress field $\sigma = -1$. The angle θ that define the extent of the arc crack is $\dfrac{\pi}{2}$, i.e. the pre-existing arc crack is half of a circumference. 127

5.18 Comparison between numerical and analytical results in terms of opening (left) and slip (right) distribution along the arc crack subjected to tensile remote stress. . . . 128

5.19 Sketch of a stair-like fracture located in an unbounded elastic medium. The pre-existing fracture is subjected to a remote compressive stress $\sigma > 0$, such that the fracture's internal surfaces are in contact. . . . 128

5.20 Comparison between our numerical results and the ones Phan et al. (2003) in terms of slip (left) and normal traction (right) distribution along the kinked (inclined) branch of the stair-like fracture. . . . 129

5.21 Sketch of a planar fracture located in an unbounded elastic medium, subjected to i) an initial far field stress whose normal and shear components are denoted respectively by σ_{yy} and σ_{xy} and ii) to a time-dependent mechanical force $F(t)$ applied over an extent of $2d$. For time t lower than a critical value t_c, the mechanical force pulls away the fracture internal surfaces (tension), while the opposite occurs for $t > t_c$ (compression). The pre-existing fracture is characterized by softening constitutive relations (with dilatant behavior in case of shear plastic deformations), except over an extent of $2b$ where only the friction coefficient is at its residual value. . 130

5.22 Normalized profiles of shear (left) and normal (right) plastic deformations in function of time/load evolution t/t_{max}. . . . 131

5.23 Normalized profiles of cohesion (left) and tensile stress (right) in function of time/load evolution t/t_{max}. . . . 131

5.24 Time evolution of normalized shear tractions (top-left), normal tractions (top-right) and shear plastic deformations at the middle of the pre-existing fracture, i.e. at $x = 0$. . . . 132

6.1 Evolution of micro-seismic events in terms of distances from injection source versus their occurrence for (a) Fenton Hill experiment (1983) and (b) the Soultz-sous-Forets experiment (1993). Taken from Shapiro et al. (2002). . . . 134

6.2 Evolution of normalized half crack length a/L with normalized time $\sqrt{4\alpha t}/L$, for a marginally pressurized fault ($\tau_o/\tau_p = 0.55$) subjected to a moderate injection over-pressure $\Delta P/\sigma'_o = 0.5$ (such that $T = 0.9$). The friction coefficient is constant and equal to $f = 0.6$. The inset plot represents the benchmark of our numerical result (red dot) with the analytical solution in terms of self-similar coefficient λ provided by Bhattacharya & Viesca (2019) (grey curves). . . . 137

6.3 Stress criticality evolution as a function of fracture orientation θ and increasing values of effective stress anisotropy ratio κ, for a fixed value of friction coefficient $f = 0.6$ (or critical internal friction angle $\phi_c \simeq 0.54$ radiants). The grey vertical line corresponds to the critical fracture orientation $\theta_c = \pi/4 + \dfrac{\phi_c}{2}$. . . . 141

6.4 Left: critically stressed discrete fracture network. The color of each fracture denotes the stress criticality Λ at ambient condition. Right: initial effective stress state in the Mohr-Coulomb plane for the critically stressed discrete fracture network. Along the circle, which is identified by the two principal effective stresses σ'^{o}_{xx} and σ'^{o}_{yy}, all the uniform stress states of each pre-existing fracture are reported. Since all the pre-existing fractures are randomly oriented within the region $L \times L$, the whole circle is uniformly "covered" by the fractures' initial stress states. 142

6.5 Hiearchical matrix pattern upon compression (with $\eta = 5$, $\epsilon_{ACA} = 10^{-6}$ and $n_{leaf} = 10^3$) with low-rank blocks in green. 143

6.6 Evolution of normalized over-pressure (left column) and plasticity localization (shear deformations - right column) along the pre-existing critically stressed fracture network in function of normalized time/fluid front position $\frac{\sqrt{4\alpha t}}{L/2}$. Fluid is injected at moderate over-pressure $\Delta P / t_{n,o}^{\prime,k_{inj}} = 0.5$ into one fracture that intersect the injection point located at $(1, 1)$. 144

6.7 Maximum number of GMRES iterations required to solve the mechanical problem at each time step. A convergence tolerance $tol = 10^{-6}$ was used for the GMRES iterative solver. 145

6.8 Left: marginally pressurized discrete fracture network. The color of each fracture denotes the stress criticality λ at ambient condition. Right: initial effective stress state in the Mohr-Coulomb plane for the marginally pressurized discrete fracture network. Along the circle, which is identified by the two principal effective stresses σ'^{o}_{xx} and σ'^{o}_{yy}, all the uniform stress states of each pre-existing fracture are reported. Since all the pre-existing fractures are randomly oriented within the region $L \times L$, the whole circle is uniformly "covered" by the fractures' initial stress states. 146

6.9 Evolution of normalized over-pressure (left column) and plasticity localization (shear deformations - right column) along the pre-existing marginally pressurized ($\kappa = 2$) fracture network in function of normalized time/fluid front position $\frac{\sqrt{4\alpha t}}{L/2}$. Fluid is injected at moderate over-pressure $\Delta P / t_{n,o}^{\prime,k_{inj}} = 0.5$ into one fracture that intersect the injection point located at $(1, 1)$. 147

A.1 Normalized stress components due to unit linear displacement discontinuity acting on the reference element. 155

B.1 Evolution of normalized σ_{22} stress along the normalized $\bar{r} = \frac{r}{a}$ -direction due to a linear shear displacement discontinuity acting on an element of length a. The stress evolution decays with normalized distance $\bar{r}$ due to the fast decay of the elastic displacement discontinuity kernel. 159

B.2 Example of block domain decomposition of a discrete fracture network via geometric clustering algorithm introduced by Börm et al. (2003). Three recursive clusterings ($p = 3$) have been computed, thus obtaining 8 nodes of the geometric cluster tree. 163
B.3 Example of block hierarchical partitioning of a dense matrix resulting from discretization of non-local elastic operator. Based on the admissibility condition (B.3), the matrix is subdivided into admissible blocks (green), for which low-rank approximation is applied, and inadmissible blocks (red). Note that all the sub-blocks located along the main diagonal are inadmissible (self-effects). 165

C.1 Sketch of multi-staged fracturing operation in a contained reservoir. The wellbore is drilled in the direction of the minimum horizontal in situ stress σ_h. At each pumping operation, multiple fractures propagate in the direction of the maximum horizontal in situ stress σ_H. This picture is taken from Lecampion & Desroches (2015). 170
C.2 Part 1 of class diagram of HFPx2D core. 174
C.3 Part 2 of class diagram of HFPx2D core. 175
C.4 Part 3 of class diagram of HFPx2D core. 176

List of Tables

5.1 Comparison of the normalized crack initiation pressure obtained here and the ones of Lecampion (2012) for different Irwin numbers $\mathcal{I}$. 114

5.2 Scaled total CPU time and the maximum relative difference obtained during the simulation for different values of η for the hierarchical approximation. The reference numerical solution corresponds to the $\eta = 0$ case (no compression of the elasticity matrix). 124

1 Introduction

1.1 Preamble

Understanding the physical mechanisms associated with fluid injection at depth is of critical importance to all industrial geo-energy projects (geothermal, carbon storage, oil and gas production). In a large number of cases, the rock formation permeability is insufficient to allow economic production and/or injection of fluids, even when the rock mass is naturally fractured. Enhancement of the in-situ permeability is an essential component of field developments. This can be achieved via hydraulic stimulation. This technique consists in injecting fluid into the rock mass in order to shear already pre-existing fractures/faults and/or to create new fractures. The success of the process is ultimately measured by the overall increase of hydraulic conductivity which can be of several order of magnitudes (Economides & Nolte 2000) in the case of hydraulic fracturing.

In this thesis, our focus is on the shear stimulation of pre-existing fractures and faults. Although the mechanism of reduction of effective normal stress and therefore shear strength upon fluid injection is physically simple, the details of the evolution of the hydro-mechanical systems are intricate even for the simple configuration of a planar fault. In particular, depending on rock properties, in-situ and injection conditions, one may observe either solely aseismic slip, or the nucleation of a transient or unabated dynamic ruptures combined with significant aseismic deformation. Keeping in mind the fact that the knowledge of reservoir properties and in-situ conditions are always uncertain at depth, we use simple models including the basic physical ingredients required to explore the different regimes of fluid induced deformation of fractures. We pay particular attention to the development of robust numerical tools and perform in-depth verifications. Our focus on the re-activation of pre-existing fractures is driven by the development of hydraulic stimulation for deep geothermal reservoirs in crystalline rocks.

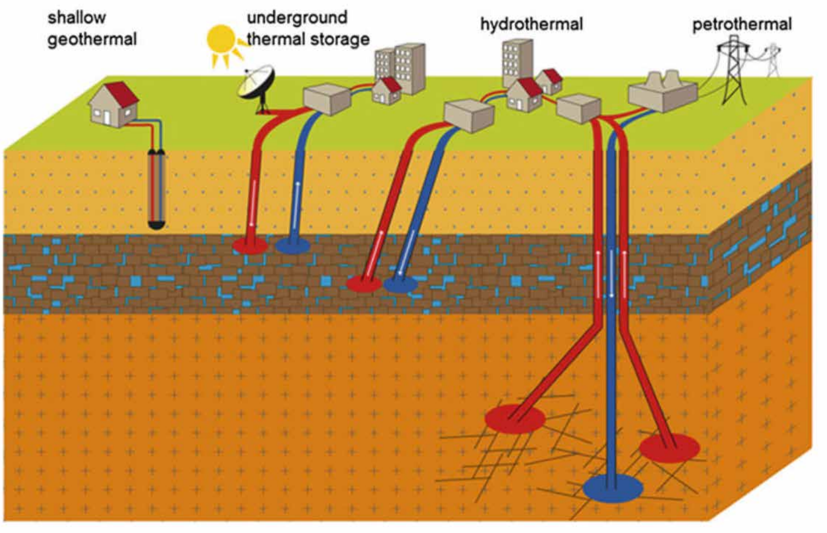

Figure 1.1 – Different existing geothermal systems used to extract thermal energy from sub-surface. Taken from Shao et al. (2016).

1.2 Motivations

1.2.1 Geothermal energy extraction

As suggested by its name, geothermal energy is thermal energy (heat) stored below the Earth surface. Thanks to the low thermal conductivity of the upper Earth crust, heat is trapped at depth with a limited outflow of 0.03% of the total inner Earth heat. The temperature increases with depth a rate of $\sim 25°C$ per kilometer in the lithosphere (away from plate boundaries and hot spots). 99% of the Earth is hotter than 1000°C and only 0.1% is colder than 100°C (Stober & Bucher 2013). According to an estimation of Armstead (1983), the total amount of heat stored by the planet is $\sim 12 \times 10^{24}$ MJ, a number that can be contrasted with the total primary energy supply per year (TPES) of $\sim 6 \times 10^{14}$ MJ (IEA 2019 2019). Geothermal energy, therefore, appears as truly enormous resource, always available and omnipresent.

The idea of geothermal systems is to extract heat from the sub-surface by circulating fluid either in one or between two or more boreholes. This can be done at different depth levels, with different techniques and for different purposes (see Figure 1.1). At shallow depths, geothermal systems extract heat via geothermal probes for heating/cooling of existing buildings. Much larger temperatures are required to generate base load electricity. Geothermal systems in that category are i) hydrothermal systems (also known as conventional geothermal systems) and ii) deep petrothermal systems (also referred as enhanced geothermal systems or hot dry rock systems).
Hydrothermal systems extract thermal energy at depths between 0.2 to 3 Km below Earth surface, typically in regions near tectonic plate boundaries, extensional settings

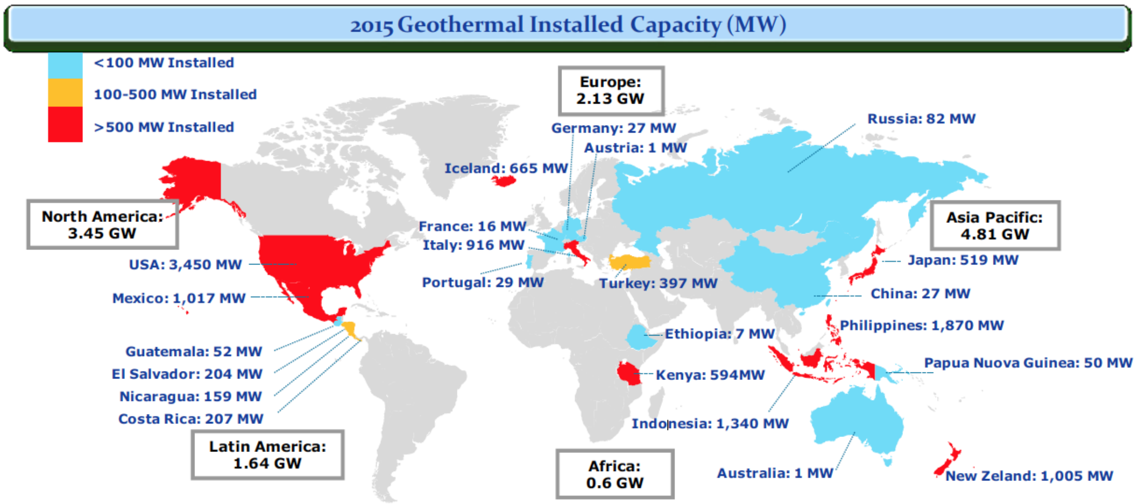
2015 Geothermal Installed Capacity (MW)
<100 MW Installed
100-500 MW Installed
>500 MW Installed
Europe: 2.13 GW
Germany: 27 MW
Austria: 1 MW
Russia: 82 MW
Iceland: 665 MW
North America: 3.45 GW
Asia Pacific: 4.81 GW
France: 16 MW
Italy: 916 MW
USA: 3,450 MW
Japan: 519 MW
Portugal: 29 MW
Turkey: 397 MW
China: 27 MW
Mexico: 1,017 MW
Philippines: 1,870 MW
Ethiopia: 7 MW
Guatemala: 52 MW
Papua Nuova Guinea: 50 MW
El Salvador: 204 MW
Kenya: 594MW
Nicaragua: 159 MW
Costa Rica: 207 MW
Indonesia: 1,340 MW
Latin America: 1.64 GW
Africa: 0.6 GW
Australia: 1 MW
New Zeland: 1,005 MW

Figure 1.2 – Total installed capacity from worldwide geothermal power plants. Taken from Bertani (2015).

or volcanic areas (with temperatures of around 150°C to 300°C). Thanks to a relatively large permeability/transmissivity of rocks at those depths, sufficiently large heat fluxes can be obtained to generate clean and nearly CO_2 free electricity (Beltrami et al. 2000). The first shallow geothermal power plant used to convert thermal energy into electricity date back to 19th century when in Lardarello[1] (Italy) thermal springs have been first used to light few bulbs and then to produce several mega-watts of electricity (Stober & Bucher 2013). Since then, conventional geothermal resources have been developed at different places around the world. Nearly all the installed capacity comes from these reservoirs (see Figure 1.2).

Despite the constant development of conventional geothermal systems, their existence is limited to zones characterised by the simultaneous occurrence of i) sufficient high temperatures in the sub-surface, ii) presence of hot water bearing geological formations and iii) sufficiently high transmissivity of the rock (Hirschberg et al. 2015). In order to overcome these geological constraints, the concept of deep petrothermal systems was introduced in the late of 20th century. The concept is similar to conventional geothermal systems. In this case fluid circulation occurs at larger depths, where temperature is high enough to guarantee a commercial production of energy (generally depths of $\sim 4 - 10$ Km where the temperature is higher than 150°C). Unfortunately at those depths the overall permeability is not sufficient to achieve and maintain production flow rates sufficient for a base electrical load (which typically must range between 30 and 100 l/s (Liu et al. 2019)). In order to let the fluid sweep larger volumes between injection and production well and avoid a thermal breakthrough (i.e. premature cooling of circulating fluid), hydraulic stimulation is used to enhance the permeability of these reservoirs. For this reason, these geothermal systems are typically called enhanced geothermal systems (EGS). The increase of flow transmissivity of these reservoirs is achieved by creating new fracture surfaces or by enhancing the permeability of already pre-existing fractures/faults via shear-induced dilation. Depending on the type of injection conditions, different types of hydraulic stimulation exist. In the following section, a review of these techniques applied to Enhanced Geothermal Systems is reported.

---

[1] Today, the Lardarello's hydrothermal power plant produces about 1.6% circa of the total electrical energy production in Italy.

1.2.1.1 Hydraulic stimulation mechanisms in EGS

Two conceptual models for stimulation mechanism have been adopted and tested over the past 40 years.

The first one, called hot dry rock (HDR) concept, was proposed during the first EGS project at Fenton Hill (Los Alamos National Laboratory in the United States) in 1970 (Murphy et al. 1983). It is based on the idea that the reservoir is regarded as an intact almost impermeable rock mass and only new, propagating opening fractures contribute to permeability enhancement between injection and extraction well. It is nothing else but hydraulic fracturing which is routinely used in oil and gas production (injection of fluid at a rate and pressure sufficient to form and propagate opening mode fractures perpendicular to the minimum effective principal stress).

The second and more recent concept is often referred to as hydro-shearing stimulation. Basically, it consists in injecting fluid into the sub-surface at a pressure sufficiently large to induce shear deformations on favourably oriented pre-existing fractures/faults, but always below the local minimum principal effective normal stress at depth. The resulting deformations contribute to enhance the overall permeability of the fractured rock mass. This stimulation mechanism started to be adopted by the scientific community after the Fenton Hill HDR project, where fluid injection into granitic rock triggered various micro-seismic events on favourably oriented pre-existing fractures (Fehler 1989). Although this concept in itself is relative simple, further investigations of the stimulated rock masses has led to different interpretations on the relevant mechanisms responsible for permeability enhancement. A review of EGS modelling after 1980 shows that the majority of authors assumed shear-induced dilatancy as the governing mechanism to enhance the permeability of deep geothermal reservoirs upon stimulation (Bruel 1995, Willis-Richards et al. 1996, Rahman et al. 2002). Few years later, however, observations of the seismicity cloud pattern associated with hydraulic stimulation together with observations of the corresponding flow rates achieved suggested that a combination of shear-induced dilatancy and propagation of opening fractures (and their coalescence via "wing" cracks) was the main mechanism for permeability enhancement (Jeffrey et al. 2015). Therefore, pre-existing fractures not oriented perpendicular to the minimum principal stress could be forced to open, or partially open, by both increased fluid pressure and local stress perturbations created by the opening and sliding of surrounding fractures.

Regardless of the type of hydraulic stimulation mechanism adopted to enhance the permeability of deep geothermal reservoirs, the stress perturbation caused by fluid injection combined possibly with deformations of pre-existing fractures at depth always lead to micro-seismic events (dynamic shear ruptures of finite size characterised by a moment magnitude M_w that mostly ranges between -4 to 2). In the following, induced seismicity associated with injection of fluid in the sub-surface is briefly reviewed.

1.2.1.2 Injection-induced seismicity

Anthropogenic fluid injection in the sub-surface generate seismicity. This appears during stimulation of geothermal and hydrocarbon reservoirs (Majer et al. 2007, Giardini 2009, Chan & Zoback 2006, Shapiro et al. 2006, Bao & Eaton 2016*a*), geological CO_2 sequestration (Cappa & Rutqvist 2011, Rinaldi et al. 2015) or waste disposal (Healy et al. 1968), where a cloud of events characterized by low/moderate magnitude $M_w \sim [-4, 2]$ is always recorded, typically using existing or dedicated seismic networks (Carnec & Delacourt 1999). Large increase of pore pressure at depth reduces the effective normal stress and thus the frictional strength of pre-existing faults or fractures. When the resistance to sliding is not enough to guarantee equilibrium with applied stresses, then a shear failure (slip) occur. This shear failure can translate into a seismic rupture if the frictional strength decreases faster than the elastic unloading associated with slip (Cornet 2015*b*), a condition that typically occurs along critically stressed faults exhibiting a frictional weakening behaviour. In the context of deep geothermal energy, resounding examples of earthquakes triggered by the activation of critically stressed faults (via direct pressurization or remote stress transfer) are represented by the EGS projects of Soultz (France) (Baria et al. 1999), Cooper Basin (Australia) (Asanuma et al. 2005), Landau (Germany) (Vasterling et al. 2017), Basel (Switzerland) (Majer et al. 2007, Deichmann & Giardini 2009) and Pohang (South Korea) (Grigoli et al. 2018). These events have raised concern about the correlation between extraction of deep geothermal energy and induced seismicity. Some people, in fact, believe that induced seismicity may result in structural damage similar to the one caused by larger natural earthquakes (Majer et al. 2007). For these reasons, large research programs on EGS seismicity have been thus recently pursued (e.g (*Deep Geothermal Energy - R&D Roadmap for Switzerland, 2014* 2014, McKittrick et al. 2019)) with the purpose of providing new systems and tools that can control, to some degree, injection-induced seismicity. Among others, an outcome of these programs is the so called traffic light system (TLS) or advanced traffic light system (ATLS) that enable a real-time monitoring and management of induced seismic vibrations (Mignan et al. 2017, Baisch et al. 2019). An example of EGS with a built-in warning traffic light system for monitoring, quantifying and controlling the risk associated with induced seismicity is the Berlín project (El Salvador) (Bommer et al. 2006). Although it can be useful in principle, the statistical models behind these TLS/ATLS systems, however, have not been extensively validated on larger datasets yet (Mignan et al. 2017). Driven by the increasing attention to geothermal energy and the potential risks associated with fluid injection into the sub-surface, a number of research groups have started to develop numerical simulators that can help the engineering of hydraulic stimulation of fractured rock masses and possibly induced seismicity. In the next section, a short review of some of these simulators is reported.

1.2.2 A short review of existing numerical simulators for hydraulic stimulation of fractured rock masses

Over the past years, several 2-dimensional and 3-dimensional numerical simulators have been introduced and tested in the context of hydraulic stimulation of deep georeservoirs. In the following only the most used will be described.
Among the 2-dimensional solvers, the most used are the “CFRAC-UT" and “CFRAC-Stanford", which are research codes developed respectively by McClure & Horne (2013) and Norbeck et al. (2016). They are both capable of modelling coupled thermo-hydraulic-mechanical (THM) problems using an implicit time integration scheme. They are both boundary element based for elastic continuum (with hierarchical matrix approximation as acceleration technique), while fluid flow is solved with finite volume method or finite difference scheme. They include the presence of discrete fractures, fracture propagation (with a varying number of assumptions), stress-dependent permeability and shear-induced dilatancy. However, the stresses induced by deformations are neglected in “CFRAC-UT" solver (McClure & Horne 2013). Others similar 2D numerical simulators are “GeoFrac-Mech” and “GeoFram-Stim” developed by University of Oklahoma (OU), which in addition to the THM coupling include poro-elasticity. The former is boundary element based as it is a purely mechanical solver, while the latter combine boundary element method for elasticity with finite element method for fluid flow. They are capable of modelling hydraulic stimulation of thermo-poroelastic fractured reservoirs with pre-existing fracture network (White et al. 2017).
Among the 3-dimensional solvers, a widely used THM simulator is “FLAC3D", which is capable of simulating advanced geotechnical analysis of soil, rock and structural support. It is a finite element based solver with fully explicit time integration scheme (Itasca Consulting Group, Inc. (2017) Minneapolis: Itasca. 2017). It can also model slip along plane faults, joints or frictional boundaries. Another used THM simulator that include also the chemical coupling is “GEOS”, which was developed by Lawrence Livermore National Laboratory (LLNL). It is based on finite element method for elastic continuum and finite volume for flow. Both a fully implicit and explicit Euler time integration scheme are implemented is this simulator. It was devised mainly to address hydraulic stimulation of fractured formations and long term production from fractured reservoirs.
Among the 3-dimensional simulators mainly used for flow modelling, “THOUGH2” developed by Lawrence Berkeley National Laboratory (LBNL) in the early 1980s is the most used. It is a TH simulator that adopts an integral finite difference method for spatial discretization of continuum equations and a first-order fully implicit finite difference for time integration (Finsterle 2007). It is capable of addressing nonisothermal multiphase flow in fractured porous media, primarily designed for geothermal reservoirs. This simulator can be linked to “TOUGHREACT” to include the chemical coupling and thus address

problems like mineral alteration in hydrothermal systems (Xu & Pruess 2001) or mineral trapping for CO_2 disposal in basaltic rock (Audigane et al. 2007). Typically, “THOUGH2” is coupled with “FLAC3D", resulting in a THM simulator.

1.3 Organisation of this manuscipt

This thesis is organized as follows.

Chapters 2 and 3 provide the theoretical basis and numerical methods used throughout this thesis. They can be skipped by informed readers.

In Chapter 2, after a brief description of the basic notions of continuum mechanics, the elastic boundary integral equations for fracture problems are summarized as well as their solution via the displacement discontinuity method.
Chapter 3 describes the mathematical modelling of fluid flow in fractures as well as full details about a finite volume scheme that is used in this contribution to discretize the fluid mass conservation equation.

Chapters 4, 5 and 6 are the main contribution of this thesis. The effect of dilatancy on the transition from aseismic to seismic slip along a pressurized planar fault is extensively investigated in chapter 4 using a specific developed fully coupled hydro-mechanical solver. In chapter 5, a new boundary element localized plasticity solver is proposed. A large number of numerical examples highlight its capabilities and its performance. This solver is then used in Chapter 6 to investigate the aseismic slip propagation and fluid diffusion inside fractured rock masses.

Conclusions and perspectives are reported in chapter 7. Additional information about the numerical solvers are described in the appendices.

2 Boundary integral equation for fracture problems

The present work is based on concepts of continuum mechanics under the assumption of quasi-static equilibrium (which is relaxed to quasi-dynamic approximation when explicitly mentioned in the manuscript). Forces or displacements are thus increased or decreased in a quasi-static manner, i.e. slowly enough to guarantee static equilibrium between external and internal forces at any time.
In this chapter, a brief recall of theory of continuum mechanics is first included. This represents the foundation of all the boundary integral equations that will be subsequently introduced. This chapter is finally concluded by presenting the displacement discontinuity method for fracture problems that will be used in all the numerical algorithms proposed in this Ph.D. work.

2.1 Conventions and notations

A Cartesian reference system (O, x_1, x_2, x_3), defined by the basis vectors e_i (with $i = 1, 2, 3$), is used throughout this manuscript. Following this notation, displacement is denoted by u_i, with $i = 1, 2, 3$ denoting the components with respect to x_1, x_2 and x_3 axis of the global reference system. Einstein[1] convention of summation over repeated indices is used otherwise specified. Tensile stresses are considered positive, in line with the convention used by majority of continuum mechanics books. In this contribution this assumption may change prior explicit mentioning. The normal and the shear components of the traction vector are denoted respectively as t_n and t_s. When explicitly mentioned, however, the following change of notation is considered

$$\sigma = t_n, \qquad \tau = t_s$$

Finally, the derivatives with respect to the first or the second argument of a generic multivariable function $g(x, y)$ are represented respectively as

---

[1] Albert Einstein, 14 March 1879 - 18 April 1955.

$$\begin{aligned} g_{,\bar{j}}(x,y) &= \partial_{x_j} g(x,y) \\ g_{,j}(x,y) &= \partial_{y_j} g(x,y) \end{aligned}$$

2.2 Conservation of momentuum

A generic deformable body subjected to generic system of external forces $\mathbf{F}(\mathbf{t})$ is in equilibrium if the Newton's[2] second law (conservation of momentum) under quasi-static assumption is satisfied

$$\sum \mathbf{F}^{\mathbf{ext}}(\mathbf{t}) = \mathbf{0} \tag{2.1}$$

Forces acting on a deformable body can be distributed over its volume Ω (body forces) or can be applied on its external surfaces S (surface forces). The transmitted surface force $\Delta\mathbf{T}$ over a sufficiently small surface area ΔS^- that arise from the virtual splitting into two pieces of the elastic body in equilibrium with applied loads (see Figure 2.1) is called internal *traction* and defined as

$$\lim_{\Delta S^- \to 0} \frac{\Delta \mathbf{T}}{\Delta S^-} = \frac{d\mathbf{T}}{dS^-} = \mathbf{t}_{\mathbf{n}^-}, \tag{2.2}$$

where the subscript $^-$[3] refers to the internal surface associated with unit normal vector $\mathbf{n}^-$, whose components with respect to the global reference system (O, x_1, x_2, x_3) are denoted by n_i^-, with $i = 1, 2, 3$. Note that the internal surfaces that arise from virtual splitting of the deformable body are denoted by S^- and S^+ and they are univocally determined by their orthonormal vectors $\mathbf{n}^-$ and $\mathbf{n}^+$, respectively.
The projection of the traction vector $\mathbf{t}_{\mathbf{n}^-}$ onto the local reference system (see Figure 2.1) leads to normal and tangential stress definition

$$\begin{aligned} \sigma_{nn} &= \sigma_n = t_{n^-i} n_i^- \\ \sigma_{nb} &= \tau_{nb} = t_{n^-i} b_i^- \\ \sigma_{nc} &= \tau_{nc} = t_{n^-i} c_i^-, \end{aligned} \tag{2.3}$$

where $i = 1, 2, 3$. Note that these stress components are applied on a specific point of the deformable body, whose location lies on a specific internal surface S^- univocally identified by the unit normal vector $\mathbf{n}^-$. If the internal traction vector applied on a point of the deformable body is known is one coordinate system (for instance in the global reference system), then it is possible to evaluate the stress components on any infinite surfaces passing through that point by simply applying a rotation transformation. This requires only the knowledge of the direction cosine matrix.

The enforcement of equilibrium (translation and rotation) on a generic tetrahedron

---

[2] Issac Newton, 25 December 1642 - 20 March 1726.

[3] $n^- = -n^+ = -n_i$.

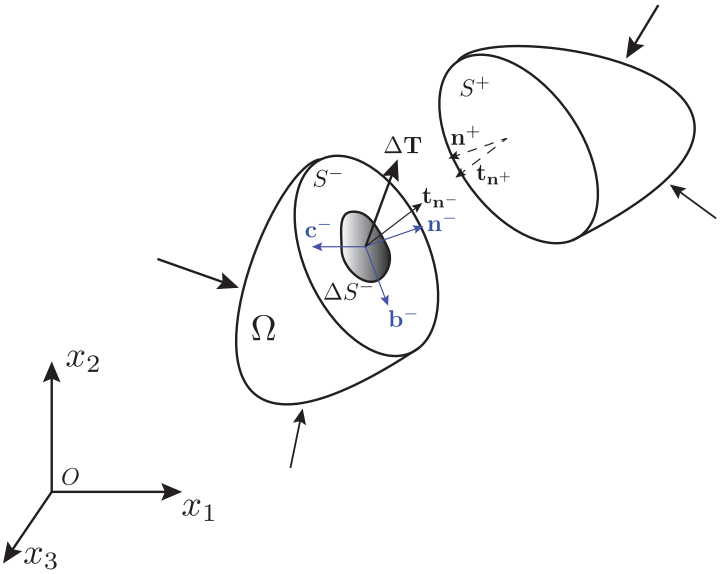

Figure 2.1 – Traction vector definition from virtual splitting of an elastic deformable body subjected to a generalised system of forces.

subjected to internal tractions leads to the so called Cauchy[4] equations

$$t_{ni} = \sigma_{ij} n_j, \tag{2.4}$$

where σ_{ij} are the components of the 2nd order symmetric stress tensor Σ. Note that the superscript $^-$ for the orthonormal vector $\mathbf{n}^-$ has been dropped for sake of simplicity and compactness. The traction vector applied on the internal surface with orthornormal vector $\mathbf{n}^-$ will be simply denoted as $\mathbf{t_n}$. Given the stress tensor at a point of a deformable body, the local analysis of equilibrium thus allows to define tractions at any plane passing through that point. When a deformable body is subjected to a generalised system of forces, the stress state changes point by point within the body. In order to determine its stress distribution, the local analysis of equilibrium must be extended to the whole body, i.e. the Newton's second law must be generalised to the whole body.

The application of Newton's second law to an arbitrary infinitesimal volume $\Delta\Omega$ of deformable body in equilibrium with a generalised system of forces (composed of body forces $\mathbf{f}$ and surface forces $\mathbf{p}$) leads to the following equilibrium equation

$$\int_{\Delta S} \mathbf{t_n} \mathrm{d}(\Delta S) + \int_{\Delta\Omega} \mathbf{f} \mathrm{d}(\Delta\Omega) = 0, \tag{2.5}$$

which can be projected onto the axis of the global reference system, leading to a set of three scalar equations for momentum conservation

---

[4] Augustin-Louis Cauchy, 21 August 1789 - 23 May 1857.

$$\int_{\Delta S} t_{ni} \mathrm{d}(\Delta S) + \int_{\Delta\Omega} f_i \mathrm{d}(\Delta\Omega) = 0, \tag{2.6}$$

with $i = 1, 2, 3$.
Upon application of Green theorem[5] and knowing that equation (2.6) is valid for any infinitesimal volumes inside the deformable body, the conservation of momentum reduces in compact form to

$$\sigma_{ij,j} + f_i = 0, \tag{2.7}$$

being $i, j = 1, 2, 3$.

Equation (2.7) must be satisfied at any point inside the deformable body. When the generic point lies on its lateral surface, then the conservation of momentum at boundary conditions dictates that

$$t_{ni} = \sigma_{ij} n_j = p_i \tag{2.8}$$

Equation (2.7) together with equation (2.8) represent a *statically admissible stress field.*

2.3 Kinematics and compatibility

In continuum mechanics, the kinematics analysis of a deformable body quantifies its relative deformation with respect to a reference state, regardless of the causes that have led to the deformation (Viola 2003). Mathematically, the deformation process can be described by a vectorial function **u**

$$\mathbf{u} : \mathcal{C} \to \mathcal{C}' \tag{2.9}$$

whose domain is represented by the reference state $\mathcal{C}$, while its codomain is the new deformed configuration $\mathcal{C}'$ (see Figure 2.2). This vectorial function is the *displacement field* and it must be compatible with respect to some requirements: i) it must belong to C1 class of functions and ii) it must have the property of being univocal (i.e. for one point in the configuration $\mathcal{C}$, there is only one corresponding point in the configuration $\mathcal{C}'$). The components with respect to the global reference system of displacement field in a generic point P of the deformable body can be obtained by taking a Taylor series expansion in a point P_o located in the infinitesimal neighbourhood of point P, i.e.

$$u_k = u_{ok} + \left(u_{k,l}\right)_o \mathrm{d}x_l, \tag{2.10}$$

---

[5] Green's theorem gives the relationship between a line integral around a simple closed curve C and a double integral over the plane region D bounded by C.

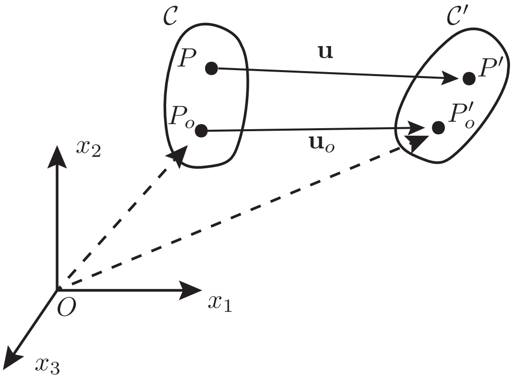

Figure 2.2 – Displacement field of an elastic body subjected to generalised system of forces.

with $k, l = 1, 2, 3$. Note that in equation (2.10), the vectorial function $\mathbf{u}$ has been linearised. This approximation is generally valid for deformations that occur in infinitesimal neighbourhood, i.e. when small (infinitesimal) strain approximation is valid (which is employed throughout this manuscript). The components $\left(u_{k,l}\right)_o$ define a square Jacobian matrix for the functions u_k. By removing the rigid body motion that does not produce any deformation, equation (2.10) reduces to

$$u_k = u_{o,k} + \epsilon_{kl} d_l, \tag{2.11}$$

where d_l are the components of the displacement vector, whereas ϵ_{kl} are the components of the 2nd order strain tensor $\bar{\bar{\epsilon}}$. These strain components are linear with respect to displacements and they are define as

$$\epsilon_{kl} = \frac{1}{2}\left(u_{k,l} + u_{l,k}\right) \tag{2.12}$$

The displacement field at boundary conditions must also be compatible, i.e. the following relation must be satisfied at all the points that lie on the later surface of the elastic body where deformations are prescribed

$$u_k = \hat{u}_k \tag{2.13}$$

The displacement field defined by the components u_k and the corresponding deformations ϵ_{kl} defined in equation (2.12) represent a *kinematically admissible displacement field.*

2.4 Link between equilibrium and compatibility

Equilibrium and compatibility of a deformable body subjected to a generalised system of forces have been derived independently from each other. Principle of virtual work represents a fundamental link between them. Starting from the compatibility equations, principle of virtual work allows to determine equilibrium equation or vice-versa. Assuming an independent statically admissible stress field q (for which equations (2.7) and (2.8) are satisfied) and another independent kinematically admissible displacement field p, principle of virtual work states that the inner work done by internal forces equals the external work done by external forces (body $\mathbf{f}$ or surface $\mathbf{p}$ forces):

$$\underbrace{\int_\Omega f_i^q u_i^p \mathrm{d}\Omega + \int_S p_i^q u_i^p \mathrm{d}S}_{L_{ve}} = \underbrace{\int_\Omega \sigma_{ij}^q \epsilon_{ij}^p \mathrm{d}\Omega}_{L_{vi}} \tag{2.14}$$

It is worth mentioning that the principle of virtual work is valid for any kind of material composing the generic deformable body, i.e. it is independent from material's mechanical properties.

2.5 Constitutive law

The three equilibrium equations derived from momentum conservation (2.7) are necessary but not sufficient conditions to define univocally the stress state in a generic point of a deformable body subjected to a generalised system of forces (three equations with six unknowns due to symmetry of stress tensor). In other words, the stress state in a point is intrinsically hyperstatic. In order to solve the equilibrium problem, links between stresses and strains must be introduced.

In the present work, the theory of linear elasticity is used. For a deformable body under equilibrium conditions, stresses and strains at each material point are proportional to each other (Hooke's law)

$$\sigma_{ij} = c_{ijkl}\epsilon_{kl}, \tag{2.15}$$

where c_{ijkl} are the components of 4-th order stiffness tensor. Under the assumption of isotropic material (which is valid throughout this manuscript), equation (2.15) reduces to

$$\sigma_{ij} = \frac{2G\nu}{1-2\nu}\delta_{ij}\epsilon_{kk} + 2G\epsilon_{ij}, \tag{2.16}$$

where δ_{ij} is the Kronecker delta defined as

$$\delta_{ij} = \begin{cases} 1 & \text{if} \quad i = j, \\ 0 & \text{if} \quad i \neq j, \end{cases} \tag{2.17}$$

G is the shear modulus and ν is the Poisson's ratio. The shear modulus G is related to the Young's modulus E by the following relation

$$G = \frac{E}{2\left(1+\nu\right)} \tag{2.18}$$

The equilibrium of a linear elastic material in terms of displacement is thus obtained by combining equations (2.7), (2.12) and (2.16), leading to the so called Navier-Cauchy equilibrium equation

$$\frac{2G\nu}{1-2\nu}u_{i,ik} + G\left(u_{k,jj} + u_{j,kj}\right) + f_k = 0 \tag{2.19}$$

A deformable body subjected to generalised system of forces (body and/or surface forces applied on its boundary) and/or to prescribed displacements, therefore, deforms in order to conserve its momentum. The unknown elastic field, which is defined by compatible displacements, strains and stresses inside the deformable body can be found by solving equation (2.19) with the appropriate boundary conditions, i.e. by solving the corresponding *well-posed boundary value problem.*

2.6 Maxwell-Betti reciprocity theorem

The assumption of isotropic linear elasticity (Hooke's law) combined with small deformations and quasi-static loading implies the principle of superposition. Stresses and displacements that arise from simultaneous application of generic forces are the same, respectively, of the sum of stresses and displacements that arise from single virtual application of generic forces (applied separately). The principle of virtual work (2.14) as well as the superposition principle of effects are fundamental ingredients of the Maxwell-Betti reciprocity theorem[6], which states the equivalence of the cross elastic energy between two states (distinguished by the superscripts $^{(1)}$ and $^{(2)}$) belonging to the same material space, i.e.

$$\int_\Omega \sigma_{ij}^{(1)}\epsilon_{ij}^{(2)}\mathrm{d}\Omega = \int_\Omega \sigma_{ij}^{(2)}\epsilon_{ij}^{(1)}\mathrm{d}\Omega \tag{2.20}$$

Due to validity of principal of virtual work (2.14) and upon application of divergence theorem, the Maxwell-Betti reciprocity theorem can be written as

$$\int_S \left(\sigma_{ij}^{(1)}n_j\right)u_j^{(2)} - \left(\sigma_{ij}^{(2)}n_j\right)u_j^{(1)}\mathrm{d}S = \int_\Omega f_i^{(2)}u_i^{(1)} - f_i^{(1)}u_i^{(2)}\mathrm{d}\Omega \tag{2.21}$$

The superposition principle of effects leads to another important consequence with respect to the solution of a well-posed elastic boundary value problem: its uniqueness (also known as principle of Kirchhoff[7]). For a given set of boundary conditions, there exist one and only one solution of the associated elastic boundary value problem. This important principle does not necessarily imply that the solution can be obtained analytically. Only in some particular cases, under specific conditions, equation (2.19) can be solved analytically. This is the case, for instance, of the Kelvin fundamental solution (point force solution), which will be presented in the next section. Generally, however, boundary value problems in continuum mechanics can only be solved using numerical methods.

---

[6] Discovered by Enrico Betti in 1872.

2.7 Kelvin fundamental solution

The fundamental solution of a unit point force in the direction of k-th Cartesian coordinate axis ($k = 1, 2, 3$), located at point $\mathbf{x}$ in an infinite[8], homogeneous, isotropic and linear elastic medium Ω is attributed to Lord Kelvin[9] and is referred to as the Kelvin fundamental solution. It is the analytical solution of the following well-posed boundary value problem

$$\begin{aligned} &\sigma_{ij,j} + \delta_{ik}\delta(\mathbf{y} - \mathbf{x}) = 0, \\ &\sigma_{ij} = c_{ijkl}\epsilon_{kl} = c_{ijkl}u_{k,l} \end{aligned} \tag{2.22}$$

with the following boundary conditions (that are valid only for the case of full space)

$$\lim_{y\to\infty} \sigma_{ij} = 0, \qquad \lim_{y\to\infty} u_i = 0 \tag{2.23}$$

By transforming the balance of momentum in equation (2.22) into Navier equations, one obtains

$$U^k_{i,ll} + \frac{1}{1-2\nu} U^k_{l,li} + \delta_{ik}\delta(\mathbf{yx})/G = 0, \tag{2.24}$$

where the notation $U_i^k(\mathbf{x}, \mathbf{y})$ denotes the ith displacement component at $\mathbf{y}$ (observation point) due to a point force in the direction k located at $\mathbf{x}$ (source point). The displacement solution can be sought in the following form

$$U_i^k = 2\,(1-\nu)\, g^k_{i,jj} - g^k_{j,ji} \tag{2.25}$$

where g_i^k denotes the Galerkin tensor, which must be the solution of the following fundamental bi-harmonic equation

$$g^k_{i,jjll} = -\frac{\delta_{ik}\delta(\mathbf{y} - \mathbf{x})}{2G\,(1-\nu)} \tag{2.26}$$

---

[7] Gustave Robert Kirchhoff, Konigsberg 1824-Berlin 1887.

[8] Note that this fundamental solution is known also for other domains, such as half-space and bi-material, for both isotropic and anisotropy elasticity (e.g. transverse isotropy or orthotropy).

[9] 26 June 1824 - 17 December 1907.

Restricting to the bi-dimensional case, by solving equation (2.26) for the Galerkin tensor g_i^k and then by introducing it in equation (2.25), one can obtain the analytical expression of the second order tensor U_i^k, whose components are given by

$$U_i^k(\mathbf{x},\mathbf{y}) = \frac{-\left(3-4\nu\right)\delta_{ki}\ln r + r_{,k}r_{,i}}{8\pi G\left(1-\nu\right)} \tag{2.27}$$

where $r = |\mathbf{y}-\mathbf{x}|$ is the relative distance between source and observation point and $r_{,k} = \partial r/\partial y_k$. Note that this fundamental solution is valid at any point $\mathbf{y}$, except when $\mathbf{y}=\mathbf{x}$ for which it is singular (due to the presence of $\ln(r)$).

The tensor $\mathbf{U}$ has also the property of being symmetric, i.e. the displacement component i due to unit point force in direction k is equal to the displacement component k due to unit point force in direction i, i.e.

$$U_i^k(\mathbf{x},\mathbf{y}) = U_k^i(\mathbf{y},\mathbf{x}) \tag{2.28}$$

The ij stress tensor components at point $\mathbf{y}$ due to a unit point force in the direction k located at point $\mathbf{x}$ is obtained via the following relation (restricting to the 2-dimensional case)

$$\begin{aligned} S_{ij}^k(\mathbf{x},\mathbf{y}) &= C_{ijmn}U_{m,n}^k(\mathbf{x},\mathbf{y}) \\ &= -\frac{1}{4\pi(1-\nu)r}\left[2r_{,i}r_{,j}r_{,k} + (1-2\nu)(\delta_{ik}r_{,j}+\delta_{jk}r_{,i}-\delta_{ij}r_{,k})\right], \end{aligned} \tag{2.29}$$

which can be rewritten in terms of traction vector as

$$T_i^k = S_{ij}^k(\mathbf{x},\mathbf{y})n_j(\mathbf{y}) \tag{2.30}$$

Note that the second order stress tensor presents a higher singularity as $\mathbf{x}\to\mathbf{y}$ compared to displacement tensor.

2.8 Boundary integral representation

The application of the Maxwell-Betti reciprocity theorem (2.21) between two elastic states corresponding to i) Kelvin fundamental solution[10] and ii) unknown elastostatic state $(\mathbf{u},\bar{\bar{\sigma}},\mathbf{F})$, leads to the so called Somigliana[11] identities (Bonnet 1999*a*):

$$\bar{\kappa}u_k(\mathbf{x}) = \int_S \left[\sigma_{ij}(\mathbf{y})U_j^k(\mathbf{x},\mathbf{y}) - S_{ij}^k(\mathbf{x},\mathbf{y})u_j(\mathbf{y})\right] n_i(\mathbf{y})\mathrm{d}S + \int_\Omega f_i(\mathbf{y})U_i^k(\mathbf{x},\mathbf{y})\mathrm{d}\Omega \tag{2.31}$$

where $\bar{\kappa}=1$ for $\mathbf{x}\in\Omega$ and $\bar{\kappa}=0$ for $\mathbf{x}\notin\Omega$. Equation (2.31) represents a boundary integral representation for the displacement at any point $\mathbf{x}$ within the elastic deformable

---

[10] Because of its singularity when observation and source point coincide, a limiting process has to be taken into account. See XXX for more details.

[11] Carlo Somigliana, 20 September 1860 - 20 June 1955.

body. In other words, the displacement (and thus strain and stress) at any point located inside the elastic deformable body can be calculated only by knowing the distribution of tractions and displacements on its boundary. The resulting elasto-static state satisfies the conservation of momentum and its deformation field is intrinsically compatible.
It is also important to note that the fundamental Kelvin solution for displacement (2.27) and stresses (2.29) tends to infinity when $\mathbf{x} \in S$. The above integral representation is thus singular and undefined for $\mathbf{x} \in S$. In order to overcome this problem, regularization techniques must be adopted (for more details see Bonnet (1999*a*), Mogilevskaya (2014*a*), Mogilevskaya & Nikolskiy (2014)).

Introducing the generic traction vector $t_i = \sigma_{ij} n_j$ and its fundamental counterpart T_i^k (2.30), one can rewrite equation (2.31) as

$$\kappa u_k(\mathbf{x}) = \int_S \Big[t_i(\mathbf{y}) U_j^k(\mathbf{x},\mathbf{y}) - T_i^k(\mathbf{x},\mathbf{y}) u_j(\mathbf{y}) \Big] \mathrm{d}S + \int_\Omega f_i(\mathbf{y}) U_i^k(\mathbf{x},\mathbf{y}) \mathrm{d}\Omega \tag{2.32}$$

A similar integral representation can be obtained for strains and stresses. For $\mathbf{x} \in \Omega$ and not belonging to S, equation (2.31) can be differentiated, leading to the boundary integral representation in terms of strain

$$u_{k,l} = \int_S \Big[\sigma_{ij}(\mathbf{y}) U^k_{j,\bar{l}}(\mathbf{x},\mathbf{y}) - S^k_{ij,\bar{l}}(\mathbf{x},\mathbf{y}) u_j(\mathbf{y}) \Big] n_i(\mathbf{y}) \mathrm{d}S + \int_\Omega f_i(\mathbf{y}) U^k_{i,\bar{l}}(\mathbf{x},\mathbf{y}) \mathrm{d}\Omega, \tag{2.33}$$

which in turn provide the following integral representation for the stress tensor

$$\begin{aligned} \sigma_{ij}(\mathbf{x}) = & \int_S \Big[\sigma_{ab}(\mathbf{y}) c_{ijkl} U^k_{b,\bar{l}}(\mathbf{x},\mathbf{y}) - c_{ijkl} S^k_{ab,\bar{l}}(\mathbf{x},\mathbf{y}) u_a(\mathbf{y}) \Big] n_b(\mathbf{y}) \mathrm{d}S \\ & + \int_\Omega f_a(\mathbf{y}) c_{ijkl} U^k_{a,\bar{l}}(\mathbf{x},\mathbf{y}) \mathrm{d}\Omega \end{aligned} \tag{2.34}$$

In the following, a particular application of equation (2.34) to **bi-dimensional** fracture problems is reported using the so called displacement discontinuity method.

2.9 Displacement discontinuity method for fractures

Let us consider an infinite elastic medium of domain $\Omega \in \mathbb{R}^2$ and boundary Γ, with symmetric stiffness tensor c_{ijkl}. In this specific case, Γ represents the plane of a pre-existing fracture in the medium[12], whose unit normal is denoted by n_i (see Figure 2.3).
It is common practice in geomechanics to solve boundary value problems in terms of changes with respect to an initial state. Denoting σ^o_{ij} the initial elasto-static stress state,

---

[12] Note that multiple pre-existing fractures can also be considered and the principle of superimposition of effect is still valid.

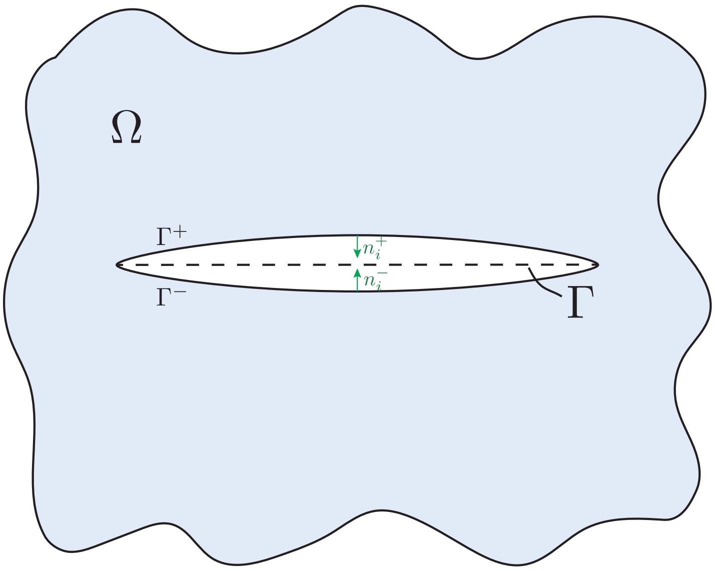

Figure 2.3 – Pre-existing crack in an infinite, linear elastic, isotropic and homogenous medium. This crack lies along the boundary Γ, which has been ideally divided in upper and lower part in order to differentiate respectively the upper and the lower surface of the fracture.

the balance of momentum (2.7) in absence of body forces reduces to

$$\sigma_{ij,j} - \sigma^o_{ij,j} = 0 \tag{2.35}$$

with $i, j = 1, 2$.
Several boundary element methods have been developed for fracture problems, notably the dual boundary element method or the multi-region approach which model the two opposite fracture surfaces. In this contribution, the so called displacement discontinuity method (sometimes also named as distributed dislocations technique) is adopted. This numerical method is a particular type of boundary element method. It fits very well solid mechanics' problems that involve slit-like opening, such as fractures or faults (Crouch & Starfield 1983). In this framework, in fact, displacement jumps (either parallel or perpendicular to fractures' planes) are directly discretised, thus avoiding the modelling of the two faces of the fractures. Restricting to the bi-dimensional case, this method is built on the analytical solution of a plane dislocation located in an infinite elastic space (or equivalently on the Kelvin fundamental point force solution). Specifically, the numerical solution makes use of superimposition of plane dislocations (or unit point forces) along the boundary of the body such to satisfy approximately its specified boundary conditions (which are necessary conditions for a well-posed elastic boundary value problem). Or, in other words, the solution of a well-posed boundary value problem reduces to find the distribution of dislocations (or point forces) along the boundary of a generic elastic body such that its boundary conditions are approximately satisfied. This distribution can then

be used to calculate the unknown elasto-static field within the body via the Somigliana identities (2.31)-(2.34).

In the context of displacement discontinuity method, therefore, the primary kinetic variables are the displacement jumps across the fracture(s). For sake of clarity, a generic fracture is composed of two surfaces: the top surface Γ^+ with unit normal n_i^+, and the bottom surface Γ_- whose unit normal is denoted by n_i^- (such that $n_i^+ = -n_i^- = -n_i$[13]). The displacement discontinuity across the fracture is defined as

$$d_i = u_i^- - u_i^+, \tag{2.36}$$

and is positive in overlap (consistent with the unit normal vector considered). The corresponding traction vector across the fracture is assumed continuous across its surfaces[14]

$$\rho_i = \left(\sigma_{ij}^- - \sigma_{ij}^+\right) n_j = 0 \tag{2.37}$$

The fracture is thus self-equilibrated. These considerations are valid for all the potential pre-existing fractures located in the elastic medium.

2.9.1 Displacement boundary integral representation

Restricting to the case of an infinite (full) space with fracture surface Γ, the boundary integral representation for the stress tensor (2.34) reads (accounting for an initial state of stress and neglecting any body forces):

$$\begin{aligned} \sigma_{ij}(\mathbf{x}) - \sigma_{ij}^o(\mathbf{x}) = \int_{\Gamma^+} &\left[\left(\sigma_{ab}^+(\mathbf{y}) - \sigma_{ab}^o(\mathbf{y})\right) c_{ijkl} U_{b,\bar{l}}^k - c_{ijkl} S_{ab,\bar{l}}^k(\mathbf{x},\mathbf{y}) u_a^+(\mathbf{y})\right] n_b^+ \mathrm{d}S_y \\ \int_{\Gamma^-} &\left[\left(\sigma_{ab}^-(\mathbf{y}) - \sigma_{ab}^o(\mathbf{y})\right) c_{ijkl} U_{b,\bar{l}}^k - c_{ijkl} S_{ab,\bar{l}}^k(\mathbf{x},\mathbf{y}) u_a^-(\mathbf{y})\right] n_b^- \mathrm{d}S_y, \end{aligned} \tag{2.38}$$

which for (2.36) and (2.37) reduces to:

$$\sigma_{ij}(\mathbf{x}) - \sigma_{ij}^o(\mathbf{x}) = \int_\Gamma \rho_i(\mathbf{y}) c_{ijkl} U_{b,\bar{l}}^k(\mathbf{x},\mathbf{y}) \mathrm{d}S_y - \int_\Gamma c_{ijkl} S_{ab,\bar{l}}^k(\mathbf{x},\mathbf{y}) d_a(\mathbf{y}) n_b(\mathbf{y}) \mathrm{d}S_y \tag{2.39}$$

---

[13] n_i is thus positive toward the interior of Ω. This is consistent with the definition of positive eigenstrain in tension.

[14] Note that it can also be discontinuous in case, for instance, fluid flow inside the fracture induces a very small shear stress. In this contribution, it is neglected.

Since the fracture is self-equilibrated, the boundary integral representation written in terms of stress and total tractions is respectively

$$\begin{aligned}\sigma_{ij}(\mathbf{x}) - \sigma^o_{ij}(\mathbf{x}) &= -\int_\Gamma c_{ijkl} S^k_{ab,\bar{l}}(\mathbf{x},\mathbf{y}) d_a(\mathbf{y}) n_b(\mathbf{y}) \mathrm{d}S_y, \\ t_i(\mathbf{x}) - t^o_i(\mathbf{x}) &= -n_j(\mathbf{x}) \int_\Gamma c_{ijkl} S^k_{ab,\bar{l}}(\mathbf{x},\mathbf{y}) d_a(\mathbf{y}) n_b(\mathbf{y}) \mathrm{d}S_y,\end{aligned} \tag{2.40}$$

or equivalently

$$\begin{aligned}\sigma_{ij}(\mathbf{x}) - \sigma^o_{ij}(\mathbf{x}) &= \int_\Gamma c_{ijkl} S^k_{ab,l}(\mathbf{x},\mathbf{y}) d_a(\mathbf{y}) n_b(\mathbf{y}) \mathrm{d}S_y, \\ t_i(\mathbf{x}) - t^o_i(\mathbf{x}) &= n_j(\mathbf{x}) \int_\Gamma c_{ijkl} S^k_{ab,l}(\mathbf{x},\mathbf{y}) d_a(\mathbf{y}) n_b(\mathbf{y}) \mathrm{d}S_y,\end{aligned} \tag{2.41}$$

It is interesting to note that the integral $\int_\Gamma c_{ijkl} S^k_{ab,l}(\mathbf{x},\mathbf{y}) d_a(\mathbf{y}) n_b(\mathbf{y}) \mathrm{d}S_y$ corresponds to the stress at point $\mathbf{x}$ due a distribution of displacement discontinuity $d_a(\mathbf{y})$ located along the fracture surface Γ of normal $n_b(\mathbf{y})$. The product $d_a(\mathbf{y}) n_b(\mathbf{y})$ is thus akin to a point dislocation dipole, which is a combination of two edge dislocations of opposite sign (see next sections for more details).

Integrating by parts the boundary integral equations in (2.41), assuming that $d_a = 0$ at the crack tips, one obtains

$$\begin{aligned}\sigma_{ij}(\mathbf{x}) - \sigma^o_{ij}(\mathbf{x}) &= -\int_\Gamma c_{ijkl} S^k_{ab}(\mathbf{x},\mathbf{y}) \left[d_a(\mathbf{y}) n_b(\mathbf{y})\right]_{,l} \mathrm{d}S_y \\ t_i(\mathbf{x}) - t^o_i(\mathbf{x}) &= -n_j(\mathbf{x}) \int_\Gamma c_{ijkl} S^k_{ab}(\mathbf{x},\mathbf{y}) \left[d_a(\mathbf{y}) n_b(\mathbf{y})\right]_{,l} \mathrm{d}S_y\end{aligned} \tag{2.42}$$

where the term $[d_a(\mathbf{y}) n_b(\mathbf{y})]_{,l}$ represents the surface gradient[15] of $d_a(\mathbf{y}) n_b(\mathbf{y})$ and its expression is given by

$$[d_a(\mathbf{y}) n_b(\mathbf{y}])]_{,l} = d_{a,l}(\mathbf{y}) n_b(\mathbf{y}) - n_l(\mathbf{y}) d_{a,b}(\mathbf{y}) \tag{2.43}$$

Substituting equation (2.43) into equation (2.42), the following boundary integral equations for traction vectors can be obtained

$$t_i(\mathbf{x}) - t^o_i(\mathbf{x}) = -n_j(\mathbf{x}) \int_\Gamma c_{ijkl} S^k_{ab}(\mathbf{x},\mathbf{y}) \left[d_{a,l}(\mathbf{y}) n_b(\mathbf{y}) - n_l(\mathbf{y}) d_{a,b}(\mathbf{y})\right] \mathrm{d}S_y, \tag{2.44}$$

which are valid for $\mathbf{x} \in \Omega$. Knowing the tractions applied on the fracture plane Γ, equation (2.44) represents a set of scalar integral equations that can be solved to obtain the corresponding distribution of the unknown dislocations (this is the reason why displacement discontinuity method is also referred to as distributed dislocation technique). In the next two sections, the fundamental solution of an edge dislocation and dislocation dipole are described. This is important in order to show the link between the fundamental displacement discontinuity tensor $c_{ijkl}S^k_{ab,l}(\mathbf{x},\mathbf{y})$ and the one obtained with dislocation dipoles.

---

[15] For a scalar function f, the surface gradient is defined as $\nabla_S f = f_{,i} - (f_{,j} n_j) n_i$.

2.9.1.1 Fundamental edge dislocation solution

The edge[16] dislocation solution is another fundamental solution in plane elasticity that is widely used for crack problems. In two dimensions, a dislocation in an infinite elastic solid can be viewed as a slit whose starting- and end- points are respectively the centre of the dislocation itself and any infinitely remote point (Hill et al. 1996). Along this slit, a constant displacement is imposed such that two adjacent points located on either sides move relatively between each other (for this reason they are commonly called Volterra[17] type of dislocations). This constant relative displacement is known in literature as the Burger vector $\mathbf{b} = (b_1, b_2)$. Depending on the relative position between the Burger vector and the slit (or path cut), different types of dislocation can be identified. By definition, *climb* dislocations are the ones characterised by a Burger vector perpendicular to the path cut, whereas *glide* dislocations are those with Burger vector parallel to the slit (for this reason they are often called shear dislocations).
The fundamental solution in terms of stress and displacement due to an edge dislocation in an infinite, homogenous, linear elastic and isotropic material can be obtained by solving the corresponding well-posed elastic boundary value problem. Restricting to the 2-dimensional case, the fundamental solution in terms of displacements due to a generic dislocation with Burger vector $\mathbf{b} = (b_1, b_2)$ reads (Hill et al. 1996)

$$\begin{aligned} u_1 &= +\frac{b_1}{2\pi(\kappa+1)\left[(\kappa+1)\theta + \dfrac{2x_1x_2}{r^2}\right]} \\ u_2 &= -\frac{b_2}{2\pi(\kappa+1)\left[(\kappa-1)\mathrm{log}r + \dfrac{2x_1^2}{r^2}\right]}, \end{aligned} \tag{2.45}$$

where $r^2 = x_1^2 + x_2^2$ is the Euclidean distance between the centre of dislocation and observation point, θ is the angle between r and x_1-axis and $\kappa = \dfrac{3-4\nu}{1+\nu}$ is the Kolosov's[18] constant for plane stress (or $\kappa = 3 - 4\nu$ in case of plane strain). Because of the validity of the Hooke's law, the corresponding fundamental solution in terms of stress is given by

$$\sigma_{ij} = \underbrace{\frac{2G}{\pi(\kappa+1)}h_{ijk}}_{s_{ijk}} b_k, \tag{2.46}$$

---

[16] The terminology "edge" refers to the plane strain case.

[17] Vito Volterra, 3 May 1860 - 11 October 1940.

[18] Gury Vasilievich Kolosov, 25 August 1867 - 7 November 1936

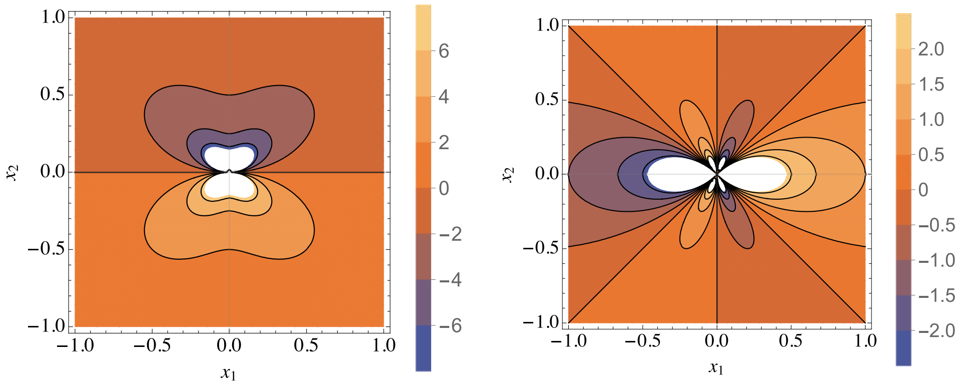

(a) h_{111}, i.e. $\frac{\pi(\kappa+1)}{2G}\sigma_{11}$ due to unit b_1

(b) h_{112} or h_{121}, i.e. $\frac{\pi(\kappa+1)}{2G}\sigma_{11}$ due to unit b_2 or $\frac{\pi(\kappa+1)}{2G}\sigma_{12}$ due to unit b_1.

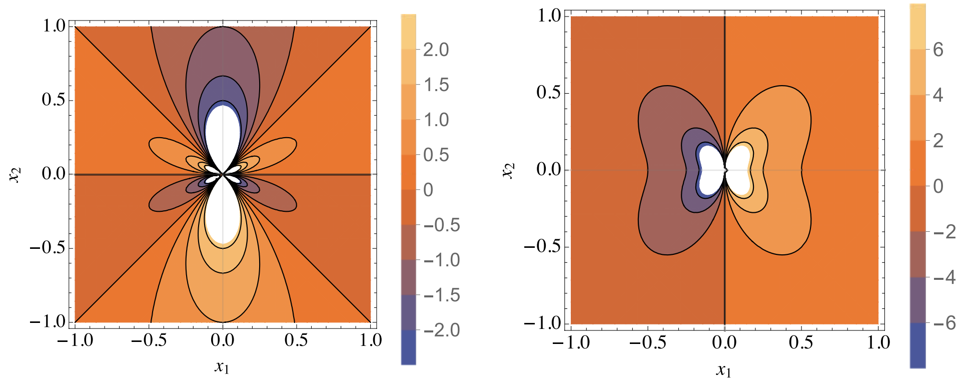

(c) h_{221} or h_{122}, i.e. $\frac{\pi(\kappa+1)}{2G}\sigma_{22}$ due to unit b_1 or $\frac{\pi(\kappa+1)}{2G}\sigma_{12}$ due to unit b_2.

(d) h_{222}, i.e. $\frac{\pi(\kappa+1)}{2G}\sigma_{22}$ due to unit b_2.

Figure 2.4 – Effects in terms of normalized stress components $\frac{\pi(\kappa+1)}{2G}s_{ijk}$ of a unit edge dislocation located at the origin of an infinite, linear elastic, isotropic and homogenous medium. These components are derived analytically by solving the corresponding well-posed elastic boundary value problem.

where the analytical expressions of the h_{ijk} components are given by

$$\begin{aligned}
h_{111} &= \frac{-x_2(3x_1^2+x_2^2)}{r^4}, & h_{112} &= \frac{x_1(x_1^2-x_2^2)}{r^4}, \\
h_{221} &= \frac{x_2(x_1^2-x_2^2)}{r^4}, & h_{222} &= \frac{x_1(x_1^2+3x_2^2)}{r^4}, \\
h_{121} &= \frac{x_1(x_1^2-x_2^2)}{r^4}, & h_{122} &= \frac{x_2(x_1^2-x_2^2)}{r^4},
\end{aligned} \tag{2.47}$$

Note that $h_{221} = h_{122}$ and $h_{121} = h_{112}$. In Figure 2.4 the normalized stress components due to a unit edge dislocation located at the origin of an infinite elastic medium are reported. For a dislocation with unit Burger vector b_1, along the glide plane ($x_2 = 0$), the shear stress σ_{12} has a singularity when the core is approached (see sub-figure 2.4b),

whereas the other two components are null (see sub-figures 2.4a and 2.4c). Along the axis perpendicular to the glide plane (i.e. $x_1 = 0$), the shear stress is zero, whereas σ_{11} and σ_{22} are singular. Similarly, one can obtain the effects in terms of stress due to a plane dislocation with Burger vector b_2 (and $b_1 = 0$).
It is important to note that this fundamental solution for plane elasticity can also be obtained using the 2D plane-strain fundamental point force solution introduced in Section 2.7. It can be proved, in fact, that a distribution of a number of point forces applied along the internal faces of a slit (in order to reproduce a discontinuity) leads to the same elasto-static state.

2.9.1.2 Fundamental solution of plane dislocation dipoles

The combination of two edge dislocations of opposite sign, located at an infinitesimal distance between each others, leads to a so called dislocation dipole. By using the analytical solutions in terms of stress of an edge dislocation (introduced in the previous section), it is possible to obtain the corresponding analytical solutions for a plane dislocation dipole. For instance, if two climb dislocations with opposite Burger vector b_2 (and $b_1 = 0$) are combined along the axis $x_2 = 0$, one positioned at $x_1 = \xi$ and the other at $x_1 = \xi + \mathrm{d}\xi$, then the stress σ_{22} induced by such dislocation dipole along the glide plane is (Hill et al. 1996)

$$\frac{\pi(\kappa+1)}{2G}\sigma_{22}^{\text{dipole},2} = \frac{b_2 \mathrm{d}\xi}{(x_1-\xi)(x_1-\xi-\mathrm{d}\xi)} \approx \frac{b_2 \mathrm{d}\xi}{(x_1-\xi)^2} = b_2 \frac{\partial s_{222}(x_1-\xi)}{\partial \xi} \tag{2.48}$$

Note that the analytical expression of equation (2.48) is obtained by superimposing the effect of each single plane dislocation, i.e. using equation (2.46) with the components h_{ijk} defined in equation (2.47). Equation (2.48) can thus be generalized to obtain the stress tensor Σ_{ij}^{22} due to a unit climb dislocation dipole (with normal given by axis x_2 and Burger vector $\mathbf{b} = (0, b_2 = 1)$):

$$\Sigma_{ij}^{22} = -\frac{\partial s_{ij2}(x_1-\xi, x_2)}{\partial \xi} \tag{2.49}$$

Similarly, for a unit glide dislocation with normal given by axis x_2 and Burger vector $\mathbf{b} = (b_1 = 1, 0)$, the stress tensor is given by

$$\Sigma_{ij}^{21} = -\frac{\partial s_{ij1}(x_1-\xi, x_2)}{\partial \xi} \tag{2.50}$$

By switching x_1 with $-x_2$, the analogous stress tensor due to unit plane dislocation dipole whose orientation is defined by the normal of axis x_1 can be obtained as

$$\begin{aligned}\Sigma_{ij}^{11} &= \frac{\partial s_{ij1}(x_1, x_2-\eta)}{\partial \eta}\\ \Sigma_{ij}^{12} &= \frac{\partial s_{ij2}(x_1, x_2-\eta)}{\partial \eta}\end{aligned} \tag{2.51}$$

In the most general case, the fundamental tensor Σ_{ij}^{kl} due to a generic unit plane dislocation dipole reads

$$\begin{aligned}\Sigma_{ij}^{kl} = c_{ijkl}S_{ab,l}^{k}(\mathbf{x},\mathbf{y}) = \frac{2G}{\pi(\kappa+1)}&(8r_{,i}r_{,j}r_{,k}r_{,l} - (1-2\nu)(\delta_{il}\delta_{jk} + \delta_{ik}\delta_{jl} - \delta_{ij}\delta_{kl}\\ &+ 2\delta_{kl}r_{,i}r_{,j} + 2\delta_{ij}r_{,k}r_{,l}) - 2\nu(\delta_{ij}\delta_{kl}\\ &+ \delta_{lj}r_{,i}r_{,k} + \delta_{il}r_{,j}r_{,k} + \delta_{jk}r_{,i}r_{,l} + \delta_{ik}r_{,j}r_{,l})),\end{aligned} \tag{2.52}$$

with $r = \sqrt{(x_i - \xi_i)^2}$ is the Euclidean distance between the observation point $\mathbf{x}$ and the dislocation (source) point ξ and $r_{,i} = \dfrac{x_i - \xi_i}{r}$.

2.10 Numerical discretization, collocation and regularization after integration

In this section, the numerical resolution of the boundary integral equation (2.44) (or equation (2.41)) is presented. Specifically, its resolution restricts to $\mathbf{x} \in \Gamma$, for which displacement discontinuities can be determined if traction vectors are known along the fracture plane or vice-versa.

2.10.1 Fracture discretization

Restricting to the 2-dimensional case, the fracture surface Γ is discretized into a set of N linear elements (or segments - see Figure 2.5), whose size h can vary between different elements. The fracture surface Γ thus reduces to

$$\Gamma \approx \sum_{e=1,\ldots,N} \Gamma_e, \tag{2.53}$$

which imply that the boundary integral equation (2.41) in terms of tractions can be rewritten as

$$t_i(\mathbf{x}) - t_i^o(\mathbf{x}) = n_j(\mathbf{x}) \sum_{e=1,\ldots,N} \int_{\Gamma_e} c_{ijkl}S_{ab,l}^{k}(\mathbf{x},\mathbf{y})d_a(\mathbf{y})n_b^e \mathrm{d}S_y \tag{2.54}$$

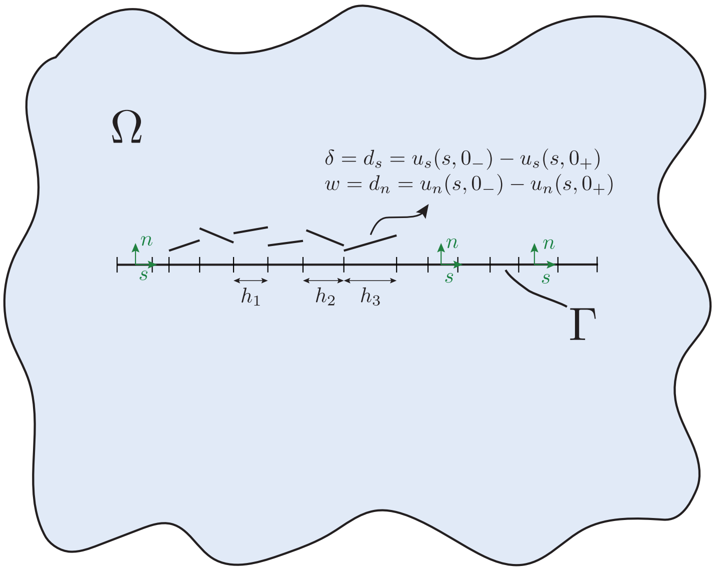
Ω
$\delta = d_s = u_s(s,0_-) - u_s(s,0_+)$
$w = d_n = u_n(s,0_-) - u_n(s,0_+)$
n
s
h_1
h_2
h_3
Γ

Figure 2.5 – Example of a discretized planar fracture embedded in a 2-dimensional, infinite medium. Piecewise linear shape functions are used to discretize the displacement jumps across the fracture plane Γ. Therefore, there are four primary unknowns per element.

Therefore, thanks to the superimposition principle of effect, the boundary integral equation (2.54) reduces to a sum of integral equations over each fracture elements.

2.10.2 Shape functions and collocation of elasticity equations

Like in others numerical methods, the unknowns of the problem can be approximated as a linear combination of nodal values, modulated by shape functions. In the context of displacement discontinuity method applied to fracture problem, the unknowns of the problem are typically the nodal displacement discontinuities along the discretized fracture mesh. Knowing the traction distribution along the fracture plane, the boundary integral equation introduced in the previous section allows to determine the corresponding distribution of displacement discontinuities.

Here the nodal displacement discontinuities are approximated (interpolated) with piecewise linear shape functions[19]: $p = 1$, being p the order of the interpolating polynomial. The resulting displacement discontinuities are linear but discontinuous between adjacent elements (see Figure 2.5). This is of great beneficial when modelling intersections between several fractures.

Because of the singular nature of the boundary integral equation (2.54) when $\mathbf{x}$ coincides with the mesh nodes, its resolution can not be collocated at nodal points of Γ. Since piecewise linear interpolation is used in this contribution, the boundary integral equation is collocated at $(p+1) \times N$ points. Each element of the discretized fracture is characterised

---

[19] Note that others shape functions can also be used, such us constant or quadratic for instance.

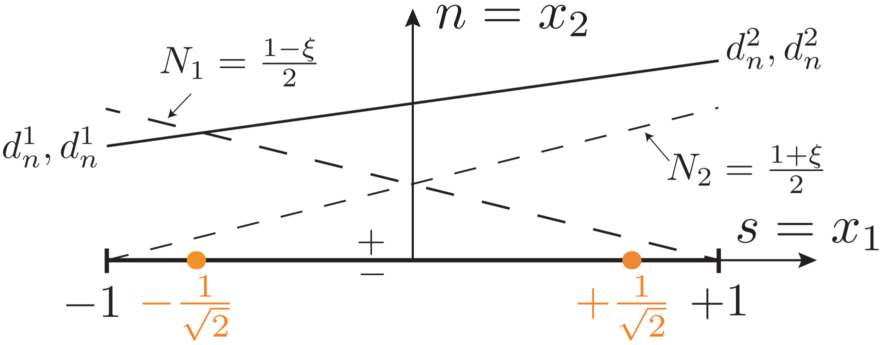

Figure 2.6 – Reference displacement discontinuity element. The normal $d_n = u_n^- - u_n^+$ and shear displacement discontinuity $d_s = u_s^- - u_s^+$ are linearly evolving within an element. The boundary integral equation is enforced at the collocation points (orange points), located at $\pm 1/\sqrt{2}$ within the element. The unknown displacement discontinuities are located at the nodes $(-1, 1)$.

by two collocation points.

2.10.3 Analytical integration over a reference element

The elastic problem reduces to evaluate the integrals in (2.54) over each element of the discretized fracture, when $\mathbf{x}$ lies inside each element.
Because of the assumption of linear elasticity, the solution of this elastic boundary value problem can be obtained by evaluating one integral of (2.54)

$$I_i^e(\mathbf{x}) = n_j(\mathbf{x}) \int_{\Gamma_e} c_{ijkl} S_{ab,l}^k(\mathbf{x}, \mathbf{y}) d_a(\mathbf{x}) n_b^e \mathrm{d}S_y \tag{2.55}$$

over a reference unit element (see Figure 2.6) and then use its analytical solutions to evaluate the effects of each displacement discontinuity acting on one element, over all the other elements (only a change of coordinates is thus required).

Expressing the shear and the normal displacement discontinuity over the reference element as a linear combination of nodal values (denoted by the superscripts 1 or 2 for left node and right node respectively) modulated by shape functions $N_i(\xi)$

$$\begin{aligned} d_s(\xi) &= N_1(\xi) d_s^1 + N_2(\xi) d_s^2 \\ d_n(\xi) &= N_1(\xi) d_n^1 + N_2(\xi) d_n^2 \end{aligned} \tag{2.56}$$

with

$$N_1(\xi) = \frac{1-\xi}{2} \qquad N_2(\xi) = \frac{1+\xi}{2}, \tag{2.57}$$

the integral (2.55) resolved onto the local reference system (denote by $'$) of the reference element reduces to

$$I_i^e(x'_1, x'_2) = n_j(x'_i, x'_2)\sigma_{ij}^s(x'_i, x'_2) + n_j(x'_i, x'_2)\sigma_{ij}^n(x'_i, x'_2), \tag{2.58}$$

where σ_{ij}^s and σ_{ij}^n are the stress components at x_i due to a shear and normal displacement discontinuity applied on the reference element and they are given by (thanks to the link between displacement discontinuity stress tensor and the one obtained with dislocation dipole solution - see section 2.9.1.2)

$$\begin{aligned}
\sigma_{ij}^s(x'_1, x'_2) &= \underbrace{\int_{-1}^{+1} \Sigma_{ij}^{12}(x'_1 - \xi, x'_2) N_1(\xi) \mathrm{d}\xi \times d_s^1}_{\sigma_{ij}^{s,1}} + \underbrace{\int_{-1}^{+1} \Sigma_{ij}^{12}(x'_1 - \xi, x'_2) N_2(\xi) \mathrm{d}\xi \times d_s^2}_{\sigma_{ij}^{s,2}} \\
\sigma_{ij}^n(x'_1, x'_2) &= \underbrace{\int_{-1}^{+1} \Sigma_{ij}^{22}(x'_1 - \xi, x'_2) N_1(\xi) \mathrm{d}\xi \times d_n^1}_{\sigma_{ij}^{n,1}} + \underbrace{\int_{-1}^{+1} \Sigma_{ij}^{22}(x'_1 - \xi, x'_2) N_2(\xi) \mathrm{d}\xi \times d_n^2}_{\sigma_{ij}^{n,2}}
\end{aligned} \tag{2.59}$$

By using the fundamental dislocation dipole tensor introduced in Section 2.9.1.2, all the integrals in equation (2.59) (in total 12 integrals) can be obtained analytically (see Appendix A). In Figure A.1 of Appendix A all the normalized stress components due to unit linear displacement discontinuity acting on the reference element are reported. Note that all the stress components are singular for $x_1 = \pm 1$ and $x_2 = 0$. This is the reason why the boundary integral equation that relate tractions to displacement discontinuities is collocated at points inside each element (collocation points).

It is worthwhile also to note that due to the symmetry of Σ_{ij}^{kl} (or s_{ijk}), the number of integrals to be evaluated are 8, reducing thus the computational cost.

2.10.4 Assembly of the final elastic system

Once the effects in terms of stresses or tractions of a linear displacement discontinuity over the reference element are known, the problem reduces to calculate and superimpose the effects of all the displacement discontinuities of all the elements on themselves such that the induced tractions balance the in-situ tractions t_i^o as well as the applied tractions t_i inside the fracture Γ.

Let us first consider the case of one element e, whose unit normal and shear vectors are denoted respectively by n^e and s^e (see Figure 2.7). In order to calculate the effects of a linear displacement discontinuity applied on element e (source element) over a collocation point of another element k (receiver element, with unit normal vectors n^k and s^k), it is simpler to perform a change of coordinate (see Figure 2.7) such that element e corresponds to the reference element. In this way the stress field induced by a

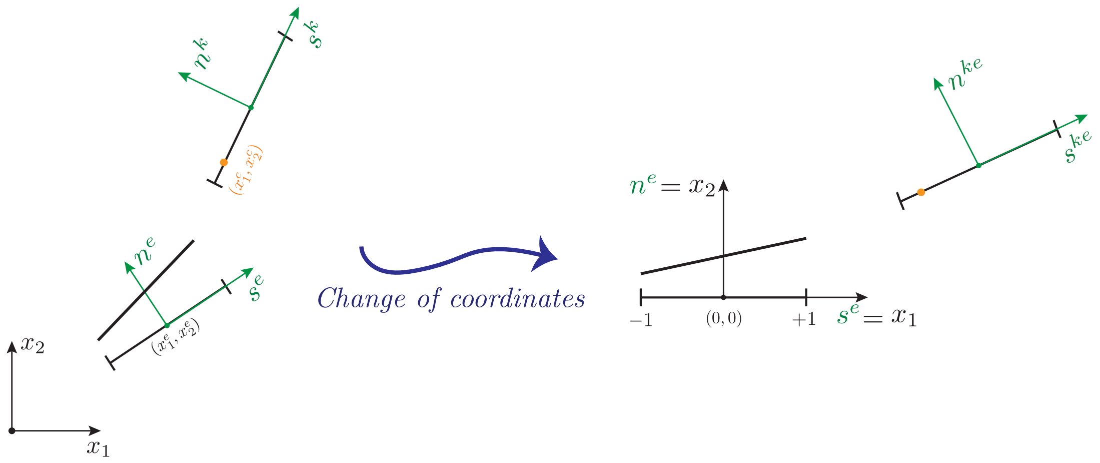

Figure 2.7 – Influence of displacement discontinuity on source element e over receiver element k. A change of coordinates is performed in order to make the source element e coincide the unit reference element. The stress field is then computed at a collocation point of element k.

displacement discontinuity over a collocation point of generic element can be evaluated using (2.59). Denoting R the rotation matrix to switch from local to global reference system, the normal and the tangential unit vector for the receiver element k upon rotation transformation and change of coordinates are given by

$$n_i^{ke} = R_{ij}^T n_j^k, \qquad s_i^{ke} = R_{ij}^T s_i^k, \tag{2.60}$$

Similarly, the coordinated of one of its collocation points $x_i'^k$ are given by

$$x_i'^k = R_{ij}^T (x_j^k - \bar{x}_j^e), \tag{2.61}$$

where $\bar{x}_j^e$ denotes the centre of the unit reference element.
Therefore, the induced shear $t_s^{ek}(x^k)$ and normal $t_n^{ek}(x^k)$ tractions by a linear variation of a displacement discontinuity over a source element e at the collocation point x_m^k located in the receiver element k are

$$\begin{aligned} t_s^e(x_m^k) &= s_i^{ke}\sigma_{ij}^{s1}(x_i'^k)n_j^{ke}d_s^1 + s_i^{ke}\sigma_{ij}^{s2}(x_i'^k)n_j^{ke}d_s^2 + s_i^{ke}\sigma_{ij}^{n1}(x_i'^k)n_j^{ke}d_n^1 + s_i^{ke}\sigma_{ij}^{n2}(x_i'^k)n_j^{ke}d_n^2 \\ t_n^e(x_m^k) &= n_i^{ke}\sigma_{ij}^{s1}(x_i'^k)n_j^{ke}d_s^1 + n_i^{ke}\sigma_{ij}^{s2}(x_i'^k)n_j^{ke}d_s^2 + n_i^{ke}\sigma_{ij}^{n1}(x_i'^k)n_j^{ke}d_n^1 + n_i^{ke}\sigma_{ij}^{n2}(x_i'^k)n_j^{ke}d_n^2 \end{aligned} \tag{2.62}$$

In order to simplify the notation, equation (2.62) can be re-written as

$$\begin{aligned} t_s^e(x_m^k) &= K_{ss}^{el}(x_i^k)d_s^l + K_{sn}^{el}(x_i^k)d_n^l \qquad l = 1, 2 \\ t_n^e(x_m^k) &= K_{ns}^{el}(x_i^k)d_s^l + K_{nn}^{el}(x_i^k)d_n^l \qquad l = 1, 2 \end{aligned} \tag{2.63}$$

Finally, the contributions of all the elements of the discretized fracture to the induced shear and normal tractions at the collocation point x_i^k of the receiver element k must be summed up, i.e.

$$\begin{aligned} t_s(\mathbf{x}^k) - t_s^o(\mathbf{x}^k) &= \sum_{e=1}^{N}\sum_{l=1}^{2}\left(K_{ss}^{el}(\mathbf{x}^k)d_s^l + K_{sn}^{el}(\mathbf{x}^k)d_n^l\right) \\ t_n(\mathbf{x}^k) - t_n^o(\mathbf{x}^k) &= \sum_{e=1}^{N}\sum_{l=1}^{2}\left(K_{ns}^{el}(\mathbf{x}^k)d_s^l + K_{nn}^{el}(\mathbf{x}^k)d_n^l\right) \end{aligned} \tag{2.64}$$

Note that in equation (2.64), there is no summation over repeated indices. Furthermore, for a planar fracture $K_{sn}^{el} = K_{ns}^{el} = 0$, i.e. a normal displacement discontinuity does not induce shear traction on any other element and vice-versa. The two degrees of freedom are therefore uncoupled.

By writing equations (2.64) at all $2N$ collocation points, a linear system of $4N$ equations with $4N$ unknowns can be built. Introducing the total vector of displacement discontinuity $\mathbf{d}$ (of size $4N$), obtained by stacking the unknowns as

$$\mathbf{d} = (d_s^{e=1,l=1}, d_n^{e=1,l=1}, d_s^{e=1,l=2}, d_n^{e=1,l=2}, \dots)$$

and the total vector of applied tractions (and similarly for in-situ tractions) at the collocation points

$$\mathbf{t} = (t_s^{e=1,l=1}, t_n^{e=1,l=1}, t_s^{e=1,l=2}, t_n^{e=1,l=2}, \dots),$$

the final elastic system of equations reduces to

$$\mathbb{E}\mathbf{d} = \mathbf{t} - \mathbf{t}^o \tag{2.65}$$

The final elastic matrix of coefficient $\mathbb{E}$ is a $4N \times 4N$ fully populated matrix and typically non-symmetric. The memory requirements to store such a matrix set strict constraints for current available laptops and, in order to overcome this limit, several computational techniques have been proposed. In this contribution, the hierarchical matrix technique combined with adaptive cross approximation is used. This acceleration technique is shortly described in Appendix B.

The final elastic matrix $\mathbb{E}$ is, however, always diagonal dominant as the self-effects (i.e. source element coincide with receiver element) are always the biggest in magnitude. In Figure 2.8, an example of resulting final elastic matrix $\mathbb{E}$ for a planar fracture with unit half-length (similar the one in Figure 2.5) is presented. Its size is 96×96, as the fracture has been discretized with 24 linear elements. Note that, since the fracture is planar, the shear and the normal degree of freedom are uncoupled, so that such a matrix is only composed of 2304 entries (instead of $96^2 = 9216$ entries). Furthermore, since the

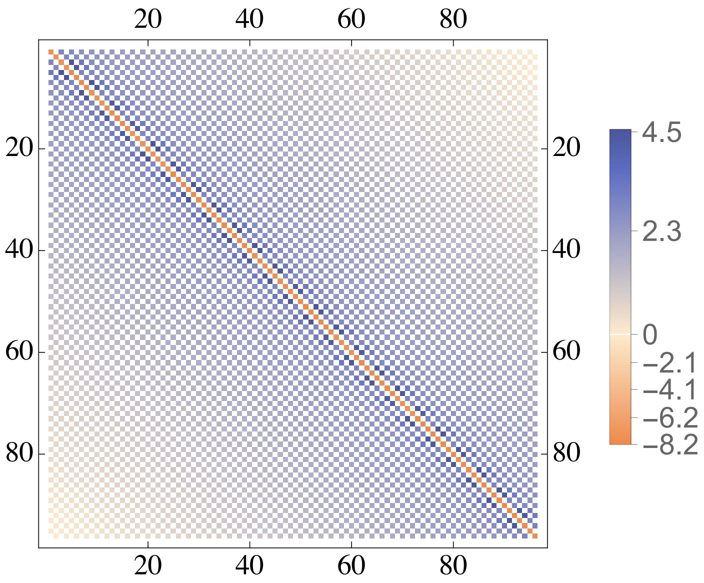

Figure 2.8 – Final elastic boundary element matrix for a planar fracture with unit half-length, discretized with 24 linear elements. This fracture is embedded in an infinite, linear elastic, isotropic and homogenous medium, whose plane strain modulus is $E_p = 1$. Note that shear and normal degrees of freedom are uncoupled and $K^{el}_{sn} = K^{el}_{ns} = 0$ (white spots in the matrix plot).

planar fracture is symmetric with respect to a vertical axis passing through its centre, the resulting elastic matrix is also symmetric.

2.10.5 Extension to quasi-dynamic approximation

The displacement discontinuity method presented so far has been derived under the assumption of quasi-static equilibrium (quasi-static elasticity), i.e. the inertial effects have been neglected. In the context of fracture propagation, this assumption is reasonable for cracks that propagate in quasi-static manner, i.e. slowly enough to guarantee static equilibrium at any time. When fractures start to propagate dynamically, due to for instance weakening of material strength parameters during their propagation, inertial effects (proportional to cracks acceleration) are no longer negligible. Therefore, a fully elasto-dynamic formulation of the boundary element method must be taken into account, which usually incorporates a spectral method based on Fast Fourier Transform for solving the boundary integral equations (Peirce et al. 1992). In the early nineties, however, a quasi-dynamic formulation of the boundary element method has been proposed by Rice (1993). In this formulation, a viscous term proportional to crack velocity is added to the quasi-static elastic equilibrium in order to account for energy outflow as seismic waves during fast crack(s) propagation. During very fast events, such as earthquakes-like episodes, this radiation damping term assures that the governing system of equations continues to have a finite solution, i.e. it avoids unrealistic unbounded crack(s) propagation. Mathematically, the quasi-dynamic formulation of equilibrium is equal to the quasi-static formulation plus a term related to the rate of deformation multiplied by the ratio between elastic moduli and wave speeds. Equation (2.64) under quasi-dynamic approximation can thus be rewritten as

$$\begin{aligned} t_s(\mathbf{x}^k) - t_s^o(\mathbf{x}^k) &= \sum_{e=1}^{N}\sum_{l=1}^{2}\left(K_{ss}^{el}(\mathbf{x}^k)d_s^l + K_{sn}^{el}(\mathbf{x}^k)d_n^l\right) - \frac{G}{c_s}\frac{\partial d_s}{\partial t} \\ t_n(\mathbf{x}^k) - t_n^o(\mathbf{x}^k) &= \sum_{e=1}^{N}\sum_{l=1}^{2}\left(K_{ns}^{el}(\mathbf{x}^k)d_s^l + K_{nn}^{el}(\mathbf{x}^k)d_n^l\right) - \frac{G}{c_p}\frac{\partial d_n}{\partial t}, \end{aligned} \tag{2.66}$$

where c_s and c_p denotes the shear and compressional wave speeds, which are function of elastic properties of the medium and its density ρ

$$c_s = \sqrt{G/\rho}, \qquad c_p = \sqrt{(\kappa + 4/3G)/\rho}$$

Therefore, upon numerical discretization, the quasi-dynamic formulation of the elastic equilibrium leads to an additional damping (diagonal) matrix $\mathbb{Q}_d$ proportional to the rate of deformations. For a given mesh node i, such a matrix reads

$$\mathbb{Q}_{d,i} = -\begin{bmatrix} G/c_s & 0 \\ 0 & G/c_p \end{bmatrix} \cdot \frac{\partial}{\partial t}\begin{bmatrix} d_{s,i} \\ d_{n,i} \end{bmatrix}$$

The final elastic system of equations (2.65) under quasi-dynamic approximation can thus be rewritten as

$$\mathbb{E}\mathbf{d} - \mathbb{Q}_d\dot{\mathbf{d}} = \mathbf{t} - \mathbf{t}^o \tag{2.67}$$

In this contribution, elasticity is always solved in incremental form over a given time step Δt. Using a fully implicit time integration scheme and denoting a generic space and time dependent variable at current time $n+1$ as $X^{n+1} = X^n + \Delta X$, the final system of equations (2.67) reduces to

$$\left(\mathbb{E} - \mathbb{Q}_d\right)\Delta\mathbf{d} = \mathbf{t}^{n+1} - \mathbf{t}^{o,n+1} - \mathbb{E}\mathbf{d}^{\mathbf{n}} \tag{2.68}$$

Typically, the current tractions along pre-existing discontinuities are known at each time step as well as the elastic deformations at the previous time step. The linear system of equation (2.68) can thus be solved for the current increment of elastic deformations.

2.11 Conclusions

This chapter presented boundary integral equations specific for fracture problems. Notably, the quasi-static elastic boundary integral equations have been discretized using a particular boundary element method that fits very well unbounded elastic problems with slit-like opening, such as fractures or faults possibly intersecting with each others. This numerical method is called displacement discontinuity method. The final discretized equations form a linear system of equations for the unknown elastic deformations along pre-existing fractures or faults (supposing that the corresponding applied tractions distribution is known). In the context of fluid driven fracture propagation, for instance, the applied tractions are explicitly known when the pore pressure evolution is not coupled with elasticity, otherwise they have to be solved simultaneously in a fully coupled way. Both scenarios will occur in this contribution.

3 Fluid flow in fractures

Pre-existing fractures or material discontinuities at depth are subjected to a compressive effective stress state due to the weight of everything overhead (soil, water, surface loadings etc.). In absence of any external perturbations, fractures are said to be mechanically closed, i.e. fractures' internal surfaces are partially in contact depending on their surface topology (see an idealization in Figure 3.1). Although mechanically closed, however, they are more hydraulically conductive than the surrounding host rock, especially in deep formations characterised by low permeability. In the case of deep granite reservoirs, for instance, the matrix permeability of the intact rock can vary between $10^{-18} \div 10^{-19}\text{m}^2$ (Kranz et al. 1979), which is considerably smaller than the longitudinal fracture permeability at depth that can range between $10^{-12} \div 10^{-10}\text{m}^2$. Obviously, these fracture permeability values are effective stress dependent (contact condition dependency) and they can vary depending on the fracture surface topology as well as on the mechanical properties of the surrounding rock.

When an external perturbation is introduced at depth (e.g. fluid injection into a pre-existing fracture) such that the local effective normal stress is no longer compressive, then the fracture is mechanically open, i.e. the fracture opens elastically and it can be viewed as an open channel for fluid flow (see Figure 3.1). The transition between mechanically closed and open, however, is smooth due to the presence of roughness along the fracture's internal surfaces that prevent a quick detachment (see Renshaw (1995) for more details). In this manuscript, pre-existing fractures are initially mechanically closed, i.e. the local effective normal stress is always compressive, but they can open during hydraulic stimulation (i.e. fluid injection and diffusion or elastic interaction between active fractures). In the following, therefore, a brief recall of main governing equations of fluid dynamics is reported. This will be followed by the numerical discretization of fluid mass conservation equation via a finite volume scheme that represents part of the numerical framework for all the solvers that will be presented later.

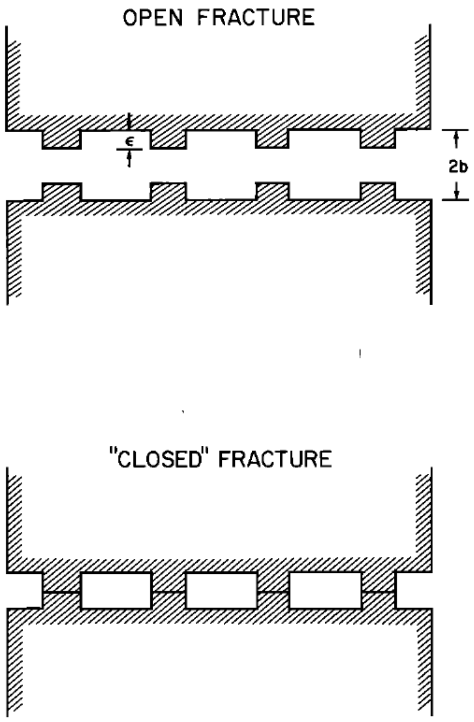

Figure 3.1 – Idealization of mechanically open versus mechanically closed fractures. In this picture, taken from Witherspoon (1980), ϵ denotes the asperity size, while $2b$ the fracture width.

3.1 Governing equations of fluid dynamics

Fluid flow in fractures is governed by two fundamental laws of fluid mechanics: i) conservation of mass and ii) conservation of momentum. Note that conservation of energy (that comes from thermodynamics) is neglected due to the null compressibility of the fluid considered in this contribution. Isothermal conditions are thus considered throughout this manuscript.

In the following a brief description of the two laws is reported, assuming a macroscopic point of view in line with continuum mechanics, which means that the fluid local properties (such as fluid density, viscosity etc.) are averaged over the fluid element and they vary smoothly on the macroscopic scale of the flow.

Conservation of mass Let us consider a volume V bounded by a surface S fixed in a bi-dimensional space. The conservation of mass states that the rate of decrease of mass in V (i.e. $-\frac{d}{dt}\int_V \rho \mathrm{d}V$) must equal the total rate of mass flux out of V. In absence of any source/sink terms, this condition reads

$$\frac{\partial \rho}{\partial t} + \frac{\partial (\rho v_i)}{\partial x_i} = 0, \tag{3.1}$$

where $\rho(\mathbf{x}, t)$ is the fluid density function of space and time and v_i are the local bulk flow velocity vector components with respect to x_i (with $i = 1, 2$). Note that in equation (3.1) the Green's formula has been used to convert the rate of mass flux across the surface S to a volume integral. If a source/sink term is considered, the right hand side of equation (3.1) includes an additional term $Q_{inj}(t)\delta(x - x_{inj})$, where x_{inj} denotes the injection point.

For un incompressible fluid (with ρ=const.) that is independent of space and time, the continuity equation (3.1) reduces to

$$\frac{\partial v_i}{\partial x_i} = 0, \tag{3.2}$$

which upon extension of repeated indices reads

$$\frac{\partial v_1}{\partial x_1} + \frac{\partial v_2}{\partial x_2} = 0 \tag{3.3}$$

Conservation of momentum and constitutive relations Let us consider the same volume V bounded by a surface S that now moves with the flow. The conservation of momentuum (i.e. the Newton's second law (2.1)) dictates that the rate of change of momentuum ($i.e. \frac{d}{dt} \int_V \rho \mathbf{v}$) must equal the sum total forces (body + surface) applied on the fluid element, i.e.

$$\rho \left(\frac{\partial v_i}{\partial t} + v_j \frac{\partial v_i}{\partial x_j} \right) = \rho g_i + \frac{\partial \sigma_{ij}}{\partial x_j} \tag{3.4}$$

where g_i are the gravity vector components with respect to x_i and σ_{ij} represent the fluid stress tensor components (force per unit area in the i direction across a plane with normal in the j direction). Notably, these fluid stress components can be written in terms of pressure p and viscous friction as

$$\sigma_{ij} = - \left(p + \lambda \frac{\partial v_k}{\partial x_k} \right) \delta_{ij} + \mu \left(\frac{\partial v_i}{\partial x_j} + \frac{\partial v_j}{\partial x_i} \right), \tag{3.5}$$

where μ and λ are the coefficients of dynamic and bulk (volumetric) viscosity, respectively. These expressions assume that the relationships between stress and velocity gradients is linear (valid for Newtonian fluid, which is the type of fluid used throughout this contribution) and isotropic.

For incompressible flow, $\frac{\partial v_i}{\partial x_i} = 0$ (see equation (3.2)), and the constitutive relations (3.5) reduce to

$$\sigma_{ij} = -p\delta_{ij} + \mu\left(\frac{\partial v_i}{\partial x_j} + \frac{\partial v_j}{\partial x_i}\right) \tag{3.6}$$

Boundary conditions Like in all the boundary value problems, boundary conditions must be provided in order to solve the flow equations. Assuming a rigid wall moving at velocity $\bar{\mathbf{v}}$ and having a unit normal $\hat{\mathbf{n}}$, the boundary conditions adopted are

- the wall is impermeable, i.e. $v_i \cdot \hat{n}_i = \bar{v}_i \cdot \hat{n}_i$
- no slip condition between fluid and wall, i.e. $v_i \times \hat{n}_i = \bar{v}_i \times \hat{n}_i$

3.1.1 Lubrication approximation and width averaging

Assuming that the fluid can flow in a very thin channel composed of two parallel smooth plates representative of a fracture at depth with small aperture w and that the regime of flow is laminar[1], for which inertial terms can be neglected, the Navier-Stokes equation (3.4) obtained from momentuum conservation simplifies to

$$\begin{aligned} -\frac{\partial p}{\partial x_1} + \mu\frac{\partial}{\partial x_2}\left(\frac{\partial v_1}{\partial x_2}\right) &= 0 \\ -\frac{\partial p}{\partial x_2} + \mu\frac{\partial}{\partial x_2}\left(\frac{\partial v_2}{\partial x_2}\right) &= 0, \end{aligned} \tag{3.7}$$

where μ is the constant fluid viscosity. Integrating the relations in equation (3.7) and enforcing the no slip-boundary conditions at the channel/fracture walls, one can obtain the classical parabolic velocity profiles, which for the x_1 longitudinal direction reads

$$v_1(x_2) = -\frac{w^2}{8\mu}(1 - 4x_2^2/w^2)\frac{\partial p}{\partial x_1} \tag{3.8}$$

In the context of uni-dimensional fluid flow within a thin channel/fracture under plane strain conditions, it is common to average both the continuity equation (3.1) and the conservation of momentum (3.4) across the channel/fracture width w, allowing, however, its variation with time. By doing so, the continuity equation reduces to

$$\frac{\partial \rho w}{\partial t} + \frac{\partial(\rho w\langle v_1\rangle)}{\partial x_1} = 0, \tag{3.9}$$

where $\langle v\rangle$ is the width averaged fluid velocity (that can be obtained from averaging the Navier-Stokes equation (3.4)). Specifically, under the assumption of laminar flow, the width averaged velocity can be obtained by integrating the velocity profile (3.8) across w, i.e.

---

[1] Laminar flow is a type of flow regime characterised by low values of Reynolds number, which is the ratio of the inertial force to the shearing force of the fluid.

$$\langle v_1 \rangle = \frac{1}{w}\int_{-w/2}^{w/2} v_1(x_2)\mathrm{d}x_2 = -\frac{w^2}{12\mu}\frac{\partial p}{\partial x_1}, \tag{3.10}$$

obtaining a total fluid flux that reads

$$q_x = w\langle v_1 \rangle = -\frac{w^3}{12\mu}\frac{\partial p}{\partial x_1} \tag{3.11}$$

In literature, equation (3.11) is so-called Poiseuille[2] law (sometimes referred to as cubic law). Allowing for a slightly compressible fluid of compressibility β (for which $\rho = \rho_o(1 + \beta(p - p_o))$, with ρ_o denoting the fluid density at the reference pressure p_o), the width averaged fluid continuity equation (3.9) under lubrication approximation thus reduces to

$$\beta w \frac{\partial p}{\partial t} + \frac{\partial w}{\partial t} + \frac{\partial q_x}{\partial x_1} = 0 \tag{3.12}$$

It is worth mentioning, however, that the fluid mass conservation equation (3.12) is valid for mechanically open fractures, for which laminar flow occurs along an open channel. When mechanically closed fractures are taken in account, Poiseuille law is typically not valid and fluid flow follows the Darcy's law[3] that reads

$$q_x = -\frac{w \cdot k_f}{\mu}\frac{\partial p}{\partial x_1} \tag{3.13}$$

where k_f is the longitudinal permeability of the fracture that typically includes the link with its mechanical properties. In literature, indeed, several permeability relations have been proposed (see Rutqvist & Stephansson (2003) for a review). Rice (1992*a*), for instance, proposed an effective stress-dependent permeability law that reads

$$k_f = k_{f_*} e^{-\sigma'_n/\sigma_*} \tag{3.14}$$

where k_{f_*} is the maximum fault permeability and σ_* is a normalizing stress constant. Another effective stress-dependent permeability evolution that is commonly used for mechanically closed fractures/joints is the Bandis model (Bandis et al. 1981). In this empirical model the fracture permeability is related to effective normal stress through the following non linear relation

$$k = k_{ni}\left(1 - \frac{\sigma}{v_m k_{ni} + \sigma}\right)^{-2}, \tag{3.15}$$

---

[2] It was experimentally derived by Jean Léonard Marie Poiseuille in 1838 and Gotthilf Heinrich Ludwig Hagen.

[3] Herny Darcy, Digione 1803 - Paris 1858

where k_{ni} is the normal stiffness at zero normal stress and v_m is the maximum closure of the fracture/joint. Typically these parameters are determined by performing compression tests on jointed rock samples (Nguyen & Selvadurai 1998). Although the relations (3.14) and (3.15) are mathematically different, they result in a very similar fracture permeability evolution with effective normal stress.

Note that under lubrication approximation, the fracture permeability k_f is equal to $\frac{w^2}{12}$.

3.2 Flow in rough fractures

The presence of roughness does affect the fluid flow. Experimentally, indeed, it has been observed that rough fracture exhibit larger flow resistance compared to the smooth parallel case, leading to a deviation from the Poiseuille law (3.11) even in laminar case. Such a deviation can be quantified by introducing a roughness friction factor f_r in the cubic law, i.e.

$$q = -\frac{1}{f_r}\frac{w^3}{12\mu}\frac{\partial p}{\partial x}, \quad \text{with} \quad f_r = \frac{w^3}{w_h^3} \tag{3.16}$$

In literature, a number of different laws have been proposed for the evolution of f_r with the fracture roughness ratio, the latter being defined as the ratio of the variance of the fracture width σ_w over the mean fracture width w. Among others, Zimmerman & Bodvarsson (1996) suggest that

$$f_r = 1/(1 - 1.5(\sigma_w/w)^2),$$

while Patir & Cheng (1978) proposed

$$f_r = \tfrac{1}{1 - 0.9\exp(-0.56/(\sigma_w/w))}$$

and Renshaw (1995)

$$f_r = (1 + 6.(\sigma_w/w)^2)^{3/2}$$

Although different in their expression, these roughness friction factors laws lead to a similar evolution of f_r with σ_w/w.

In the following a finite volume scheme is described. This numerical method will be used to discretize the governing equation that control fluid flow inside hydraulically conductive pre-existing fractures, specifically the width averaged fluid mass conservation equation (3.12).

3.3 Finite volume method for fluid flow inside hydraulically conductive fractures

Similarly to finite element method or finite difference method, the unknown field with finite volume method is calculated approximately at discrete points on a mesh of the geometry. Specifically, each node of the computational mesh is surrounded by a finite volume (often called control volume) and the corresponding nodal unknown is averaged across it. The integral conservation law is enforced for each control volume, making the finite volume method a locally *conservative* method (Schäfer 2006). Furthermore, unlike finite difference methods, finite volume method does not require a structured mesh (even though a structured mesh can also be used) and the application of boundary conditions is not invasive.
Thanks to these advantages, the finite volume method can be easily applied to solve numerically fluid flow problem inside hydraulically conductive pre-existing fracture(s), whose computational mesh is not necessarily structured (see Figure 2.5).
In the next sub-section, a complete description of this method applied to a specific uni-dimensional fluid flow problem inside a generic fracture is presented.

3.3.1 Discretization of fluid mass conservation equation

In this contribution, fluid (i.e. water) is injected into a pre-existing fracture, either controlling the flux or the maximum pressure at injection point. The initial (ambient) pore pressure distribution p_o is thus altered by the injected fluid whose diffusion is only localized inside the pre-existing fracture, i.e. the surrounding medium is considered impermeable. Fluid flow is thus governed by the uni-dimensional width averaged fluid mass conservation equation (3.12) with the Darcy's flux defined in equation (3.13) extended to account for the initial pore pressure distribution p_o.

Upon discretization of the fracture with linear elements, pore pressure is supposed to vary linearly and continuously between adjacent elements (unlike the displacement discontinuities, which are piecewise linear), with pressure nodes located at the vertexes of the displacement discontinuity elements (see Figure 3.2). Equation (3.12) is integrated over each control volume centred on pressure nodes (see Figure 3.2). The generic control volume centred on pressure node i is denoted as CV_i. This control volume can then be subdivide into n_{ei} sub-control volumes, being n_{ei} the number of mesh elements connected to node i, i.e.

$$CV_i = \bigcup_{j=1}^{n_{ei}} CV_{ij}$$

Upon application of integral conservation law for CV_i combined with divergence theorem,

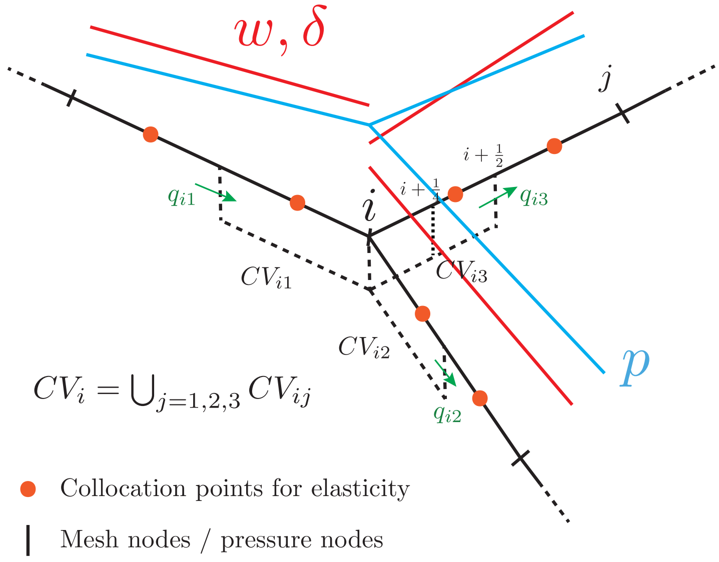

Figure 3.2 – Sketch of displacement discontinuities and fluid pressure variation along three mesh elements converging in one generic node i. The former vary linearly and discontinuously between different elements, whereas the latter is continuous at mesh node i. The control volume for finite volume scheme is centred at pressure node i inside which fluid is conserved. Note that this numerical scheme can be easily extended to the case where more than three mesh elements intersect at node i (and obviously to the case where only two elements converge at each pressure node, which is the case of the planar fracture of Figure 2.5).

fluid mass conservation equation reads

$$\underbrace{\int_{CV_i} \frac{\partial w}{\partial t} \mathrm{d}x}_{1} + \underbrace{\int_{CV_i} w_h \beta \frac{\partial p}{\partial t} \mathrm{d}x}_{2} + \sum_{j=1}^{n_{ei}} q_{ij} = 0, \tag{3.17}$$

where the fluxes q_{ij} entering the control volume CV_i via sub-control CV_{ij} are easily obtained from the Poiseuille law, knowing that the pressure gradient is constant over each mesh element:

$$q_{ij} = w_{h,CV_{ij}} \frac{k_{CV_{ij}}}{\mu} \frac{(p_j - p_j^o) - (p_i - p_i^o)}{h_{ij}} \qquad w_{h,CV_{ij}} = (w_i + w_j)/2 \tag{3.18}$$

In equation (3.18), $w_{h,CV_{ij}}$ and $k_{CV_{ij}}$ are respectively the opening and permeability at the ends of each sub-control volume CV_{ij}, p_i and p_j are the nodal pressure values at i and j and finally h_{ij} is the euclidean distance between node i and node j. The fluxes therefore enter into each control volume from the middle of each mesh element.

When aggregating the conservation over all the control volumes (their total number coincides with mesh nodes), the effect of fluxes entering the different control volume results in a banded matrix $\mathbb{L}$ whose components are given by

$$\begin{aligned} \mathbb{L}_{ij}(\mathbf{w}) &= -w_{h,CV_{ij}} \frac{k_{CV_{ij}}}{\mu \cdot h_{ij}} \quad i \neq j \\ \mathbb{L}_{ii}(\mathbf{w}) &= \sum_{j=1,\ldots,n_{ei}} w_{h,CV_{ij}} \frac{k_{CV_{ij}}}{\mu h_{ij}} \quad i = j \end{aligned} \tag{3.19}$$

In the case of one planar fracture, the matrix $\mathbb{L}$ is a 4-banded diagonal matrix, whose size corresponds to the number of nodes in the mesh, i.e. $N_n \times N_n$. It is a sparse matrix and so it should be handle as such (i.e. without storing in memory all null components).

The integrals 1 and 2 of equation (3.17) can be split over each sub-control volumes CV_{ij}, i.e.

$$\int_{CV_i} \frac{\partial w}{\partial t} \mathrm{d}x = \bigcup_{j=1}^{n_{ei}} \int_{CV_{ij}} \frac{\partial w}{\partial t} \mathrm{d}x \tag{3.20}$$

$$\int_{CV_i} w_h \beta \frac{\partial p}{\partial t} \mathrm{d}x = \bigcup_{j=1}^{n_{ei}} \int_{CV_{ij}} w_h \beta \frac{\partial p}{\partial t} \mathrm{d}x \tag{3.21}$$

By applying Cavalieri-Simpson rule for space integration and backward Euler scheme for the time derivative (finite difference), the integral in (3.21) reduces to

$$\begin{aligned} &\int_{CV_{ij}} w_h \beta \frac{\partial p}{\partial t} \mathrm{d}x = \int_{o}^{h_{ij}/2} w_h \beta \frac{\partial p}{\partial t} \mathrm{d}x \approx \\ &\approx \frac{h_{ij}}{12} \beta \left[w_{h_i} \cdot \Delta p_i + 4 \cdot \left(w_{h_{i+\frac{1}{4}}} \cdot \Delta p_{i+\frac{1}{4}} \right) + w_{h_{i+\frac{1}{2}}} \cdot \Delta p_{i+\frac{1}{2}} \right] = \\ &= \frac{h_{ij}}{12} \beta \left[\left(w_{h_i} + 3 \cdot w_{h_{i+\frac{1}{4}}} + \frac{1}{2} \cdot w_{h_{i+\frac{1}{2}}} \right) \Delta p_i + \left(w_{h_{i+\frac{1}{4}}} + \frac{1}{2} \cdot w_{h_{i+\frac{1}{2}}} \cdot \right) \Delta p_j \right], \end{aligned} \tag{3.22}$$

where the subscript i refers to value at node i, $i + 1/2$ refers to values at the ends to each sub-control volume (i.e. middle of each element), $i + 1/4$ refers to values at middle of each sub-control volume and finally j refers to values at next node j. For instance, the pressure values at $i + 1/2$ and $i + 1/4$ are respectively given by

$$\Delta p_{i+\frac{1}{2}} = \frac{\Delta p_i + \Delta p_j}{2}, \qquad \Delta p_{i+\frac{1}{4}} = \frac{3\Delta p_i + \Delta p_j}{4}$$

By solving the integral (3.22) over each sub-control volume CV_{ij} of each mesh nodes, a pressure matrix of size $N_n \times N_n$ can be assembled, i.e. the second term of equation (3.17) can be rewritten as

$$\mathbb{V}_p(\mathbf{w}) \cdot \frac{\Delta \mathbf{p}}{\Delta t}$$

By applying the same procedure, the integral (3.20) reduces to

$$\begin{gathered}\int_{CV_{ij}} \frac{\partial w}{\partial t} \mathrm{d}x = \int_{o}^{h_{ij}/2} \frac{\partial w}{\partial t} \mathrm{d}x \approx \\ \approx \frac{h_{ij}}{12} \left[\Delta w_i + 4 \cdot \Delta w_{i+\frac{1}{4}} + \Delta w_{i+\frac{1}{2}} \right] = \frac{h_{ij}}{24} \left[9 \Delta w_i + 3 \Delta w_j \right],\end{gathered} \tag{3.23}$$

which leads to a mass matrix of size $N_n \times 2N$ due to piecewise nature of linear displacement discontinuities over each element. The first term of equation (3.17) can thus be rewritten as

$$\mathbb{V}_w \cdot \frac{\Delta \mathbf{w}}{\Delta t}$$

Therefore, the final form of the fluid mass conservation equation (3.12) discretized with a finite volume scheme can be written in matrix form as

$$\mathbb{V}_w \cdot \frac{\Delta \mathbf{w}}{\Delta t} + \mathbb{V}_p \left(\mathbf{w} \right) \cdot \frac{\Delta \mathbf{p}}{\Delta t} + \mathbb{L} \left(\mathbf{w} \right) \cdot \left(\mathbf{p} - \mathbf{p}^o \right) = 0 \tag{3.24}$$

Note that in equation (3.24), the source term is not included. In case of continuous injection, for instance, the right hand side of equation (3.24) contains a vector $\Delta t \mathbf{S}$ of size N_n.
Denoting $X^{n+1} = X^n + \Delta X$ a generic space and time dependent variable a current time $n+1$, the implicit time formulation of equation (3.24) reads

$$\mathbb{V}_w \cdot \frac{\Delta \mathbf{w}}{\Delta t} + \mathbb{V}_p \left(\mathbf{w^{n+1}} \right) \cdot \frac{\Delta \mathbf{p}}{\Delta t} + \mathbb{L} \left(\mathbf{w^{n+1}} \right) \cdot \Delta \mathbf{p} = - \mathbb{L} \left(\mathbf{w^{n+1}} \right) \cdot \left(\mathbf{p^n} - \mathbf{p}^o \right) \tag{3.25}$$

As one can notice, the first term of this implicit equation depends on the current increment of opening deformations. Therefore, when this term is different than zero (e.g. in the case of shear-induced dilatancy), equation (3.25) must be coupled with the discretized elasticity equations (2.68), resulting in a monolithic non-linear system of equations for the unknown increment of pore pressure and increment of deformations. On the contrary, pore pressure evolution is uncoupled from elasticity and equation (3.25) can be solely solved for the current increment of pore pressure. In this contribution, both scenario will be used.

3.4 Conclusions

This chapter presented the governing equations for fluid flow inside hydraulically conductive fractures, together with a finite volume scheme (with vertex centred control volumes) used to discretized the width averaged fluid mass conservation equation. Notably, this numerical method

- conserves the fluid mass locally in each control volume
- is well suited for problems that involve multiple fracture intersections
- can readily be used with unstructured meshes

4 Effect of shear-induced dilatancy on the transition from aseismic to seismic slip along a pressurized fault

This chapter studies the effect of dilatancy on shear crack propagation along a pressurized fault. A pre-existing fault is embedded in an infinite, homogeneous, isotropic and linear elastic medium and it is subjected to hydro-shearing stimulation. Fluid is directly injected into the fault at a pressure below the local minimum principal effective normal stress at ambient condition with the specific purpose of activating a shear crack. Aseismic crack growth may or may not lead to the nucleation of a dynamic rupture depending on in-situ conditions, frictional properties of the fault and the value of overpressure. In particular, a fault is coined as unstable if its residual frictional strength τ_r is lower than the in-situ background shear stress τ_o. We study here how fault dilatancy associated with slip affect shear crack propagation due to fluid injection. We use a planar bi-dimensional model with frictional weakening and assume that fluid flow only takes place along the fault (impermeable rock / immature fault). Dilatancy induces an undrained pore-pressure drop during crack acceleration, locally strengthening the fault. We introduce an undrained residual fault shear strength τ_r^u (function of dilatancy) and show theoretically that under the assumption of small scale yielding, an otherwise unstable fault ($\tau_r < \tau_o$) is stabilized when τ_r^u is larger than τ_o. We numerically solve the complete coupled hydro-mechanical problem and confirm this theoretical estimate. It is important to note that the undrained residual strength is fully activated only if residual friction is reached. Dilatancy stabilizes an otherwise unstable fault if the nucleation of an unabated dynamic rupture -without dilatancy- is affected by residual friction, which is the case for sufficiently large injection pressure. We also discuss the effect of fault permeability increase due to slip. Our numerical results show that permeability increases lead to faster aseismic growth but do not impact the stabilizing effect of dilatancy with respect to dynamic rupture.

This chapter is a modified version of the following scientific article:

Ciardo, F., & Lecampion, B. (2019). Effect of dilatancy on the transition from aseismic to seismic slip due to fluid injection in a fault. *Journal of Geophysical Research: Solid Earth*, 124, 3724-3743.

Authors contributions
Federico Ciardo: Conceptualization, Methodology, Formal analysis, Investigation, Software, Visualization, Validation, Writing - original draft.
Brice Lecampion: Conceptualization, Methodology, Formal analysis, Investigation, Writing - review & editing, Supervision.

4.1 Introduction

Seismic and aseismic ruptures associated with anthropogenic fluid injection at depth have been observed in variety of settings (Healy et al. 1968, Hamilton & Meehan 1971, Scotti & Cornet 1994, Cornet et al. 1997*a*, Shapiro et al. 2006, Ellsworth 2013, Skoumal et al. 2015, Bao & Eaton 2016*b*) to cite a few. Industrial applications involved range from waste water disposal to the stimulation of enhanced geothermal systems and hydraulic fracturing.

Injection of fluid into the sub-surface alters the local stress state. Pre-existing fractures/-faults or intact rock mass can fail due to the local reduction of effective stresses associated with pore pressure increase. Shear fractures can thus be activated and propagate along favourably oriented planes of weaknesses/faults. In some cases, the aseismic slip may lead to the nucleation of a dynamic rupture (seismic event). A necessary ingredient for such a transition from aseismic to seismic slip is the reduction of fault frictional strength with slip, i.e. when the frictional resistance decreases faster than the elastic unloading associated with slip (Cornet 2015*a*).

The transition from the activation of aseismic slip to the nucleation of a seismic event due to fluid injection has been discussed theoretically (Garagash & Germanovich 2012) and observed in-situ (Scotti & Cornet 1994, Cornet et al. 1997*a*, Guglielmini et al. 2015, Wei et al. 2015, Cornet 2016). We investigate here the effect of fault/fracture dilatancy associated with slip on the transition from aseismic crack propagation to seismic slip in the context of fluid injection. The physical mechanism of dilatancy associated with sliding over fault's asperities leads to a pore pressure drop under undrained conditions and thus to a fault strengthening denoted as dilatant hardening (Segall & Rice 1995, Segall et al. 2010, Rudnicki & Chen 1988). Strong dilatant behavior has been observed during aseismic crack propagation in scaled laboratory experiments by Lockner & Byerlee (1994), Samuelson et al. (2009) and inferred during field experiment of the stimulation of geothermal reservoir (Batchelor 1985) suggesting that dilatancy possibly plays an important role on shear fracture propagation in some cases.
Although the concept of dilatant hardening associated with undrained conditions has been studied on saturated rock masses (Rice 1975) as well as on frictional weakening faults loaded by tectonic strain (Rudnicki 1979, Segall & Rice 1995, Shibazaki 2005, Segall et al. 2010), the quantification of its effect on the transition from aseismic to seismic slip propagation in association with fluid injection remains elusive.

The interplay between fluid injection, in-situ conditions, frictional properties and evolution of the hydraulic properties of fault present a highly coupled problem leading to a wide range of possible behaviour even under 'simple' homogeneous in-situ conditions (Garagash & Germanovich 2012, Viesca & Rice 2012, Zhang et al. 2005). In this paper, we extend previous work to account for fault dilatancy and quantify its impact on the propagation of a shear crack induced by a constant pressure injection. For simplicity, we reduce to a 2D configuration and model the fault / joint as a planar thin strip where both shear slip and fluid flow are localized. We adopt a simple linear weakening slip-dependent friction law Ida (1972) combined with a non-associated flow rule to account for dilatancy, assume isothermal conditions and neglect poroealastic stress changes in the surrounding rock. We pay particular attention to the verification of our numerical solver and discuss the different type of crack propagation (aseismic/seismic) as a function of in-situ and injection conditions. We also put in perspective our results at the light of theoretical arguments under the small-scale yielding approximation (Rice 1968, Palmer & Rice 1973).

4.2 Problem formulation

We consider an infinite planar fault in an infinite homogeneous isotropic elastic medium (see Figure 4.1) under plane-strain conditions. We also assume that the host rock has a much lower permeability than the fault. As a result, the fluid flow only occurs along the fault plane from a source injection located at the middle of the fault in the 2D space - more precisely a line-source in the out-of-plane direction to satisfy plane-strain conditions. Furthermore, we assume a uniform initial in-situ stress and pore pressure field prior to the start of the injection. Such a homogeneous model is obviously only valid for small fault slippage length compared to the background in-situ gradient but it allows to isolate and understand the different type of responses in a clearer way. Although different type of injection conditions, either away or directly on the fault, can be investigated, we restrict here to the case of a constant pressure injection from a point source directly in the fault.

4.2.1 Equilibrium, activation and dilatancy of slip-weakening fault

We consider the occurrence of a mode II shear crack of length $2a$ on the fault plane due to a constant pressure fluid injection. Initially, we assume the fault to be in static equilibrium with the uniform in-situ stress state. Upon activation of slip due to the increase of fluid pressure along the fault, the bi-dimensional quasi-static elastic equilibrium can be written as the following integral equations relating fault tractions and displacement discontinuities in the local normal and tangential frame along the fault plane (using the convention of summation on repeated indices):

$$t_i(x,t) = t_i^o(x) + \int_{-a}^{a} K_{ij}(\xi, x) d_j(\xi, t) \mathrm{d}\xi, \text{ for } i,\, j = n,\, s \tag{4.1}$$

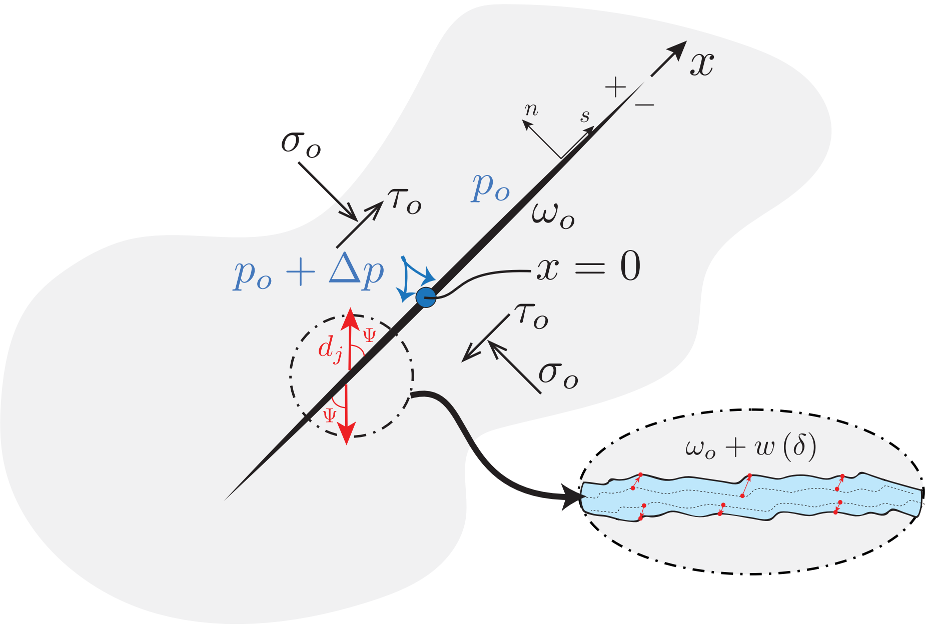

Figure 4.1 – Model of frictional weakening dilatant fault & loading conditions. Zoom represents schematically the dilatant process that occur during shear fracture propagation.

where $t_i = \sigma_{ij} n_j$ is the current traction vector acting along the fault, t_i^o its value under the initial in-situ stress and d_j denotes the vector of displacement discontinuities on the fault:

$$d_j = u_j^+ - u_j^- \tag{4.2}$$

The quasi-static fundamental elastic displacement-discontinuity tensor K_{ij} is known in closed-form for a bi-dimensional infinite medium (see e.g. Gebbia (1891), Crouch & Starfield (1983), Hill et al. (1996)). It is worthwhile to recall that for a planar crack, the shear and normal boundary integration uncouples as $K_{sn} = K_{ns} = 0$. As a result, shear slip does not induce any changes in the normal stress along the planar fault. However, if shear slip induces plastic dilatancy, the corresponding normal displacement discontinuity associated with dilatancy modify the normal stress along the fault. We note that the use of a quasi-static approach will obviously overshoot any finite dynamic rupture. Although a quasi-dynamic approximation (Rice 1993) would provide more realistic results without the expense of a complete dynamic simulation, we restrict our-self mostly to the nucleation of a dynamic rupture for which a quasi-static approximation is granted.

We adopt the convention of normal stresses positive in compression. The normal and shear components of the traction vector on the fault plane $t_i = (t_n, t_s)$ (in the local $s - n$ reference system on Figure 4.1) will be noted as $\sigma = -t_n = -(n_i \sigma_{ij} n_j)$ and $\tau = s_i \sigma_{ij} n_j$ for the normal and shear component respectively. We will also write the normal displacement

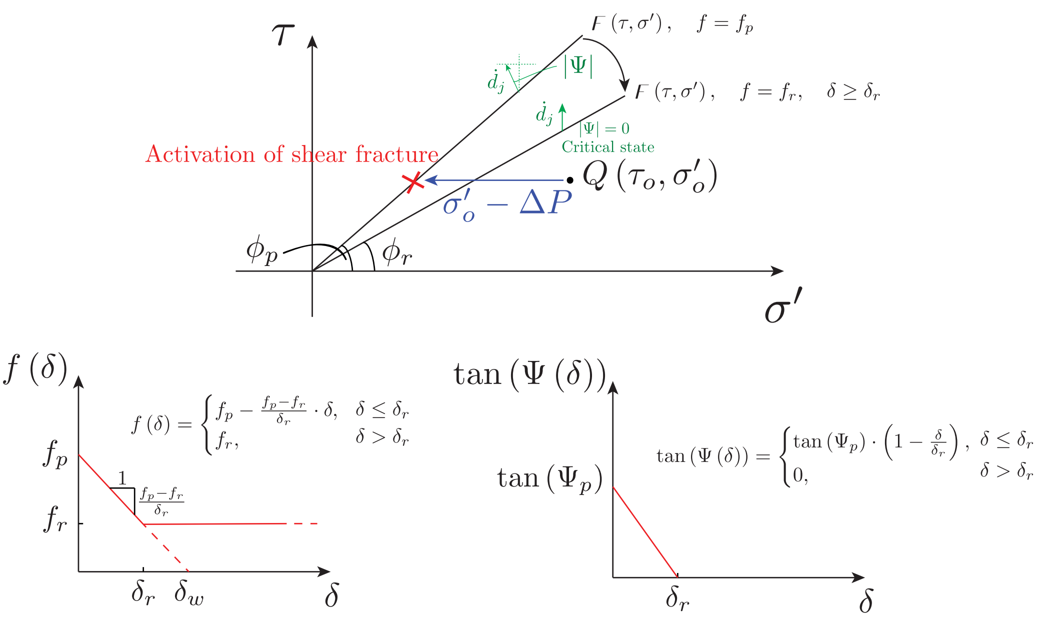
τ
$F(\tau,\sigma'),\quad f=f_p$
$\dot{d}_j$
$|\Psi|$
$F(\tau,\sigma'),\quad f=f_r,\quad \delta\geq\delta_r$
$\dot{d}_j$
$|\Psi|=0$
Critical state
Activation of shear fracture
$Q(\tau_o,\sigma'_o)$
$\sigma'_o-\Delta P$
ϕ_p
ϕ_r
σ'
$f(\delta)$
$f(\delta)=\begin{cases}f_p-\frac{f_p-f_r}{\delta_r}\cdot\delta, & \delta\leq\delta_r\\ f_r, & \delta>\delta_r\end{cases}$
f_p
1
$\frac{f_p-f_r}{\delta_r}$
f_r
δ_r
δ_w
δ
$\tan(\Psi(\delta))$
$\tan(\Psi(\delta))=\begin{cases}\tan(\Psi_p)\cdot\left(1-\frac{\delta}{\delta_r}\right), & \delta\leq\delta_r\\ 0, & \delta>\delta_r\end{cases}$
$\tan(\Psi_p)$
δ_r
δ

Figure 4.2 – The Mohr-Coulomb plot (top) illustrates the evolution of the yielding surface $F(\tau,\sigma')$ with weakening of friction coefficient as well as the evolution of plastic displacement discontinuity vector $\dot{d}_j$ with slip after shear fracture activation due to fluid over-pressure ΔP. The linear evolution of friction coefficient $f=\tan(\phi)$ (left) and dilatancy angle $\tan(\psi)$ (right) with slip δ are displayed in the bottom plots.

discontinuities as $d_n=w$ (positive for opening) and the shear displacement discontinuities (slip) as $d_s=\delta$ (positive in a clockwise rotation).

4.2.1.1 Activation and plasticity

We assume that the fault obeys a Mohr-Coulomb yield criterion without cohesion, accounting for a slip weakening of friction. The yield criterion is:

$$F(\tau,\sigma')=|\tau|-f(\delta)\sigma'\leq 0, \tag{4.3}$$

where $f(\delta)=\tan(\phi(\delta))$ is the friction coefficient (ϕ the corresponding friction angle), which is supposed to weaken linearly with slip δ, from a peak value f_p to a residual value f_r for slip larger than δ_r (see Figure 4.2-bottom-left). $\sigma'=\sigma-p(x,t)>0$ is the local effective normal stress acting on the fault plane. We will write the initial in-situ conditions (prior to fluid injection) as $\sigma'_o=\sigma_o-p_o$ and τ_o for the ambient effective normal stress and shear stress respectively.

The fault is activated when the injection overpressure is sufficient to reach the Mohr-Coulomb criterion at peak initial friction (see Figure 4.2-top), and shear slip starts to occur on the fault. We model the fault as rigid plastic and account for a possible dilatant behavior. Using a non-associative flow rule, the rate of displacement discontinuities (denoted with a dot) derive from a plastic potential function of the corresponding effective tractions when the yield criterion is satisfied (i.e. $\mathcal{F} = 0$):

$$\dot{d}_i = \lambda \frac{\partial G}{\partial t'_i} \tag{4.4}$$

The (scalar) plastic multiplier λ is either greater than zero as long as the local stress state satisfies the Mohr-Coulomb yield criterion (4.3), or equals to zero for non-yielded stress state (for which $\mathcal{F}(\tau, \sigma') < 0$ and the fault is not activated). Plastic slip takes place along the yielding surface (see plastic strain vector in Figure 4.2-top). This can be summarized by the following set of conditions (Lubliner 2005, Maier et al. 1993):

$$\lambda \geq 0, \quad \mathcal{F}\left(\tau, \sigma'\right) \leq 0, \quad \lambda \mathcal{F}\left(\tau, \sigma'\right) = 0 \tag{4.5}$$

In order for plastic flow to occur, the tractions on the fault must persist on the yield surface $\mathcal{F} = 0$, while upon unloading plastic flow stops as soon as $\mathcal{F} < 0$. This requirement is often denoted as a consistency condition and written as

$$\lambda \dot{\mathcal{F}}\left(\tau, \sigma'\right) = 0, \quad \left(\text{if} \quad \mathcal{F}\left(\tau, \sigma'\right) = 0\right) \tag{4.6}$$

It allows to obtain the plastic multiplier λ (see e.g. (Lubliner 2005, Simo & Hughes 1997) for more details).

We use a non-associated Mohr-Coulomb criterion with a dilatancy angle ψ decreasing with accumulated slip δ. We write the plastic potential as

$$G\left(\tau, \sigma'_n\right) = |\tau| - \tan\left(\psi\left(\delta\right)\right) \sigma' \tag{4.7}$$

As a result, the rate of slip and opening displacement discontinuity are related to each other as:

$$\dot{d}_s = \dot{\delta} = \lambda \text{sign}(\tau) \tag{4.8}$$

$$\dot{d}_n = \dot{w} = \lambda \tan\left(\psi(\delta)\right) \tag{4.9}$$

We assume that the dilatancy coefficient (tangent of the dilatancy angle ψ) decreases linearly with slip from an initial peak value $\tan\psi_p$ to zero: the fault is assumed to reach a critical state (where the dilatancy angle is zero) over the same slipping distance δ_r at which it reaches residual friction (see Figure 4.2-bottom-right). Such a choice is consistent with experimental observations that a critical state (where no change of volume occur) is reached after sufficient plastic deformation for most rocks and granular material.

Integration of (4.8)-(4.9) provides the following quadratic evolution of fracture width due to the dilatancy induced by slip:

$$w\left(\delta\right)=\int_{0}^{\delta}\tan\left(\psi\left(\delta'\right)\right)\mathrm{d}\delta'=\begin{cases}2\Delta w\left(\dfrac{\delta}{\delta_r}\right)-\Delta w\left(\dfrac{\delta}{\delta_r}\right)^{2} & \delta<\delta_r\\ \Delta w & \delta>\delta_r\end{cases}\tag{4.10}$$

where Δw denotes here the maximal / final dilatant opening at residual friction:

$$\Delta w=\int_{0}^{\delta_r}\tan\left(\psi\left(\delta'\right)\right)\mathrm{d}\delta'=\tan\left(\psi_p\right)\frac{\delta_r}{2}\tag{4.11}$$

A similar law for the dilatancy evolution with frictional slip has been proposed by Rudnicki & Chen (1988) to model uplift in sliding over asperities of a long homogeneous slab subjected to shear and normal mechanical loadings. Initially, the fault is supposed to have a constant uniform 'hydraulic aperture' ω_o which can be considered as the fault gouge thickness in such a model. The ratio between the maximal dilatant increment of fracture width Δw and this initial aperture ω_o defines a dilatant strain $\epsilon_d=\dfrac{\Delta w}{\omega_o}$ which can be related to the maximum change of fault porosity due to slip. Such a quantity will directly appear in the hydro-mechanical coupling.

Dilatancy is known to be function of effective normal stress - with lower dilatancy angle typically measured under larger confinement (Matsuki et al. 2010, Barton et al. 1985). Measured value of the peak dilatancy angle (at small slip) ranges from $\sim 40°$ at 5 MPa of confinement to $\sim 6°$ at 30 MPa for Inada granite (Matsuki et al. 2010), leading to values of ϵ_d in a range of $10^{-3}-10^{-2}$. Laboratory experiments on quartz fault gouge (Samuelson et al. 2009) provides value of ϵ_d in the range $10^{-4}-10^{-3}$ at effective confinement up to 20 MPa, values which appears of similar order than the one measured at larger confinement (Marone et al. 1990).

In what follows, for sake of simplicity, we do not explicitly account for the complete details of the dependence of dilatancy with normal effective stresses. The peak dilatancy angle can be implicitly taken to be a function of the level of in-situ confinement prior to injection. Moreover, we acknowledge that a relatively large range of possible value of the dilatant strain ϵ_d may exist from 10^{-4} to 10^{-2}.

4.2.1.2 Slip weakening and nucleation length-scale

Following Uenishi & Rice (2003), Garagash & Germanovich (2012), we introduce a characteristic nucleation patch length-scale a_w

$$a_w=\frac{E'}{2\tau_p}\delta_w\tag{4.12}$$

to scale the crack length. This characteristic nucleation length-scale is obtained by normalizing the slip δ and shear stress τ in the elasticity equation (4.1) by $\delta_w = \dfrac{f_p}{f_p - f_r}\delta_r$ and $\tau_p = f_p \sigma'_o$, respectively. δ_w denotes the amount of slip at which the friction coefficient goes to zero if an unlimited linear slip-weakening friction law is considered (see Figure 4.2-bottom-left). Typically δ_w is of the order the fault's asperities and thus ranges between 0.1 mm to 10 mm. $\tau_p = f_p \sigma'_o$ defines the peak frictional strength at ambient conditions, its difference from the ambient shear stress τ_o quantify the fault stress criticality. Such a peak fault shear strength can vary widely with depth, fault orientation as well as hydrogeological conditions (normally pressurized versus over-pressured formations) and thus can range between a fraction to hundred of MegaPascals. We thus deduce that the range of characteristic patch length-scale a_w (e.g. for a crystalline rock with E$'$ $\sim$ 60 GPa) can approximately ranges between tens of centimeters to tens of meters depending on geological conditions.

4.2.2 Fluid flow

Under the assumption of much smaller rock permeability compared to the longitudinal fault permeability, the fluid flow is confined within the fault zone. This case corresponds to an immature fault with little accumulated slip for which the extent of the damage zones around the fault core remains limited. For active and mature fault, the permeability structure around the fault can not be neglected. Much larger permeabilities have indeed been measured in the damage zone (that can have decameters thickness) of active mature fault compared to the fault gouge unit (Lockner et al. 1999). Here, we restrict to the case of an immature / young fault for which the flow is confined in the gouge. Such a hypothesis could also be valid for inactive mature fault that would have exhibited a plugging of their damage zone permeability (e.g. via long term thermo-hydro-chemical effects).

The mass balance equation width-averaged across the fault hydraulic aperture w_h of the gouge layer thus reduces to:

$$\frac{\partial \rho w_h}{\partial t} + \frac{\partial \rho w_h V}{\partial x} = 0, \tag{4.13}$$

where ρ is the fluid density and V is the averaged fluid velocity. The fault hydraulic aperture $w_h = \omega_o + w(\delta)$ is the sum of its initial value ω_o and the additional dilatant aperture function of slip (see eq. (4.10)).

By combining fluid compressibility (taken as liquid water) and pore compressibility of the fault gouge in an unique parameter β $\left[M^{-1}TL^2\right]$, the width averaged fluid mass conservation (4.13) along the fault (x-axis) reduces to

$$w_h \beta \frac{\partial p}{\partial t} + \tan(\psi(\delta)) \frac{\partial \delta}{\partial t} + \frac{\partial q}{\partial x} = 0, \tag{4.14}$$

where $q = w_h V$ is the uni-dimensional local fluid flux given by Darcy's law:

$$q = -\frac{w_h k_f(\delta)}{\mu} \frac{\partial p}{\partial x}, \tag{4.15}$$

with μ the fluid viscosity $\left[ML^{-1}T^{-1}\right]$ and $k_f(\delta)$ the fault intrinsic permeability $\left[L^2\right]$. The hydraulic diffusivity of the fault α $\left[L^2/T\right]$ is defined as:

$$\alpha = \frac{k_f}{\mu\beta} \tag{4.16}$$

In particular, the location of the fluid / pressure front evolves as $\sqrt{4\alpha t}$ for such type of diffusion problem (Carslaw & Jaeger 1959).

In conjunction with the increase of the fault aperture with dilatant slip (4.10), the longitudinal fault permeability may also evolve with shear slip. A number of different models have been proposed in the literature for the evolution of permeability with slip, from using the cubic law for the fault transmissivity (product of permeability $k_f = w_h^2/12$ and hydraulic aperture w_h), to an exponential dependence of permeability with normal stress, or Cozeny-Karman type relations. Here, we first make the assumption of a constant fault permeability $k_f = \omega_o^2/12$ before relaxing such an approximation in Section 4.6 in order to properly gauge its effect.

It is important to note that even in the absence of permeability evolution, the changes of hydraulic aperture induced by dilatancy still impact the fluid flow in a non-trivial and non-linear way. This is notably due to the sink term $\tan(\psi(\delta))\frac{\partial \delta}{\partial t}$ associated with slip induced dilatancy. Fluid flow can not be uncoupled from mechanical equilibrium and fault slip, contrary to the case of zero dilatancy (Garagash & Germanovich 2012), where for a constant pressure injection ΔP, the pore pressure on the fault plane is simply given by $p(x,t) = p_o + \Delta P \text{Erfc} \left| \frac{x}{\sqrt{4\alpha t}} \right|$. No simple analytical solution does exist for this complete non-linear hydro-mechanical coupling.

The effect of slip induced dilatancy leads to a pore-pressure drop under undrained conditions (denoted here as Δp_u). At large slip rate, the change of hydraulic width from its initial value up to its maximum value $\omega_o + \Delta w$ (4.11) will be sudden. In such an undrained limit the fluid has no time to flow and the associated pore pressure change can be directly obtained from mass conservation (4.14):

$$\Delta p_u = -\frac{\Delta w}{\omega_o \beta} = -\frac{\epsilon_d}{\beta} \tag{4.17}$$

This undrained pore-pressure drop will be localized at the crack tips, where frictional slip weakening occurs. From the previously discussed range of the dilatant strain $\epsilon_d \in [10^{-4} - 10^{-2}]$, for a compressibility coefficient β between the one of liquid water and usual pore compressibility ($\beta \in [5 - 100]\, 10^{-10}\text{Pa}^{-1}$), we obtain a range of values $[0.01 - 20]$ MPa for such an undrained pore-pressure drop. The previous estimate corresponds to the maximum possible amount of undrained pore-pressure drop (sudden slip from zero to δ_r). A re-strengthening of the fault is thus expected as the effective normal stress increase locally as a result of this undrained pore-pressure drop. Similar dilatant hardening is typically observed in fluid-saturated porous medium subject to undrained loading (Rice 1975, Rudnicki 1979). It is important to underline that such re-strengthening effect is less pronounced for “mature" faults, for which pore fluid diffusion normal to fault plane (across the permeable units of damaged zone) may prevail against fluid diffusion along the fault gouge unit.

4.2.3 Initial and injection conditions

Initially, the (peak) fault strength $\tau_p = f_p \sigma'_o$ at ambient condition is everywhere larger than the in-situ shear traction on the fault τ_o. In other words, the fault is initially stable (i.e. $\digamma(\tau_o, \sigma'_o) < 0$) and locked before the start of fluid injection. We consider here the case of a constant over-pressure ΔP at the injection point:

$$p(x = 0, t) = p_o + \Delta P, \tag{4.18}$$

We assume that the choice of the injection over-pressure ΔP is such that the minimum principal effective stress σ'_n always remain compressive (positive) such that no hydraulic fracture type failure occurs: i.e. $\Delta P < \sigma'_o$. A constraint often enforced in practice for large scale injection but also sometimes during hydraulic stimulation of geothermal reservoirs. We investigate here the activation of a shear crack that would occur if the overpressure ΔP at the injection point is sufficient to lower the effective normal stress and reach Mohr-Coulomb failure. Such a minimum over-pressure ΔP for activation is directly related to the fault criticality:

$$\frac{\Delta P}{\sigma'_o} \geq 1 - \frac{\tau_o}{\tau_p} \tag{4.19}$$

The ratio τ_o/τ_p represents the stress criticality of the fault at ambient condition (quantifying how far the fault is from failure). For a critically stressed fault ($\tau_o/\tau_p \sim 1$), slip is activated for small over-pressure. On the other hand, a fault whose initial uniform stress state is much lower than its peak frictional strength ($\tau_o/\tau_p \ll 1$) requires a larger over-pressure to activate a shear crack, and is sometimes referred to as a marginally pressurized fault.

4.3 Activation and transition between aseismic and seismic slip

4.3.1 Case of a non-dilatant fault

We first briefly recall the results obtained for the case of a non-dilatant fault by Garagash & Germanovich (2012) using the the same linear frictional weakening model. This summary is required in order to properly put in perspective the effect of a dilatant fault behavior.

After activation of aseismic slip, there exist two ultimate fault stability behaviors depending on the relative value of the residual strength (defined at ambient condition) $\tau_r = f_r \sigma'_o$ compared to the in-situ background shear stress τ_o. Notably, if the residual frictional strength τ_r exceeds the ambient shear stress τ_o, the fault is *ultimately stable*. On the other hand, for a residual frictional strength τ_r lower than τ_o, the fault is unstable. Figure 4.3 summarizes the different behaviors, as a function of the dimensionless fluid over-pressure $\Delta P/\sigma'_o$, stress criticality τ_o/τ_p and relative value of τ_r with respect to the initial shear stress τ_o. Region 1 on Figure 4.3 corresponds to the trivial case of an injection without activation of any slip.

For an ultimately stable fault (for which the residual strength τ_r is larger than the ambient shear stress τ_o), it can be shown that for an over-pressure sufficient to activate slip, at large time / large crack length the shear crack grows quasi-statically (aseismically) as long as the fluid injection continues (regions 2 and 3 on Figure 4.3). However, because of the weakening of its frictional properties, an ultimately stable fault may host an episode of seismic slip followed by an arrest (region 2 on Figure 4.3). Such a 'seismic event' depends on both the stress-criticality and the amount of over-pressure. For a moderate over-pressure (sufficient to activate slip), the shear-crack first lags behind the fluid diffusion front and, due to the interplay between fluid pressurization and frictional weakening, a dynamic event nucleate and grows until it catches up the fluid pressure diffusion front ahead of which the over-pressure is minimal. The subsequent propagation is then a-seismic and tracks the fluid front as long as injection continues. In other words, depending on the value of fluid over-pressure applied in the middle of the fault, the local accumulation of slip during the (aseismic) crack propagation varies. If the fluid over-pressure induces a large local slip accumulation during the aseismic propagation (such that it exceeds the residual slip δ_r), the fault never exhibits a dynamic event (strictly aseismic propagation - region 3), otherwise a nucleation of a dynamic rupture episode occurs (region 2 in Figure 4.3) .

The situation is different for unstable fault ($\tau_r < \tau_o$) - regions 4a, b, c on Figure 4.3. It can be proved that an unabated dynamic rupture will always occur when $\tau_r < \tau_o$. The nucleation length (and time of nucleation) depends again on stress criticality, the value of over-pressure and in some cases (region 4c) on the value of the residual friction

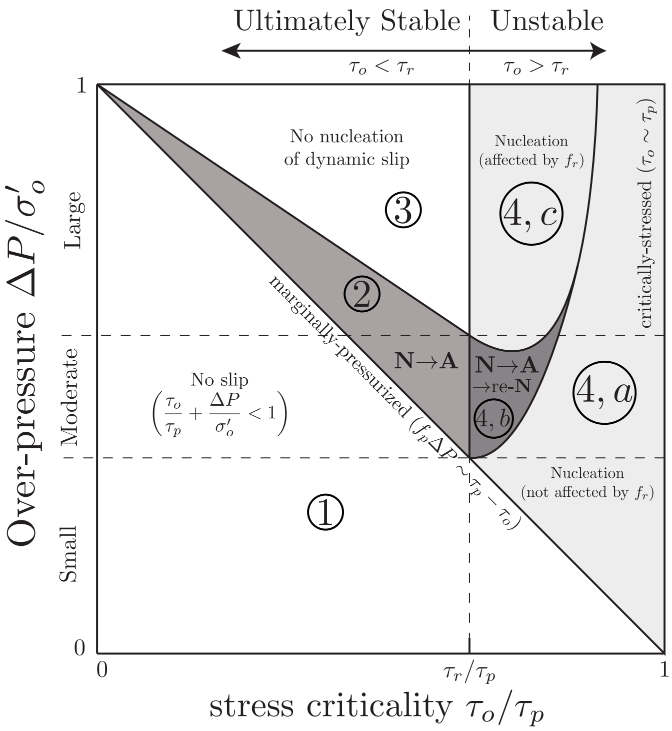
Ultimately Stable
Unstable
$\tau_o < \tau_r$
$\tau_o > \tau_r$
1
0
0
τ_r/τ_p
1
Over-pressure $\Delta P/\sigma'_o$
Large
Moderate
Small
stress criticality τ_o/τ_p
No nucleation of dynamic slip
③
Nucleation (affected by f_r)
$4, c$
critically-stressed ($\tau_o \sim \tau_p$)
②
marginally-pressurized ($f_p \Delta P \sim \tau_p - \tau_o$)
N→A
N→A →re-N
$4, b$
$4, a$
No slip
$\left(\frac{\tau_o}{\tau_p} + \frac{\Delta P}{\sigma'_o} < 1\right)$
①
Nucleation (not affected by f_r)

Figure 4.3 – Phase diagram of Garagash & Germanovich (2012) that describes the different regimes of propagation for a non-dilatant fault, as a function of the dimensionless fluid over-pressure $\Delta P/\sigma'_o$ and stress criticality τ_o/τ_p. Region 1 corresponds to the trivial case of an injection without fault re-activation. Regions 4a, b, c corresponds to the unstable fault case for which an unabated dynamic rupture occurs as the residual shear strength (defined at ambient conditions) is lower than the in-situ shear stress ($\tau_r < \tau_o$). Regions 2 and 3 corresponds to the case of ultimately stable faults ($\tau_r > \tau_o$) for which most of the crack growth is aseismic although transient seismic slip may occur (region 2).

f_r. For criticality stress fault (region 4a - $\tau_o/\tau_p \sim 1$), the nucleation patch size a_c is independent of the overpressure $a_c = 0.579\, a_w$ (Garagash & Germanovich 2012). In these cases, even a small over-pressure is sufficient to nucleate a dynamic rupture and the fluid front lies well within the crack when the unabated instability occurs. For unstable but marginally pressurized fault (moderate stress criticality), subjected to a moderate value of over-pressure, a transient seismic event may occur and then arrest when the crack front catches up with the fluid front. However, here (region 4b in Figure 4.3) a re-nucleation always occurs (affected by residual friction) leading then to an unabated dynamic rupture. For larger of over-pressure, a single nucleation of an unabated dynamic rupture occur (region 4c).

4.3.2 Effect of dilatancy

4.3.2.1 Undrained fault response

At high slip rate, the undrained response associated with dilatancy causes a pore-pressure drop (4.17). Scaling the fluid pressure by effective normal in-situ stress, we express the undrained response via the following dimensionless undrained pressure change

$$\frac{\Delta p_u}{\sigma'_o} = -\frac{\epsilon_d}{\beta \sigma'_o} \tag{4.20}$$

The dimensionless ratio $\frac{\epsilon_d}{\beta \sigma'_o}$ quantifies the effect of dilatancy in terms of pore pressure drop under undrained conditions with respect to the initial confining stress. For a realistic range of effective in-situ normal stress of [1-200] MPa, whose extremes may represent the case of normally pressurized and over-pressurized fault located approximately between 0.1 and 5 Km below the Earth's surface, and for the previously reported range for undrained pore-pressure drop ϵ_d/β, the dimensionless dilatancy parameter $\frac{\epsilon_d}{\beta \sigma'_o}$ ranges between 0.01 (deeper conditions/low dilatancy) and 20 (shallow conditions / large dilatancy).

Dilatancy is mobilized in the frictional weakening zone. Moreover, it's impact on pore-pressure is modulated by the slip rate $\partial\delta/\partial t$ (see eq. (4.14)). In proximity of a dynamic event when the slip rate increases rapidly, the undrained pore pressure drop leads to a local strengthening at the crack tip (dilatant hardening). In the case where the slip rate and crack velocity is larger than the fluid flux, the undrained dilatant pore-pressure drops will be at its maximum (4.17) and will persist inside the crack away from the crack tip. We can thus quantify the associated strengthening by adding its effect to the fault residual strength - defining an undrained residual shear strength τ_r^u as:

$$\tau_r^u = \tau_r - f_r \Delta p_u = \tau_r \left(1 + \frac{\epsilon_d}{\beta \sigma'_o}\right) \tag{4.21}$$

From the ranges of value previously discussed, we see that the undrained shear strength can be from 1.01 to 2 times larger than the drained residual strength.

On the other hand, the shear-induced dilation impact (via the non-associated flow rule (4.9)) the distribution of normal stress along the fault through the effect of corresponding opening displacement discontinuity in the elasticity equation (4.1). Inside the crack, the opening of the fault leads to an increase of compressive normal stress, whereas ahead the crack tips it induces tensile stresses therefore reducing the fault frictional strength. There is thus an interplay between the non-local stress-induced perturbation due to fault opening and dilatant hardening. The tensile stresses ahead of the tip have however a lower magnitude than the undrained pore-pressure drop. For instance, if we suppose that the weakening region is small compared to the whole crack size (small scale yielding conditions), the mechanical opening is uniform and equal to Δw along the whole crack.

We can thus estimate the tensile normal stress ahead of the crack front using the solution for an edge dislocation (e.g. (Hill et al. 1996)) of intensity Δw. Scaling the distance $\hat{x}$ from the dislocation by the nucleation lengthscale a_w, we have

$$\Delta\sigma = -\frac{E'}{4\pi a_w}\frac{\Delta w}{\hat{x}/a_w} \tag{4.22}$$

The corresponding stress intensity for such a singular field is thus $E'\Delta w/(4\pi a_w)$. For a maximum increment of dilatant width Δw of the order of few millimeters and corresponding estimate of the nucleation patch size a_w gives an order of magnitude of about $\sim$ 1 MPa or less for such stress perturbation. Taking the ratio of such stress intensity with the estimate of the undrained pore-pressure drop (4.17), after re-arranging, one obtain $E'\beta\omega_o/(4\pi a_w)$ which will be always smaller than one as $E'\beta \simeq O(10)$ and $\omega_o/a_w \simeq O(10^{-2})$. We therefore conclude that the mechanical effect of dilatancy induced tensile stresses ahead of the crack tip is lower than the undrained pore pressure change Δp_u. The dilatant hardening effect dominates. This is confirmed by our fully coupled numerical simulations (see Section 4.5).

4.3.2.2 Small scale yielding & stability condition

Following the work of Garagash & Germanovich (2012), we extend their ultimate stability condition to account for the effect of dilatant hardening. This stability condition can be obtained under the assumption of small scale yielding (s.s.y) which holds when the shear crack of half-length a is sufficiently larger than the characteristic length scale a_w such that all the frictional weakening occurs in a small zone near the crack tip. Such a localization of the frictional weakening in a small zone near the crack tip can be observed on our numerical results (see Section 4.5.1). Under such assumption, the fracture energy G_c (Rice 1968, Palmer & Rice 1973) for the linear frictional weakening model can be estimated as:

$$G_c = \int_0^{\delta} \tau(\delta) - \tau_r \, \mathrm{d}\delta \simeq \frac{\delta_r}{2}(f_p - f_r) \times \sigma'(a) \tag{4.23}$$

under the assumption that the effective normal stress $\sigma'(a)$ is constant within the weakening region. The condition for quasi-static crack growth of such a shear crack reduces to the classical linear elastic fracture mechanics criteria. The driving force for propagation G (the energy release rate) must equal G_c for quasi-static growth to occur. A criteria which for such a shear crack reduce to:

$$G = \frac{K_{II}^2}{E'} = G_c, \tag{4.24}$$

where K_{II} is the stress intensity factor for the given loading and crack size.

As all the crack -besides the small weakening zone at the tips- is at residual frictional strength, the stress intensity factor can be obtained by superposition of the effect of the loading of the crack by i) the residual frictional strength at ambient condition $\tau_r = f_r \sigma'_o$ minus the far-field in-situ shear stress τ_o (which are both uniform along the crack) and ii) the effect of the over-pressure due to the fluid injection on the decrease of shear strength $f_r \Delta p(x,t)$. The stress intensity factor for such a configuration is thus given as (Rice 1968, Tada et al. 2000)

$$K_{II} = (\tau_o - \tau_r)\sqrt{\pi a} + \underbrace{f_r \sqrt{\frac{a}{\pi}} \int_{-a}^{+a} \frac{\Delta p\,(x,t)}{\sqrt{a^2 - x^2}} \mathrm{d}x}_{\Delta K_{II}(a,t)} \tag{4.25}$$

On the contrary to the non-dilatant case, the exact solution for the over-pressure $\Delta p\,(x,t)$ evolution along the fault is not known analytically. It is the complete solution of the coupled hydro-mechanical problem in the dilatant case. However, in order to obtain an ultimate stability condition for large crack length, it can be approximated as follow. If the shear crack a is much larger than both the slipping patch length scale a_w (which is required for the s.s.y approximation to be valid) and the diffusion length scale $\sqrt{4\alpha t}$, the over-pressure can be approximated as the sum of a point source term of intensity ΔP for the effect of the injection (as $a \gg \sqrt{4\alpha t}$) and the response of the undrained pore-pressure drop. Moreover, if the crack velocity is much larger than the fluid velocity - which would be true in all cases if the crack accelerates - the undrained pore-pressure drop can be assumed to remain constant and equal to Δp_u (eq. (4.17)) over the entire crack. Under those conditions, the stress intensity factor reduces to:

$$\begin{aligned} K_{II} &\simeq (\tau_o - \tau_r)\sqrt{\pi a} + \frac{f_r \Delta P}{\sqrt{\pi a}} + \frac{\tau_r \Delta p_u}{\sigma'_o}\sqrt{\pi a} \\ &\simeq (\tau_o - \tau_r^u)\sqrt{\pi a} + f_r \frac{\Delta P}{\sqrt{\pi a}} \end{aligned} \tag{4.26}$$

where the undrained shear strength previously introduced appear. This expression is strictly similar to the one derived in Garagash & Germanovich (2012) pending the replacement of the residual shear strength τ_r by its undrained counterpart $\tau_r^u = \tau_r(1 + \epsilon_d/(\beta\sigma'_o))$ (4.21). As previously anticipated the effect of dilatancy is akin to an increase of the residual shear strength.

The reasoning of Garagash & Germanovich (2012) for the ultimate stability can thus be directly transposed to the dilatant case. In the limit of infinitely large crack $a \to \infty$, one directly see that the stress intensity factor tends to either $+\infty$ if $\tau^o > \tau_r^u$ and $-\infty$ if $\tau^o < \tau_r^u$. In other words, if the initial shear stress τ^o is larger than the undrained residual strength, the fault is ultimately unstable as the stress intensity factor diverges for large crack length: the nucleation of a dynamic rupture will thus always appear. On the other hand, the fault is ultimately stable when $\tau^o < \tau_r^u$. We therefore see that as the undrained residual shear strength τ_r^u is larger than τ_r, sufficient dilatancy may stabilize a fault that otherwise would be unstable. The minimal/critical amount of dilatancy ϵ_d^c required for such a stabilization to occur is simply given as:

$$\epsilon_d^c = \beta\sigma_o'\left(\frac{\tau_o}{\tau_r} - 1\right) = \beta\sigma_o'\left(\frac{\tau_o}{\tau_p}\frac{f_p}{f_r} - 1\right) \tag{4.27}$$

It is interesting to note that it directly depends on the residual stress criticality τ_o/τ_r, and the in-situ effective normal stress.

It is important to note that - obviously - in the ultimately stable case ($\tau_r^u > \tau_o$) the stress intensity factor does not tend to $-\infty$ in reality as the propagation can only occur for $G = G_c$. Upon continuous fluid injection, a stable quasi-static growth will occur and will be modulated by the fluid diffusion: i.e the crack will decelerate for large crack length at constant injection. It is actually possible to devise an approximated solution for such a quasi-static growth by hypothesizing that the crack length evolves as a factor of the fluid front: $a = \gamma\sqrt{4\alpha t}$. An approximation of the pore-pressure evolution accounting for the undrained pore-pressure drop at the tip can be obtained and used in eqns. (4.24) and (4.25) to obtain an estimate of γ. Such an approximated solution is detailed and compared to our numerical results in Supporting Information in Section 4.8.5. Such a refined (but still largely approximated) solution for the pore-pressure evolution gives the exact same limit for the stability condition at large crack length as well as critical dilatancy than the simpler profile postulated previously.

To conclude, before moving to the complete numerical solution of the problem, a word of caution is required with respect to the stability condition $\tau_o < \tau_r^u$. Such a stability condition holds on the premise that most of the crack is at residual friction pending a small weakening zone (s.s.y approximation). It is valid for sufficiently large crack length compared to a_w and peak slip larger than δ_r. Only under this assumption, the maximum undrained pore-pressure (4.20) can be achieved. If a dynamic rupture nucleates for slip smaller than the residual δ_r, the s.s.y is invalid: the undrained pore-pressure response will not be fully activated and thus not sufficient to quench the nucleation of a dynamic rupture. However, upon reaching larger crack length (and thus residual friction), the complete undrained pore-pressure will ultimately kicks in such that a dynamic rupture should arrest if the ultimate undrained s.s.y stability condition ($\tau_r^u > \tau_o$) is satisfied.

4.4 Numerical scheme description

Although approximation of the complete problem have allowed to highlight the stabilizing effect of dilatancy on the nucleation of a dynamic rupture associated with fluid injection, a full numerical solution is needed to investigate the complete parametric space and test the concept of a critical dilatancy.

The complete problem described in Section 5.2 is fully coupled due to the dilatant fault behavior as well as non-linear due to the evolution of the fault hydraulic width (even if the fault permeability remains constant). It also involves the tracking of the moving crack tips. The shear crack evolves in space and time along the fault, paced by pore pressure evolution. Equation (4.1), which links tractions t_i on the fault plane with displacement discontinuities d_j, evolves in time due to the moving crack domain Γ. The developed numerical scheme solve this coupled problem by determining simultaneously the plastic multipliers λ in the 'active' zone of the domain (i.e. where $\mathcal{F}(\tau, \sigma'_n) = 0$) through equations (4.1)-(4.8)-(4.9) and the increment of pore pressure Δp along the whole fault (through equation (4.14) and Darcy's law (4.15)). We then recompute the increment of tractions (due to both increment of slip and the associated increment of hydraulic width) along the rest of the domain via the non-local elasticity equation (4.1). We have chosen a backward-Euler (implicit) time integration scheme for stability and robustness. A choice that stems from the restrictive CFL condition on the time-step for diffusion problem (e.g. (Quarteroni et al. 2000*a*)) - which even deteriorates for strong non-linear variation of permeability similar to the hydraulic fracturing case (Lecampion et al. 2018).

We discretize the elasticity equations using the displacement discontinuity method (Crouch & Starfield 1983, Bonnet 1995) with piece-wise linear element (Crawford & Curran 1982). Because of the singular nature of the elastic kernel, the integral equation is collocated at points inside the displacement discontinuity segments. Knowing the effect in terms of traction of a single piece-wise linear displacement discontinuity, the problem reduces to the one of determining the distribution of displacement discontinuities that generates tractions along the fault such that equilibrium with initial tractions and the failure criterion is satisfied (Crouch & Starfield 1983). The fluid flow equation combining fluid mass conservation and Darcy's law is discretized via a vertex centered finite volume scheme. The fluid pore-pressure is assumed to vary continuously and linearly between element vertex.

In all the simulations reported here, the fault is discretized by N straight equal-sized elements (of size h) - with a total mesh extent of $20 \times a_w$. We therefore have $2N_a$ unknown shear displacement discontinuities (more precisely the plastic multiplier) for the N_a active elements, and $N+1$ unknowns for pore-pressure for all the element in the grid. After discretization, we obtain a non-linear system of size $2N_a + N + 1$, whose unknowns are composed of the plastic multipliers λ (which are linked to increment of slip $\Delta\delta$ through equation (4.8)) in the N_a active yielded elements, and increment of fluid pressure Δp at every nodes of the grid ($N+1$ unknowns). The size of such a non-linear system evolves with the shear crack propagation as more elements yield mechanically. The non-linearities of such a system are related to shear induced dilatancy and frictional weakening. For a given set of active elements, we use a fixed point iterative scheme to solve for this non-linear system - ending iterations when subsequent estimates of both the increment of slip and pore-pressure are within a relative tolerance of 10^{-6}.

The yielding/active set of element is then re-checked using the Mohr-Coulomb criteria. It is worth noting that an element is at failure when the Mohr-Coulomb criteria is reached for both collocation points in the piece-wise linear displacement discontinuity element.

Over one time-step, such a fully implicit algorithm thus solves the coupled problem by means of two nested loops. The outer loop identify the shear crack position by enforcing implicitly the friction weakening Mohr-Coulomb criterion (4.3) along the whole fault. The inner loop solve the aforementioned coupled non-linear hydro-mechanical system of equations for a trial set of active/yielded elements.

Full details about the numerical solver are included in Section 4.8.1.

For numerical efficiency, the time step is adjusted based on the current crack velocity v^n, which is calculated via finite difference:

$$\Delta t^{n+1} = \zeta \frac{h}{v^n}, \tag{4.28}$$

where h is the element size and ζ is a user-defined constant parameter. This allows to better capture the response of the system during high slip rate, and increase time-step size during slow a-seismic growth. However, a constraint is required to avoid a too small time step that would necessarily occur when the shear crack is approaching a dynamic instability, for which the slip rate and crack velocity diverge. Notably, in our simulation, if the variation is such that $\Delta t^{n+1} < 0.8\Delta t^n$, we set $\Delta t^{n+1} = 0.8\Delta t^n$. Similarly, time-step should remain reasonable in order to avoid sampling the pore pressure evolution too coarsely. In our simulations, if $\Delta t^{n+1} > 3\Delta t^n$, then the time step change is constrained to $\Delta t^{n+1} = 3\Delta t^n$, and the initial time-step is taken as a small fraction of the characteristic diffusion time scale.

Thanks to the semi-analytical results of Garagash & Germanovich (2012) for the non-dilatant case, we have performed a thorough benchmarking of this numerical solver. Some of these verifications are described in the Supporting Information together with a mesh convergence study (see Sections 4.8.2 and 4.8.3). Notably, our mesh convergence study have shown that the mesh size h must be such that at least 15 elements cover the characteristic lengthscale a_w to obtain accurate results (i.e. $h \leq a_w/15$). All the simulations reported herein have been performed with $h = a_w/25$.

4.4.1 Characteristic scales for dimensionless governing problem

By introducing properly chosen characteristic scales to normalize the governing equations, relevant physical processes can be systematically investigated. As already stated in Section 4.2.1.2, we follow the scaling of Uenishi & Rice (2003) and Garagash & Germanovich (2012) in order to normalize the elasticity equation (4.1) and friction weakening Mohr-Coulomb criterion (4.3). We thus scale the slip δ and the tractions t_i by the slip weakening scale δ_w and the peak fault strength $\tau_p = f_p \sigma'_o$, respectively. By doing so, one can identify the nucleation patch length-scale a_w (see equation (4.12)), which is used to scale all the spatial variables: half crack length a and longitudinal spatial coordinate x. We scale the time t by the characteristic fluid diffusion timescale $a_w^2/(4\alpha)$. The characteristic scale for the fluid over-pressure, is taken as the in-situ effective normal stress σ'_o. Upon scaling the governing equations with the previous characteristic scales, the normalized solution is given by δ/δ_w, τ/τ_p, σ/σ'_o, $(p-p_o)/\sigma'_o$ and $2a/a_w$ and is function of only the following four dimensionless parameters (besides space and time):

- normalized injection over-pressure $\Delta P/\sigma'_o$
- dimensionless frictional weakening ratio f_r/f_p
- fault stress criticality τ_o/τ_p at in-situ conditions (prior injection)
- dimensionless dilatancy coefficient $\epsilon_d/(\beta\sigma'_o)$

All the numerical results of the following sections have been obtained and will be presented in dimensionless form. For all simulations, we fix the dimensionless frictional weakening ratio to $f_r/f_p = 0.6$ and explore the effect of the remaining dimensionless parameters: $\Delta P/\sigma'_o$, τ_o/τ_p and $\epsilon_d/(\beta\sigma'_o)$.

4.5 Dilatant hardening effect on a fault characterized by constant permeability

4.5.1 Case of unstable fault without dilatancy $\tau_o > \tau_r$

We first investigate numerically the effect of dilatancy on otherwise unstable fault, i.e. for which the in-situ shear stress is larger than the residual shear strength and the nucleation of a run-away dynamic rupture is always expected in the absence of dilatancy. We display the time-evolution of the different variables (crack length, maximum slip) using the square root of dimensionless time $\sqrt{4\alpha t}/a_w$ as the x-axis. Such a choice stems from the fact than the injection is diffusion controlled and $\sqrt{4\alpha t}/a_w$ is directly the ratio between the diffusion front over the nucleation lengthscale.

Figures 4.4-top-left and 4.4-top-right display the time evolution of half-crack length and peak slip for different values of the dimensionless dilatancy coefficient $\epsilon_d/(\beta\sigma'_o)$ for the case of a rather critically stressed fault $\tau_o/\tau_p = 0.75$ and a moderate injection over-pressure $\Delta P/\sigma'_o = 0.5$. The theoretical estimate of the critical dilatancy sufficient (4.27) to stabilize the fault is $\epsilon_{d,c}/(\beta\sigma'_o) = 0.25$ in that particular case. We clearly observe that an increase of dilatancy delays the occurrence of a dynamic rupture (highlighted by a red dot on these plots) for values below the critical dilatancy. However, for values of dilatancy equal or larger than the critical one, no nucleation is observed: the propagation is always aseismic. This can be better observed on the time evolution of crack velocity

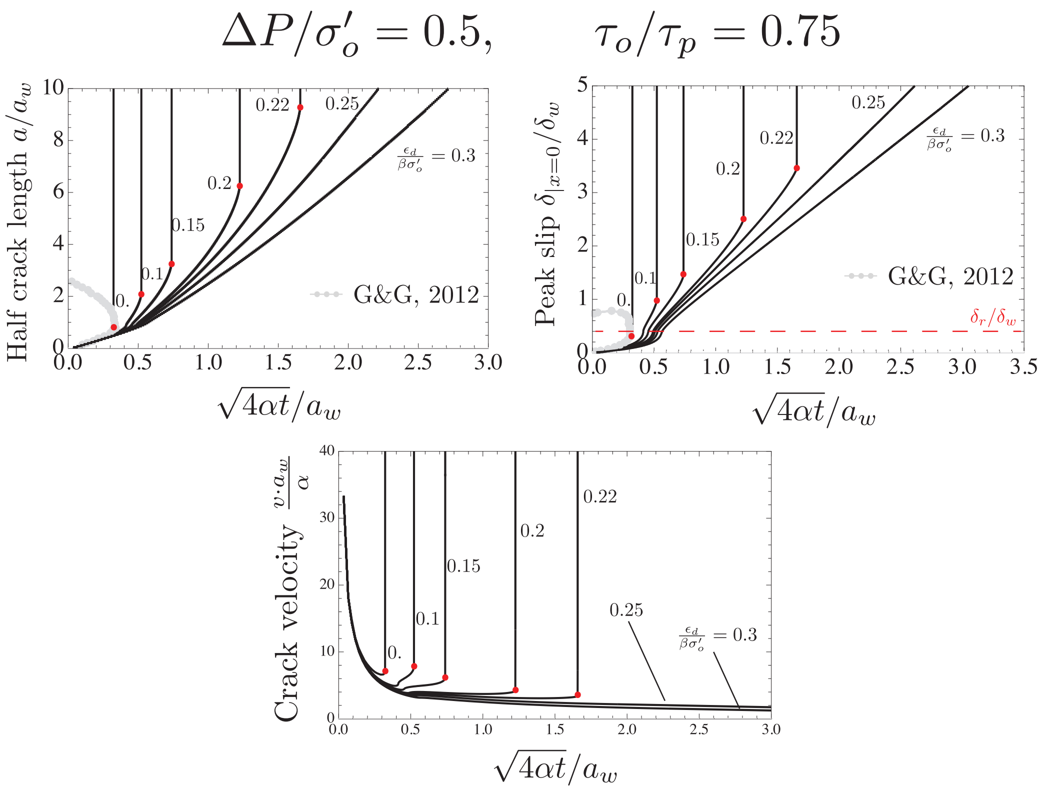

Figure 4.4 – Time evolution of normalized half crack length a/a_w (top-left) and normalized peak slip δ/δ_w at the middle of the fault (top-right), i.e. at $x = 0$, for an otherwise unstable fault ($\tau_o/\tau_p = 0.75$), subjected to moderate over-pressure $\Delta P/\sigma'_o = 0.5$. The friction weakening ratio considered here is $f_r/f_p = 0.6$. The corresponding time evolution of normalized crack velocity va_w/α is showed in the plot at the bottom. We vary the dimensionless dilatancy parameter $\dfrac{\epsilon_d}{\beta\sigma'_o}$ below and above the critical stabilizing value- which is $\epsilon_{d,c}/(\beta\sigma'_o) = 0.25$ in this particular case. Red dots point the onset of unabated dynamic ruptures (color online).

(Figure 4.4-bottom), where we see how dilatancy larger than the critical value kills the acceleration preceding the nucleation of a dynamic rupture.

Figure 4.5 displays the profile along the fault of the fluid over-pressure, friction coefficient, shear slip, effective normal stress and shear fault strength at different times for two distinct values of dilatancy, below and above the critical value. For insufficient dilatancy (left panel on figure 4.5), although an undrained pore-pressure drop can be seen in the weakening zone close to the crack tip, it is not strong enough to stabilize the fault and the last profiles reported in these plots is right before the nucleation of an unabated dynamic rupture. For this particular case without any dilatancy the nucleation occurs early and is not influenced by residual friction. We see that a dilatancy lower than the critical value delays the occurrence of nucleation which is now occurring when a significant part of the crack is at

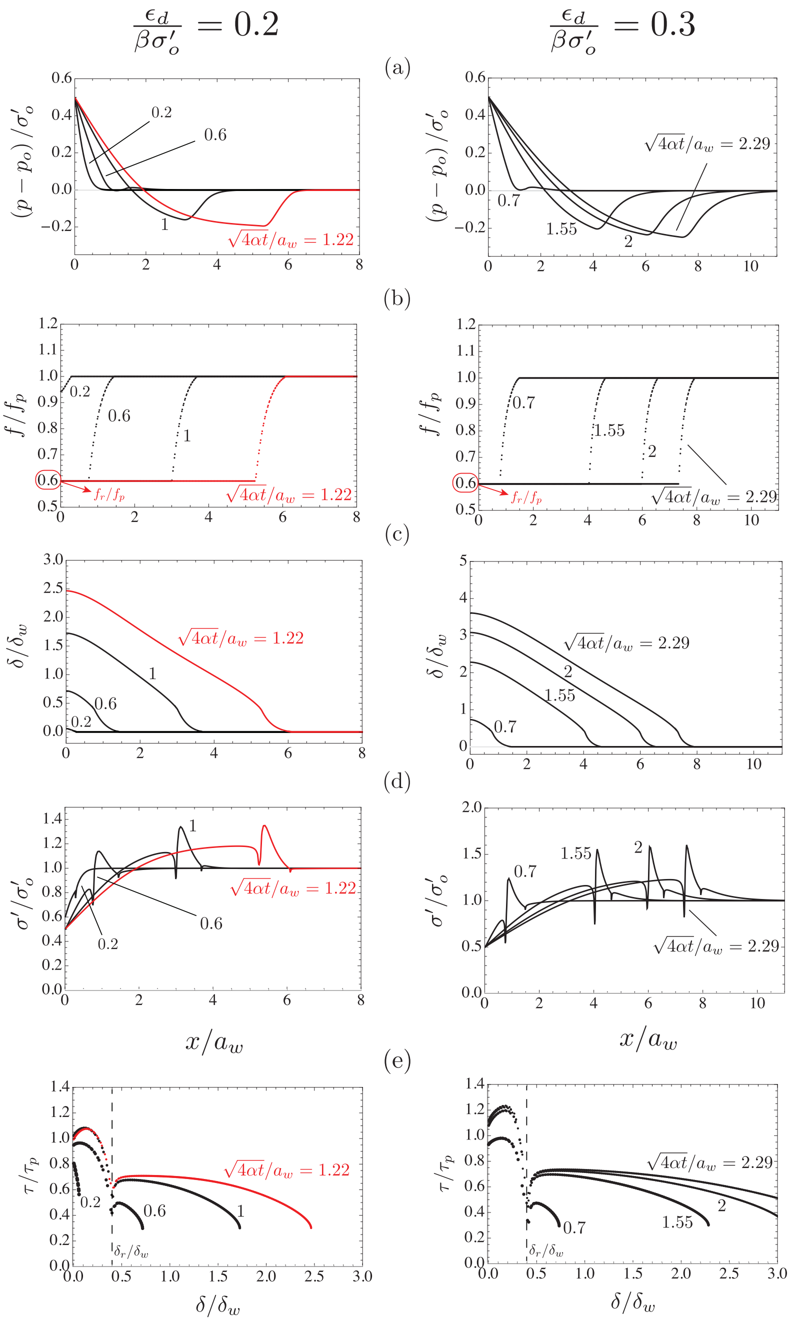

Figure 4.5 – Spatial profile of a) dimensionless pore pressure, b) friction coefficient, c) slip, d) effective normal stress for a critically stressed dilatant fault ($\tau_o/\tau_p = 0.75$), subjected to a moderate overpressure $\Delta p/\sigma'_o = 0.5$, at different (normalized) time snapshots. Sub-figures (e) show the evolution of normalized shear strength with slip, at the same time snapshots. Results for two dimensionless dilatancy parameters are reported: left) ultimately unstable fault for which $\epsilon_d/\beta\sigma'_o$ is lower than the critical stabilizing value for that particular set of parameter ($\epsilon_{d,c}/\beta\sigma'_o = 0.25$), right) ultimately stable for a dimensionless dilatancy above the stabilizing value. Red curves (color online) denote the numerical results at nucleation time for the unstable case (left).

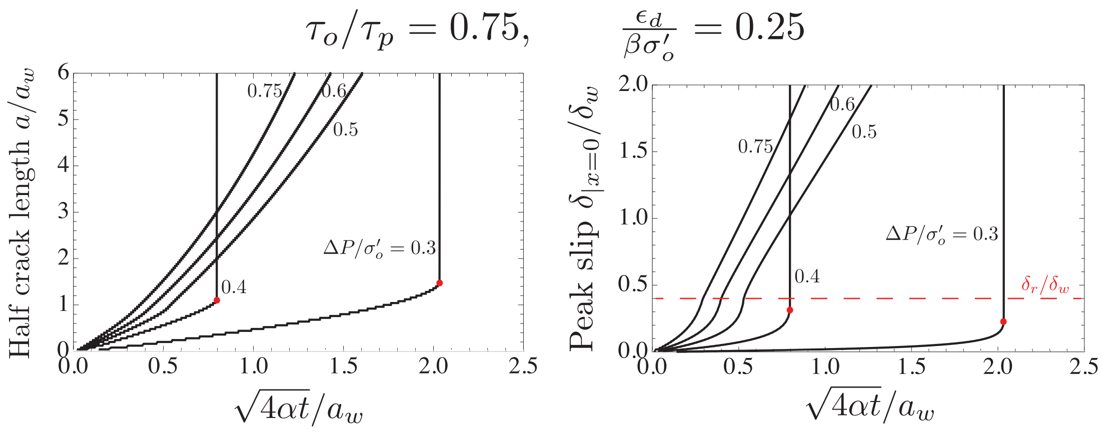

Figure 4.6 – Effect of dimensionless overpressure $\Delta P/\sigma'_o$ on a critically stressed dilatant fault ($\tau_o/\tau_p = 0.75$), in terms of time evolution of dimensionless half crack length a/a_w and dimensionless peak slip $\delta/\delta_{|x=0}$. The dimensionless dilatancy parameter equals the critical value for such configuration: $\epsilon_{d,c}/(\beta\sigma'_o) = 0.25$.

residual friction. For a value of dilatancy larger than the critical one (right panel on figure 4.5), the crack growth is always quasi-static. The undrained pore-pressure drops is now well developed and its minimum reaches the critical value $\Delta p_u/\sigma'_o = -\epsilon_{d,c}/(\beta\sigma'_o) = -0.25$ locally at the tip. The local fault re-strengthening can be observed on the corresponding effective normal stress profiles as well as on the corresponding shear strength versus slip results of our simulation (Figure 4.5). Under undrained conditions, near the crack tips dilatancy leads to a slip hardening phase before the onset of weakening, a response often observed in healed fault rocks. Brantut & Viesca (2015) used a non-monotonic, piecewise linear slip-dependent strength constitutive law (accounting for a strengthening phase followed by a weakening phase) to investigate earthquake nucleation in healed rocks. They solved semi-analytically an uncoupled problem for which stress perturbation is obtained through a mechanical loading whose time and space dependency is known analytically. They notably show that the strengthening phase that occur before the slip weakening phase considerably increases the critical nucleation size. This is in line with our numerical results for increasing values of dilatancy parameter (see Figure 4.5-(e) and the crack length at nucleation time for increasing values of dilatancy in Figure 4.4). We can also observe on these profiles that the weakening zone at the crack tip is small such that the stability condition derived previously under the assumption of small scale yielding is valid.

These simulations confirm the fact that dilatancy can stabilize an otherwise unstable fault if it is above the critical theoretical dilatancy previously derived in Section 4.3.2.2. It is worth noting that this would have been difficult to demonstrate solely numerically even with very long simulations.

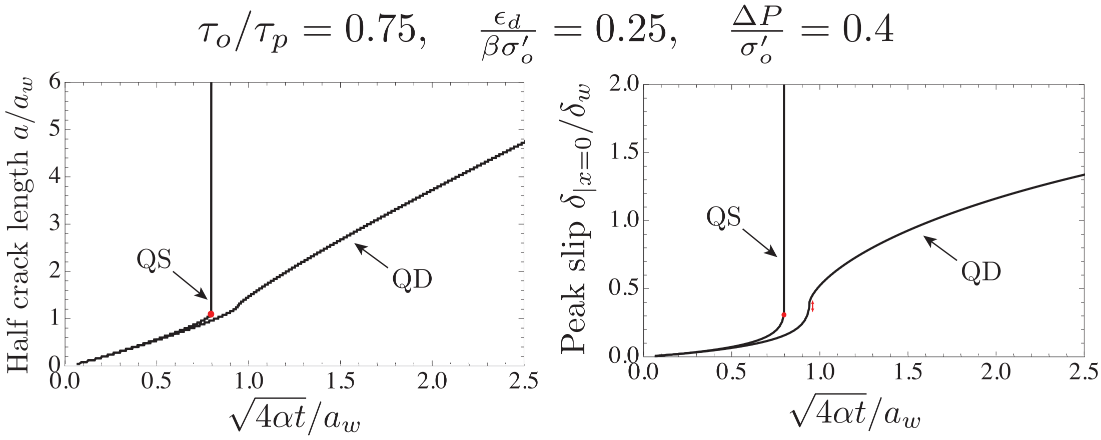

Figure 4.7 – Time evolution of normalized half crack length and peak slip under quasi-static (QS) and quasi-dynamic (QD) approximation of elastic equilibrium. The latter is obtained by adding a seismic radiation damping term proportional to slip rate to elasticity equations in order to take into account energy dissipation through seismic waves orthogonal to fault plane during high slip rate (Rice 1993). The radiation damping term in normalized form reads $\frac{G\delta_w 4\alpha}{2c_s\tau_p a_w^2}$, being c_s the shear wave speed and G the shear modulus. We use here a very large value of 40 for such a dimensionless damping term, therefore over-damping the dynamic rupture.

Effect of the injection over-pressure ΔP For the same value of stress criticality $\tau_o/\tau_p = 0.75$, placing ourselves at critical dilatancy ($\epsilon_{d,c}/(\beta\sigma'_o) = 0.25$ in that case), we test the influence of the amount of over-pressure. Figure 4.6 displays the time evolution of crack length and peak slip for different amount of injection over-pressure ΔP. As expected the larger the injection over-pressure, the faster the crack grows and the propagation remains quasi-static (aseismic). However, an interesting situation occurs for lower value of over-pressures (here $\Delta P/\sigma'_o = 0.4$ and lower) where the nucleation of an unrestricted dynamic rupture is observed. This somehow invalidates the existence of an universal value of stabilizing dilatancy independent of the over-pressure. However, we can clearly see that, for these low over-pressure cases, the peak-slip at the instant of nucleation is lower than the residual slip. In other words, the whole crack is weakening and has not yet reached residual friction. As a result, the undrained pore-pressure is not fully developed and not sufficient to stabilize the fault via dilatant hardening. In these cases, the small scale yielding assumption (small weakening zones at the crack tip) is invalid and the stability condition previously derived for large crack length compared to the characteristic nucleation patch size does not hold. It is worth noting that the nucleation of an unrestricted dynamic rupture is a consequence of the assumption of quasi-static elastic equilibrium. The shear crack velocity at nucleation time diverges instantaneously. Such an unbounded slip rate at nucleation will disappears if inertial terms are accounted for (full elastodynamic or quasi-dynamic formulation): energy dissipation via radiation of elastic waves always ensure a finite crack velocity. In Figure 4.7, we show that using

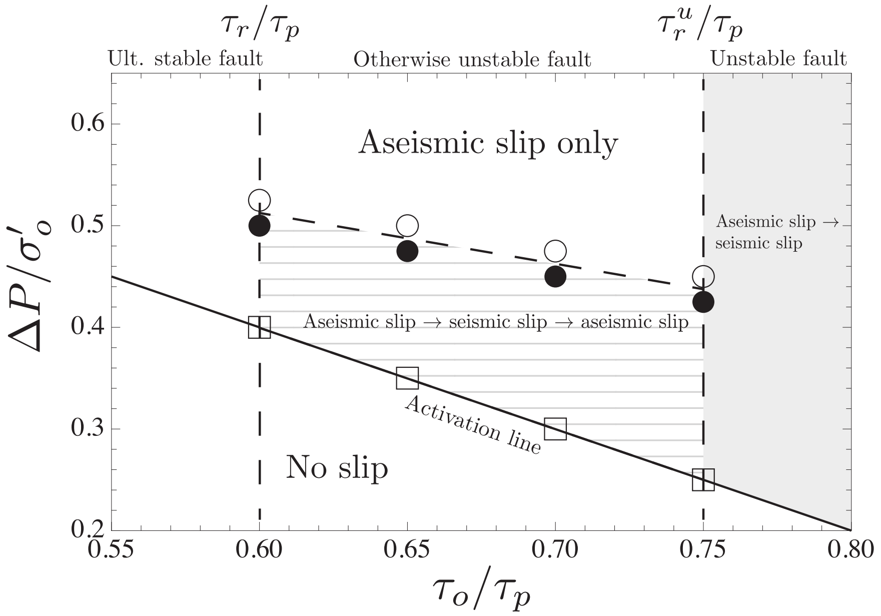

Figure 4.8 – Numerical estimation of the minimum amount of over-pressure required to activate the full benefit of dilatant hardening and stabilize an otherwise unstable fault ($\tau_r < \tau_o$) for different stress criticality between the ultimately stable limit ($\tau_r/\tau_p = f_r/f_p = 0.6$ in that case) and the undrained dilatant residual strength ($\tau_r^u/\tau_p = 1.25\tau_r/\tau_p = 0.75$ in that case). The black filled circle denotes the maximum value of over-pressure below which a finite dynamic event always nucleate (for over-pressure above the slip activation limit), while the empty circle corresponds to the minimum normalized over-pressure required to stabilize such a fault (aseismic slip only for larger over-pressure). The minimum over-pressure required for slip activation ($\Delta P/\sigma'_o = 1 - \tau_o/\tau_p$) is also displayed as empty square/continuous line. Stress criticality τ_o/τ_p larger than τ_r^u/τ_p always result in the nucleation of unrestricted dynamic rupture for any value of over-pressure larger than the activation limit.

a quasi-dynamic formulation (with a rather large damping for illustrative purpose) the slip rate remains bounded and the crack propagation eventually slows down at later time compared to the quasi-static formulation where a divergence of the slip rate occurs at nucleation.

In summary, if residual friction is reached during a-seismic crack propagation, the dilatant hardening effect stabilizes the fault for $\tau_r^u > \tau_o$ and the shear crack always propagates quasi-statically. This always occurs for sufficiently large values of over-pressure ΔP, which promotes larger initial aseismic slip rate thus maximizing the effect of dilatant hardening (i.e. sink term associated with dilatancy in the fluid mass conservation (4.14) is proportional to slip rate - $\tan(\psi(\delta))\dfrac{\partial \delta}{\partial t}$). On the contrary, a lower over-pressure significantly slows down the initial aseismic crack growth and the beneficial effect of dilatancy can not develop sufficiently to avoid the nucleation of a dynamic rupture even when $\tau_r^u > \tau_o$. If inertia effects are included during crack acceleration (fully dynamic or quasi-dynamic elastic equilibrium), the slip rate will remain bounded and the full effect of dilatant hardening would eventually kick in for sufficient crack length (larger than a_c) - therefore leading to an arrest of the dynamic rupture due to sufficient dilatancy ($\tau_r^u > \tau_o$). Full elastodynamic simulations would be needed to confirm that the dynamic rupture would indeed arrest upon full activation of dilatant hardening under those conditions of low injection over-pressure and large dilatancy.

For a given set of parameters, the exact minimum value of over-pressure required to fully stabilize the fault can not be estimated analytically, but can be estimated numerically via a series of simulations varying the injection over-pressure. Figure 4.8 displays such an estimation for different stress criticality τ_o/τ_p below or equal to the undrained residual strength - i.e. the domain where dilatant hardening can stabilize an otherwise unstable fault. More precisely, Figure 4.8 displays both the maximum overpressure for which a nucleation of finite dynamic event occur and the minimum over-pressure for which the propagation is solely aseismic (the fault is stabilized). A linear increase of the required over-pressure as the stress criticality decreases can be clearly observed. This can again be understood as a larger driving force is required to reach residual friction for lower stress criticality.

4.5.2 Case of an ultimately stable fault even without dilatancy ($\tau_o < \tau_r$)

We now turn to the case of ultimately stable fault ($\tau_o < \tau_r$), where only a transient seismic episode occurs for moderate over-pressure (region 2 of Figure 4.3) while crack growth is strictly aseismic for large over-pressure (region 3 of Figure 4.3).

For a configuration representative of region 2 in Figure 4.3 ($\tau_o/\tau_p = 0.55, \Delta P/\sigma_o' = 0.5$) a transient seismic episode occurs for a low accumulated slip: the residual friction is not yet reached anywhere in the crack. Such a seismic event is directly linked with the crack "catching" up the fluid front in association with frictional weakening. Figure 4.9 displays the crack evolution and peak slip for such configuration for different values of dilatancy. Increasing dilatancy slow down the initial quasi-static crack growth and thus delay the nucleation of this finite seismic slip episode. Interestingly, because with larger dilatancy, the quasi-static crack lags even more behind the fluid diffusion front prior to nucleation, the dynamic run-out increases for larger dilatancy. After this finite seismic slip episode, upon continuous injection, the shear crack propagates quasi-statically on par with the evolution of the diffusion front $a \propto \sqrt{4\alpha t}$. Larger dilatancy slows down the quasi-static crack growth. The corresponding profiles of over-pressure, friction coefficient, slip and effective normal stress along the fault at different time snapshots are reported in Figure 4.10. The finite seismic episode can be clearly seen where we observe that prior to nucleation the weakening zone occupies the whole crack. Because the fault is ultimately stable, beside the seismic episode, the fault propagates quasi-statically: due to the low

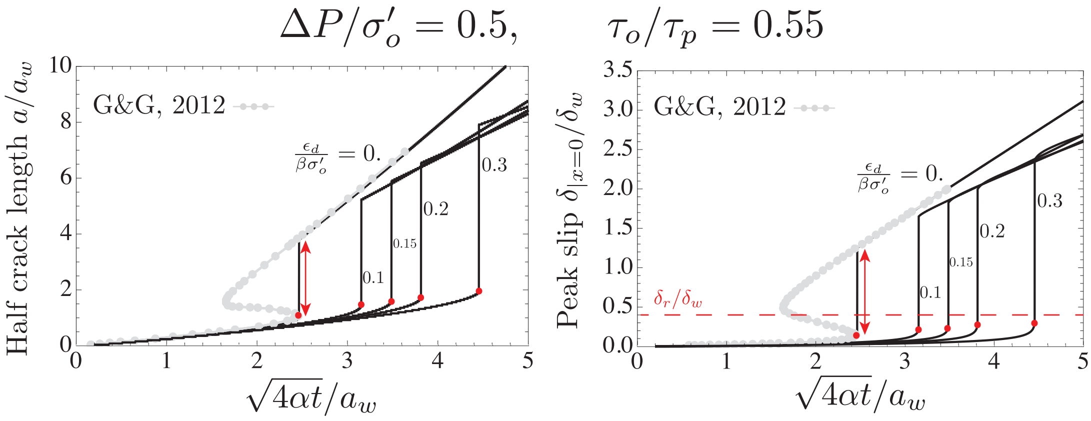

Figure 4.9 – Time evolution of normalized half crack length a/a_w and normalized peak slip δ/δ_w at the middle of the fault, i.e. at $x = 0$, for an ultimately stable fault ($\tau_o/\tau_p = 0.55$ and $\tau_o < \tau_r$, for $f_r/f_p = 0.6$), subjected to moderate over-pressure $\Delta P/\sigma'_o = 0.5$. We span several dilatancy cases by varying the dimensionless dilatancy parameter $\epsilon_d/(\beta\sigma'_o)$. Red dots denote the onset of dynamic event, which is always characterized by a nucleation followed by an arrest (red arrow). The run-out distance increases with increase values of dimensionless dilatancy parameter $\epsilon_d/\beta\sigma'_o$.

slip rate, dilatancy does not significantly alter the pore-pressure profile although the effect can be observed on the effective normal stress profiles (see Figure 4.10).

Finally for large over-pressure (region 3 of Figure 4.3), the crack growth is always quasi-static (aseismic). Results for such aseismic growth are reported in Section 4.8.6. For similar stress and fault strength conditions, an increase of the fault dilatancy slows down the crack velocity as expected.

4.6 Effect of shear-induced permeability changes

The results presented so far are based on the assumption of a constant fault permeability - although in our numerical results the fault transmissivity $w_h k_f$ is changing in conjunction with the dilatant behavior. Experimental (Makurat et al. 1985, Lee & Cho 2002, Li, Jiang, Koyama, Jing & Tanabashi 2008, e.g.) and field evidences (Evans, Genter & Sausse 2005, Evans, Moriya, Niitsuma, Jones, Phillips, Genter, Sausse, Jung & Baria 2005) have shown that deep fractures under fluid induced slip exhibit an increase of fault permeability (Cornet 2015*a*, Evans, Genter & Sausse 2005, Evans, Moriya, Niitsuma, Jones, Phillips, Genter, Sausse, Jung & Baria 2005, McClure & Horne 2014). It is important to note that, although possibly significant, the increase of permeability with slip remains small compared to the drastic increase observed when the fracture opens (i.e. when the effective normal stress becomes tensile) such as in hydraulic fracturing. Like previously, we restrict here to the case of compressive effective normal stress, where permeability changes with

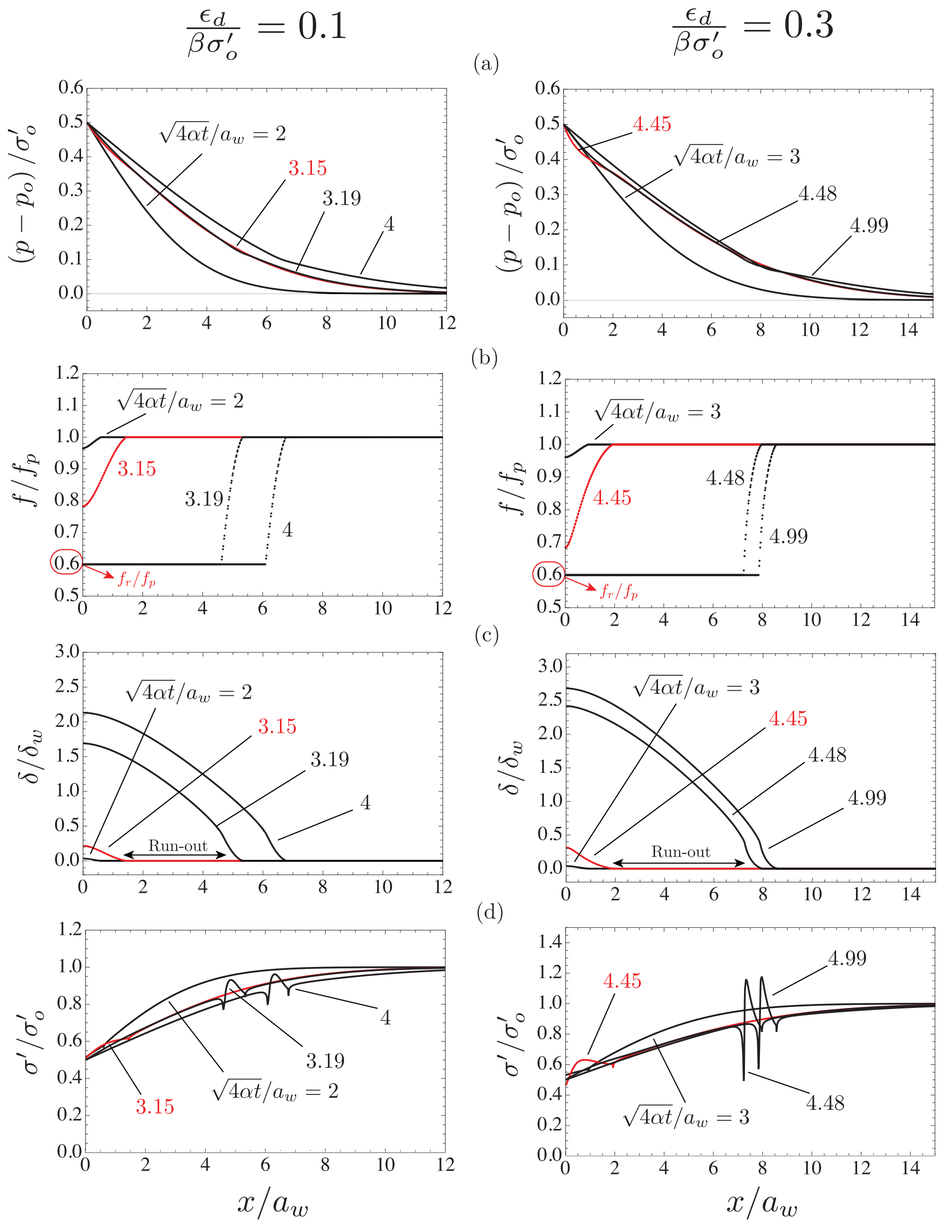

Figure 4.10 – Spatial profiles of dimensionless pore pressure (a), friction coefficient (b), slip (c) and effective normal stress (d) at different (normalized) time snapshots, for an otherwise ultimately stable fault ($\tau_o/\tau_p = 0.55$ - $f_r/f_p = 0.6$), subjected to a moderate over-pressure $\dfrac{\Delta P}{\sigma'_o} = 0.5$. Two dimensionless dilatancy parameters are considered: $\dfrac{\epsilon_d}{\beta\sigma'_o} = 0.1$ and $\dfrac{\epsilon_d}{\beta\sigma'_o} = 0.3$. Red lines refer to numerical results at nucleation time of a dynamic rupture. Since the background shear stress τ_o is lower than the residual fault strength τ_r at ambient conditions, the dynamic event is always followed by an arrest.

slip are strictly associated with shear-induced dilatancy.

Several empirical models have been proposed and used in literature for permeability evolution. Some of them account for porosity changes, while some others include explicit dependency on effect stress changes (see e.g. (Rutqvist & Stephansson 2003) for a review). For example, Rice (1992*b*) used an effective stress-dependent permeability law, in which the permeability is a non-linearly decreasing function of the local (compressive) effective normal stress:

$$k_f = k_* e^{(-\sigma'/\sigma_*)}, \tag{4.29}$$

where k_* is the maximum fault permeability $\left[L^2\right]$ and σ_* is a normalizing stress level $\left[ML^{-1}T^{-2}\right]$ which ranges between 3 to 40 MPa Rice (1992*b*) - see also (Seront et al. 1998). Another common choice is to use the cubic law for the fault transmissivity ($k_f w_h$), relating the fault permeability directly to the changes of aperture - i.e. a parallel plate idealization of the fluid flow in the fault (Bawden et al. 1980, McClure & Horne 2014, Ucar et al. 2018, e.g.):

$$k_f\left(\delta\right) = \frac{w_h\left(\delta\right)^2}{12} \tag{4.30}$$

Under this assumption, the maximum constant fault permeability that is exerted when the slip δ is larger than the critical value δ_r is directly function of dilatant strain ϵ_d as $k_{f,max} = \frac{\omega_o^2}{12}(1+\epsilon_d)^2$. Such a maximum increase of longitudinal permeability with respect to its initial value $\omega_o^2/12$ is actually rather small since the dilatant strain ϵ_d ranges between $10^{-4} - 10^{-2}$. This is clearly in contradiction with experimental and field evidences which mention much larger permeability increase (Makurat et al. 1985, Evans, Genter & Sausse 2005, Evans, Moriya, Niitsuma, Jones, Phillips, Genter, Sausse, Jung & Baria 2005).

In order to investigate cases in which fault dilatancy induces significant increases of fault permeability with inelastic deformations (for instance due to change of fault porosity, for which $\Delta k_f \propto \Delta\varphi^{7-8}$ for dense rocks - see Bernabé et al. (2003)), we generalize the fault permeability evolution law as

$$k_f = \frac{\omega_o^2}{12}\left(1 + a\frac{w(\delta)}{\omega_o}\right)^b, \tag{4.31}$$

where a and b are two constant parameters. Note that when $a = 1$ and $b = 2$, the fault transmissivity obeys the cubic law. By varying these two parameters, one can obtain ten-fold permeability increase associated with shear slip at maximum dilatancy compared to the initial value $\omega_o^2/12$. We use this permeability law (4.31) to gauge the impact of permeability change with slip on the stabilization by dilatancy of an otherwise unstable fault. In particular, our aim is to see if an increase of permeability affect the stabilizing

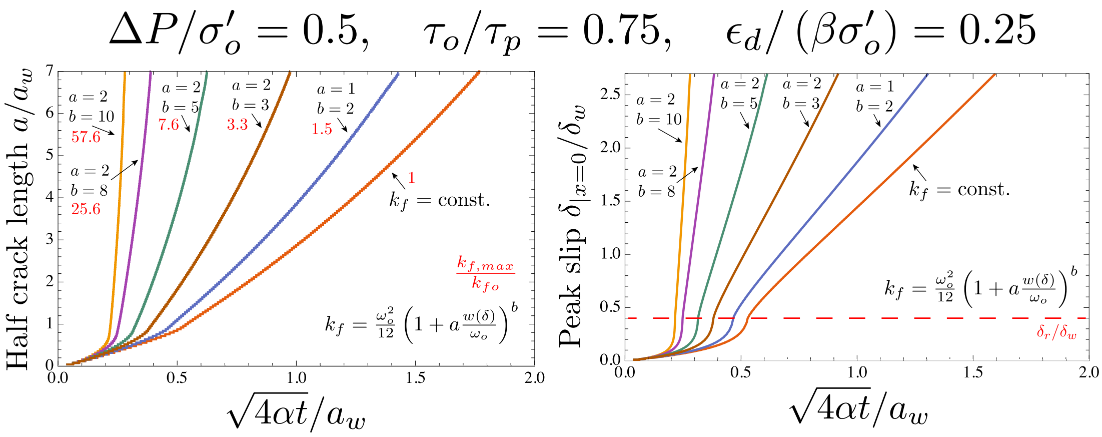

Figure 4.11 – Effect of permeability increase on a critically stressed ($\tau_o/\tau_p = 0.75$, $f_r/f_p = 0.6$) dilatant fault under moderate over-pressure ($\Delta P/\sigma'_o = 0.5$): time evolution of normalized half crack length a/a_w and corresponding peak slip $\delta_{|x=0}/\delta_w$. The dimensionless dilatancy parameter $\epsilon_d/(\beta\sigma'_o)$ is set to the corresponding critical stabilizing value (4.27), equal here to 0.25. The effect of permeability evolution following the slip dependent law (4.31) is investigated for five different values of the parameters (a, b) spanning small and large permeability increase from 1.5 to ~ 60 times the initial fault permeability.

effect of the undrained pore pressure drop associated with dilatancy.

We focus on the case of an otherwise unstable fault $\tau_o/\tau_p = 0.75$ ($f_r/f_p = 0.6$) and a moderate over-pressure case $\Delta P = 0.5$ with a dilatancy equal to the critical stabilizing value $\epsilon_{d,c}/(\beta\sigma'_o) = 0.25$ for these conditions. Figure 4.11 displays the crack length and peak slip evolution for the case of a constant permeability as well as for different values of a and b for the permeability evolution law (4.31). We span $a = 1$, $b = 2$ (cubic law) and $a = 2$, $b = 3$, 5, 8, and 10 which entails respectively a 1.5 (cubic law), 3.3, 7.6, 25.6 and 57.6 fold increases of permeability at maximum dilatancy.

We observe that although the increase of permeability directly enhance the crack velocity, the propagation always remains aseismic. The permeability increase has a very significant effect on aseismic growth and this effect increases with the value of b as expected. For example, for the strongest permeability variation with dilatancy ($a = 2$, $b = 10$ resulting in $k_{f,max}/k_{fo} \sim 57.6$), we observe a $\sim 550\%$ increase in crack length at $\sqrt{4\alpha t}/a_w = 0.27$ compared to the constant permeability case (see Figure 4.11). A difference that will obviously continue to grow with time. For such a evolution of permeability with slip (4.31), the permeability profile is similar to the dilatancy strain: constant at is maximum value all along the crack except in the weakening zone near the tip - see Figure 4.12. The large permeability increases with slip, however, do not modify the stabilizing effect of undrained dilatant hardening. As the permeability accelerates quasi-static crack growth, the undrained pore-pressure response remains strong at the crack tip (see the pore-pressure profiles in Figure 4.12). Moreover, due to the quasi-static acceleration with increasing permeability, residual friction is reached earlier such that the undrained shear strength is fully mobilized - even possibly for smaller value of over-pressure compared to the constant permeability case. Note that similar results are obtained with other type of permeability evolution (such as the one described by eq. (4.29)) as reported in Figures 4.21 and 4.22 of the Supporting Information (see Section 4.8.7). In conclusions, in the case of an impermeable surrounding, the increase of permeability with slip along the fault does not affect the ultimate stability condition ($\tau_o < \tau_r^u$).

4.7 Conclusions

We have investigated the effect of dilatancy on the transition from seismic to aseismic slip due to sustained fluid injection regulated at a constant pressure in a fault. Although simple in its nature (planar bi-dimensional fault, uniform in-situ stress and rock properties, linear weakening friction), the model investigated properly couples, via non-associated plasticity, the hydro-mechanical interplay between slip, dilatancy, frictional weakening and fluid flow. We have developed a robust fully implicit numerical scheme - which properly reproduces existing semi-analytical solutions for the case of non-dilatant fault (Garagash & Germanovich 2012). We notably would like to emphasize the necessity of numerical model verification for such type of non-linear fracture propagation problem which -similarly to hydraulic fracturing problem- necessitates to resolve multiple scales (weakening zone and diffusion lengthscale here).

We have shown that dilatant hardening can stabilize an otherwise unstable fault ($\tau_o > \tau_r$), as long as the weakening of friction occurs in a small zone near the tip of the shear crack (small scale yielding). This is captured by an ultimate stability condition defined with an undrained residual strength $\tau_r^u = \tau_r(1 + \epsilon_d/(\beta\sigma_o'))$ function of the dilatant strain of the fault at critical state (when dilatancy saturates). We have demonstrated theoretically that under the assumption of small scale yielding, dilatancy ultimately stabilize the fault if $\tau_o < \tau_r^u$. In other words, for a given fault criticality, there exists a critical dilatancy above which the fault will remain stable and shear slip is solely aseismic. However, the hypothesis behind small scale yielding (small frictional weakening zone near the crack tips) must be satisfied for such an ultimate stability condition to hold. This is the case if and only if the injection over-pressure is sufficient to propagate quasi-statically the shear crack / slipping patch fast enough to reach residual friction and activate the beneficial effect of dilatancy prior to the crack reaching the nucleation length of the non-dilatant case. For injection pressures below a limiting value, the crack propagates too slowly initially. The nucleation of a dynamic rupture occurs prior to reaching residual friction such that the maximum dilatancy is not activated prior to nucleation. For such small injection over-pressure, dilatancy cannot prevent the nucleation of a dynamic rupture for an unstable fault ($\tau_o > \tau_r$) even for large dilatancy $\tau_o < \tau_r^u$ (see Figure 4.8 for the evolution of the minimum overpressure). However, such a dynamic rupture for low over-pressure and a-priori sufficient dilatancy ($\tau_o < \tau_r^u$) - which occurs prior to reaching residual friction -

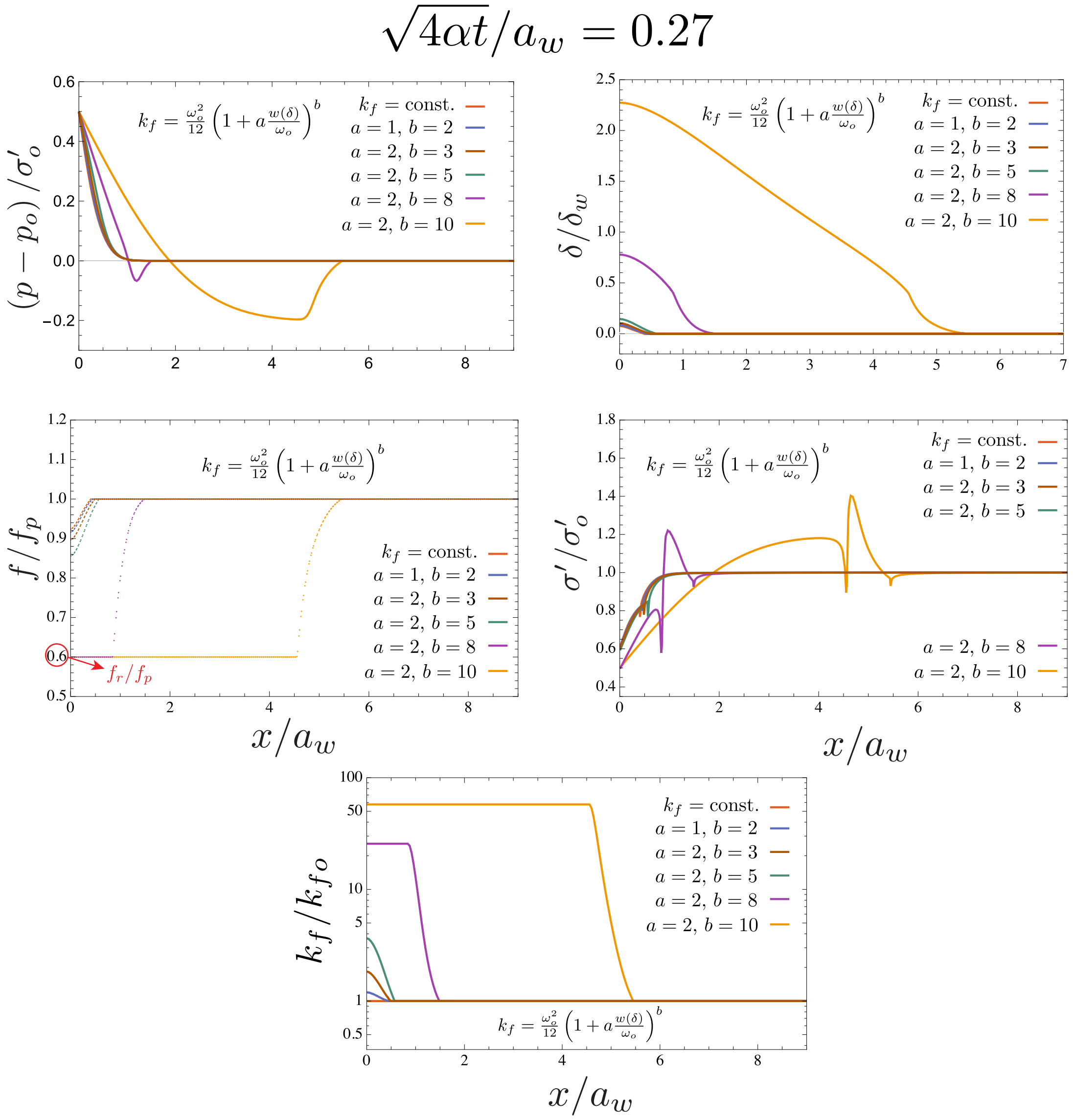

Figure 4.12 – Spatial profiles of dimensionless pore pressure, friction coefficient, slip, effective normal stress and fault longitudinal permeability (in linear-log scale) at a given normalized time snapshot $\sqrt{4\alpha t}/a_w = 0.27$, for unstable fault ($\tau_o/\tau_p = 0.75$ - $f_r/f_p = 0.6$), subjected to a moderate over-pressure $\dfrac{\Delta P}{\sigma'_o} = 0.5$ and a dimensionless dilatancy parameter equal to the critical value, i.e. $\dfrac{\epsilon_{d,c}}{\beta\sigma'_o} = 0.25$. The different numerical results are obtained with different fault permeability evolution laws: i) constant permeability $k_f = \dfrac{\omega_o^2}{12}$, ii) slip-dependent permeability law $k_f = \dfrac{\omega_o^2}{12}\left(1 + a\dfrac{w(\delta)}{\omega_o}\right)^b$, with $a = 1\&b = 2$ (cubic law for fault transmissivity) and $a = 2\&b = 3, 5, 8, 10$.

will eventually arrest as the dilatant hardening effect kicks in for sufficient crack length. Although observed with quasi-dynamic damping (see Supplemental Information), a fully elastodynamics simulation would be required to confirm such arrest.

For an ultimately stable fault ($\tau_o < \tau_r$), our numerical results indicate that dilatancy delays the occurrence of a finite episode of dynamic slip for moderate overpressure. Such a finite seismic event is associated with the abrupt catch up of the diffusion front by the crack front and the fact that the residual friction has not yet reached all along the crack. For large over-pressure and stable fault, an increasing dilatant behavior simply slows down the quasi-static propagation (strictly aseismic slip).

Permeability increases with slip leads to faster aseismic crack growth for the different permeability evolution tested. However, it does not affect the critical dilatancy stabilizing an otherwise unstable fault. It appears evident that the details of the slip-permeability law greatly influence aseismic growth - a discussion on the most appropriate permeability model clearly require more investigation and necessarily better controlled hydro-mechanical laboratory experiments for sufficient slippage length.

The strengthening effect of dilatancy discussed here must be put perspective with some well-known dynamic weakening mechanisms that may occur as the crack accelerates: notably, thermal pressurization and flash heating of asperities. Although the effect of these weakening mechanisms have been already studied (Garagash & Rudnicki 2003, Segall & Rice 2006, Rice 2006, Garagash & Germanovich 2012) in the scope of earthquake nucleation via remote loading, a complete investigation of such competition would be required in the context of fluid injection. This is out of the scope of this paper. We note however that both of these dynamic weakening mechanisms requires dynamic slip rates (m/s and above) while dilatant hardening is activated quasi-statically. A probably more important point with respect to the stabilizing effect of dilatant hardening is related to the assumption of an impermeable host rock. Although possibly acceptable for young fault/fractures, this is highly doubtful for most mature fault structure. With a permeable surrounding (of say hydraulic diffusivity α_r), the undrained pore-pressure drop associated with the fault dilatant behavior may be short-lived as fluid will be sucked in the fault and re-pressurize it. The importance of dilatant hardening will directly depend on the ratio between the changes due to dilatancy (which scales with slip rate) and the influx of fluid from the rock mass (which scales as α_r/h_w with $h_w \approx \omega_o$ the gouge thickness). A thorough investigation for the case of injection induced slip is required to clarify that competition further, along the lines of Segall & Rice (1995), Segall et al. (2010) in the context of the seismic cycle. In the sequel, we have also used a simple linear weakening friction law compared to a more elaborate rate-state model. It is nevertheless worthwhile to note that some work (Uenishi & Rice 2003, Viesca 2016*b*,*a*) have demonstrated a correspondence between linear weakening friction and rate and state at the onset of nucleation. Investigations of the combined effect of rate and state and dilatancy in the case of fluid injection combined with proper scaling and stability analysis would surely produce a more refined understanding of the mechanisms of induced seismicity.

Finally, we conclude by recalling the decreases of dilatancy with confinement, such that the effect of dilatant hardening is likely to be more prominent mostly at shallow depths. Additional experimental data of fault dilatant behavior in conjunction with frictional properties would enable to further decipher its impact on fluid induced a-seismic and seismic slip with the help of the type of model presented here.

4.8 Supporting Information

4.8.1 Fully implicit hydro-mechanical solver for frictional planar fault: algorithm description

We report here the details of the hydro-mechanical solver developed for purely shear crack propagation along the planar dilatant fault. This solver includes the propagation of a frictional shear crack paced by fluid flow, shear induced-dilatancy and possibility of nucleation of dynamic rupture due weakening nature of friction coefficient along the fault. We use displacement discontinuity method with piece-wise linear displacement discontinuities (see Section 2.9) to discretize elasticity equations (4.1) and a finite volume scheme (see Section 3.3) for discretization of fluid mass conservation equation in the fault (4.14). In this scheme, the fault is discretized with finite sized straight elements (see Section 2.10.1) and time integration is performed via Backward-Euler scheme[1]. Fracture front is tracked by solving for the set of element satisfying the Mohr-Coulomb criterion (4.3), here with zero cohesion. Note that this solver does not include tensile failure, i.e. the injection over-pressure is set such that the effective normal stress remain always compressive.

The algorithm marches in time, from t^n to $t^{n+1} = t^n + \Delta t$. The solution at each time step consists of the set of yielded / active element $\mathcal{A}_{elm}$ (of length N_a), displacement discontinuities on yielded elements and fluid pressure at all N mesh nodes. For sake of compactness, we use the notation of $X^{n+1} = X^n + \Delta X$ for referring to a generic time and space dependent variable $X(x,t)$ at time t^{n+1} (and we denote the initial state with the superscript o). Furthermore, normal and shear displacement discontinuities hereunder are respectively denoted as d_n and d_s (instead of w and δ), whereas normal and shear tractions are denoted as t_n and t_s, respectively (instead of σ and τ) .

For a given trial set of active elements, the discretized hydro-mechanical equations at current time read:

- Elasticity (quasi-static formulation):

$$\mathbb{E} \cdot (\mathbf{d}^n + \Delta \mathbf{d}) = \mathbf{t}^n + \Delta \mathbf{t} - \mathbf{t}^o \tag{4.32}$$

  or in incremental form

$$\mathbb{E} \cdot \Delta \mathbf{d} = \Delta \mathbf{t} \tag{4.33}$$

- Mohr-Coulomb criterion (with frictional weakening) enforced at collocation points, and the dilatancy relation:

---

[1] This ensures stability and no restriction given by the Courant-Friedrichs-Lewy condition.

$$\Delta \mathbf{t}_s + \mathbf{t}_s^n = f\left(\mathbf{d}_s^n + \Delta \mathbf{d}_s\right)\left(\mathbf{t}_n^n + \Delta \mathbf{t}_n - \mathbf{p}_{coll}^n - \Delta \mathbf{p}_{coll}\right) \tag{4.34}$$

$$\Delta \mathbf{d}_n = \Delta \mathbf{d}_s \tan\left(\psi(\mathbf{d}_s^n + \Delta \mathbf{d}_s)\right) \tag{4.35}$$

- Discretized fluid flow equation (over the whole mesh) where the pressure unknowns are located at the mesh nodes N:

$$\mathbb{V}_w \left(\left. \frac{\partial \mathbf{d_n}}{\partial \mathbf{d_s}} \right|^{n+1} \right) \cdot \Delta \mathbf{d}_s + \mathbb{V}_p(\mathbf{d}_n^{n+1}) \cdot \Delta \mathbf{p} + \Delta t \times \mathbb{L}(\mathbf{d}_n^{n+1}) \cdot \Delta \mathbf{p} = -\Delta t \times \mathbb{L}(\mathbf{d}_n^{n+1}) \cdot (\mathbf{p}^n - \mathbf{p}^o) \tag{4.36}$$

All the finite volume matrices in equation (4.36) are defined in Section 3.3. Note that, in order to couple the dilatancy term in the fluid mass conservation equation with the elasticity equations related to only shear degrees of freedom, a chain rule must be applied to the time derivative of the opening $\mathbf{d_n}$, such that

$$\frac{\partial d_n}{\partial t} = d_{n,s} \cdot \frac{\partial d_s}{\partial t} \qquad \text{with} \qquad d_{n,s} = \frac{\partial d_n}{\partial d_s}, \tag{4.37}$$

The term $d_{n,s}$ can then be obtained analytically from equation (4.10) and, upon integration over each control volume, the dilatancy matrix $\mathbb{V}_w$ can be easily assembled (note again the change of notation, for which $w = d_n$ and $d_s = \delta$).

Since the elasticity equations are collocated at points inside the displacement discontinuity element (see Figure 3.2), whereas fluid pressure is discretized at nodal points, equation (4.35) must be expressed in terms of nodal increment of pore pressure in order to couple it with fluid flow. The pore pressure increment at a collocation point $\Delta p(\xi_j)$ is obtained from the nodal pore pressure increments Δp_i, via the definition of the linear shape functions (see equation (2.57)):

$$\Delta p(\xi_j) = \sum_{i=1,2} N_i(\xi_j) \Delta p_i, \tag{4.38}$$

where Δp_i denotes the value of the over-pressure at node i. Equation (4.38) can be expressed in matrix form as

$$\Delta \mathbf{p}_{coll} = \mathbb{N}_{pc} \Delta \mathbf{p}, \tag{4.39}$$

where $\mathbb{N}_{pc}$ is a $2N_a \times N$ matrix for the transfer of the value of pressure from node to collocation points.

The set of discretized equations previously introduced can be re-arranged to yield a non-linear system in terms of the increments of shear displacement discontinuity and increment of pore pressure along the planar fault (for which the elastic equations for shear and normal degree of freedom uncouple):

$$\begin{aligned} \begin{bmatrix} \mathbb{E}_{ss} & f^{n+1} \times \mathbb{N}_{pc} \\ \mathbb{V}_w(d_{n,s}^{n+1}) \cdot \tan\left(\psi^{n+1}\right) & \mathbb{V}_p(\mathbf{d}_n^{n+1}) + \Delta t \times \mathbb{L}(\mathbf{d}_n^{n+1}) \end{bmatrix} \begin{bmatrix} \Delta \mathbf{d}_s \\ \Delta \mathbf{p} \end{bmatrix} &= \\ = \begin{bmatrix} \mathrm{sign}\left(\mathbf{t}_s^{n+1}\right)\left(f^{n+1}\left(\mathbf{t}_n^{n+1} - \mathbf{p}^n\right)\right) - \mathbf{t}_s^n \\ -\Delta t \times \mathbb{L}\left(\mathbf{d}_n^{n+1}\right) \cdot \left(\mathbf{p}^n - \mathbf{p}^o\right) \end{bmatrix} \end{aligned} \tag{4.40}$$

where $\tan(\psi^{n+1})$ and f^{n+1} are identity matrices containing respectively the current dilatancy angle and current friction coefficient at the nodal points (they are both functions of the current shear slip $\mathbf{d}_s^{n+1}$), and the current normal stress is simply given by

$$\mathbf{t}_n^{n+1} = \mathbf{t}_n^n + \mathbb{E}_{nn} \tan\left(\psi^{n+1}\right) \Delta \mathbf{d}_s \tag{4.41}$$

The system of equations (4.40) is non-linear as both dilatancy, friction and permeability evolves with slip. Starting from a known solution at time n (denote as $\mathcal{L}^n$) and thus from a given active set of elements $\mathcal{A}_{elm}^n$, we solve it[2] via fixed point iterations combined with an under relaxation scheme, upon application of the following boundary condition due to injection condition:

$$\Delta p(x=0,t) = p_o + \Delta P - p^n(x=0,t) \tag{4.42}$$

Convergence is reached when the relative difference between successive estimate of slip and fluid pressure increment falls below a fixed tolerance (typically $tol = 10^{-6}$). Upon convergence of this non-linear hydro-mechanical system, we check the Mohr-Coulomb criterion on the full mesh (re-computing shear and effective normal tractions on the full mesh) and modify accordingly the set of active elements. This is done through an iterative checking loop, whose convergence is reached when the set of active elements do not change between two successive iterations or when the current slippage length sl^{n+1} coincides with the length of the fault. The algorithm devised is thus composed of two nested iterative loops. The outer loop allows to determine the current shear crack position by checking the active set of elements (for which $\mathcal{F}(t_s, t_n') = 0$) at current time $n+1$, whereas the inner one is used to solve the non-linear system of equations (4.40). Upon convergence of the two loops, the new numerical solution $\mathcal{L}^{n+1}$ is obtained and the algorithm move to the next time step.

---

[2] Note that the non-linear system (4.40) can be solved equivalently for the plastic multiplier λ, instead of for increment of displacement discontinuities. This can be achieved by replacing the vector $\Delta \mathbf{d}_s$ with the vector $\lambda \cdot \mathrm{sign}\left(\mathbf{t}_s^{n+1}\right)$ containing all the plastic multiplier of the active elements N_a.

Hereunder, we sum up the algorithm devised for a better comprehension:

```
Store the primary variable from previous time $t^n$:
$\mathcal{L}^n = (t_i^n, p^n, d_i^n, sl^n, \mathcal{A}_{elm}^n, \Delta t^{n+1}, v^n)$
Set $sl^{n+1} = sl^n$ & $t^{n+1} = t^n$
**While** $(t^{n+1} \leq t_{max}$ & $sl^{n+1} \leq sl_{max})$
  Set $j = 0$
  Set $\mathcal{L}_j^{n+1} = \mathcal{L}^n$
  **While**$(\mathcal{F}(t_{s,j}, t'_{n,j})^{n+1} \leq 0$ everywhere & $j < j_{max})$
    $j = j + 1$
    Determine $\mathcal{A}_{elm,j}^{n+1}$ from $\mathcal{L}_j^{n+1}$, i.e. elements for which $\mathcal{F}(t_{s,j}, t'_{n,j})^{n+1} \geq 0$
    Set $k = 0$, $\Delta d_{i,k} = 0$, $\Delta p_k = 0$
    **While**$(k \leq k_{max}$ & $err_{\Delta d_i} > tol$ & $err_{\Delta p} > tol)$
      $k = k + 1$
      Determine $d_{i,k}^{n+1} = d_{i,j}^{n+1} + \Delta d_{i,k}$
      Build $\mathbb{V}_w$, $\mathbb{V}_p$, $\mathbb{L}$, $\mathbb{N}_{pk}$ with current deformations
      Solve the system (4.40) to get $\Delta d_{s,k+1}$ and $\Delta p_{k+1}$
      Calculate new pressure $p_{k+1}^{n+1} = p_k^{n+1} + \Delta p_{k+1}$
      Calculate new increment of opening DD $\Delta d_{n,k+1}$ using flow rule
      Calculate new stress state along the fault via elasticity equations and (4.41)
      Under relaxation:
      $\Delta p_{k+1} = (1-\omega)\Delta p_k + \omega \Delta p_{k+1}$ & $\Delta d_{i,k+1} = (1-\omega)\Delta d_{i,k} + \omega \Delta d_{i,k+1}$

      Compute errors on increments

  $err_{\Delta d_i} = ||\Delta d_{i,k+1} - \Delta d_{i,k}||/||\Delta d_{i,k+1}||$ and $err_{\Delta p} = ||\Delta p_{k+1} - \Delta p_k||/||\Delta p_{k+1}||$

      Update: $\Delta d_{i,k} = \Delta d_{i,k+1}$ & $\Delta p_k = \Delta p_{k+1}$
    **End while**
    Set new trial solution $\mathcal{L}_{j+1}^{n+1} = (t_{i,k}^{n+1}, p_k^{n+1}, d_{i,k}^{n+1}, sl^n, \mathcal{A}_{elm,j}^{n+1}, \Delta t^{n+1}, v^n)$
    Determine $\mathcal{A}_{elm,j+1}^{n+1}$ from $\mathcal{L}_{j+1}^{n+1}$
    Determine $sl^{n+1}$ from $\mathcal{A}_{elm,j+1}^{n+1}$
    Update $\mathcal{L}_j^{n+1} = \mathcal{L}_{j+1}^{n+1}$
  **End while**
  Calculate $v^{n+1} = \frac{sl^{n+1} - sl^n}{\Delta t^{n+1}}$ via finite difference.
  Calculate new time step $\Delta t^{n+2}$
  Update variables, i.e. $\mathcal{L}^n = \mathcal{L}_{j+1}^{n+1}$
**End while**
```

Algorithm 1: Fully implicit H-M solver for frictional fluid driven crack propagation along a planar fault.

In the Algorithm 1, sl_{max} is the extension of the whole fault, j_{max} is the maximum number of iterations for the determination of shear crack position and ω is the under-relaxation parameter $(0 \leq \omega \leq 1)$.

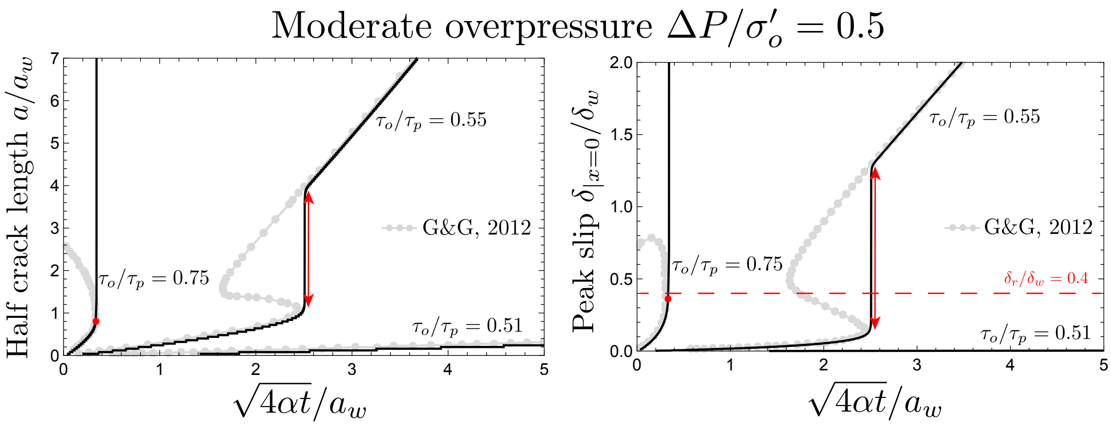

Figure 4.13 – Benchmark of numerical results against semi-analytical ones of Garagash & Germanovich (2012) in terms of time evolution of normalized half crack length a/a_w and normalized peak slip δ/δ_w at $x = 0$, for a non-dilatant fault subjected to moderate overpressure $\Delta P/\sigma'_o = 0.5$ and three initial stress conditions: i) $\tau_o/\tau_p = 0.75$ (unstable fault), ii) $\tau_o/\tau_p = 0.55$ (ultimately stable fault) and iii) $\tau_o/\tau_p = 0.51$ (ultimately stable fault). The friction weakening ratio is $\dfrac{f_r}{f_p} = 0.6$, so that $\dfrac{\delta_r}{\delta_w} = 0.4$. The red dots denote the nucleation/onset of an unabated dynamic rupture, whereas the red arrows denote the nucleation of dynamic event followed by an arrest.

4.8.2 Verification of the numerical scheme: benchmark for the non-dilatant case

The governing problem is uncoupled when elasticity does not affect fluid flow along the fault and vice-versa. This scenario occurs for a non dilatant fault, i.e. when the fault hydraulic aperture does not change during crack propagation, i.e. $w_h = \omega_o$. The pore pressure evolution in such a case is given by the solution of the linear diffusion equation in a fault characterized by constant hydraulic diffusivity $\alpha = \dfrac{k_f}{\mu\beta}$ (Carslaw & Jaeger 1959):

$$p\,(x,t) = p_o + \Delta P \cdot \text{Erfc}\left|\frac{x}{\sqrt{4\alpha t}}\right| \tag{4.43}$$

This pore pressure evolution along the fault is linked to elasticity through the shear weakening Mohr-Coulomb criterion (one way coupling): the change of local effective normal stress associated with pore pressure increment reduces locally the fault frictional strength, affecting in turn elasticity.

Garagash & Germanovich (2012) investigated extensively this particular case. Semi-analytical results are thus available, allowing to verify the numerical scheme. This is of great importance for these kind of non-linear (coupled) problems. Indeed, the dynamic instability that may occur during shear crack propagation due to weakening nature of friction coefficient may lead to numerical errors.

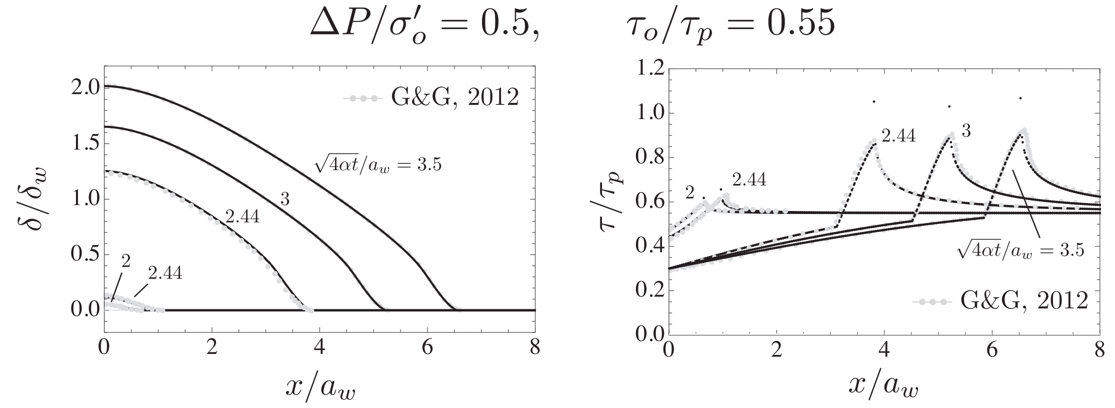

Figure 4.14 – Benchmark of numerical results against semi-analytical ones of Garagash & Germanovich (2012) in terms of normalized slip δ/δ_w and shear stress τ/τ_p profiles, for a non-dilatant ultimately stable fault subjected to moderate over-pressure $\Delta P/\sigma'_o = 0.5$. The stress criticality is $\tau_o/\tau_p = 0.55$ and the friction weakening ratio is $f_r/f_p = 0.6$.

We show in Figure 4.13 the benchmark of our numerical results against the semi-analytical ones of Garagash & Germanovich (2012), both in terms of dimensionless half-crack length a/a_w and dimensionless peak slip accumulated in the middle of the fault $\delta_{|x=0}/\delta_w$. Notably, we chose three scenarios by changing the stress criticality τ_o/τ_p, while keeping a moderate over-pressure $\dfrac{\Delta P}{\sigma'_o} = 0.5$ and a friction weakening ration of $f_r/f_p = 0.6$, in order to test the numerical solver for different regimes of propagation: i) purely aseismic slip ($\tau_o/\tau_p = 0.51$), ii) aseismic crack propagation with nucleation and arrest of dynamic event ($\tau_o/\tau_p = 0.555$) and iii) aseismic slip followed by an unabated dynamic rupture ($\tau_o/\tau_p = 0.75$). We can observe in Figure 4.13 that our numerical results match perfectly with the semi-analytical ones of Garagash & Germanovich (2012). The discrepancy in terms of half-crack length a/a_w between the numerical solutions and the semi-analytical ones is of the order of the element size h, the latter adopted such to have 25 elements within the frictional weakening zone (i.e. $a_w/h = 25$ - see the mesh convergence study reported in the following pages for relative error estimation). In Figure 4.14, the benchmark in terms of normalized slip δ/δ_w and shear stress τ/τ_p profile is reported (only for the case of aseismic crack propagation with nucleation and arrest of dynamic event). Again, we observe that the numerical results match the semi-analytical results of Garagash & Germanovich (2012) with good accuracy.

All the numerical results in terms of time evolution of half crack length a/a_w show a step-like behaviour. This is intrinsically related to the modeling of the fault as a sum of adjacent finite elements of equal size h. Indeed, in one increment of time, the pore pressure perturbation might not be enough to activate further elements - i.e. to induce $\mathcal{F}(\tau, \sigma'_n) = 0$. Time-stepping management as well as mesh resolution play an important role on this kind of step-like crack propagation. For a given increment of time Δt, the

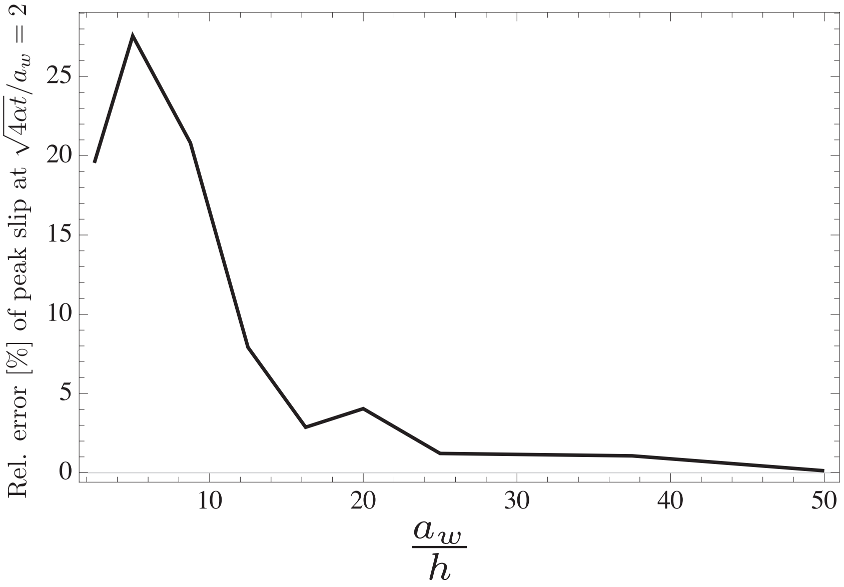

Figure 4.15 – Evolution of relative error in terms of normalized peak slip $\delta_{|x=0}/\delta_w$ at normalized time $\sqrt{4\alpha t}/a_w = 2$, as a function of number of elements within the nucleation length scale a_w. The test case investigated is a non-dilatant ultimately stable fault ($\tau_o/\tau_p = 0.55$ and $f_r/f_p = 0.6$), subjected to moderate overpressure $\dfrac{\Delta P}{\sigma'_o} = 0.5$. Semi-analytical results of Garagash & Germanovich (2012) in terms of normalized half crack length and peak slip at the fault center are available, allowing to calculate the relative error.

finer is the mesh the smaller are these steps. A local dynamic mesh refinement at the crack tips can reduce significantly this behaviour, although the computational cost might considerably increase.

4.8.3 Mesh convergence study

In order to check the accuracy of our numerical results, we have performed a mesh convergence study. Similarly to cohesive zone models for fracture propagation, the non linearity of the problem lies in a small zone near the crack tips. As already mentioned in Section 4.2.1.2, such a small zone is approximately defined by the characteristic nucleation length-scale a_w, over which the friction coefficient weakens from a peak value to its residual value during crack propagation. It is of great importance, therefore, to have enough mesh resolution within that length-scale so as to be able to capture the non-linearity with good accuracy. A local dynamic mesh refinement at the crack tips can help in doing it, although the computational cost might considerably increase.

Since semi-analytical results of Garagash & Germanovich (2012) for non-dilatant frictional weakening fault are available, we have performed a mesh convergence study for the following test case: ultimately stable fault $\tau_o/\tau_p = 0.55$ (for a friction weakening ratio of $f_r/f_p = 0.6$), subjected to moderate overpressure $\dfrac{\Delta P}{\sigma'_o} = 0.5$ (and $\dfrac{\epsilon_d}{\beta\sigma'_o} = 0.$ - no dilatancy, uncoupled problem). Notably, we run bunch of simulations with the same initial configuration, while changing the total number of equal-sized elements (of size h) in a given mesh. The nucleation length-scale a_w is thus fixed for all the simulations (as it depends on friction weakening length-scale δ_w, initial stress conditions and elastic property of the medium, which are kept constant for all the simulations), while the element size h varies. In this way, we investigated the fault response in terms of half-crack length a/a_w and peak slip at the middle of the fault $\delta_{|x=0}/\delta_w$ as a function of the ratio a_w/h, which indicates the number of elements within the non-linear length-scale.

Figure 4.15 shows the relative error in terms of normalized peak slip $\delta_{|x=0}/\delta_w$ at a given normalized time $\sqrt{4\alpha t}/a_w = 2.$, between the numerical results and the semi-analytical result of Garagash & Germanovich (2012), as a function of the number of elements within the nucleation length-scale a_w. We observe, not surprisingly, that the higher is the number of elements withing a_w, the lower is the relative error. For $a_w/h > 25$, the relative error is below 1%, up to reach 0.1% for $a_w/h = 50$. The non-monotonic decrease of the relative error for increasing values of a_w/h is related to step-like behaviour of the numerical solutions that inevitably appear for low values of a_w/h (already discussed in Section 4.8.2). This intrinsic behaviour is, in fact, more pronounced for decreasing values of a_w/h, for which the accuracy deteriorates considerably.

4.8.4 Case of otherwise unstable fault $\tau_o > \tau_r$ - Nucleation and Arrest

In the case of zero dilatancy, for unstable fault with relatively low stress criticality, under moderate over-pressure (region 4,b in Figure 4.3), a finite seismic episode occurs prior to the nucleation of dynamic rupture. We investigate the effect of different dilatancy in such a configuration ($\tau_o/\tau_p = 0.65$, $\Delta P/\sigma'_o = 0.5$, $f_r/f_p = 0.6$). Figure 4.16 displays the time evolution of crack length and peak slip for different level of dilatancy.

Interestingly, the 'transient' seismic episode which is linked to the fact that the fluid front is initially ahead of the slipping patch (see Figure 4.17 - comparison between pore pressure and slip profile at $\sqrt{4\alpha t}/a_w = 0.5$) does not disappear even for a dilatancy larger than the theoretical critical value $\epsilon_{d,c}/\beta\sigma'_o = 1/12$ in this case. Indeed such a seismic episode occurs with little accumulated slip and its nucleation is not influenced by residual friction: in such cases, the maximum dilatancy is not mobilized and no undrained strengthening of the fault occur. This can well be grasped by looking at the pore pressure profiles in Figure 4.17 at dimensionless time $\sqrt{4\alpha t}/a_w = 1$, i.e. at a given time after the arrest of the seismic episode. The pore pressure drop is not fully developed due to the limited slip rate associated with crack propagation. However, the subsequent re-nucleation is increasingly delayed as the dilatancy increases (see Figure 4.16 for $\dfrac{\epsilon_d}{\beta\sigma'_o} = 0.05$) and do not occur for

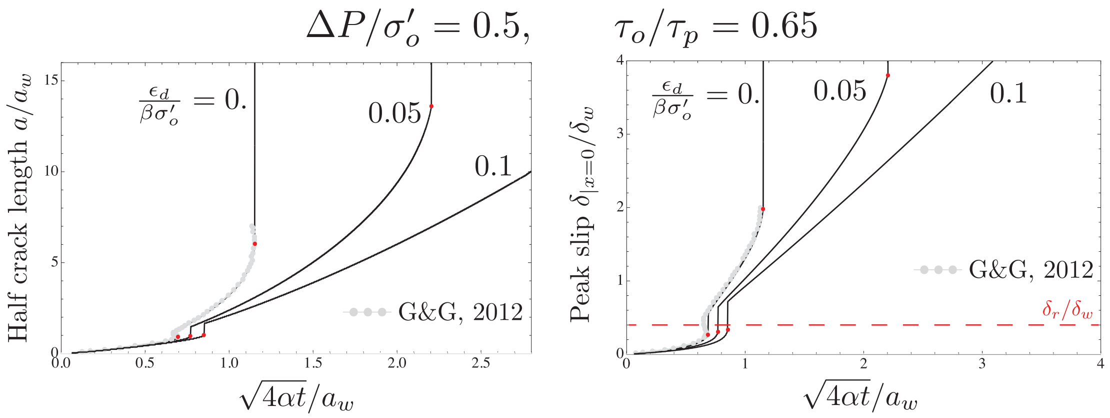

Figure 4.16 – Evolution of normalized half crack length a/a_w and normalized peak slip $\delta_{|x=0}/\delta_w$ with normalized time $\sqrt{4\alpha t}/a_w$ for a frictional weakening dilatant fault. The fault is subjected to an initial uniform background shear stress $\tau_o/\tau_p = 0.65$ (unstable fault in the non-dilatant case for a friction weakening ratio of $f_r/f_p = 0.6$ - with relative low stress criticality though) and a moderate constant over-pressure $\dfrac{\Delta P}{\sigma'_o} = 0.5$ applied in the middle of the fault. Two dimensionless dilatancy parameters are considered: $\dfrac{\epsilon_d}{\beta\sigma'_o} = 0.05 < \dfrac{\tau_o}{\tau_r} - 1 = \dfrac{\epsilon_{d,c}}{\beta\sigma'_o}$ and $\dfrac{\epsilon_d}{\beta\sigma'_o} = 0.1 > \dfrac{\tau_o}{\tau_r} - 1 = \dfrac{\epsilon_{d,c}}{\beta\sigma'_o}$. Grey dotted lines denote semi-analytical results of Garagash & Germanovich (2012), whereas red dots denote nucleation of dynamic rupture.

values of dilatancy equal of above the critical value (case of $\dfrac{\epsilon_d}{\beta\sigma'_o} = 1/10$). Note that for such configurations, the nucleation of the unabated dynamic rupture occurs when a significant portion of the crack size is at residual friction, the weakening zone is small and confined near the tip (see friction coefficient profile in Figure 4.17 at $\sqrt{4\alpha t}/a_w = 2.2$ - case of $\dfrac{\epsilon_d}{\beta\sigma'_o} = 0.05$). In such cases, the s.s.y assumption is valid, the maximum dilatancy is active and the theoretical estimate for the critical dilatancy / undrained shear strength is valid.

4.8.5 Approximated solution for quasi-static growth assuming $a \propto \sqrt{4\alpha t}$

The numerical results showed in Section 4.5.1 and 4.5.2 suggest that when the shear crack propagation is stable for large crack length, it appears to be synchronized with the fluid front position: i.e. $a = \gamma\sqrt{4\alpha t}$ for $a \gg a_w$ - at least for the constant permeability case. Following the approximated small scale yielding solution obtained for the non-dilatant case (Garagash & Germanovich 2012), we make some further assumptions in order to extend it to account for dilatancy. The main difficulty lies in the determination of the pore-pressure changes in the dilatant case. With an approximated pore-pressure perturbation solution in hand, we can use the small scale yielding approximation of the fracture energy (4.23)

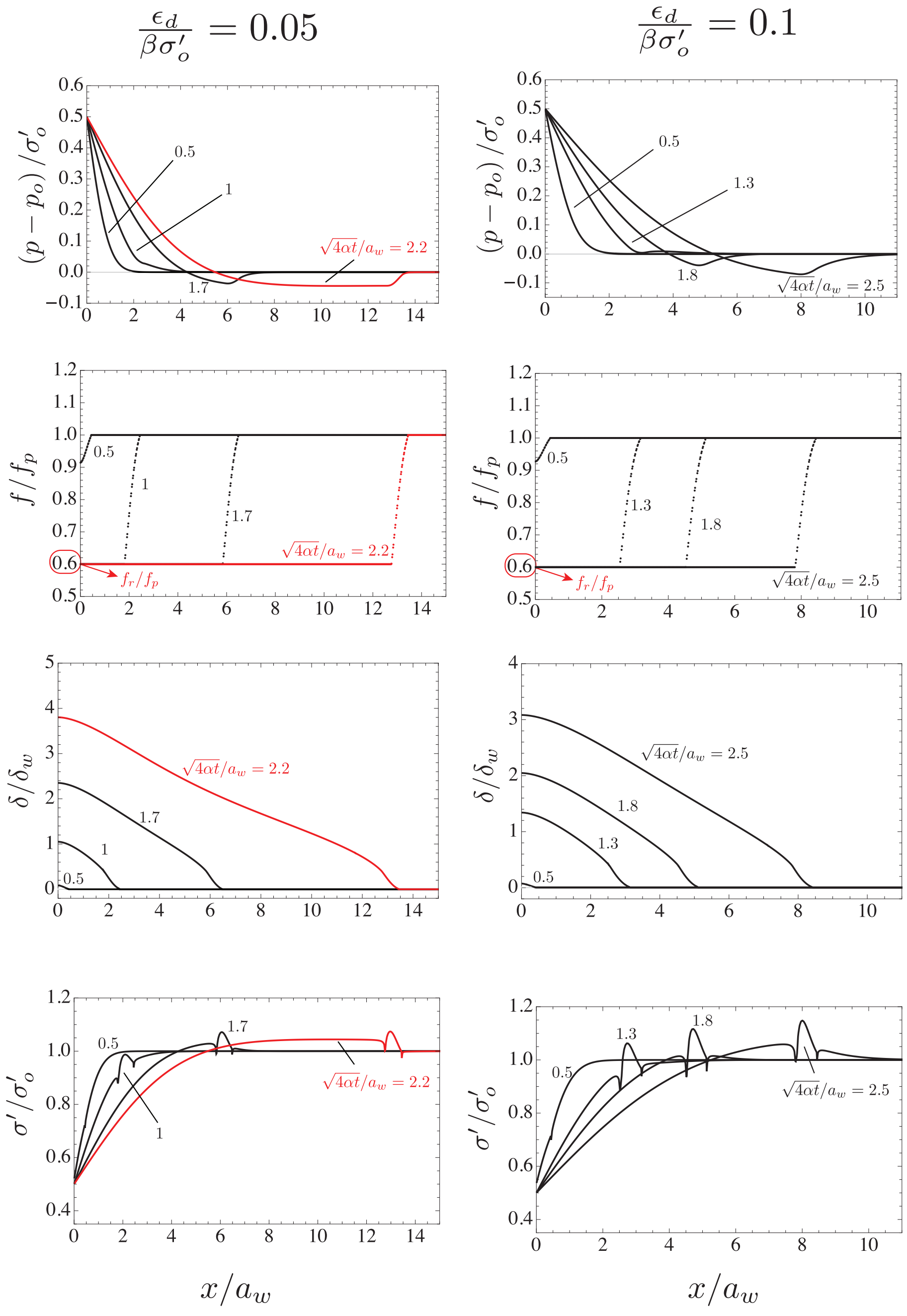

Figure 4.17 – Spatial profiles of dimensionless pore pressure (a), friction coefficient (b), slip (c) and effective normal stress (d) at different (normalized) time snapshots, for an otherwise unstable fault ($\tau_o/\tau_p = 0.65$ - relative low stress criticality for $f_r/f_p = 0.6$), subjected to a moderate over-pressure $\frac{\Delta P}{\sigma'_o} = 0.5$. Two dimensionless dilatancy parameters are considered: $\frac{\epsilon_d}{\beta\sigma'_o} = 0.05 < \frac{\tau_o}{\tau_r} - 1 = \frac{\epsilon_{d,c}}{\beta\sigma'_o}$ and $\frac{\epsilon_d}{\beta\sigma'_o} = 0.1 > \frac{\tau_o}{\tau_r} - 1 = \frac{\epsilon_{d,c}}{\beta\sigma'_o}$. Red lines refer to numerical results at nucleation time of an unabated dynamic rupture.

and the expression of the stress intensity factor (4.25) to estimate γ from the quasi-static propagation condition.

We make from the onset the hypothesis that $a = \gamma\sqrt{4\alpha t}$, and that the permeability remains constant with slip. We further assume that the increment of hydraulic width with dilatancy is rather small such that $wk_f \approx w_o k_f$. In other words, we assume the fault hydraulic conductivity to remain constant. Under the small scale yielding approximation, we approximate the sink term due to dilatancy by two moving sink of intensity ϵ_d at the crack tips.

By scaling the variables of equation (4.14) with the following characteristic scales

$$\Pi = \tfrac{p(x,t)}{\Delta P}, \qquad \xi = \tfrac{x}{\ell_d(t)}, \qquad \gamma = \tfrac{a}{\ell_d(t)}$$

where $\ell_d = \sqrt{4\alpha t}$, the fluid flow equation reduces to the following ODE when γ is assumed to remain constant

$$-\frac{1}{4}\frac{\partial^2\Pi}{\partial\xi^2} - \frac{1}{2}\xi\frac{\partial\Pi}{\partial\xi} + \frac{1}{2}\xi\cdot\frac{\epsilon_d}{\beta\cdot\Delta P}\cdot\left(\delta_{dirac}\left(\xi-\gamma\right)+\delta_{dirac}\left(\xi+\gamma\right)\right) = 0 \tag{4.44}$$

We note in the previous equation (4.44) the presence of two moving sink terms that represent the undrained fault response occurring at small end zone of crack tips. With the following dimensionless boundary conditions

$$\Pi\left(0\right) = 1, \qquad \Pi\left(\infty\right) = 0, \tag{4.45}$$

equation (4.44) can be solved analytically:

$$\begin{gathered}\Pi(\xi,\gamma) = 1 - \mathrm{Erf}(\xi) - e^{\gamma^2}\sqrt{\pi}\gamma\Gamma_d\cdot \\ \left(-\mathrm{Erf}(\gamma)\left(1+\mathrm{Erf}(\xi)\right) + \left(\mathrm{Erf}(\gamma)-\mathrm{Erf}(\xi)\right)\cdot H(-\gamma+\xi) + \left(\mathrm{Erf}(\gamma)+\mathrm{Erf}(\xi)\right)\cdot H(\gamma+\xi)\right),\end{gathered} \tag{4.46}$$

where H is the Heaviside step function and $\Gamma_d = \dfrac{\epsilon_d}{\beta\cdot\Delta P} = \dfrac{\epsilon_d}{\beta\sigma'_o}\dfrac{\sigma'_o}{\Delta P}$ is a dimensionless parameter capturing the effect of the undrained pore pressure drop with respect to the injection fluid over-pressure. Note that the dimensionless over-pressure at the tip simplify to:

$$\Pi(\gamma,\gamma) = \mathrm{Erfc}\left(\gamma\right)\Big(1 - \gamma\sqrt{\pi}\ \mathrm{e}^{\gamma^2}\Gamma_D\mathrm{Erf}\left(\gamma\right)\Big) \tag{4.47}$$

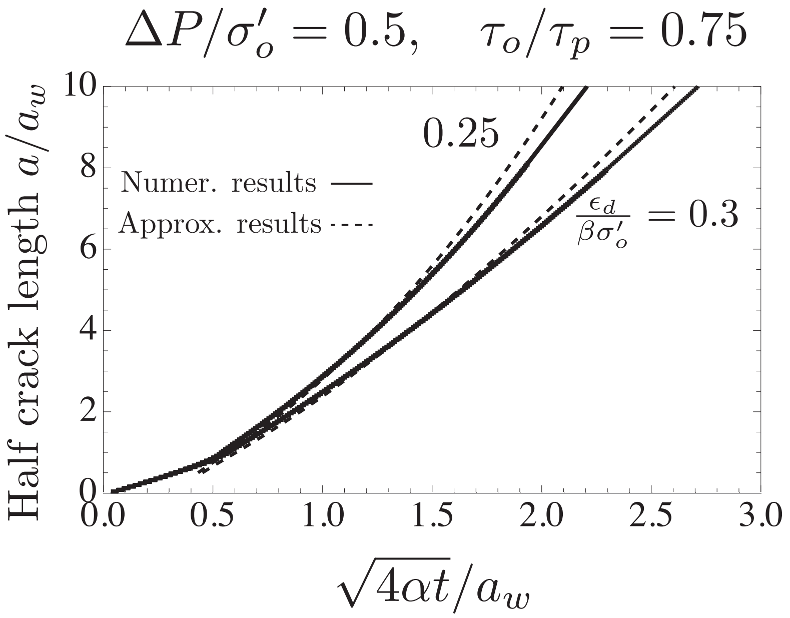

Figure 4.18 – Comparison between numerical results and results associated with approximated solution for quasi-static crack growth ($a \propto \sqrt{4\alpha t}$) in terms of time evolution of normalized half-crack length a/a_w. The case investigated is a critically stressed fault ($\tau_o/\tau_p = 0.75$), subjected to moderate over-pressure $\Delta P/\sigma'_o = 0.5$ and two values of dimensionless dilatancy parameter $\dfrac{\epsilon_d}{\beta\sigma'_o} = 0.25 - 0.3$.

Equation (4.46) thus allows to calculate analytically the SIF (through equation (4.25)):

$$K_{II} = \tau_p\sqrt{\ell_d} \times \left(\sqrt{\pi}\left(\frac{\tau_o}{\tau_p} - \frac{f_r}{f_p}\right) + \frac{f_r}{f_p}\frac{\Delta P}{\sigma'_o}\Delta k_{II}(\gamma, \Gamma_d)\right) \tag{4.48}$$

$$\Delta k_{II}(\gamma, \Gamma_d) = \sqrt{\pi} - \frac{4\gamma}{\pi}\left(1 + \gamma\sqrt{\pi}\ \mathrm{e}^{\gamma^2}\Gamma_D \mathrm{Erfc}\left(\gamma\right)\right)\ {}_p\mathrm{F}_q(\{1/2, 1\}, \{3/2, 3/2\}, -\gamma^2) \tag{4.49}$$

where ${}_p\mathrm{F}_q$ denotes the generalized hypergeometric function. Note that interestingly, in the limit of large crack length (i.e. large $\gamma\ell_d$), we recover the exact same limit than the simpler approximation of the superposition of a point source with an uniform undrained pore-pressure drop used in Section 4.3.2.2:

$$\lim_{a\to\infty} K_{II} = \infty\left(\tau_o - \frac{\epsilon_d}{\beta\sigma'_o}f_r - \tau_r\right) = \infty\left(\tau_o - \tau_r^u\right), \tag{4.50}$$

and therefore the same critical value of dilatancy (4.27) required to stabilize an otherwise unstable fault.

Under such a small scale yielding approximation, assuming that the over-pressure is uniform in the weakening zone and equal to its value at the crack tip, the fracture energy

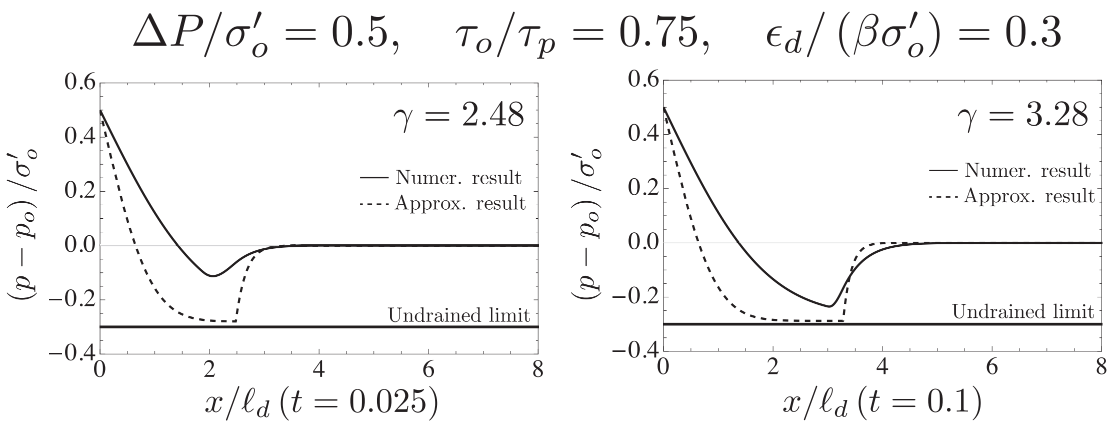

Figure 4.19 – Comparison between numerical results and results associated with approximated solution for quasi-static crack growth ($a \propto \sqrt{4\alpha t}$) in terms of pore pressure profiles. The case investigated is a critically stressed fault ($\tau_o/\tau_p = 0.75$), subjected to moderate over-pressure $\Delta P/\sigma'_o = 0.5$ and a dimensionless dilatancy parameter $\frac{\epsilon_d}{\beta\sigma'_o} = 0.3$. The relative (and constant) position between crack tip and fluid front ($\gamma = \frac{a}{\ell_d(t)}$) is 2.48 and 3, which correspond to a dimensionless time of $\sqrt{4\alpha t}/a_w = 1$ and $\sqrt{4\alpha t}/a_w = 2$, respectively.

G_c (see eq. (4.23)) can be approximated as

$$G_c = (f_p - f_r)\frac{\delta_r \sigma'_o}{2}\left(1 - \frac{\Delta P}{\sigma'_o} \times \Pi(\gamma, \gamma)\right) \tag{4.51}$$

The quasi static propagation condition (24) can thus be re-written as:

$$\frac{a_w}{\ell_d}\left(\frac{f_p - f_r}{f_p}\right)^2\left(1 - \frac{\Delta P}{\sigma'_o} \times \Pi(\gamma, \gamma)\right) = \left\{\sqrt{\pi}\left(\frac{\tau_o}{\tau_p} - \frac{f_r}{f_p}\right) + \frac{f_r}{f_p}\frac{\Delta P}{\sigma'_o}\Delta k_{ii}(\gamma, \Gamma_d)\right\}^2 \tag{4.52}$$

The previous equation can be solved for γ for a given set of problem parameters (τ_o/τ_p, f_r/f_p, $\Delta P/\sigma'_o$, $\epsilon_d/(\beta\sigma'_o)$) and a given value of a_w/ℓ_d. Although, we made the assumption of a time-independent γ to obtain the pore-pressure profile, we can relax it to see its evolution with a_w/ℓ_d. The obtained approximated solution captures the order of magnitude of the aseismic shear crack propagation as can be seen on Figure 4.18. However, it is not precise enough essentially due to i) the impact of the change of hydraulic conductivity with slip which prevent to properly captured the pore-pressure profile (as can be seen on Figure 4.19) and ii) the fact that the pore-pressure is clearly not uniform in the weakening zone which impact the estimation of the fracture energy in the small scale assumption.

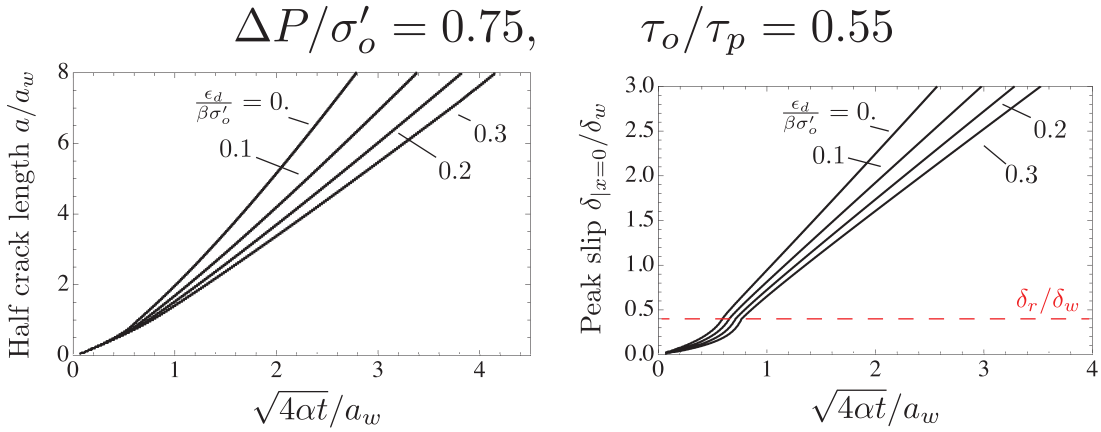

Figure 4.20 – Dilatancy effect on normalized crack length a/a_w and peak slip δ/δ_w at $x = 0$ for a frictional weakening fault subjected to large overpressure $\Delta P/\sigma'_o = 0.75$. The fault is ultimately stable in the hypothetical absence of dilatancy as the uniform background shear stress $\tau_o = 0.55 \cdot \tau_p$ is lower than the fault residual strength at ambient conditions τ_r, for a friction weakening ratio of $f_r/f_p = 0.6$. Under such stress criticality and large over-pressure, the fault always exhibits seismic crack propagation (zone 3 of Figure 4.3). However, the crack velocity slows down for increasing values of dimensionless dilatancy parameters.

4.8.6 Dilatancy effect on purely aseismic crack propagation

In Figure 4.20 we show the numerical results for an ultimately stable dilatant fault ($\tau_o/\tau_p = 0.55$) subjected to large overpressure $\Delta P/\sigma'_o = 0.75$. The dilatancy ratio $\epsilon_d/\beta\sigma'_o$ varies in order to investigate the effect of dilatancy during the aseismic crack propagation. As one can observe from the time evolution of half-crack length a/a_w or from the time evolution of peak slip $\delta_{|x=0}/\delta_w$, dilatancy slows down the aseismic propagation. Although the undrained fault response is not well pronounced at crack tips due to its aseismic propagation, it is enough to further slow down the crack velocity.

4.8.7 Effect of shear-induced permeability changes: case of effective stress-dependent permeability

We report in Figure 4.21 the numerical results in terms of half crack length a/a_w and peak slip $\delta_{|x=0}/\delta_w$ at the centre of a critically stressed fault ($\tau_o/\tau_p = 0.75$) as function of normalized time $\sqrt{4\alpha t}/a_w$, both obtained using the effective stress-dependent permeability law (4.29). The normalized dilatancy ratio $\dfrac{\epsilon_d}{\beta\sigma'_o}$ is kept constant at critical stabilizing value 0.25 as well as the overpressure at injection point $\Delta P/\sigma'_o$ at the moderate value 0.5, whereas the dimensionless ratio σ'_o/σ_* varies in order to span low and large fault permeability increase during shear crack propagation (by calibrating different values of k_*).

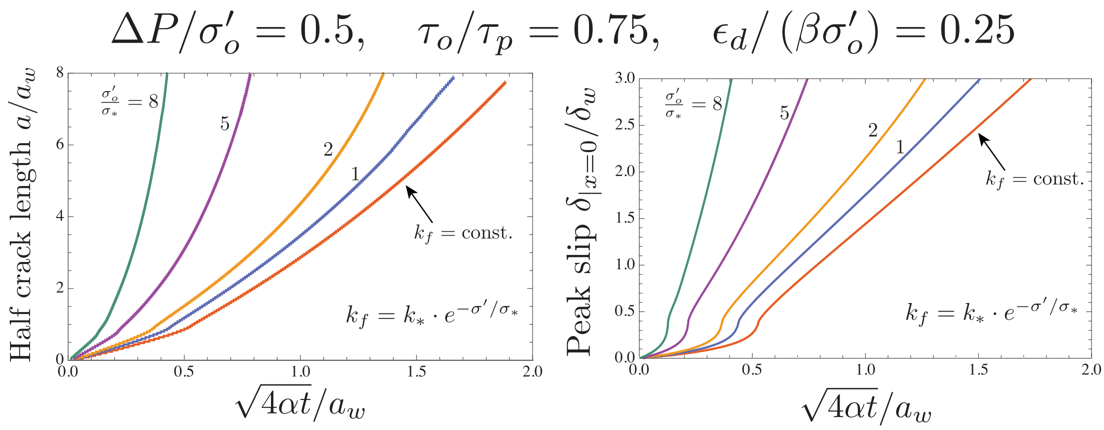

Figure 4.21 – Effect of permeability increase on a critically stressed ($\tau_o/\tau_p = 0.75$, $f_r/f_p = 0.6$) dilatant fault in terms of time evolution of normalized half crack length a/a_w and peak slip $\delta_{|x=0}/\delta_w$. The dimensionless dilatancy parameter $\epsilon_d/(\beta\sigma'_o)$ is taken here equal to the critical stabilizing value 0.25. Under such conditions a fault with constant fault permeability $k_f = \omega^2/12$, subjected to moderate overpressure $\Delta P/\sigma'_o = 0.5$, never exhibit seismic slip. An effective stress-dependent permeability law has been considered ($k_f = k_* e^{(-\sigma'/\sigma_*)}$), with four different ratios of σ'_o/σ_* spanning low and large permeability increase.

As already mentioned in Section 4.6, these numerical results are qualitatively similar to the ones of Figure 4.11. Large increase of permeability associated with strong reduction of effective normal stress enhance the crack velocity, but the crack propagation always remains quasi-static. The peak slip that the fault can experience is always aseismic even for large increase of fault permeability (see Figure 4.22-right, case $\sigma'_o/\sigma_* = 8.$).

In Figure 4.22 the profiles of normalized pore-pressure, slip, friction coefficient, effective normal stress and permeability are reported, all obtained at normalized time snapshot $\sqrt{4\alpha t}/a_w = 0.4$. Although the maximum permeability in the case of $\sigma'_o/\sigma_* = 8$ is nearly two order of magnitude larger than its initial value at ambient conditions, the undrained fault response at crack tips remains strong, preventing the crack velocity from diverging.

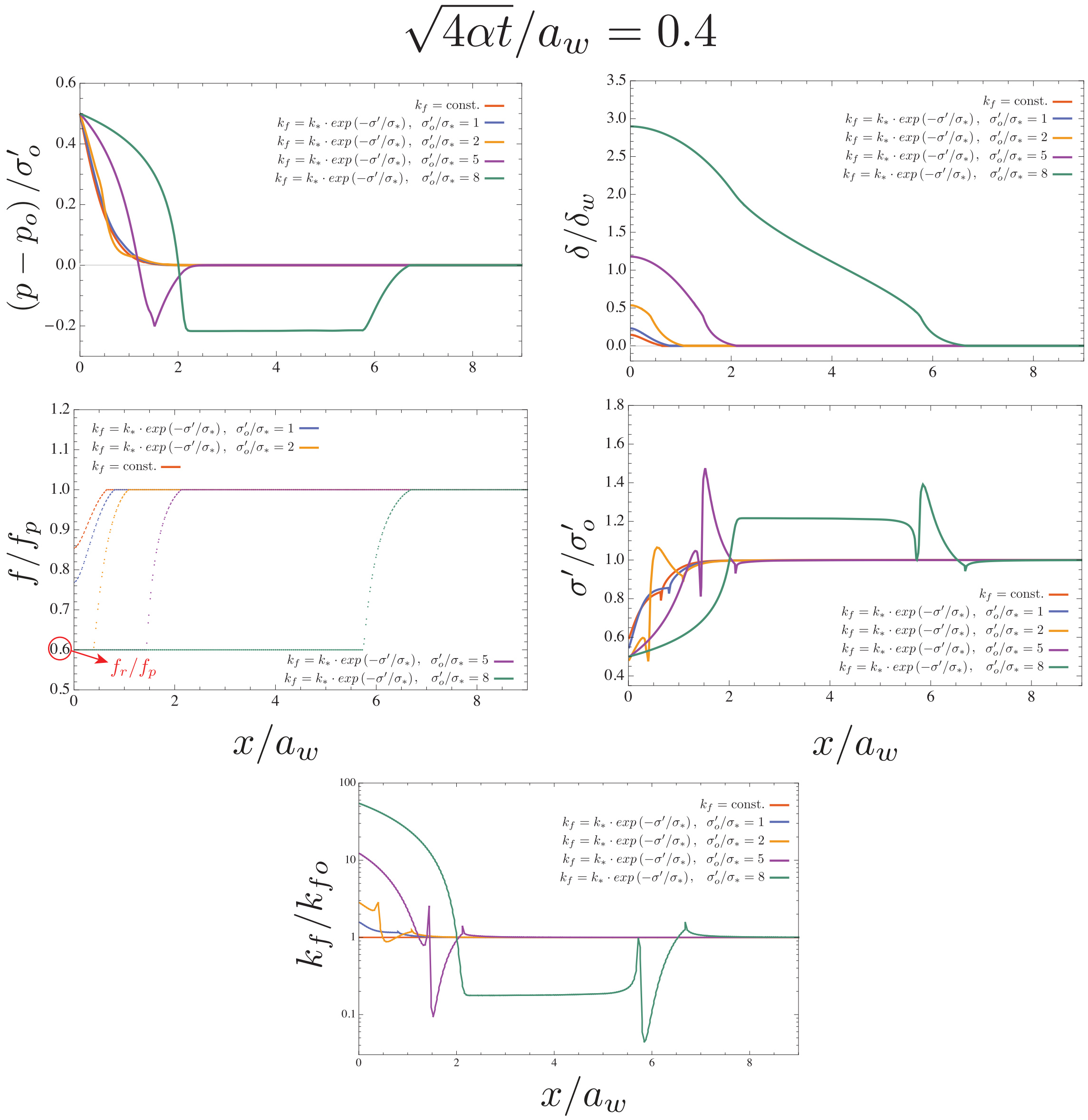

Figure 4.22 – Spatial profiles of dimensionless pore pressure, friction coefficient, slip, effective normal stress and fault longitudinal permeability (in linear-log scale) at a given normalized time snapshot $\sqrt{4\alpha t}/a_w = 0.4$, for unstable fault ($\tau_o/\tau_p = 0.75$ - $f_r/f_p = 0.6$), subjected to a moderate over-pressure $\dfrac{\Delta P}{\sigma'_o} = 0.5$ and a dimensionless dilatancy parameter equal to the critical value, i.e. $\dfrac{\epsilon_{d,c}}{\beta\sigma'_o} = 0.25$. The different numerical results are obtained with different fault permeability evolution laws: i) constant permeability $k_f = \dfrac{\omega_o^2}{12}$, ii) effective stress-dependent permeability law $k_f = k_* \cdot e^{(-\sigma'/\sigma_*)}$, with $\sigma'_o/\sigma_* = 1-2-5-8$.

5 A boundary element based solver for localized inelastic deformations

This chapter present a numerical method for the solution of non-linear geo-mechanical problems involving localized deformation along shear bands and fractures. Boundary element method is leveraged to solve for the quasi-static elastic deformation of the medium while rigid-plastic constitutive relations govern the behavior of displacement discontinuity (DD) segments capturing localized deformations. A fully implicit scheme is developed using a hierarchical approximation of the boundary element matrix. Combined with an adequate block pre-conditioner, this allows to tackle large problems via the use of an iterative solver for the solution of the tangent system. Several examples of the initiation and growth of shear-bands and tensile fractures illustrate the capabilities and accuracy of this technique. The method does not exhibit any mesh dependency associated with localization provided that i) the softening length-scale is resolved and ii) the correct plane of localized deformations is discretized a-priori using DD segments.

This chapter is a modified version of the following scientific article:

Ciardo, F., Lecampion, B. & Fayard, F. A boundary element based solver for localized inelastic deformations. To be submitted to *Comp. Meth. Appl. Mech. Engng.*

Authors contributions
Federico Ciardo: Conceptualization, Methodology, Formal analysis, Investigation, Software, Visualization, Validation, Writing - original draft.
Brice Lecampion: Conceptualization, Methodology, Formal analysis, Investigation, Writing - review & editing, Supervision.
François Fayard: Investigation, Software, Validation.

5.1 Introduction

Driven by geomechanical applications such as faulting, shear-banding and fracturing typically occurring in large domains, we develop a computational method for the solution of problems exhibiting localized inelastic deformations. We use the boundary element method for the solution of quasi-static elasticity in the medium and accounts for the presence of potential displacement discontinuity (DD) segments where inelastic deformations take place. We use a rigid-plastic like constitutive relation for these DD segments. In particular, we combine a non-associated Mohr-Coulomb frictional behavior with a tensile cut-off, allowing for softening of cohesion, friction and tensile strength. Although the method can be further coupled with fluid flow, we restrict here for clarity to the case where mechanical deformation does not affect flow.

Elasto-plastic problems leading to localized plastic deformations have been extensively investigated using both finite element (FEM) (Needleman 1972, Needleman & Tvergaard 1977, Tvergaard et al. 1981, Belytschko et al. 1988) and boundary element (BEM) (Bigoni & Capuani 2002, Brum et al. 2003) where in the latter plastic deformation are accounted via volume integral terms (thus requiring a bulk discretization of the plastic zones (Bonnet 1999*b*)). The numerical solutions of this class of non-linear boundary value problems typically exhibit mesh dependencies which are the results of the non-uniqueness associated with the bifurcation of the underlying continuum problem [1] (Rice 1977). Several remedies have been proposed to overcome these difficulties: i) introduction of material rate dependence (Needleman 1988, Zhou et al. 2005) which in effect introduce a length-scale, ii) incorporation of a material length-scale in the material constitutive response via gradient based theories (Benallal et al. 2002, Mühlhaus & Aifantis 1991, De Borst & Mühlhaus 1992), non local models (Benallal et al. 2006) or Cosserat continua (De Borst 1991).

In this contribution, we adopt a different approach. Namely, we hypothesise that inelastic deformations can only be localized along displacement discontinuity segments and express the yielding criteria and flow rule only along these segments. This approach shares similarities with cohesive zone modeling in FEM where cohesive traction-separation law between interface element control crack growth (Xu & Needleman 1994, Camacho & Ortiz 1996, Pandolfi & Ortiz 2002, Zhou & Molinari 2004), or discrete dislocation plasticity (Van der Giessen & Needleman 1995), and can be traced back to Palmer & Rice (1973) for shear band growth. The use of a boundary element method for the discretization of the DD segments allows to efficiently resolve potential localization phenomena without extensive bulk domain discretization. This is particularly attractive for large domain. Moreover the DD segments are rigid if not at yield thus recovering a solely elastic response in that limit.

In the following, we first present the mathematical formulation of this method restricting to a plane strain configuration. The numerical scheme devised as well as the choice of an adequate pre-conditioner for the iterative solution of the resulting tangent system is then discussed in details. We finally illustrate the accuracy and capabilities of this approach on a series of examples involving the initiation and growth of shear-bands and tensile cracks.

---

[1] Strain-softening and non-associated is not necessary in tri-axial setting for localization to occur.

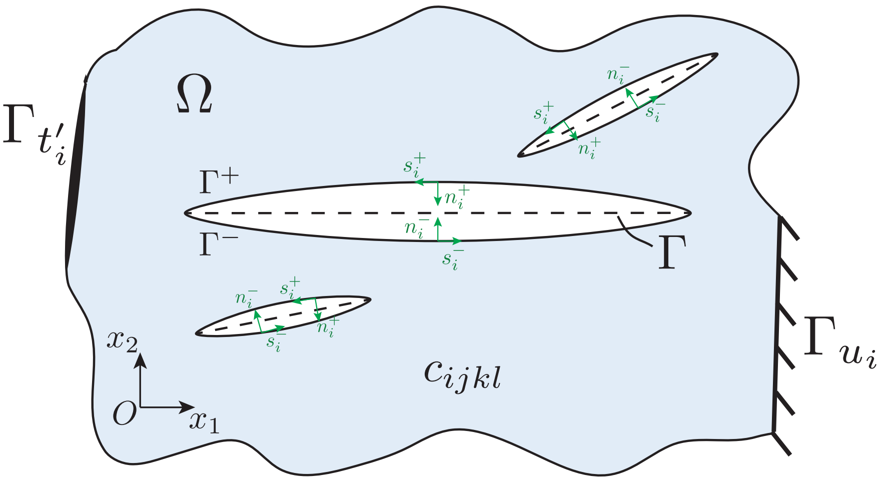

Figure 5.1 – A linearly isotropic elastic medium Ω containing a set of pre-existing potential fractures and slip planes whose mid-plane are denoted by Γ. Boundary regions with prescribed displacements or effective traction are denoted respectively as Γ_{u_i} and $\Gamma_{t'_i}$.

5.2 Problem formulation

We consider an homogeneous, isotropic and linear elastic medium under plane-strain condition. The medium is subjected to a generalized system of forces that may cause localized inelastic deformations along a set of pre-defined segments that translate into displacement discontinuities. A yield criterion controls the occurrence of displacement discontinuities along these segments. If the yield criterion is not satisfied on a particular segment, the displacement discontinuities are zero. Upon yielding, the evolution of displacement discontinuities is governed by a non-associated plastic like flow rule (Maier et al. 1993). Incorporating softening, the formalism allows to recover cohesive zone like behavior as well as friction. This enable to capture localized deformations (shear bands, open and sliding fractures). The model is thus akin to a rigid plastic one for the potentially failing segments and elastic for the rest of the solid. This translates into an elasto-plastic response for the whole medium.

5.2.1 Elastic medium with displacement discontinuities

Due to the assumption that inelastic deformations are limited to displacement discontinuity segments, the use of boundary integral equations to solve for the quasi-static elastic balance of momentum is particularly appealing especially for exterior problems. Referring to Figure 5.1, Γ denotes the locus of displacement discontinuities, located in a elastic domain $\Omega \in \mathbb{R}^2$ with an elastic stiffness tensor $\mathbf{c}_{ijkl}$. We denote the unit normal vector $n_i = n_i^- = -n_i^+$ where n_i^+ and n_i^- are the unit normal vector of the top and bottom surfaces of Γ respectively (see Fig. 5.1). The corresponding shear orthonormal vectors s follow the right-hand side rule. We use the convention of positive displacement discontinuities in opening, positive slip for clock-wise rotation of matter:

$$d_i = u_i^+ - u_i^- \tag{5.1}$$

where u_i is the displacement vector. On the other hand, following the convention of geo-mechanics, stresses are taken positive in compression.

The quasi-static elastic equilibrium is written as the following boundary integral equations, relating tractions and displacement discontinuities in the local normal (n) and tangential (s) frame along Γ (Hill et al. 1996):

$$t_i(\mathbf{x}) - t_i^o(\mathbf{x}) = n_j(\mathbf{x}) \int_\Gamma c_{ijkl} \frac{\partial S_{ab}^k}{\partial \xi_l}(\mathbf{x}, \xi) d_a(\xi) n_b(\xi) \mathrm{d}\xi \quad \text{for} \quad i, j, = n, s, \tag{5.2}$$

where $t_i = \sigma_{ij} n_j$ is the traction vector, t_i^o is the initial traction and $S_{ab}^k(\mathbf{x}, \xi)$ is the stress at ξ induced by a point force located at $\mathbf{x}$ along the kth direction. $c_{ijkl} \frac{\partial S_{ab}^k}{\partial \xi_l}(\mathbf{x}, \xi)$ corresponds to the stress induced by a dislocation dipole. We refer to Hill et al. (1996), Bonnet (1999*b*), Mogilevskaya (2014*b*) for more details and expressions for these fundamental elastic solutions. The integral equation (5.2) is hyper-singular and can be solved with either collocation methods (Crouch & Starfield 1983) or symmetric Galerkin techniques (Bonnet et al. 1998).

5.2.2 Constitutive relations for displacement discontinuities segments

We use a Mohr-Coulomb criterion combined with a tensile cut-off as the yielding function for localized failure on segments, allowing for softening (see Figure 5.2). Accounting for the presence of fluid (of pressure p), we combine two yield functions expressed in terms of the local components of effective traction vector $t'_n = t_n - p$, $t'_s = t_s$:

$$\mathcal{F}_1(t'_n) = -\sigma_c(\kappa, \kappa_m) - t'_n \leq 0, \tag{5.3a}$$

$$\mathcal{F}_2(t_s, t'_n) = |t_s| - c(\kappa, \kappa_m) - f(|d_s|, \delta_m) t'_m \leq 0, \tag{5.3b}$$

where $f(|d_s|, \delta_m)$ is the friction coefficient function of absolute value of shear slip d_s (and the maximum slip obtained during the loading history δ_m). Similarly, $\sigma_c(\kappa, \kappa_m)$ and $c(\kappa, \kappa_m)$ are the tensile strength and cohesion respectively, both function of a softening variable $\kappa = \sqrt{\xi^2 d_s^2 + d_n^2}$, where $\xi > 0$ is a phenomenological parameter accounting for the relative intensity of shear and normal displacement on softening. κ_m corresponds to the maximum value of κ obtained during the loading history.

In order to define uniquely which yield function the effective traction vector must satisfy when both criteria are violated simultaneously (when $\mathcal{F}_1(t'_n) > 0$ and $\mathcal{F}_2(t_s, t'_n) > 0$), we

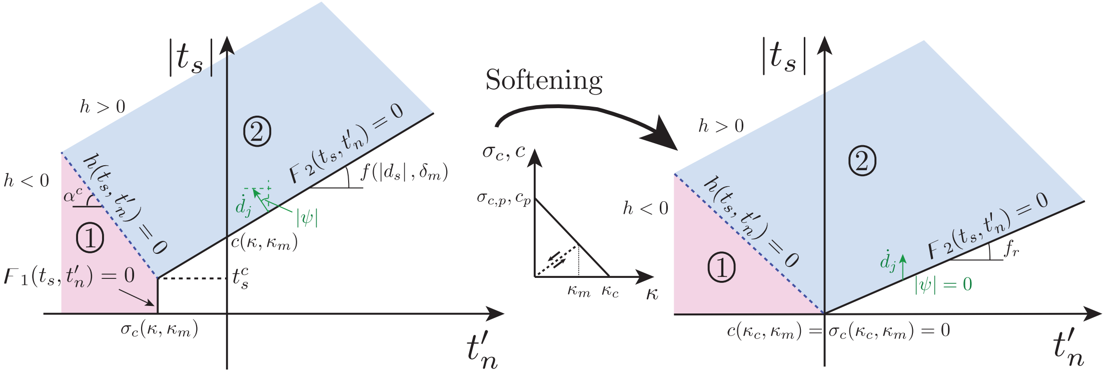
$|t_s|$
$h > 0$
$h < 0$
②
$h(t_s, t'_n) = 0$
α^c
①
$F_2(t_s, t'_n) = 0$
$f(|d_s|, \delta_m)$
d_j
$|\psi|$
$c(\kappa, \kappa_m)$
t_s^c
$F_1(t_s, t'_n) = 0$
$\sigma_c(\kappa, \kappa_m)$
t'_n
Softening
σ_c, c
$\sigma_{c,p}, c_p$
κ_m
κ_c
κ
$|t_s|$
$h > 0$
$h < 0$
②
$h(t_s, t'_n) = 0$
①
$F_2(t_s, t'_n) = 0$
f_r
d_j
$|\psi| = 0$
$c(\kappa_c, \kappa_m) =$
$\sigma_c(\kappa_c, \kappa_m) = 0$
t'_n

Figure 5.2 – Composite yielding surface for displacement discontinuity segments combining a Mohr-Coulomb (region 2) with a tensile cut-off (region 1) - left panel. Softening of tensile strength, cohesion as well as friction is possible ultimately resulting in a purely frictional behavior at complete softening - right panel. A non-associated flow rule for the frictional response limit plastic dilatancy and result in critical state flow at complete softening (right).

use a function $h(t_s, t'_n)$ similar to the one proposed in Itasca Consulting Group (2010)

$$h(t_s, t'_n) = |t_s| - t_s^c - \alpha^c(\sigma_c(\kappa, \kappa_m) + t'_n), \tag{5.4}$$

where t_s^c and α^c are two scalars function of the current friction, cohesion and tensile strength defined as

$$t_s^c = c(\kappa, \kappa_m) - f(|d_s|, \delta_m)\sigma_c(\kappa, \kappa_m)$$

$$\alpha^c = \sqrt{1 + f(|d_s|, \delta_m)^2} - f(|d_s|, \delta_m)$$

The composite yielding function $F(t_s, t'_n) = F_1(t'_n) \cup F_2(t_s, t'_n)$ represents an inequality constraint for the traction applied on Γ. Combined with the function $h(t_s, t'_n)$, it allows to split uniquely the effective traction space into admissible and inadmissible regions (see Figure 5.2): specifically, $F_2(t_s, t'_n)$ for $h(t_s, t'_n) \geq 0$ (shear failure) and $F_1(t'_n)$ for $h(t_s, t'_n) < 0$. In the following, we describe the relations that the local tractions must satisfy on a given displacement discontinuity segment Γ for the different inadmissible regions 1 and 2 of Figure 5.2 corresponding to tensile or shear failure respectively.

5.2.2.1 Shear failure

Shear failure is captured via a non-associated flow rule to better reproduce shear-induced dilatancy (with a dilatant angle typically lower than friction angle). The yield criteria constraint and corresponding evolution of the displacement discontinuity rates are thus similar to frictional contact with cohesion:

$$\mathcal{F}_2(t_s, t_n') < 0, \qquad \dot{d}_s = 0, \qquad \dot{d}_n = 0 \tag{5.5a}$$

$$\mathcal{F}_2(t_s, t_n') = 0, \qquad \dot{d}_s = \left|\dot{d}_s\right| \mathrm{sign}(t_s), \qquad \dot{d}_n = \left|\dot{d}_s\right| \tan\psi(|d_s|, \delta_m|) \tag{5.5b}$$

During shear failure, the evolution of cohesion c and friction coefficient f with non-linear deformations governs the traction separation along Γ. We assume that the cohesion c degrades linearly with softening variable κ in a similar way than the tensile strength σ_c (see the following sub-section) keeping the ratio c/σ_c constant. The friction coefficient f is supposed to weaken linearly with the absolute value of slip $|d_s|$, from a peak value f_p to a residual value f_r for slip larger than a critical slipping distance δ_c (Palmer & Rice 1973):

$$f(|d_s|, \delta_m) = \begin{cases} f_p - \frac{f_p - f_r}{\delta_c} |d_s| & |d_s| < \delta_c \;\; \& \;\; |d_s| = \delta_m \\ f_p - \frac{f_p - f_r}{\delta_c} \delta_m & |d_s| < \delta_c \;\; \& \;\; |d_s| < \delta_m \\ f_r & |d_s| > \delta_c \end{cases} \tag{5.6}$$

Similarly, we assume that the dilatancy angle $\tan\psi$ softens linearly with cumulative slip $|d_s|$, from a peak value $\tan\psi_p$ down to zero above a critical slip distance δ_c at which a critical state is reached (Ciardo & Lecampion 2019). Like for the friction coefficient, the dilatancy angle does not evolve along the unloading/reloading branch. Although one can expect a drop of dilation angle during reverse deformation (see Stupkiewicz & Mróz (2001) for discussion), we stick to that assumption for sake of simplicity in the following.

5.2.2.2 Tensile failure

Tensile failure on Γ (inadmissible region 1 of Figure 5.2) is directly controlled by the value of the effective normal traction. The relations for the evolution of the displacement discontinuities are here given by:

$$\mathcal{F}_1(t_n') < 0, \qquad \dot{d}_n = 0, \qquad \dot{d}_s = 0 \tag{5.7a}$$

$$\mathcal{F}_1(t_n') = 0, \qquad \left|\dot{d}_n\right| > 0, \qquad \dot{d}_s = 0 \tag{5.7b}$$

with the complementary condition $\mathcal{F}_1(t_n') \left|\dot{d}_n\right| = 0$. The sign of $\dot{d}_n$ depends on the loading / unloading sequence and results from the application of the constraint $\mathcal{F}_1(t_n') = 0$ in the solution of the balance of momentum.

The evolution of the critical tensile strength σ_c with softening variable κ governs the relation between tractions and displacement discontinuities along Γ in a similar way than in cohesive zone models of fracture (Camacho & Ortiz 1996, Ortiz & Pandolfi 1999, Snozzi

& Molinari 2013). In the following, we assume that σ_c softens linearly with κ, from a peak value $\sigma_{c,p}$ to zero when κ is larger than a critical value κ_c. We also account for a reversible linear unloading/re-loading branch when the softening variable κ is lower than its maximum value reached during the loading history κ_m (see Figure 5.2). This can be summarized as

$$\frac{\sigma_c(\kappa,\kappa_m)}{\sigma_{c,p}} = \begin{cases} 1-\kappa/\kappa_c & \kappa<\kappa_c \ \ \& \ \ \kappa=\kappa_m \\ (1-\kappa_m/\kappa_c)\kappa/\kappa_m & \kappa<\kappa_c \ \ \& \ \ \kappa<\kappa_m \\ 0 & \kappa>\kappa_c \end{cases} \tag{5.8}$$

At complete softening, both the tensile strength σ_c and the cohesion c are zero resulting in a purely frictional Mohr-Coulomb criterion (see Figure 5.2 right). As a result, if $\mathcal{F}_1(t'_n) = 0$ at complete softening (i.e. $t'_n = 0$), one must also enforce $t_s = 0$ (i.e. $\mathcal{F}_2(t_s, t'_n) = 0$) and as a result $\left|\dot{d}_n\right| > 0$, $\left|\dot{d}_s\right| > 0$.

Non inter-penetrability constraint at closure When the tensile mode I failure is active, the sign of the normal displacement discontinuity rate is the result of the elastic balance of momentum of the whole medium, boundary conditions and the associated interactions between failed segments. Upon unloading, crack closure is possible. Of course, the internal crack surfaces can not inter-penetrates. Accounting for the irreversible dilation $\bar{w}_d = \int_0^t \tan\psi(\kappa)\dot{d}_s \,\mathrm{d}t$ accumulated during the loading history, we generalize the non inter-penetrability condition to

$$(d_n - w_d) \geq 0 \qquad \mathcal{F}_1(t'_n) \leq 0 \qquad (d_n - w_d)\mathcal{F}_1(t'_n) = 0 \tag{5.9}$$

5.2.3 Initial and boundary conditions

We assume that the elastic medium is initially in static equilibrium under a initial stress field σ^o_{ij} resulting in traction t^o_i on Γ. We assume that the initial state is such that the yielding criterion is not violated in any potential displacement discontinuity segments. Localized inelastic deformations therefore occurs as a result of either external loading (via an history of applied loads or displacements) or via internal pore fluid pressurization p which modifies the effective traction on the potential failure segments. We assume here the pore-pressure history known and uncoupled to mechanical deformation. Such time-dependent boundary conditions can be summarized as (in the local frame $i = s$, of the boundary):

$$t'_i(\mathbf{x},t) = t^g_i(\mathbf{x},t) - p(\mathbf{x},t) \qquad \text{on} \qquad \Gamma_{t'_i} \tag{5.10}$$

$$u_i(\mathbf{x},t) = u^g_i(\mathbf{x},t) \qquad \text{on} \qquad \Gamma_{u_i} \tag{5.11}$$

with the usual conditions $\Gamma = \Gamma_{u_i} \cup \Gamma_{t'_i}$, and $\Gamma_{u_i} \cap \Gamma_{t'_i} = \emptyset$. $t_i^g(\mathbf{x}, t)$, $u_i^g(\mathbf{x}, t)$ and p denotes given applied traction vector, displacement components and fluid pore pressure respectively. Note that in the absence of fluid, the pressure p is null and t'_i reduces to t_i.

5.3 Numerical scheme

5.3.1 Boundary element method for elasto-static using a hierarchical matrix appriximation

We use the displacement discontinuity method (Crouch & Starfield 1983) to discretize the elasticity equations (5.2). Upon discretization of Γ (union of all possible failing segments) into n_{segm} straight segments such that

$$\Gamma \approx \sum_{s=1,\ldots,n_{segm}} \Gamma_s, \tag{5.12}$$

We assume that displacement discontinuities d_i vary linearly within an element but discontinuously between adjacent elements (piece-wise linear element). This assumption sets a weaker requirement at each intersecting mesh node $n_{node} = n_{segm} + 1$ (i.e. no continuity of displacement discontinuities), which notably allows to treat configurations of fractures intersection more easily. For n_{segm} straight finite segments, we thus have $n = 4n_{segm}$ nodal displacement discontinuities unknowns. By introducing this discretization into the boundary integral elasticity equations (5.2), using a collocation method, one finally obtain a $4n_{segm} \times 4n_{segm}$ linear system of equations

$$\mathbf{t} = \mathbf{t}^o + \mathbf{E}\mathbf{d}, \tag{5.13}$$

where $\mathbf{t}$ and $\mathbf{t}^o$ are respectively the current and far-field traction vectors, $\mathbf{E}$ is the fully populated elastic influence matrix and $\mathbf{d}$ is the vector of nodal displacement discontinuities. Because of the singular nature of equation (5.2), collocation is performed at points located inside the displacement discontinuity element - see Crawford & Curran (1982) for discussion on their optimal location within the reference straight element.

Due to the non-locality of the elasticity kernel, the elasticity matrix $\mathbf{E}$ is fully populated although diagonal dominant. The memory requirement to store such a square matrix thus scales as $\mathcal{O}(n^2)$, setting a strict constraint for current available laptops with 64-bit processors. Furthermore, the computational complexity to solve the system of equations (5.13) with an iterative method is $\mathcal{O}(k \cdot n^2)$ (with possibly $k \ll n$). In order to overcome these limits, we use a hierarchical matrix ($\mathcal{H}$-matrix) technique combined with adaptive cross approximation as first introduced by Hackbusch (1999). This purely algebraic acceleration technique makes use of the spatial decay of the elastic kernel to approximate its far-field contributions via a data-sparse representation (low rank approximation). This allows to reduce memory requirements and, at the same time, speed up algebraic operations

(Hackbusch 2015*a*, Bebendorf 2008*b*). A hierarchical block domain decomposition builds recursively a geometrical binary cluster tree $\mathcal{T}_{\mathcal{I}}$ associated with the location of the collocation points, whose maximum depth is governed by a scalar parameter n_{leaf} that define the minimum cardinality of each cluster. Upon recursive evaluation of the following admissibility condition

$$Adm(p,q) = \text{true} \Longleftrightarrow \min\{\text{diam}(p), \text{diam}(q)\} \leq \eta \cdot \text{dist}(p,q), \tag{5.14}$$

where the diameter of a generic cluster $p \in \mathcal{T}_{\mathcal{I}}$ is defined as

$$\text{diam}(t) := \max_{i,j \in p} ||x_i - x_j|| \tag{5.15}$$

and the distance between two clusters $p, q \in \mathcal{T}_{\mathcal{I}}$ is

$$\text{dist}(p,q) := \min_{i \in p, j \in q} ||x_i - x_j|| \, , \tag{5.16}$$

to all the pair-nodes composing the block cluster tree $\mathcal{T}_{\mathcal{I}}$, a partitioning of the elastic matrix into admissible (far-field) and inadmissible (near-field) blocks can be obtained. The former are approximated via low-rank matrices combined with an adaptive cross approximation technique (see Hackbusch (2015*a*), Bebendorf (2008*b*) for full details), whereas the latter are stored and treated as dense matrices (full rank representation). It can be proved that by replacing the full elasticity matrix $\mathbf{E}$ with its hierarchical approximation $\mathbf{E}_{\mathcal{H}}$, the generic computational complexity reduces to (Bebendorf 2008*b*) $\mathcal{O}(n \times \log(n)^{\alpha})$ where α is a scalar parameter that depends on the type of operations: $\alpha = 1$ for storage requirements and matrix-vector multiplications, $\alpha = 2$ for matrix-matrix multiplication.

The construction of the $\mathcal{H}$-matrix representation of the initial matrix depends on 3 parameters: i) $\eta \geq 0$ governs the severity of the clustering (i.e. large value of η promote a more aggressive block partitioning, while $\eta = 0$ results in no partitioning, i.e. $\mathbf{E}_{\mathcal{H}} = \mathbf{E}$), ii) $n_{leaf} > 0$ defines the maximum depth of the block cluster tree $\mathcal{T}_{\mathcal{I}}$ and iii) ϵ_{ACA} governs the accuracy of the low-rank approximation obtained via an adaptive cross approximation (see Hackbusch (2015*a*) for details). The gain in memory storage with respect to the initial dense matrix is quantified by the memory compression ratio c_r given by

$$c_r(E_{\mathcal{H}}) = \frac{1}{n^2} \left(\sum_{(p,q) \in \text{Non-adm.}} \text{rank}(|p| + |q|) + \sum_{(p,q) \in \text{Adm.}} |p| \cdot |q| \right) \tag{5.17}$$

while the accuracy of $\mathbf{E}_{\mathcal{H}}$ is function of η, n_{leaf} and ϵ_{ACA}. In the remaining, we consider only a hierarchical approximation $\mathbf{E}_{\mathcal{H}}$ of the elasticity matrix. Our implementation is directly adapted from Chaillat et al. (2017).

5.3.2 An implicit time-stepping scheme

For a given load / pore pressure history, the solution of the problem consists in the solution of the discretized elasto-static balance of momentum in combination with the set of inequalities constraints introduced in Section 5.2.2. Besides the inequalities, softening reinforce the non-linearity of the problem. We use an implicit time-stepping scheme to obtain the solution at $t^{n+1} = t^n + \Delta t$ from a known solution at t^n. We solve for both the evolution of the displacement discontinuities as well as the corresponding tractions over the whole discretized mesh Γ. We use the notation $X^{n+1} = X^n + \Delta X$ to represent a generic time and space dependent variable $X(x, t)$ at time t^{n+1}. Over a time-step, the algorithm consist of two nested loops. The most outer loops tracks the set of element satisfying the yielding constraints and non inter-penetrability condition. The inner loop - for a given trial set of constraints - solve for the balance of momentum, and enforce the different equality constraints. Softening render such an inner loop non-linear and we thus use a fixed-point scheme for its solution.

5.3.2.1 Outer yielding loop

The most outer iterative loop is used to converge on the different inequalities constraints (yielding and non inter-penetrability conditions) for all the element within the mesh. At each iteration, the algorithm identifies the set of elements $\mathcal{S}_{a,1}$ active in tensile failure (satisfying eq. (5.3a)), the set of elements $\mathcal{S}_{a,2}$ active in shear failure (satisfying eq. (5.3b)), and the set of elements $\mathcal{S}_{interp.}$ violating the inter-penetrability constraint eq. (5.9). The set of inactive elements (neither yield or interpenetrating) $\mathcal{S}_{inact.}$ is just the complement

$$\mathcal{S}_{inact.} \notin \{\mathcal{S}_{a,I} \cup \mathcal{S}_{a,II} \cup \mathcal{S}_{interp.}\}$$

such that the union of all these sets equals the total number of element in the mesh. For each set of segments, different constraints have to be enforced in combination with equilibrium, either in terms of traction or in terms of displacement discontinuity (as discussed in Section 5.2.2).

The convergence of this outer loop is achieved when all the inequality constraints are satisfied.

5.3.2.2 Solution of the equilibrium under constraints

For a given set of constraints assigned to different elements, we solve for the balance of momentum combined with the corresponding prescribed set of equality constraints. First, we rewrite the equilibrium in terms of effective traction, such that the discretized elasticity equations (5.13) becomes

$$\mathbf{t}^{\prime,n+1} = \mathbf{t}^{o} + \mathbf{E}_{\mathcal{H}}\mathbf{d}^{n+1} - \mathbf{p}_{coll}^{n+1}, \tag{5.18}$$

where $\mathbf{p}_{coll}^{n+1} = (0, p_1, 0, ..., 0, p_i, ...)$ is a vector containing the current pore pressure vector evaluated at the different collocation points, which acts only on the normal traction component.

In addition to these $4n_{elts}$ equations, we prescribe $4n_{elts}$ equations in relations to the type of constraint acting on each element. This results in a $8n_{elts} \times 8n_{elts}$ linear system with both the displacement discontinuities and the effective traction as unknowns.

We now list the different constraints assigned to the different set of elements.

Set of elements active in tensile failure $\mathcal{S}_{a,1}$: Pure tensile failure is active in an element when $\mathcal{F}_1(t_n^{\prime,n+1}) > 0$ and $h(t_s^{n+1}, t_n^{\prime,n+1}) < 0$ at both collocation points. We thus enforce eq. (5.7b), and the discretized equations for one collocation point of an active tensile element are

$$t_n^{\prime,n+1} = -\sigma_c(\kappa^{n+1}, \kappa_m^{n+}), \qquad \Delta d_s = 0, \tag{5.19}$$

which can be rewritten in matrix form as

$$\begin{bmatrix} 0 & 0 \\ 0 & 1 \end{bmatrix} \begin{bmatrix} t_s^{n+1} \\ t_n^{\prime,n+1} \end{bmatrix} = \begin{bmatrix} 0 \\ -\sigma_c(\kappa^{n+1}, \kappa_m^{n+1}) \end{bmatrix}, \qquad \begin{bmatrix} 1 & 0 \\ 0 & 0 \end{bmatrix} \begin{bmatrix} \Delta d_s \\ \Delta d_n \end{bmatrix} = \begin{bmatrix} 0 \\ 0 \end{bmatrix} \tag{5.20}$$

Set of elements active in shear failure $\mathcal{S}_{a,2}$ Similarly, an element for which $\mathcal{F}_2(t_s^{n+1}, t_n^{\prime,n+1}) > 0$ & $h(t_s^{n+1}, t_n^{\prime,n+1}) \geq 0$ at both collocation points, we must enforce $\mathcal{F}_2 = 0$ and the dilatant flow rule (5.5b). For one collocation point of an active shear segment, we have

$$\begin{aligned} t_s^{n+1} &= c(\kappa^{n+1}, \kappa_m^{n+1}) + f(\left|d_s^{n+1}\right|, \delta_m^{n+1}) t_n^{\prime,n+1}, \\ \Delta d_n &= \left|\Delta d_s\right| \operatorname{sign}(t_s) \tan(\psi(\left|d_s^{n+1}\right|, \delta_m^{n+1})), \end{aligned} \tag{5.21}$$

which can be rewritten in matrix form as

$$\begin{gathered} \begin{bmatrix} 1 & -f(\left|d_s^{n+1}\right|, \delta_m^{n+1}) \\ 0 & 0 \end{bmatrix} \begin{bmatrix} t_s^{n+1} \\ t_n^{\prime,n+1} \end{bmatrix} = \begin{bmatrix} c(\kappa^{n+1}, \kappa_m^{n+1}) \\ 0 \end{bmatrix}, \\ \begin{bmatrix} 0 & 0 \\ -\operatorname{sign}(t_s)\tan(\psi(\left|d_s^{n+1}\right|, \delta_m^{n+1})) & 1 \end{bmatrix} \begin{bmatrix} \Delta d_s \\ \Delta d_n \end{bmatrix} = \begin{bmatrix} 0 \\ 0 \end{bmatrix} \end{gathered} \tag{5.22}$$

Inter-penetrating segments $\mathcal{S}_{interp.}$ if the normal displacement discontinuity on one mesh node is lower than the minimum admissible value $\bar{w}_d$, then we enforce

$$d_n^{n+1} = \bar{w}_d \qquad \Delta d_s = 0 \ ,$$

which in incremental and matrix form reads

$$\begin{bmatrix} 1 & 0 \\ 0 & 1 \end{bmatrix} \begin{bmatrix} \Delta d_s \\ \Delta d_n \end{bmatrix} = \begin{bmatrix} 0 \\ \bar{w}_d - d_n^n \end{bmatrix} \tag{5.23}$$

Inactive elements $\mathcal{S}_{inact.}$ are neither at failure or violate the inter-penetrability constraint. The rate of displacement discontinuities is zero and we enforce

$$\begin{bmatrix} 1 & 0 \\ 0 & 1 \end{bmatrix} \begin{bmatrix} \Delta d_s \\ \Delta d_n \end{bmatrix} = \begin{bmatrix} 0 \\ 0 \end{bmatrix} \tag{5.24}$$

5.3.2.3 Solution of the tangent system for the trial active sets

By considering all the nodes and collocation points of a computational mesh, these different constraints depending on the active set of constraints provide a set of $4n_{segm}$ equations in addition to the elasto-static balance of momentum. We obtain the following system of $8n_{segm} \times 8n_{segm}$ equations

$$\underbrace{\begin{bmatrix} \mathbf{E}_{\mathcal{H}} & \mathbf{I} \\ \mathbf{B} & \mathbf{C} \end{bmatrix}}_{\mathbf{A}} \underbrace{\begin{bmatrix} \mathbf{\Delta d} \\ \mathbf{t}'^{,n+1} \end{bmatrix}}_{\mathbf{x}} = \underbrace{\begin{bmatrix} \mathbf{t}^o + \mathbf{E}_{\mathcal{H}} \mathbf{d}^n - \mathbf{p}_{coll}^{n+1} \\ \mathbf{a} \end{bmatrix}}_{\mathbf{y}} \tag{5.25}$$

for the unknowns increment of displacement discontinuities $\mathbf{\Delta d}$ and current effective tractions $\mathbf{t}'^{,n+1}$. In the system of equations (5.25), $\mathbf{I}$ is a $4n_{segm} \times 4n_{segm}$ identity matrix, $\mathbf{a}$ is a $4n_{segm} \times 1$ vector that contains the right hand sides of the different equality constraints previously described. The matrix $\mathbf{B}$ and $\mathbf{C}$ are sparse and contain the constraints in term of displacement discontinuities and effective traction respectively, given by the constitutive interface relations. The pattern of these block matrices depends on the different set of constraints and thus may differ between iterations of the yielding loop.

The system of equations (5.25) is non-linear when the material's strength parameters soften with currrent plastic deformations. For this reason, we adopt a fixed point iterative scheme combined with under-relaxation (Quarteroni et al. 2000*b*). Iterations are ended when subsequent estimates of both increment of displacement discontinuities and effective traction fall within a given relative tolerance ϵ_{tol}. At a given iteration of the fixed point scheme, the solution of the system (5.25) is obtained via a Krylov sub-space iterative method, specifically the generalized minimal residual method (GMRES).

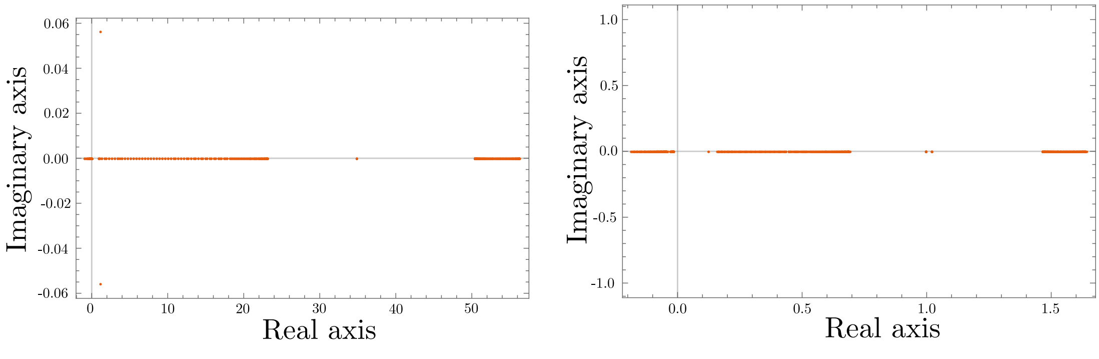

(a)

(b)

Figure 5.3 – Examples of eigenvalues distribution along the complex plane for the matrix **A** that arises from final system of equations (5.25) prior (a) and after (b) application of preconditioning matrix $\mathbf{P}_{up}$. Case of a planar fracture in an infinite domain discretized with 100 equal-sized segments with six element active in shear. The spectral radius of the original matrix **A** is $\rho(\mathbf{A}) \simeq 56.3$, while the one of the preconditioned matrix is $\rho(\mathbf{A}_p) \simeq 1.64$.

Although the sub-blocks **B** and **C** are singular sparse matrices, **A** has always full rank. Furthermore, although the final matrix **A** is sparse, it is not diagonal dominant and highly non-symmetric. Figure 5.3a displays an example of spectral properties of matrix **A** arising from the example of a a planar fracture embedded in an infinite medium discretized with 100 equal-sized elements, with 6 of them belonging to $\mathcal{S}_{a,2}$, while the others being inactive. The eigenvalues of **A** are spread over a wide range on the complex plane, both along the real and the imaginary axis (Figure 5.3a). The spectral radius for such an example is indeed $\rho(\mathbf{A}) = 56.3$, resulting in a slow convergence during GMRES iterations. In order to improve the spectral properties of matrix **A**, we develop a block preconditioner approach. Unlike preconditioners based on algebraic techniques that require little knowledge of the problem under investigation (Benzi et al. 2005), the preconditioning of system (5.25) is tailored to the pattern of matrix of coefficient **A**. Starting from the observation that if the sub-block **C** is null, which is the case when all the mesh elements are inactive, the pattern of the resulting system of equations is equivalent to the one that arise from non-symmetric saddle point problems, we adapt a preconditioner that is tailored for such class of problems (see Benzi et al. (2005), Cao (2008, 2009), Li et al. (2010) for such type of pre-conditioners). Following Benzi et al. (2005), we introduce an upper-triangular block preconditioner matrix on the right side of system (5.25) such that the latter can be rewritten as

$$\mathbf{A}\mathbf{P}_{up}^{-1}\mathbf{u} = \mathbf{y}, \qquad \mathbf{u} = \mathbf{P}_{up}\mathbf{x}, \tag{5.26}$$

where the preconditioning matrix P_{up} reads

$$\mathbf{P}_{up} = \begin{bmatrix} \mathbf{D}_{\mathbf{E}_{\mathcal{H}}} & \mathbf{I} \\ \mathbf{0} & \mathbf{S} \end{bmatrix} \tag{5.27}$$

and its inverse is given by

$$\mathbf{P}_{up}^{-1} = \begin{bmatrix} \mathbf{D}_{\mathbf{E}_{\mathcal{H}}}^{-1} & -\mathbf{D}_{\mathbf{E}_{\mathcal{H}}}^{-1}\mathbf{S}^{-1} \\ \mathbf{0} & \mathbf{S}^{-1} \end{bmatrix} \tag{5.28}$$

In equation (5.27) and (5.28), $\mathbf{D}_{\mathbf{E}_{\mathcal{H}}}$ is the diagonal of the hierarchical elasticity matrix $\mathbf{E}_{\mathcal{H}}$ and $\mathbf{S} = \mathbf{C} - \mathbf{B}\mathbf{D}_{\mathbf{E}_{\mathcal{H}}}^{-1}$ is the Schur complement with respect to $\mathbf{D}_{\mathbf{E}_{\mathcal{H}}}$. Note that if $\mathbf{D}_{\mathbf{E}_{\mathcal{H}}} = \mathbf{E}_{\mathcal{H}}$, then the spectrum of $\mathbf{A}\mathbf{P}_{up}^{-1}$ is $\rho(\mathbf{A}\mathbf{P}_{up}^{-1}) = \{1\}$ such that an iterative method like GMRES would converge in at most two iterations (Benzi et al. 2005). In practice, however, we do not want to compute the inverse of the hierarchical elasticity matrix. We consider only the inverse of the diagonal self-effect elastic contributions. It is worth mentioning that for nonsymmetric saddle point problems, this choice is commonly taken when the sub-block (1,1) is diagonal dominant, for which it is proved that a good clustering of the eigenvalues around 1, $\frac{1}{2}(1+\sqrt{5})$ and $\frac{1}{2}(1-\sqrt{5})$ is obtained (Benzi et al. 2005, Cao 2008) (although it does not prevent the preconditioned matrix from having its eigenvalues on both side of the imaginary axis). Upon application of the right upper-triangular preconditioner $\mathbf{P}_{up}^{-1}$, the system of equations (5.26) can be re-written as the following two systems:

$$\underbrace{\begin{bmatrix} \mathbf{E}_{\mathcal{H}}\mathbf{D}_{\mathbf{E}_{\mathcal{H}}}^{-1} & -\mathbf{E}_{\mathcal{H}}\mathbf{D}_{\mathbf{E}_{\mathcal{H}}}^{-1}\mathbf{S}^{-1} + \mathbf{S}^{-1} \\ \mathbf{B}\mathbf{D}_{\mathbf{E}_{\mathcal{H}}}^{-1} & -\mathbf{B}\mathbf{D}_{\mathbf{E}_{\mathcal{H}}}^{-1}\mathbf{S}^{-1} + \mathbf{C}\mathbf{S}^{-1} \end{bmatrix} \begin{bmatrix} \mathbf{u_1} \\ \mathbf{u_2} \end{bmatrix} = \begin{bmatrix} \mathbf{y_1} \\ \mathbf{y_2} \end{bmatrix}}_{\mathbf{1}}, \quad \underbrace{\begin{bmatrix} \mathbf{D}_{\mathbf{E}_{\mathcal{H}}} & \mathbf{I} \\ \mathbf{0} & \mathbf{S} \end{bmatrix} \begin{bmatrix} \mathbf{x_1} \\ \mathbf{x_2} \end{bmatrix} = \begin{bmatrix} \mathbf{u_1} \\ \mathbf{u_2} \end{bmatrix}}_{\mathbf{2}} \tag{5.29}$$

As one can notice, the exact inverse of the Schur complement is needed for numerical resolution of system 1. Although the Schur complement is a sparse matrix and fast algorithms have been developed to obtain its inverse (see Li, Ahmed, Klimeck & Darve (2008), Erisman & Tinney (1975) for examples), its inverse is typically not sparse. For large scale problems, therefore, this operation would costly memory-wise. In order to avoid computing the inverse of the Schur complement $\mathbf{S}$, we perform a change of variable

$$\mathbf{z_2} = \mathbf{S}^{-1}\mathbf{u_2}$$

such that the system 1 of equation (5.29) reduces to

$$\underbrace{\begin{bmatrix} \mathbf{E}_{\mathcal{H}}\mathbf{D}_{\mathbf{E}_{\mathcal{H}}}^{-1} & -\mathbf{E}_{\mathcal{H}}\mathbf{D}_{\mathbf{E}_{\mathcal{H}}}^{-1} + \mathbf{I} \\ \mathbf{B}\mathbf{D}_{\mathbf{E}_{\mathcal{H}}}^{-1} & -\mathbf{B}\mathbf{D}_{\mathbf{E}_{\mathcal{H}}}^{-1} + \mathbf{C} \end{bmatrix}}_{\mathbf{A}_p} \begin{bmatrix} \mathbf{u_1} \\ \mathbf{z_2} \end{bmatrix} = \begin{bmatrix} \mathbf{y_1} \\ \mathbf{y_2} \end{bmatrix}, \tag{5.30}$$

where $\mathbf{A}_p$ denotes the preconditioned matrix of coefficients. In order to highlight the effect of the preconditioner $\mathbf{P}_{up}$, we show in Figure 5.3b the spectral properties of the preconditioned matrix $\mathbf{A}_p$ that arises from the same example previously described. The improvement is clear. The eigenvalues of the pre-conditioned matrix are spread over a much more narrow range (see Figure 5.3) and more importantly all the eigenvalues are real. The spectral radius in this particular example is $\rho(\mathbf{A}_p) \sim 1.64$, roughly 3% of the one of the initial system $\mathbf{A}$. The preconditioned system of equations (5.30) is solved via GMRES iterative method for the unknown vectors $\mathbf{u_1}$ and $\mathbf{z_2}$. Once the iterative solution converges within a given tolerance, the solution of the preconditioned mechanical problem (5.26) can be simply obtained by performing the proper matrix-vector multiplications, i.e.

$$\mathbf{t}^{\mathbf{\prime,n+1}} = \mathbf{x_2} = \mathbf{z_2}, \qquad \Delta\mathbf{d} = \mathbf{x_1} = \mathbf{D}^{-1}_{\mathbf{E}_{\mathcal{H}}}(\mathbf{u_1} - \mathbf{z_2}) \tag{5.31}$$

Note that the numerical solution of the preconditioned system (5.26) via a GMRES iterative scheme does never involve any matrix inversions, but only matrix-vector products.

The non-linear mechanical problem (5.25) converges when the relative difference between two subsequent estimates of both increment of displacement discontinuities and effective tractions fall below a given tolerance (typically $10^{-6} - 10^{-8}$). The algorithm then moves back to the yielding loop to recheck the inequalities constraints.

5.4 Illustrative examples

5.4.1 A branched frictional fault system

As first example, we present the case of a branched frictional fault system embedded in an infinite domain and subjected to a remote static compressive load (see Figure 5.4 in which all material and geometrical parameters are reported). The remote load translates into applied tractions along the branched fault that are such to overcome its frictional strength and hence activate a shear crack in both branches of the system due to elastic interactions. In this example, the frictional properties are constant (no softening), cohesion as well as shear-induced dilatancy are neglected ($c = 0$, $\tan\psi_p = 0$).

No analytical solution exists for this problem. We thus compare our results with previously reported numerical results for this same problem - see Maerten et al. (2010) who also compare their solutions with the one of Cooke & Pollard (1997). We discretize the branched fault system with $2\,10^4$ equal-sized straight segments (notably $1.2\,10^4$ elements for the main branch of length $4a$ and $0.8\,10^4$ segments for the secondary branch of length $2a$) for a total of $1.6\,10^5$ degrees of freedom (tractions and displacement discontinuities). Using $\eta = 3$, $\epsilon_{ACA} = 10^{-6}$, and $n_{leaf} = 10^3$, we obtain a compression ratio of $c_r(\mathbf{E}_{\mathcal{H}}) = 0.057$ for the hierarchical matrix representation of the elastic system. This allows to solve this

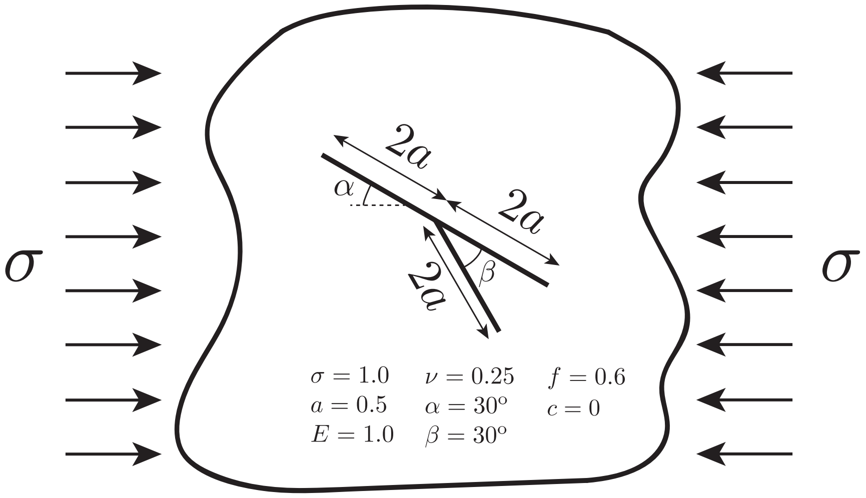

Figure 5.4 – Sketch of branched frictional fault system subjected to a remote compressive load. All the material and geometrical parameters are reported in the figure.

problem on laptop using less than 3GB of RAM. It would have been impossible using the fully populated elastic matrix which requires $\sim$ 51GB of memory storage in double precision.

The comparison of our numerical results with the one reported by Maerten et al. (2010) are displayed in Figure 5.5. A good match between our numerical results and the ones of Maerten et al. (2010) is obtained, both in terms of slip and tractions distributions. The position of the shear crack tip on the secondary branch is accurately captured, denoting thus that the algorithm devised works correctly for the frictional deformation.

5.4.2 Tensile wellbore failure

We now switch to an example associated with pure tensile failure and mode I cohesive crack initiation and growth from a wellbore located in a infinite domain (see Figure 5.6). We consider the case of an increase of the wellbore pressure, while the far-field in-situ stress remains constant. The material properties (large cohesion, finite tensile strength) as well as the in-situ stress field are taken to favor pure tensile failure. Upon increase of the wellbore pressure ($t_n(r = R) = p_b(t), \quad t_s(r = R) = 0$), a tensile fracture initiates and propagates symmetrically with respect to the centre of the wellbore along the direction of the maximum principal in-situ stress (here σ_{xx}). The “Kirsch” elastic solution (Kirsch

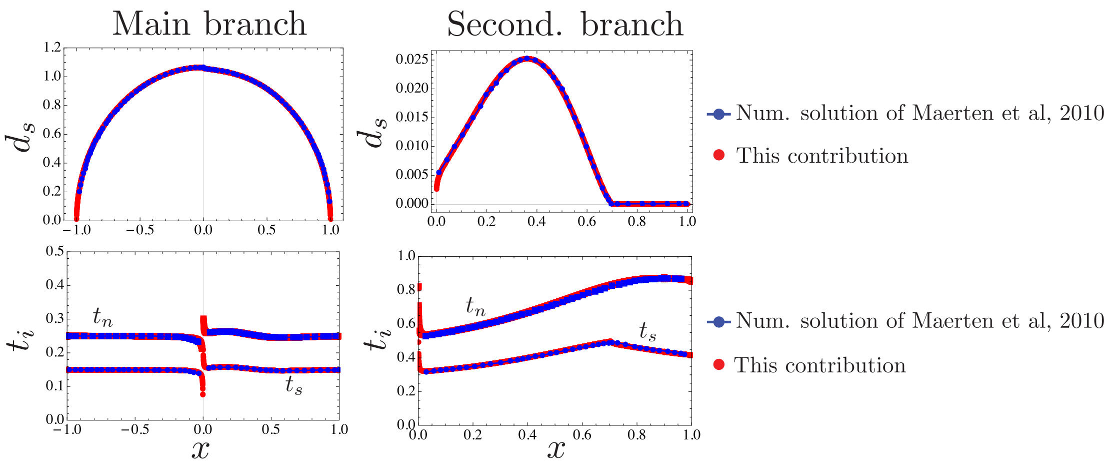

Figure 5.5 – Comparison between the numerical results obtained with the developed solver and the ones of Maerten et al. (2010) in terms of slip and tractions distribution along the main fault branch (left panel) of length $4a$ and along the secondary branch of length $2a$ (right panel).

1898)

$$\begin{aligned}
\sigma_{rr} &= \left(\frac{R^2}{r^2}p_b\right) + \left(P_\infty\left(1-\frac{R^2}{r^2}\right)\right) + \left(S_\infty\left(1-4\frac{R^2}{r^2}+3\frac{R^4}{r^4}\right)\mathrm{Cos}(2\theta)\right)\\
\sigma_{\theta\theta} &= \left(-\frac{R^2}{r^2}p_b\right) + \left(P_\infty\left(1+\frac{R^2}{r^2}\right)\right) - \left(S_\infty\left(1+3\frac{R^4}{r^4}\right)\mathrm{Cos}(2\theta)\right) \qquad (5.32)\\
\sigma_{r\theta} &= S_\infty\left(1-3\frac{R^4}{r^4}+2\frac{R^2}{r^2}\right)\mathrm{Sin}(2\theta),
\end{aligned}$$

with $P_\infty = \dfrac{\sigma_{xx}+\sigma_{yy}}{2}$ and $S_\infty = \dfrac{\sigma_{xx}-\sigma_{yy}}{2}$, allows to estimate the wellbore pressure $p_{b,\text{strength}} = \sigma_c - \sigma_{xx} + 3\sigma_{yy}$ at which the hoop stress $\sigma_{\theta\theta}$ around the wellbore reaches the material tensile strength σ_c as well as its location (here at $\theta = 0$ for the given deviatoric far-field stress and $p_{b,\text{strength}} = 0.5$ for the parameters of Figure 5.6).

Due to the softening of the tensile strength, this problem exhibit a size effect on the pressure and corresponding crack length at which the crack completely nucleates. Specifically, the crack initiation pressure of the borehole is defined as the borehole pressure at which all the fracture energy has been released (or similarly at which the opening at the borehole wall equals the critical opening κ_c at which cohesive forces vanishes).This initiation pressure is larger than $p_{b,\text{strength}}$ predicted from a strength criteria (Lecampion 2012, Leguillon et al. 2007). The size effect is governed by the Irwin number defined as the ratio $\mathcal{I}$ between the material length scale $l_m = \dfrac{G_c E_p}{\sigma_c^2}$ (with $G_c = \dfrac{\sigma_{c,p}\kappa_c}{2}$ the critical fracture energy) and the structural length scale - here the wellbore radius $l_s = R$. For that particular configuration large values of $\mathcal{I}$ corresponds to cases where fracture energy requirement govern crack nucleation, while strength dominated failure for low value of $\mathcal{I}$.

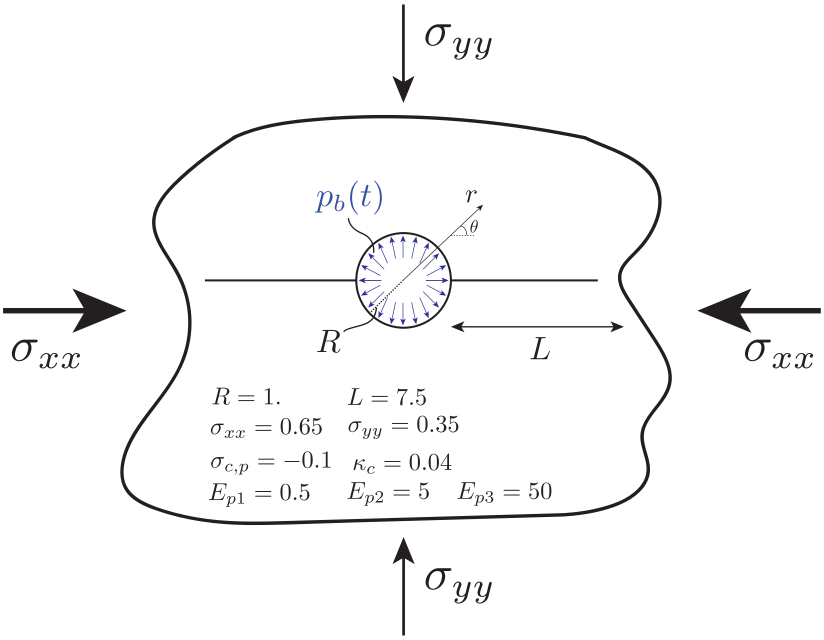
σ_{yy}
$p_b(t)$
r
θ
σ_{xx}
σ_{xx}
R
L
$R = 1.$ $L = 7.5$
$\sigma_{xx} = 0.65$ $\sigma_{yy} = 0.35$
$\sigma_{c,p} = -0.1$ $\kappa_c = 0.04$
$E_{p1} = 0.5$ $E_{p2} = 5$ $E_{p3} = 50$
σ_{yy}

Figure 5.6 – Sketch of plane strain pressurized wellbore & far field loading conditions. The elasticity matrix is compressed using : $\eta = 5$, $\epsilon_{ACA} = 10^{-6}$, $n_{leaf} = 32$ resulting in a compression ratio $c_r = 0.113$.

$\mathcal{I}$	0.1	1	10
$p_b/p_{b,\text{strength}}$	1.052	1.448	2.906
$p_b/p_{b,\text{strength}}$ from Lecampion (2012)	~ 1.1	~ 1.45	~ 2.9

Table 5.1 – Comparison of the normalized crack initiation pressure obtained here and the ones of Lecampion (2012) for different Irwin numbers $\mathcal{I}$.

We perform three different simulations, varying the plane strain Young modulus E_p to cover three distinct values of the Irwin number ($\mathcal{I}_1 = 0.1$, $\mathcal{I}_2 = 1$ and $\mathcal{I}_3 = 10$) while keeping the other parameters constant (see Figure 5.6). In addition to the wellbore boundary, we mesh a potential horizontal line where the crack can nucleate with 924 equal-sized straight elements. Table 5.1 compares our numerical results to the ones reported in Lecampion (2012) for the scaled crack initiation pressure for different value of $\mathcal{I}$. The results are similar within 5% relative difference.

Figure 5.7 displays the spatial profile of normalized opening displacement discontinuities (top-left), normal traction (top-right) and normal traction t_n (bottom) along $\theta = 0$, for increasing values of the normalized borehole pressure $p_b/\sigma_{c,p}$. For low values of $p_b/\sigma_{c,p}$ ($p_b/\sigma_{c,p} < 5$ here), the response is elastic: the spatial profile of the normal traction matches perfectly the Kirsch elastic analytical solution (see the light grey line in Figure 5.7 top-right for $p_b/\sigma_{c,p} = 0.5$). The corresponding normal plastic deformations along the

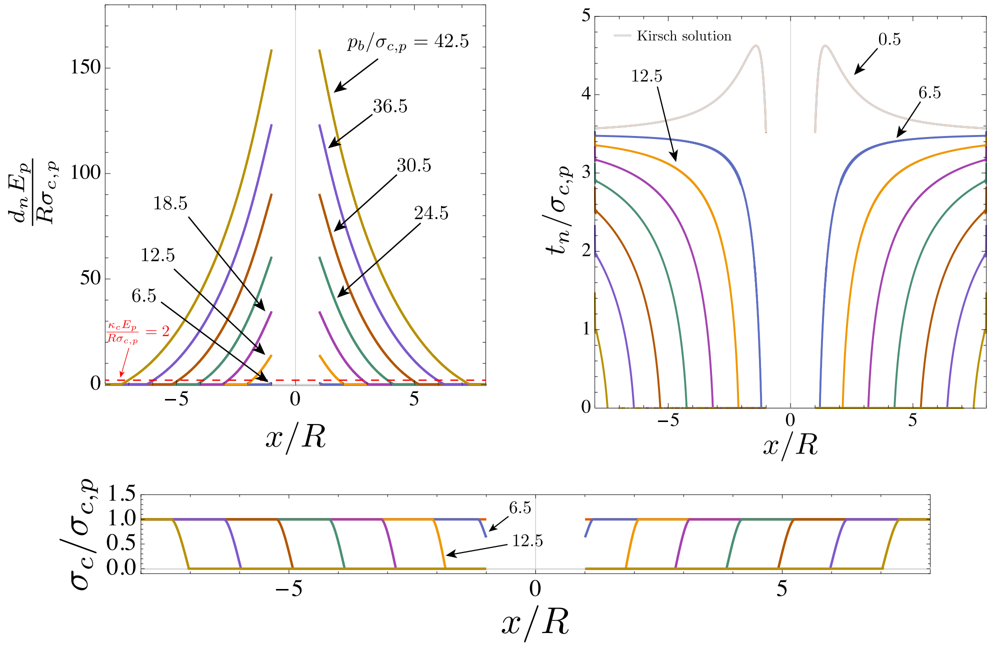

Figure 5.7 – Spatial profiles of normalized opening displacement discontinuity $\frac{d_n E_p}{R\sigma_{c,p}}$ (top-left), normal traction $t_n/\sigma_{c,p}$ (top-right) and tensile strength $\sigma_c/\sigma_{c,p}$ (bottom) along the horizontal direction (i.e. $\theta = 0$), at different normalized wellbore pressure $p_b/\sigma_{c,p}$ - $\mathcal{I}_2 = 1$ case. The light grey lines represent the Kirsch analytical solution valid in the elastic range (prior to crack nucleation).

horizontal direction are null and the tensile stress σ_c is at its maximum value $\sigma_{c,p}$ (see Figure 5.7 top-left and bottom). These observations can also be grasped from Figure 5.8 - case $\mathcal{I}_2 = 1$, in which the normalized borehole pressure is plotted against the normalized crack length and normalized opening displacement discontinuity at wellbore wall (and $\theta = 0$). Consistently with the results reported in Figure 5.7, we can observe that when the borehole pressure is lower than its activation value obtained from strength criterion, both the normal plastic deformation at wellbore wall and crack length are null.

When the borehole pressure reaches the value given by the strength criterion (here $p_b/\sigma_{c,p} = 5$) , a crack starts to propagate symmetrically, and reduction of the normal tractions associated with softening can be observed in a cohesive zone near the crack tips (see Figure 5.7). For increasing values of $p_b/\sigma_{c,p}$, the normalized opening at $r = R$ and $\theta = 0$ increases non-linearly with borehole pressure, while the corresponding normalized crack length follows a linear increase with pressurization (see Figure 5.8). It is worth mentioning, that for some values of the far-field stress and Irwin number, total 'plastic' collapse can occur under load control (Lecampion 2012).

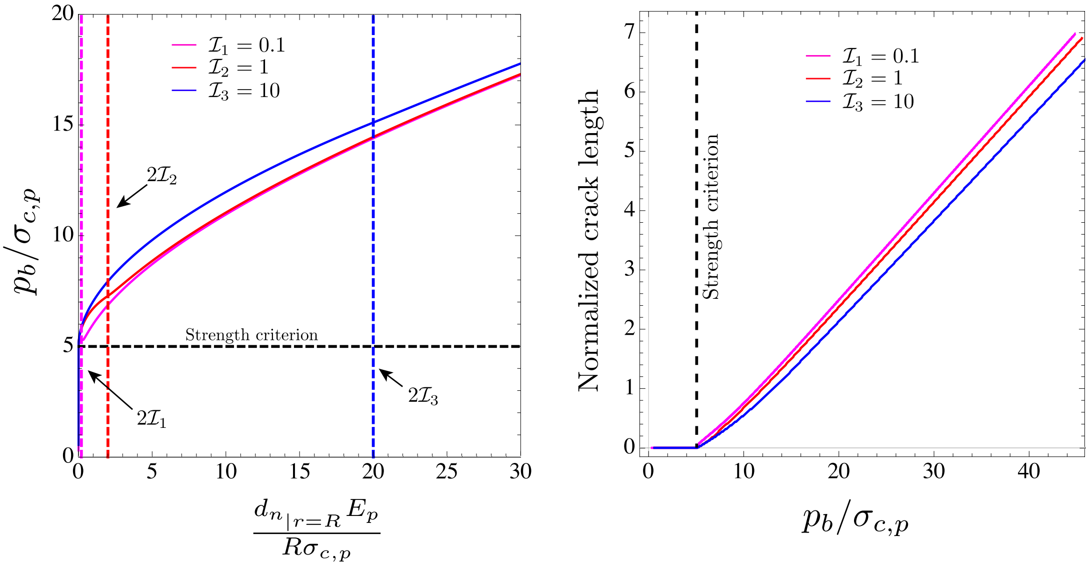

Figure 5.8 – Left: evolution of normalized opening displacement discontinuity at the wellbore $\frac{d_{n_{r=R}}E_p}{R\sigma_{c,p}}$ along the horizontal direction (i.e. $\theta = 0$), as function of normalized borehole pressurization $p_b/\sigma_{c,p}$, for different values of Irwin number $\mathcal{I}$. The dashed horizontal black line represents the theoretical value of normalized borehole pressure estimated from a pure strength criterion. Right: Normalized crack length as function of the normalized wellbore pressure for different Irwin number $\mathcal{I}$.

5.4.3 Shear-banding in uniaxial compression

The examples presented so far involved an infinite medium. However, the numerical scheme devised allows to readily investigate problems with finite domains. Effective tractions or displacement discontinuities can be easily imposed through the matrices **B** and **C** in system (5.25). We discuss now the case of a rectangular bar under plane strain conditions subjected to uni-axial compression (see Figure 5.9 for all geometrical and material parameters).

Our aim is to illustrate how by introducing a numbers of segments where localized deformation can possibly takes place, the final response of the material is akin to the one obtained with a conventional elasto-plastic approach. As a result, the mesh depicted in Figure 5.9 should not be confused with a finite element mesh as we use a boundary element method to solve for the balance of momentum. Indeed, the segments located inside the bar are solely here to capture localized inelastic deformation. For value of the uniaxial load below the yield stress, all the displacement discontinuities of the element inside the domain are zero and the elastic response is captured by the elements discretized the material boundary. The yield properties of all segments are taken to correspond to a purely cohesive material (zero friction and infinite tensile strength) - which translates in a Tresca material globally. We first investigate the case of perfect plasticity without

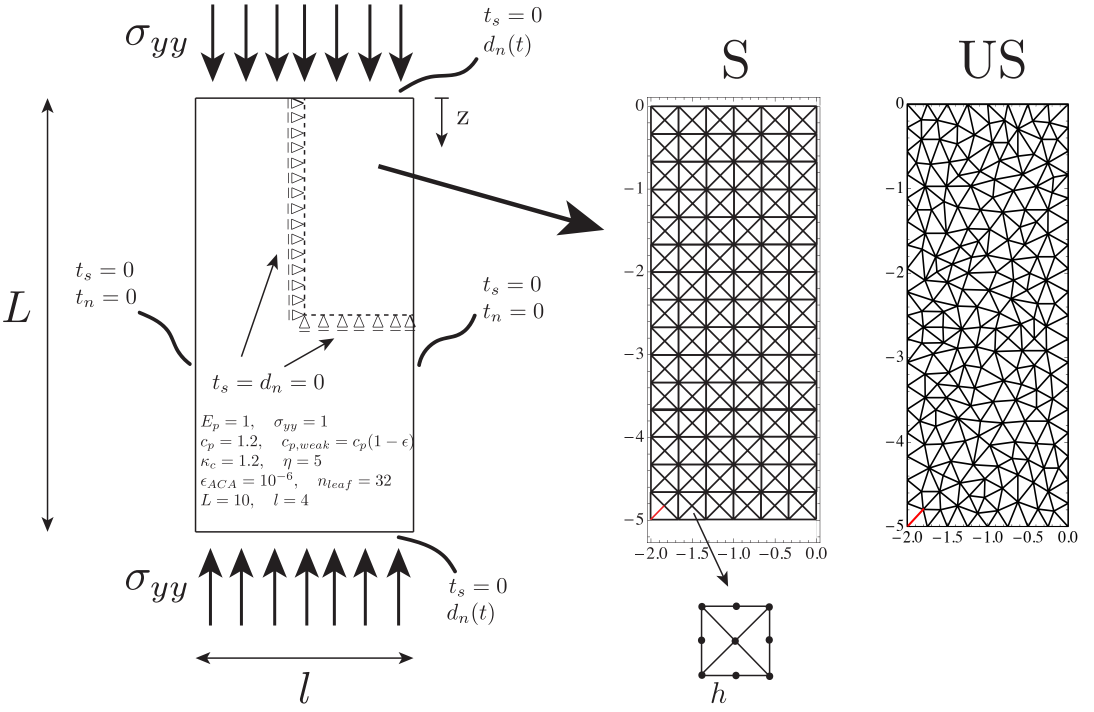

Figure 5.9 – A rectangular bar subjected to uni-axial compression. Only one quarter of the bar is modelled due to symmetry. A set of structured (S) or unstructured (US) potential segments of failures are tested to investigate the corresponding mesh dependency. A defect (segment with lower strength) is introduced near the bottom-left corner (red segment).

softening, and then discuss the effect of softening.

In absence of softening, the elasto-plastic response for such a configuration yields homogeneous plastic deformation in the case of a “defect” free homogeneous material. A elastic perfectly plastic solid with smooth yield surface is indeed quite resistant to localization of deformation into a shear band (Rudnicki & Rice 1975, Rice 1976). However, small heterogeneities in strength typically results in localization of deformation into shear bands. This is notably the case when a "defect" is introduced in the middle of the bar - see Tvergaard et al. (1981), Ortiz et al. (1987), Belytschko et al. (1988), Armero & Garikipati (1996) for discussion of the uni-axial tension case.

In order to investigate the mesh dependency and the intrinsic limits/advantages of our method, we solve the problem using two computational boundary element meshes (see Figure 5.9-right): i) a structured mesh (S), for which the potential failure segments for plasticity localization follow a specific geometrical pattern which includes the preferential 45° direction for a Tresca material, and ii) an un-structured mesh (US) whose potential failure segments are randomly oriented in the problem domain. We introduce a defect at the bottom-left corner of the bar by reducing the frictional strength of the extreme bottom-left segment such that (see red segment in Figure 5.9-right)

$$c_{p,weak} = c_p(1 - \epsilon),$$

where ϵ is a dimensionless parameter that quantify the intensity of the defect. The uniform compression within the bar is increased by prescribing increasing the normal displacement discontinuities of the top surface.

The plot in the centre of Figure 5.10 displays the load-displacement curves for both structured (S) and unstructured (US) mesh for different intensity values of in-homogeneity ϵ, without any softening of cohesion. Although the material response is qualitatively the same regardless the type of mesh and the intensity of the defect, the level of compression at which a shear band is nucleated is not mesh independent.

Referring to the case of structured mesh with $\epsilon = 0.05$, the load-displacement (using the normalized displacement at the top of the bar $\frac{\left|d_{n_{|z=0}}\right| E_p}{Lc_p}$) response of the material for compression values lower than ~ 1.05 is perfectly linear-elastic. For increasing values of compression, shear plastic deformations first take place near the inhomogeneity, up to a given value of compression after which a main shear band is triggered, from the bottom-left corner to the right side of the bar with an inclination of 45° with respect to the minimum principal direction. At this specific value of compression, a small increase of compressive normal stress leads to a large increment of inelastic deformations. Localized shearing along a favourably oriented plane occur and the intensity of slip accumulated increases significantly (see the snapshots for $\frac{\left|d_{n_{|z=0}}\right| E_p}{Lc_p} = 1.5/2.016$ in the bottom-right of Figure 5.10). Because of the structured mesh adopted (that embeds the theoretical failure line of the shear band) and the low value of inhomogeneity used in this example, the nucleation of the shear band occurs at a compression value that is slightly below the theoretical value of $2c$ that one would get if an homogeneous bar with only a pre-meshed slip line at 45° is considered (see horizontal dashed black line in Figure 5.10-plot in the centre). This picture, however, changes for defects with larger intensities (i.e. larger ϵ) or when an unstructured mesh is used. In the former case, larger stress concentrations near the bottom-left corner of the bar promote the nucleation of a shear band at lower values of compressive stress (as expected - see plot in the centre of Figure 5.10), whereas the material response in the case of the unstructured mesh is clearly stiffer (compared to the one of the structured mesh, for the same value of inhomogeneity - see the green curve in the centre plot of Figure 5.10), leading to a shear band nucleation at larger values of compression. This latter scenario is the result of a mesh dependency that kicks in when the pre-existing potential failure segments are not exactly aligned along the actual theoretical failure plane.

For specific problems that involve shear band localization along known failure planes,

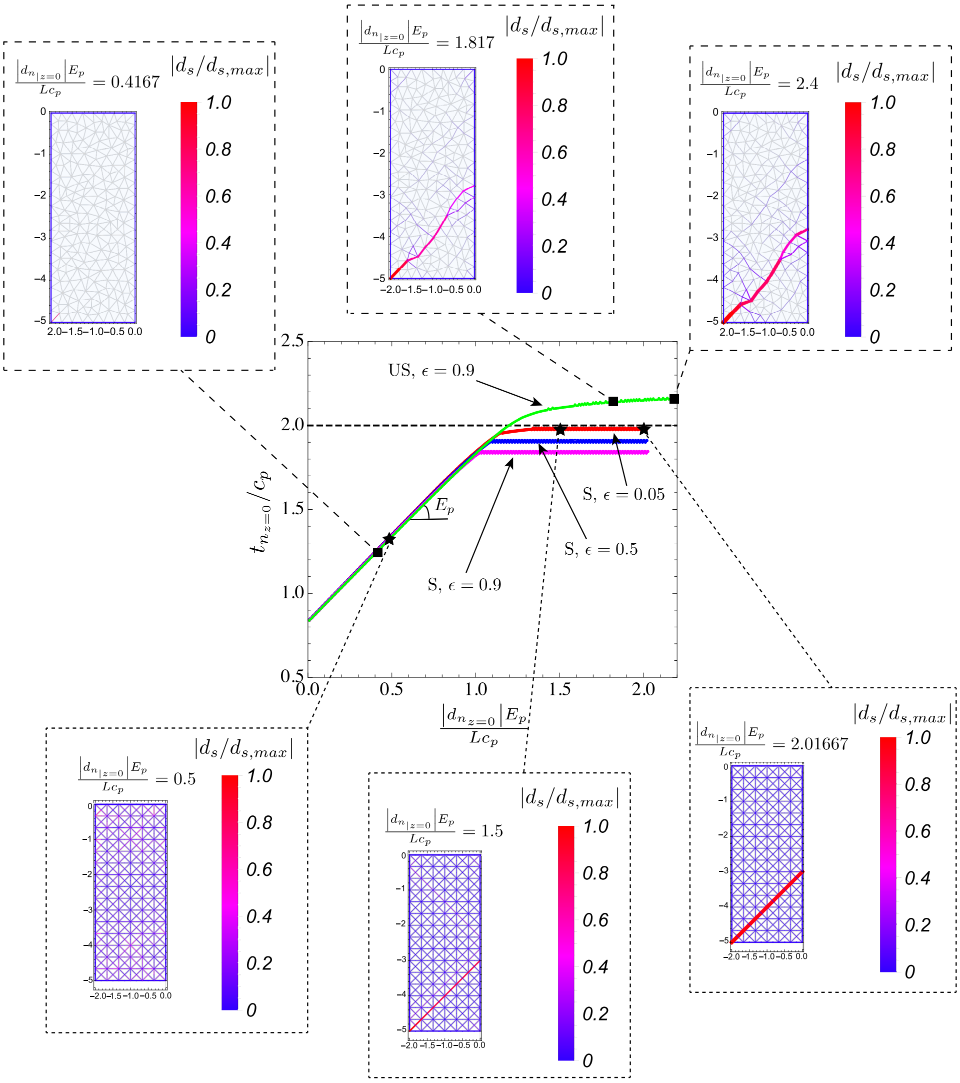

Figure 5.10 – Load-displacement curves for both structured (S) and unstructured (US) mesh, for different intensity values of in-homogeneity ϵ (center plot). The horizontal dashed black line represents the (normalized) traction value at $z = 0$ for plasticity nucleation that one would get if an homogeneous bar with only a pre-meshed slip line at 45° is considered (from the bottom-left corner of the bar to the tractions free lateral side). Evolution of normalized plastic shear deformations $|d_s/d_{s,max}|$ along pre-existing potential failure segments (structured and unstructured mesh) is displayed at different moment along the stress-strain curve. The color and the thickness of each pre-existing segment is proportional to the corresponding shear displacement discontinuity accumulated.

the numerical solver introduced in Section 5.3 is mesh independent upon meshing the a-priori known failure plane(s) with potential failing segments. More interestingly, the introduction of softening (which typically strongly re-inforce mesh dependency when using bulk elasto-plasticity) does not alter this conclusion as long as the softening material

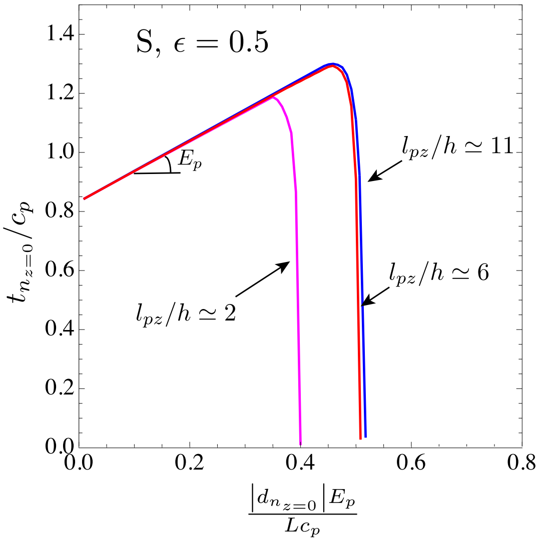

Figure 5.11 – Softening case - Load-displacement curves for a bar subjected to uni-axial compression, discretized with a structured mesh (S) with an initial defect of intensity $\epsilon = 0.5$. Effect of the mesh size h as function with respect to the softening material length scale $l_{pz} = \dfrac{E_p \kappa_c}{c_p}$.

length scale $l_{pz} = \dfrac{E_p \kappa_c}{c_p}$ is properly captured numerically. This is clearly seen in Figure 5.11, where the load-displacement curve for the structured mesh with an inhomogeneity of $\epsilon = 0.5$ is reported for different ratio of l_{pz}/h being h the element size. For a number of elements within l_{pz} larger than ~ 5, the load-displacement curves are similar both in the linear elastic and in the softening plastic range.

5.4.4 Active Earth pressure against a rigid retaining wall

As another example of interior problem, we present the case of a retaining wall under plain strain conditions, subjected to active Earth pressure (see sketch in Figure 5.12-top). We assume that the retaining wall is rigid and perfectly smooth (zero friction between the soil and the wall). We assume a purely frictional material with zero cohesion. At initial conditions, the stress state is given by two compressive principal stresses: the vertical stress $\gamma |z|$ due to the soil weight and the horizontal stress $K_o \gamma |z|$ due to the lateral confinement with $K_o = (1 - \sin(\phi))$ the coefficient of Earth pressure at rest and $\phi = \arctan(f)$ the internal friction angle of the material. The limit active state is reached by reducing the horizontal principal stresses, while keeping the vertical stress constant, until their ratio equals the active Earth pressure coefficient K_a (obtained from Rankine theory (Terzaghi 1943))

$$K_a = \tfrac{1-\sin(\phi)}{1+\sin(\phi)} = \tan^2\left(\tfrac{\pi}{4} - \tfrac{\phi}{2}\right)$$

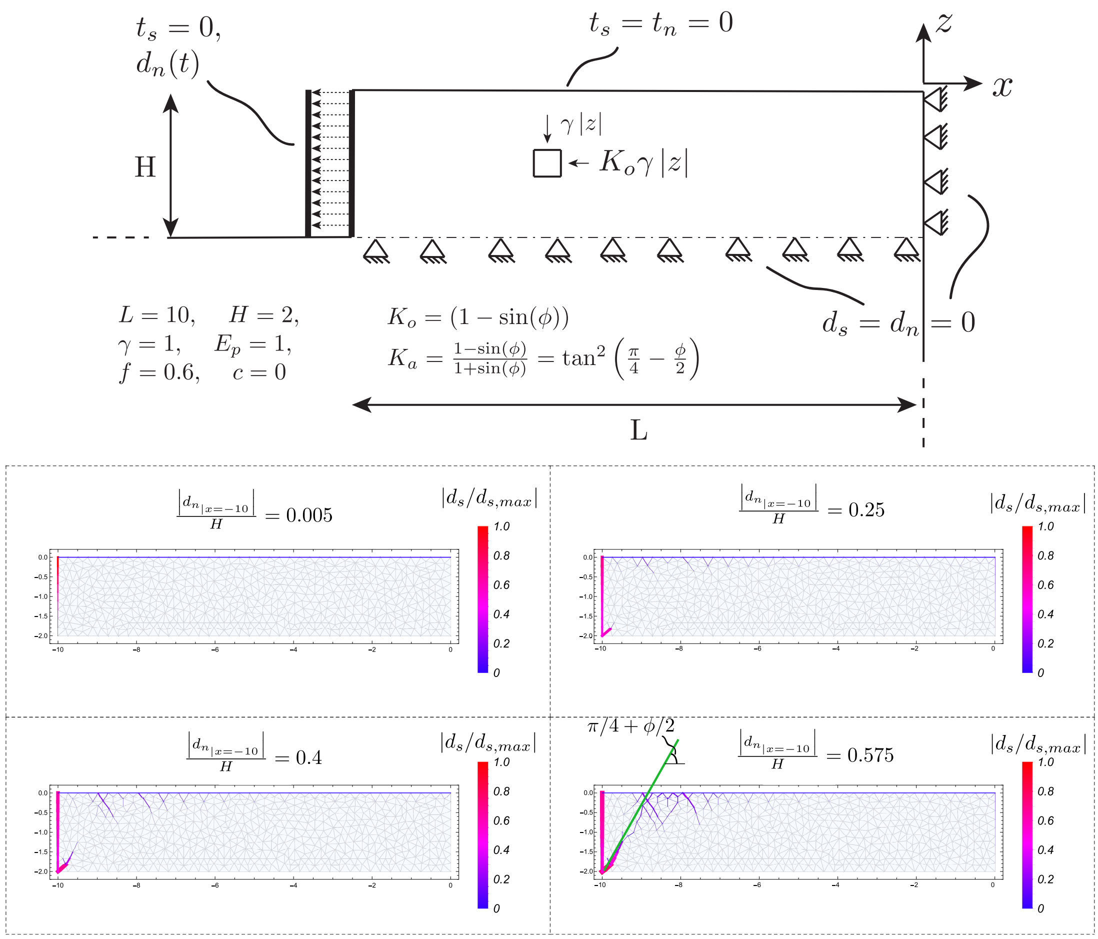
$t_s = 0,$
$d_n(t)$
$t_s = t_n = 0$
z
x
H
$\gamma\,|z|$
$K_o \gamma\,|z|$
$L = 10, \quad H = 2,$
$\gamma = 1, \quad E_p = 1,$
$f = 0.6, \quad c = 0$
$K_o = (1 - \sin(\phi))$
$K_a = \frac{1-\sin(\phi)}{1+\sin(\phi)} = \tan^2\left(\frac{\pi}{4} - \frac{\phi}{2}\right)$
$d_s = d_n = 0$
L
$\frac{|d_{n_{|x=-10}}|}{H} = 0.005$
$\frac{|d_{n_{|x=-10}}|}{H} = 0.25$
$\frac{|d_{n_{|x=-10}}|}{H} = 0.4$
$\frac{|d_{n_{|x=-10}}|}{H} = 0.575$
$|d_s/d_{s,max}|$
1.0
0.8
0.6
0.4
0.2
0
$\pi/4 + \phi/2$
0.0
−0.5
−1.0
−1.5
−2.0
−10
−8
−6
−4
−2
0

Figure 5.12 – Top: sketch of a retaining wall & boundary conditions adopted. Bottom: evolution of normalized plastic shear deformations $|d_s/d_{s,max}|$ along the pre-existing potential failure segments (unstructured mesh) as a function of normalized translation of the rigid wall $\left|d_{n_{|x=-10}}\right|/H$.

Numerically, this is obtained by translating the rigid wall along the horizontal direction by prescribing a constant normal displacement discontinuities along the wall while imposing zero shear stress at the wall (see Figure 5.12-top for geometry, input data and boundary conditions of the problem).

Figure 5.12-bottom displays the evolution of cumulative plastic shear deformations within the soil as function of the normalized lateral displacement of the wall, until the active state is reached. The progressive decrease of lateral confinement associated with the translation of the wall leads to progressive plastic failure that starts to develop from the bottom-left corner, where the stress concentration is higher, and moves up to the traction free surface. Although the progressive failure path is not straight due to the unstructured mesh of potential failing segments used, its approximate angle with respect to the minimum principal direction during active limit state is very close to the theoretical value from

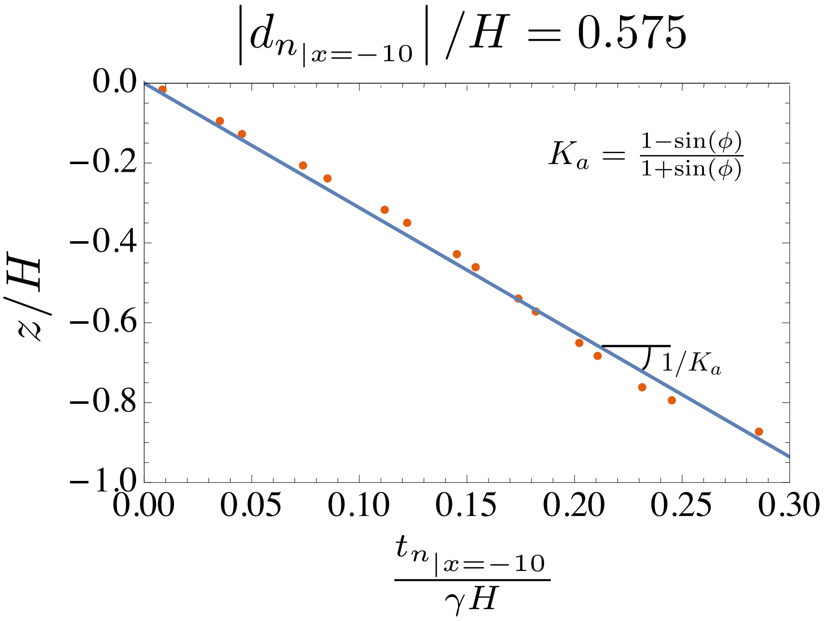

Figure 5.13 – Vertical profile of normalized horizontal stress distribution along the retaining wall (i.e. at $x = -10$) in corresponding of an active limit state. The blue solid line corresponds to the theoretical solution from Rankine theory $\left(K_a = \dfrac{1-\sin(\phi)}{1+\sin(\phi)}\right)$.

Rankine theory $\pi/4 + \phi/2$ (see Figure 5.12-bottom). The horizontal stress distribution along the wall is also following the theoretical prediction $\sigma_{xx} = K_a \sigma_{zz} = K_a(\gamma|z|)$ (see Figure 5.13).

5.4.5 Fluid injection into a frictional weakening planar fault

The numerical solver described in Section 5.3 is capable of solving one-way coupled hydro-mechanical problems, where the pore-pressure history is obtained from a flow solver. As an illustrative example, we investigate the case of fluid injection into a frictional weakening planar fault in an infinite and impermeable medium. The fault is subjected to an initial uniform effective stress state with normal and tangential component denoted respectively as σ'_o and τ_o. In this example, the fault is characterized by a constant longitudinal permeability k_f. The friction coefficient f of the fault is supposed to soften linearly with shear slip from a peak value f_p, up to a residual value f_r at large deformations. Fluid is injected at a point under constant over-pressure ΔP (above the initial pore pressure p_o) with the purpose of activating slip upon local violation of the shear weakening Mohr-Coulomb yielding criterion (no cohesion $c = 0$). This specific problem has been solved by Garagash & Germanovich (2012) semi-analytically. In order to test the accuracy of our numerical solver with a time-dependent, one-way coupled and non-linear hydro-mechanical problem, we discretize the fault plane with 10^3 equally-sized straight segments.

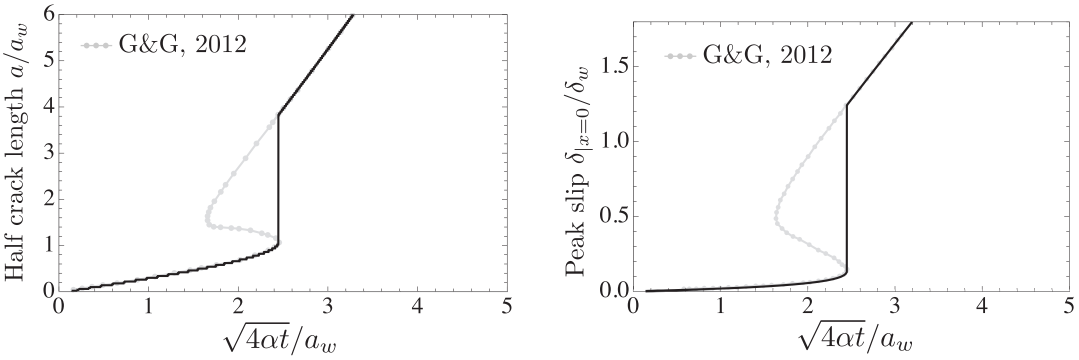

Figure 5.14 – Time evolution of the normalized half-crack length a/a_w (left) and normalized peak slip δ/δ_w at the middle of the fault (right), i.e. at $x = 0$, for an ultimately stable fault ($\tau_o/\tau_p = 0.55$), subjected to a moderate over-pressure $\Delta P/\sigma_o' = 0.5$. a_w and δ_w are the characteristic patch length and slip weakening scale, respectively (see Garagash & Germanovich (2012) for details). The friction weakening ratio considered is taken here as $f_r/f_p = 0.6$.

We vary the compression of the fully populated elasticity matrix by using four values of $\eta = 0, 0.1, 0.5, 1$, obtaining respectively compression ratios of $c_r = 0, 0.249, 0.08$ and 0.06 (for $\epsilon_{ACA} = 0.1$ and $n_{leaf} = 16$). Furthermore, we ensure that all the simulations follow the exact same time-steps evolution so as to calculate a relative difference at each time step with the results obtained without using a hierarchical matrix approximation ($\eta = 0$ that we take as reference numerical solution).

Figure 5.14 displays the time evolution of normalized half-crack length (left) and the peak slip accumulated at the middle of the fault (right), for the case of a marginally pressurized fault $\tau_o/\tau_p = 0.55$ where $\tau_p = f_p(\sigma_o - p_o) = f_p\sigma_o'$ is the peak shear strength of the fault at ambient conditions, moderate injection overpressure $\Delta P/\sigma_o' = 0.5$ and the coarser hierarchical approximation of the elasticity matrix $\eta = 1$. The numerical results are in very good agreement with the ones of Garagash & Germanovich (2012), both for the evolution of the shear crack length as well as the peak slip at $x = 0$. The aseismic crack propagation is followed by the nucleation of a dynamic rupture and an arrest related to the shear crack catching up the fluid front (see Garagash & Germanovich (2012) for discussion). This non-trivial evolution is well captured by our numerical solver. In table 5.2, we report the maximum relative difference in terms for the half crack length and peak slip at $x = 0$ obtained during their time evolution (taking the numerical results for the non-approximated elasticity matrix as a reference). Even for large compression, the relative error never exceeds 1.5%, showing a good accuracy and a significant computational gain. For a GMRES tolerance equal to 10^{-12}, the comparison of total CPU times (scaled by the total CPU time for the uncompressed case $\eta = 0$), shows that the use of a hierarchical matrix approximation leads to nearly a ~ 7 fold speed up with respect to the uncompressed case. These results have been obtained using a C++ implementation of the numerical solver, running on a computer with Intel(R) Xeon(R)

	$\eta = 0.1$	$\eta = 0.5$	$\eta = 1$
Compression ratio c_r	0.249	0.08	0.06
Scaled total CPU time	0.796	0.395	0.151
Max. rel. difference on half crack length	$1.035\,10^{-3}$	$6.747\,10^{-3}$	$1.537\,10^{-2}$
Max. rel. difference on peak slip	$6.35\,10^{-7}$	$7.42\,10^{-4}$	$1.486\,10^{-3}$

Table 5.2 – Scaled total CPU time and the maximum relative difference obtained during the simulation for different values of η for the hierarchical approximation. The reference numerical solution corresponds to the $\eta = 0$ case (no compression of the elasticity matrix).

CPU E5-2687W v3 @ 3.10 GHz.

5.5 Conclusions

We have presented a new boundary element based formulation for inelastic localized deformation along potential pre-existing failure planes. The Mohr-Coulomb criteria combined with a tensile cut-off and the linear softening laws used here can easily be replaced by more refined constitutive models if necessary. The efficiency of the numerical scheme devised rely on the use of i) a hierarchical approximation of the elastic influence matrix and ii) a block pre-conditioner specifically developed here. The proposed computational method shares similarities with the intrinsic cohesive zone element approach used in the FEM context where cohesive elements are activated upon yielding at the interfaces between finite elements (Pandolfi & Ortiz 2002, Zhou & Molinari 2004, Zhou et al. 2005). However, the use of a boundary element method allows to decouple the discretization of the failure plane and the rest of the medium (whose elasticity is built-in BEM). This is particularly attractive for problems in infinite domain as well as cases where deformation is strongly localized into a finite number of shear bands or cracks. The approach is also advantageous when fluid flow and mechanical deformation are coupled such as for hydraulic fracturing problems (Lecampion et al. 2018). The different examples reported demonstrate the versatility of the approach in dealing with various problems exhibiting localized plastic deformation as well as crack growth. Unlike others existing BEM or FEM formulations for inelastic problems based on bulk plasticity with softening, this numerical scheme does not show mesh dependency as long as the softening length-scale is properly resolved and -more importantly- that the true plane of localized deformations are discretized (in other words known a-priori). This last point can be fixed by modifying/refining the discretization of the initial DD segments in an adaptive manner according to a measure of inelastic deformation (e.g. shear dissipation) averaged in the bulk. Another possible extension of the proposed algorithm is to move to an approach where new DD elements are added in the proper direction to capture the plane of localized deformation as it progresses. Such an algorithm would require to search iteratively for direction of failure advancement ahead of the shear-bands/cracks using a similar yielding criteria.

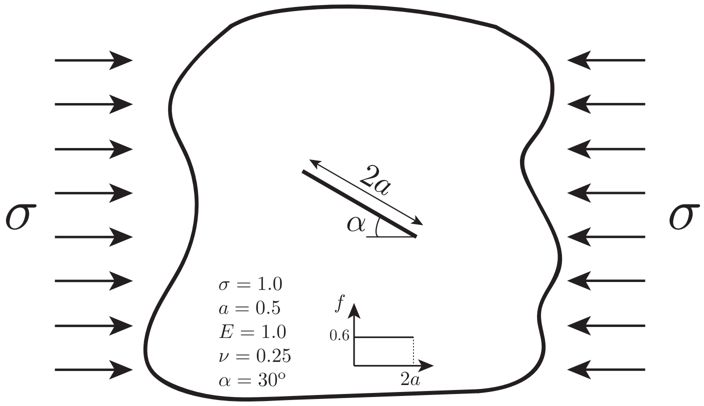

Figure 5.15 – Sketch of a planar fracture with homogeneous frictional properties, embedded in an infinite elastic medium, and subjected to a compressive remote stress $\sigma > 0$.

5.6 Supporting Information

When developing new numerical solvers, it is of great importance to reproduce existing problems whose solution is available in closed form or whose solution has already been verified with other numerical solvers. In this respect, we present hereunder other verification tests in order to show the accuracy and reliability of our one-way coupled hydro-mechanical solver. We finally conclude with another illustrative example that highlight all its capabilities.

5.6.1 Verification tests

5.6.1.1 A planar fracture with homogenous friction properties subjected to compressive far-field stress

A planar fracture with homogeneous frictional properties is located in an infinite elastic medium (see Figure 5.15). Due to its inclination α with respect to the far field compressive stress σ, the fracture is subjected to a uniform shear and normal traction distribution (denoted respectively as t_s and t_n). The corresponding shear fracture strength, which is given by the product of friction coefficient f and effective normal traction along the fracture plane (i.e. Mohr-Coulomb criterion without cohesion), is not large enough to guarantee equilibrium with the applied shear stress t_s. As a result, a distribution of slip d_s is expected.

This particular problem has been solved analytically by Phan et al. (2003) in terms of

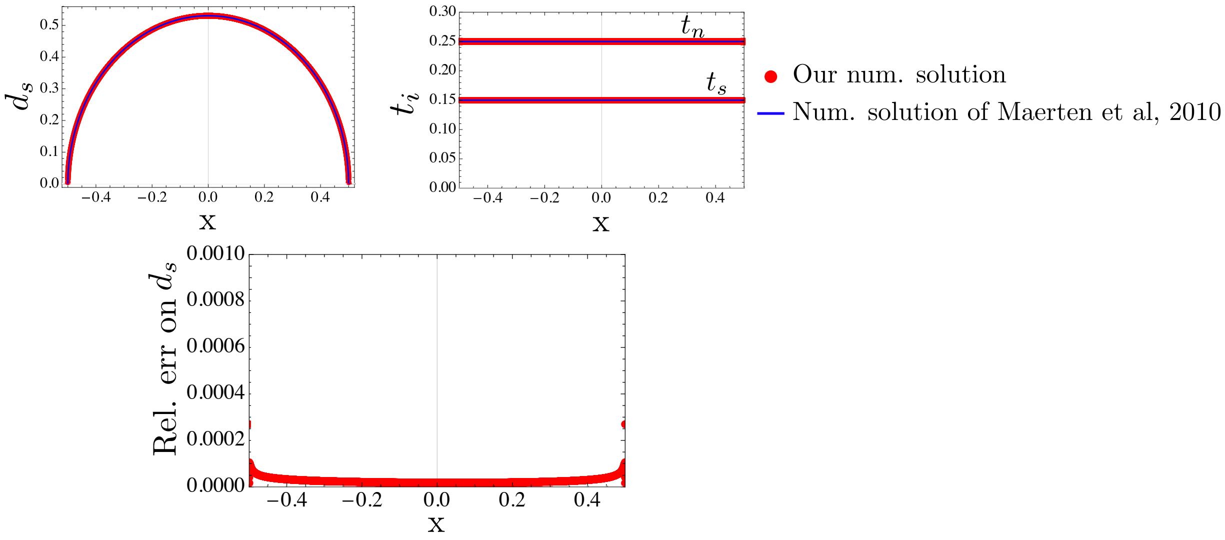

Figure 5.16 – Benchmark between our numerical results and the analytical solution of Phan et al. (2003) in terms of slip and tractions distribution. The relative error in terms of slip distribution (bottom) shows a good accuracy of the numerical results.

both slip d_s and tractions t_i distribution. The analytical solution thus reads

$$\begin{cases} t_n = -\sigma \sin^2\alpha \\ t_s = \sigma \cdot \sin\alpha(\cos\alpha - \sin\alpha\tan\phi) \\ d_s(x) = \frac{4(1-\nu^2)t_s}{E}\sqrt{a^2-(x-a)^2} \end{cases} \tag{5.33}$$

where $\sigma > 0$ is the compressive remote loading, $0 \leq x \leq 2a$ is the longitudinal coordinate of the pre-existing fracture, E is the Young's modulus of the elastic medium, ν is the Poisson's ratio and $\tan(\phi) = f$ is the friction coefficient (with ϕ as friction angle).

We solve this problem with our numerical solver, using the input data reported in Figure 5.15. Notably, we discretize the fracture with $5 \cdot 10^3$ equal-sized straight segments (obtaining $8 \cdot 10^3$ degrees of freedom) and we adopt a hierarchical approximation of the elasticity matrix with the following input parameters

$$\eta = 0, \quad \epsilon_{ACA} = 0.1, \quad n_{leaf} = 32,$$

obtaining a compression ratio of $c_r(\mathbf{E}_{\mathcal{H}}) \approx 0.075$.

In Figure 5.16, we show the comparison between the numerical and the analytical results in terms of slip and tractions distributions. As one can see from Figure 5.16, the numerical solutions match perfectly with the analytical ones. The relative error in terms of slip is everywhere less than $\sim 0.01\%$ of error, denoting thus a good accuracy. It is worth mentioning that the numerical solutions have been obtained with the hierarchical representation of the elasticity matrix. If the fully populated elasticity matrix is used

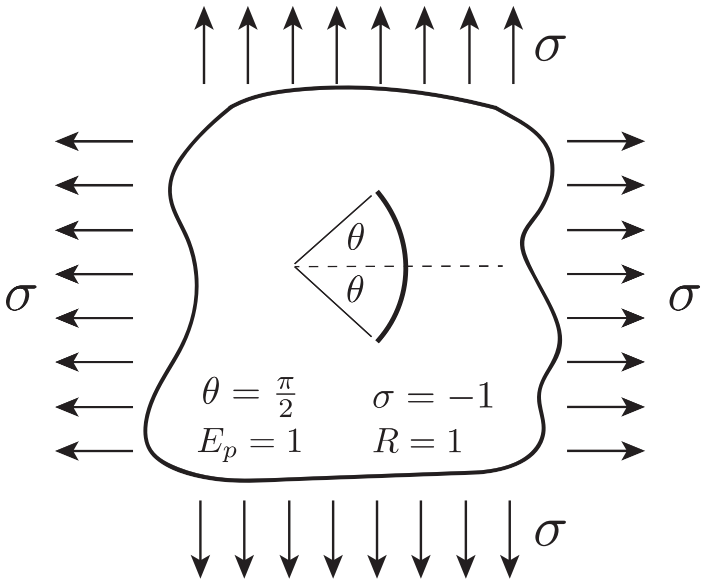

Figure 5.17 – Sketch of an arc crack subjected to a unitary tensile remote stress field $\sigma = -1$. The angle θ that define the extent of the arc crack is $\dfrac{\pi}{2}$, i.e. the pre-existing arc crack is half of a circumference.

instead, then we would expect a further decrease of the relative error.

5.6.1.2 Arc crack under remote tension

The second verification test is an arc crack located in an unbounded elastic medium, subjected to remote tension (see the configuration in Figure 5.17). Specifically, the remote tensile stress $\sigma < 0$ is applied to the medium such to induce deformations along the arc crack. This verification test is thus very important because it allows to verify the solver when the coupling of the two degrees of freedom (slip and opening) is mobilised (unlike the previous verification test). The analytical solution in terms of deformations for this particular problem is provided by Piva (1982) and it reads

$$d_n(\phi) = -4\sqrt{2} \cdot \mathrm{Re}\left[\frac{P_{net} \cdot R \cdot e^{-\frac{1}{2} i(2\theta+\phi)}\left(e^{i\phi} - e^{i\theta}\right)\left(-1 + e^{i(\theta+\phi)}\right)\sqrt{\frac{1}{\cos(\phi)-\cos(\theta)}}}{E_p(\cos(\theta)-3)}\right] \tag{5.34}$$

$$d_s(\phi) = -4\sqrt{2} \cdot \mathrm{Im}\left[\frac{P_{net} \cdot R \cdot e^{-\frac{1}{2} i(2\theta+\phi)}\left(e^{i\phi} - e^{i\theta}\right)\left(-1 + e^{i(\theta+\phi)}\right)\sqrt{\frac{1}{\cos(\phi)-\cos(\theta)}}}{E_p(\cos(\theta)-3)}\right], \tag{5.35}$$

where P_{net} is the net pressure within the arc crack, E_p is the plane strain elastic modulus of the material, θ is the angle defining the extension of the arc crack (see Figure 5.17) and R is its geometrical radius. This analytical solution allows to calculate the plastic

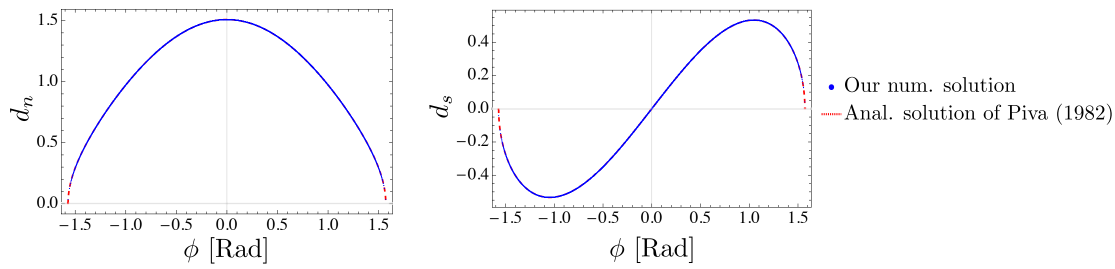

Figure 5.18 – Comparison between numerical and analytical results in terms of opening (left) and slip (right) distribution along the arc crack subjected to tensile remote stress.

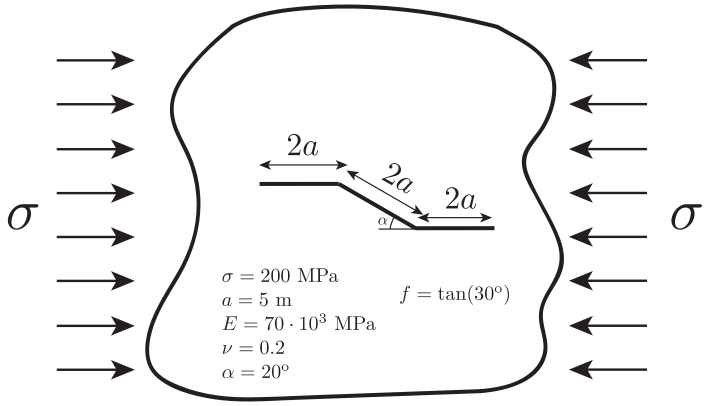

Figure 5.19 – Sketch of a stair-like fracture located in an unbounded elastic medium. The pre-existing fracture is subjected to a remote compressive stress $\sigma > 0$, such that the fracture's internal surfaces are in contact.

deformations as function of the angular coordinate ϕ.
Upon discretization of the arc crack with $2 \cdot 10^4$ finite straight segments (obtaining thus $1.6 \cdot 10^5$ degrees of freedom), this static problem has been solved numerically with our solver. A hierarchical representation of the elasticity matrix has been used with the following input parameters

$$\eta = 0.1 \qquad \epsilon_{ACA} = 0.1 \qquad n_{leaf} = 32,$$

obtaining a compression ratio of $c_r(\mathbf{E}_{\mathcal{H}}) \approx 0.0282$. Figure 5.18 shows a very good match between our numerical results and the analytical solution of Piva (1982), both in terms of slip d_s and opening d_n distribution along the fracture.

5.6.1.3 A stair-like fracture subjected to remote compressive stress

The next verification test is represented by a stair-like fracture subjected to remote compressive stress (see sketch in Figure 5.19). Specifically, this test consists in determining

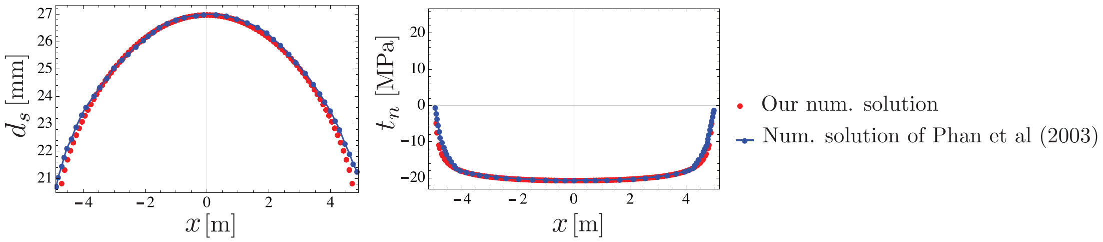

Figure 5.20 – Comparison between our numerical results and the ones Phan et al. (2003) in terms of slip (left) and normal traction (right) distribution along the kinked (inclined) branch of the stair-like fracture.

the slip d_s and normal traction t_n distribution along the kinked branch composing the stair-like fracture, which is inclined of 20° with respect to the maximum principal stress direction (i.e. horizontal direction). Due to the compressive loading, the internal surfaces of the kinked branch are in contact. The friction coefficient f is constant everywhere and all the dimensional input data are reported in Figure 5.19.

For this particular problem there is no analytical solution available in literature. However, Phan et al. (2003) have solved numerical this problem using a Symmetric-Galerkin Boundary Element Method with internal collocation points and frictional contact constraints. Their numerical solution, therefore, represent the target for our numerical solution.

In Figure 5.20 we report the comparison between our numerical results and the ones of Phan et al. (2003), both in terms of slip and normal traction distribution along the kinked (inclined) branch. As one can see, a good match is obtained. Note that this verification test is important because it allows to check the conditioning of the final linear system of equations (5.25) as all the input data are reported in dimensional form.

5.6.2 Other illustrative example

5.6.2.1 Mechanical opening and closure of a single planar fracture

As an illustrative example of mobilization of all the constraints described in Section 5.2.2 and capabilities of the numerical scheme devised, we show the case of a pre-existing planar fracture subjected to loading-unloading condition. Such a fracture represents the pre-existing potential failure plane for plastic flow localization. A time-dependent mechanical force is applied over an extent of $2d$ centered at $x = 0$ (see Figure 5.21). For time t lower than a critical time t_c, the mechanical force ‘pulls away’ the fracture's internal surfaces (i.e. tension - loading), while it changes sign at $t = t_c$ and fracture surfaces are then ‘pulled back’ (i.e. compression - unloading).

The fracture is subjected to an initial stress state whose tangential and normal components are denoted as σ_{yy} and σ_{xy}, respectively (see Figure 5.21-left). Its material constitutive properties are deformations-dependent, i.e. cohesion c, tensile stress σ_c and friction coefficient f can soften during localization of plastic deformations (following the

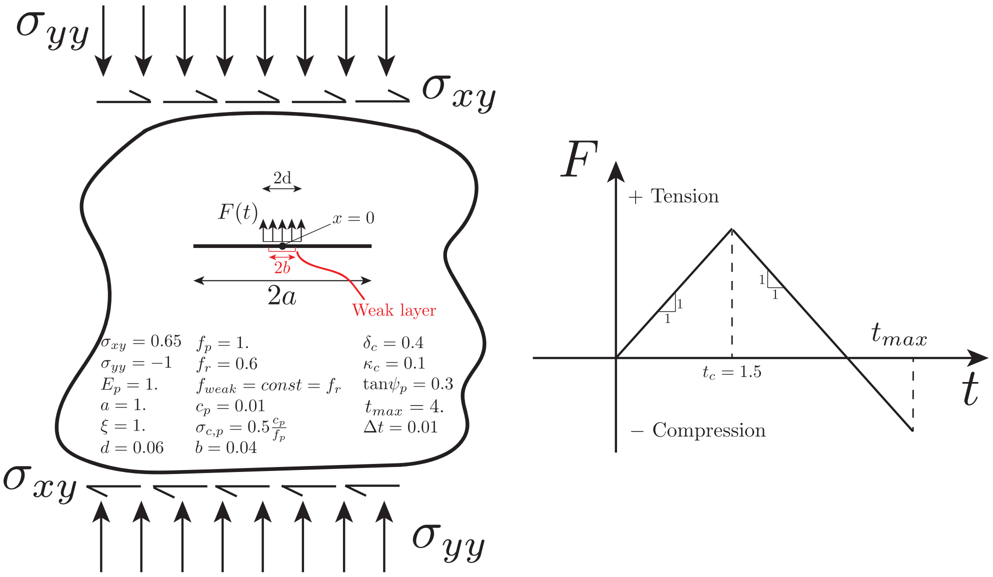

Figure 5.21 – Sketch of a planar fracture located in an unbounded elastic medium, subjected to i) an initial far field stress whose normal and shear components are denoted respectively by σ_{yy} and σ_{xy} and ii) to a time-dependent mechanical force $F(t)$ applied over an extent of $2d$. For time t lower than a critical value t_c, the mechanical force pulls away the fracture internal surfaces (tension), while the opposite occurs for $t > t_c$ (compression). The pre-existing fracture is characterized by softening constitutive relations (with dilatant behavior in case of shear plastic deformations), except over an extent of $2b$ where only the friction coefficient is at its residual value.

softening laws described in Section 5.2.2). A frictional weak layer of extent $2b$, however, is set near fracture centre in order to activate a shear crack at time $t = 0^+$ (see sketch of Figure 5.21). In addition to this, shear-induced dilatancy during crack propagation is taken into account, with softening of dilatancy angle from a peak value $\tan\psi_p$ up to vanish at large deformations (after which a critical state is reached). Opening displacement discontinuities associated with shear dilatancy define also the minimum opening that must be satisfied during the unloading condition.

Figure 5.22 shows the profiles of normalized slip d_s/κ_c and opening d_n/κ_c displacement discontinuities at different normalized time/load snapshots. During loading condition (i.e. when $t/t_{max} < 0.375$), for increasing values of tensile force F a shear crack starts to propagate along with the associated opening due to fracture dilatant behaviour. Within the shear crack tips, the cohesion c and tensile stress σ_c soften linearly with plastic deformations, up to vanish when $t/t_{max} > 0.2$ (see Figure 5.23). Simultaneously, the normal tractions t_n (normalized by the peak frictional strength of the fracture $\tau_p = f_p\sigma_{yy}$) decrease due to the tensile increase of the mechanical force F as well as the normalized shear tractions due to slip propagation (see top plots in Figure 5.24 for traction decrease

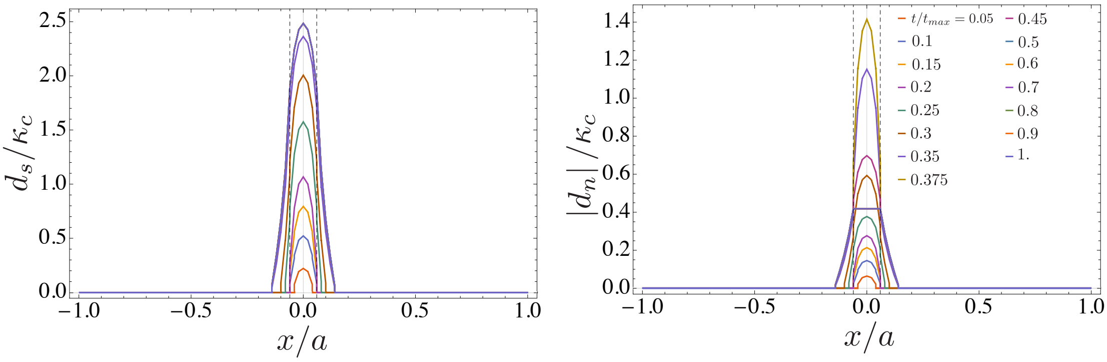

Figure 5.22 – Normalized profiles of shear (left) and normal (right) plastic deformations in function of time/load evolution t/t_{max}.

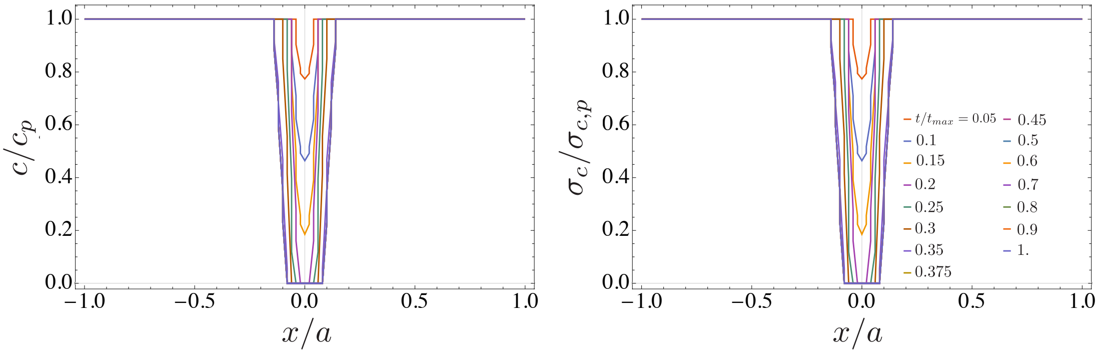

Figure 5.23 – Normalized profiles of cohesion (left) and tensile stress (right) in function of time/load evolution t/t_{max}.

at $x = 0$ during loading condition).
Around time $t/t_{max} \sim 0.275$, the normal tractions t_n at $x = 0$ violate the tensile strength of the material (i.e. $\mathcal{F}_1(t'_n) > 0$), such that the corresponding constraints described in Section 5.2.2 kick in and tractions free condition is reached, i.e. $t_s = t_n = 0$ (since both cohesion and tensile stress are at complete softening). This traction free condition persists even at early stage of unloading branch, i.e. when $t \geq t_c$. Indeed, when the mechanical force turns into compression, the shear crack stops propagating and the fracture starts to close back (see Figure 5.22). The slip accumulated during the loading condition does not vary in time (see bottom plot of Figure 5.24) and the associated maximum opening due to shear dilatancy (i.e. $|d_n|/\kappa_c \sim 0.4$) sets the minimum opening that has to be satisfied during the closure of the fracture. Around $t/t_{max} \sim 0.48$, the inter-penetrability constraint kicks in, implying a contact condition for fracture's inner surfaces. At that specific time, normal tractions start again to build up linearly (for linear increase of compressive force), while the shear tractions remain null due to their release during the loading condition (see top plots in Figure 5.24).

This specific example clearly shows that time/load-dependent physical phenomena are

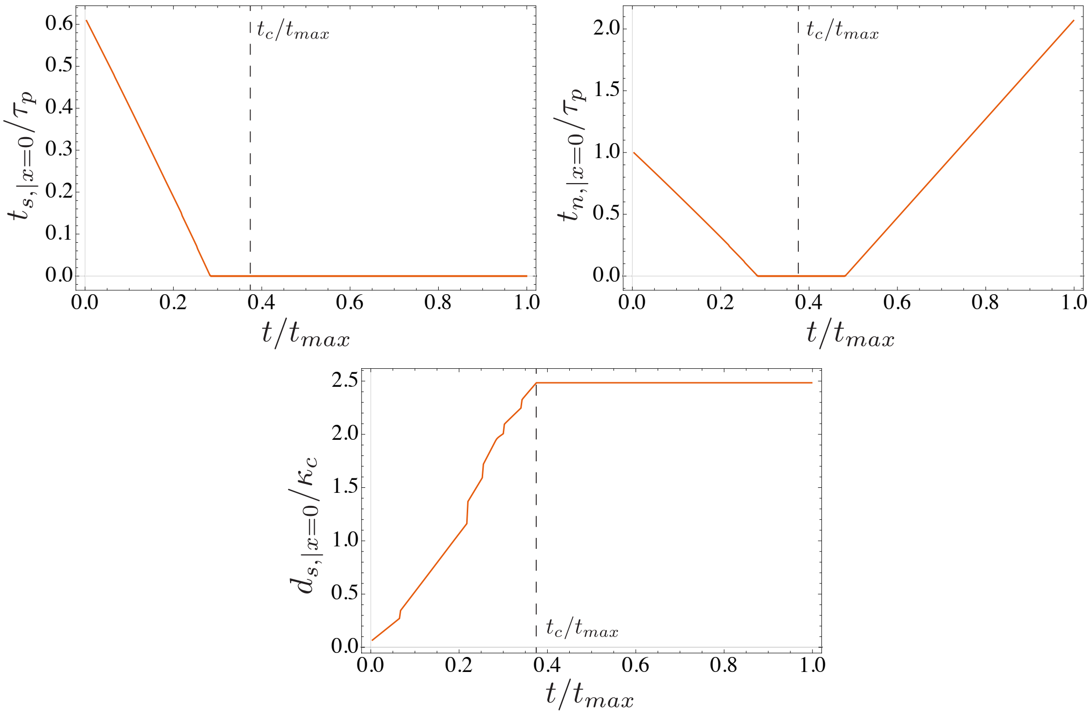

Figure 5.24 – Time evolution of normalized shear tractions (top-left), normal tractions (top-right) and shear plastic deformations at the middle of the pre-existing fracture, i.e. at $x = 0$.

properly captured by the numerical solver. Mixed mode deformations, softening of fracture strength's parameters as well as contact condition are accurately handled by the algorithm.

6 Fluid induced aseismic slip in fractured rock masses: marginally pressurized vs critically stressed conditions

In this chapter, we investigate numerically the interplay between fluid flow and aseismic (quasi-static) slipping patch growth in a fractured rock mass. We use the one-way coupled hydro-mechanical solver for localized inelastic deformations previously described in Chapter 5. We assume that the frictional properties of the fractures remain constant (friction neutral case) which necessarily imply strictly aseismic deformation (quasi-static).

The results reported here will provide the basis of a future publication.

6.1 Introduction

Anthropogenic fluid injection in the sub-surface triggers micro-seismicity (events with moment magnitudes lower than 2), which is typically manifested as a cloud of events migrating away from the injection point. Such a migration of micro-seismicity is usually related to the diffusion of the pore-pressure disturbance associated with injection (Shapiro et al. 1997, 2002, Albaric et al. 2014). The increase of pore-pressure lowers the effective stresses which can lead to inelastic deformation and slippage of pre-existing planes of discontinuities that necessarily exist at multiple scales in rocks. The enlarging cloud of micro-seismicity has been observed to correlate well with a diffusion process. Many observations (see Figure 6.1) suggest that the growth of the microseismic cloud in time is indeed bounded by a power-law which grows similarly to the diffusion length scale $\sim \sqrt{4\alpha t}$, where α is the hydraulic diffusivity. As a result, some authors have directly used the evolution of micro-seismicity to estimate a global hydraulic diffusivity obtaining in a number of cases relatively large value compared to the ones estimated in the laboratory. Townend & Zoback (2000), for instance, have shown that the diffusivities inferred from micro-seismicity over-estimated the measured values from core samples by one to three

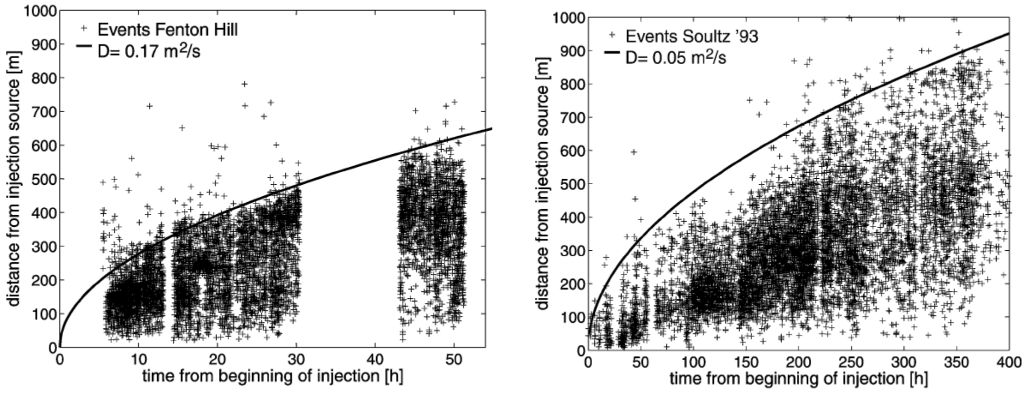

(a)

(b)

Figure 6.1 – Evolution of micro-seismic events in terms of distances from injection source versus their occurrence for (a) Fenton Hill experiment (1983) and (b) the Soultz-sous-Forets experiment (1993). Taken from Shapiro et al. (2002).

order of magnitude. Although part of the mismatch could be attributed to the presence of hydraulically conductive fractures at a large scale, it may not be the only explanation. The hypothesis that the microseismic cloud is directly coinciding with the location of the fluid front does not necessary holds. Indeed, the micro-seismic front is a direct measure of the locus of deformation which may be located ahead of the pore-pressure disturbance. Evidence of aseismic slip propagation (combined with micro-seismicity) have been observed during hydraulic stimulation of the north Brawley (Wei et al. 2015) and Soultz EGS project (Bourouis & Bernard 2007). It has also been observed in numerous fluid injection in-situ (Cornet et al. 1997*b*, Guglielmini et al. 2015, Duboeuf et al. 2017, De Barros et al. 2018) as well as laboratory experiments (Leeman et al. 2016, Noël et al. 2019). Using data derived from an in-situ fluid-injection experiment, Bhattacharya & Viesca (2019) showed using a simple fault model that aseismic fault slip activated by the increase in pore-fluid pressure can outpace pore-fluid migration. Aseismic slip patch growth faster than the diffusion front are also obtained with the theoretical model described in Chapter 4 in critically stressed cases.

In this chapter, we move away from the model of a simple planar fault, and explore the relationship between the evolution of the pore-pressure disturbance (the fluid front position) and aseismic slip in fractured rock mass. We model the fracture rock mass using a discrete fracture network (DFN) approach and focus on the case of a randomly oriented DFN. In order to set the stage, we first recall the solution of the propagation of a aseismic slip patch along a planar fault with neutral frictional property. We notably compare our numerical results obtained using the solved developed in Chapter 5 with the semi-analytical solution of Bhattacharya & Viesca (2019) valid for this particular case.

6.2 Fluid driven aseismic slip along a planar fault with neutral frictional properties

Let us consider an infinite planar fault in an infinite homogenous isotropic elastic medium under plane-strain conditions. Fluid is injected into such a fault with a constant longitudinal fault permeability assumed to be much larger than the one of the host rock. Fluid flow is therefore solely occurring along the fault and the solution for the pore-pressure disturbance can be obtained analytically for the case of a constant injection over-pressure.

The fault is subjected to a uniform initial in situ stress (with normal and tangential components denoted respectively as t_n and t_s) and pore pressure distribution p_o prior the start of the injection. Initially the fault is in static equilibrium with this uniform in situ stress state. This homogenous model is thus similar to the one described in Chapter 4, with the only difference that here the friction coefficient f is assumed to remain constant (does not evolve with slip) and shear induced-dilatancy is neglected. Upon activation of slip due to the increase of fluid pressure along the fault and violation of a Mohr-Coulomb yield criterion without cohesion

$$|t_s| \leq f\left(t_n - p(x,t)\right), \tag{6.1}$$

the quasi static elastic equilibrium equations related only to the shear degrees of freedom for a planar fault can be written as

$$t_s(x,t) - t_s^o = -\frac{E'}{4\pi}\int_{-a(t)}^{a(t)} \frac{\partial d_s(s,t)}{\partial s}\frac{\mathrm{d}s}{x-s}, \tag{6.2}$$

where $a(t)$ is half length of the slipping patch, E' is the plane-strain elastic modulus and d_s is the shear displacement discontinuity (slip). Similarly to the case of the dilatant fault introduced in Chapter 4, fluid flow is governed by the width averaged fluid mass conservation

$$w_h \beta \frac{\partial p}{\partial t} + \frac{\partial q}{\partial x} = 0, \tag{6.3}$$

where q is the unidimensional local flux given by Darcy's law (3.13). Since shear-induced dilatancy is neglected in this model, equation (6.3) is uncoupled from elasticity equations (6.2). For this reason, it can be solved analytically for the case of a constant injection over-pressure ΔP as boundary condition. The pore-pressure along the fault is thus given by:

$$p(x,t) = p_o + \Delta P \cdot \operatorname{erfc}\left(\frac{|x|}{\sqrt{4\alpha t}}\right), \tag{6.4}$$

where $l_d = \sqrt{4\alpha t}$ is the diffusion length scale and α $\left[L^2/T\right]$ is the fault hydraulic diffusivity (see eq. (4.16)). Under these specific conditions, fluid injection activates a shear crack that propagates symmetrically from injection point paced by pore fluid diffusion. Its propagation, however, is always stable (aseismic - due to the neutral frictional condition considered). No dynamic instabilities are expected. It is reasonable to think, therefore, that the shear crack propagates in a self-similar way following the fluid diffusion lengthscale, which means that the following relations must hold:

$$a(t) = \lambda\sqrt{4\alpha t}, \tag{6.5}$$

where λ is a dimensionless parameter that quantify the relative position between the shear crack and the diffusion front.

This problem has been solved semi-analytically by Bhattacharya & Viesca (2019) who showed that this problem is governed by a single dimensionless parameter T defined as

$$T = \left(1 - \frac{\tau_o}{\tau_p}\right)\frac{\sigma'_o}{\Delta P}, \tag{6.6}$$

where $\tau_p = f\sigma'_o = f(\sigma_o - p_o)$ is the peak shear strength of the fault at ambient conditions (prior to fluid injection). This dimensionless parameter has been obtained by scaling tractions t_s, spatial variables (x and $a(t)$) and slip d_s in the elasticity equation (6.2) respectively with the peak shear strength τ_p, the diffusion length scale l_d and $\frac{f\Delta P}{E'}l_d$ (where this latter directly comes from elasticity). Note that T includes the stress criticality ratio $\frac{\tau_o}{\tau_p}$ that quantify how far the fault is from failure prior fluid injection and the inverse of the normalized injection over-pressure $\frac{\Delta P}{\sigma'_o}$. For a given value of over-pressure ΔP, we would expect that λ is considerably lower than 1 for low values of stress criticality ratio and thus large values of T parameter (which means that the slipping patch is located within the pressurized region - marginally pressurized case), while $\lambda > 1$ are expected otherwise (the shear crack tips well ahead the fluid front position - critically stressed case).

Theses considerations have been quantified mathematically by Bhattacharya & Viesca (2019) who obtained two different mathematical expressions for these two regimes:

$$\begin{aligned} T &= 1 - \lambda\frac{4}{\pi^{3/2}} \qquad \text{(marginally pressurized)} \\ T &= \frac{2/\pi^{3/2}}{\lambda} \qquad \text{(critically stressed)} \end{aligned} \tag{6.7}$$

Knowing the value of T parameter[1] prior fluid injection, equation (6.7) can thus be solved to estimate the λ parameter.

---

[1] The knowledge of T fault stress parameter depends on the in-situ stress conditions applied to the fault plane, its frictional properties and the maximum over-pressure that is going to be injected into the fault.

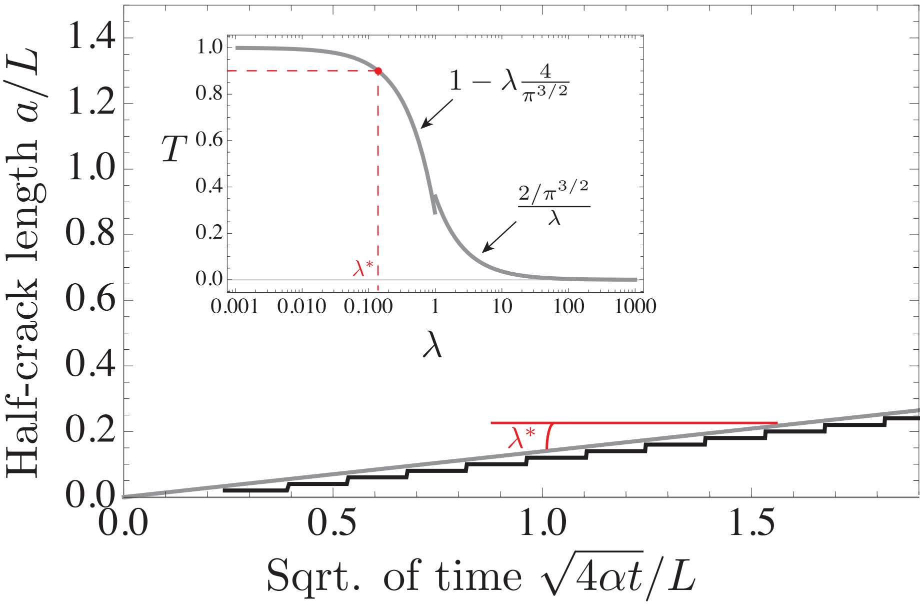

Figure 6.2 – Evolution of normalized half crack length a/L with normalized time $\sqrt{4\alpha t}/L$, for a marginally pressurized fault ($\tau_o/\tau_p = 0.55$) subjected to a moderate injection over-pressure $\Delta P/\sigma'_o = 0.5$ (such that $T = 0.9$). The friction coefficient is constant and equal to $f = 0.6$. The inset plot represents the benchmark of our numerical result (red dot) with the analytical solution in terms of self-similar coefficient λ provided by Bhattacharya & Viesca (2019) (grey curves).

We solve this problem with the one-way coupled hydro-mechanical solver described in Chapter 5. We discretize the fault with $1 \cdot 10^3$ equal-sized straight segments, obtaining thus $8 \cdot 10^3$ degrees of freedom, half related to displacement discontinuities and half related to effective tractions. In this particular problem, we do not approximate the fully populated elasticity matrix with its hierarchical representation ($\eta = 0$ during $\mathcal{H}-$matrix construction). In Figure 6.2 we show the evolution of half crack length a (normalized with half length of the fault L) with normalized time $\sqrt{4\alpha t}/L$, for a marginally pressurized fault ($\tau_o/\tau_p = 0.55$) subjected to a moderate injection over-pressure $\Delta P/\sigma'_o = 0.5$ (such that the fault stress parameter is $T = 0.9$). As one can see, the slipping patch grows always quasi-statically (i.e. aseismic slip) in time, with its tips always located inside the pressurized region. The coefficient of proportionality λ^* that physically represents the relative (constant) distance between the slipping patch and the fluid front (self-similar coefficient) matches perfectly with the theoretical one obtained from solving equation (6.7) with $T = 0.9$ (see the inset in Figure 6.2). The step-wise nature of the numerical solution (black curve) is the result of the coarse discretization of the fault in this example (similar to the case discussed in Section 4.8.2).

6.3 Fluid injection into a Discrete Fracture Network

We now extend the work of Bhattacharya & Viesca (2019) to the case in which fluid is injected in one fracture/fault, but this fracture is hydraulically connected to a large number of pre-existing fractures, forming a so called Discrete Fracture Network (DFN). A DFN can be quantitatively defined with the following mathematical expression (restricting to the 2-dimensional case) (Davy et al. 2006)

$$N_{2d}\left(L, l, \theta, \phi\right) \mathrm{d}l \mathrm{d}\theta \ldots, \tag{6.8}$$

which represents the number of fractures contained in an area of typical size L, with length between l and $l + \mathrm{d}l$, orientations in θ and $\mathrm{d}\theta$, positions in ϕ and $\mathrm{d}\phi$, and a set of other properties (denoted by the dots …). Several fracture distributions models have been introduced in literature (lognormal distribution, gamma law, exponential law among others - see Bonnet et al. (2001), Lei et al. (2017) for well done reviews), leading to a not unique choice of the expression for N_{2d}. Each distribution model, however, must contain scaling relations that enable to capture appropriately the multi-scale nature of the problem. In this contribution, we adopt a distribution model that contains two scaling laws: the fractal density (given by the fractal dimension D_{2d}) and a power-law distribution for fracture length generation (characterised by an exponent a) with cut-off for minimum and maximum fracture lengths (denoted by l_{min} and l_{max}, respectively). This choice has been demonstrated in numerous studies at different scales and in different tectonic settings (Hatton et al. 1994, Sornette et al. 1993, Anders & Wiltschko 1994, Kranz 1983, Walmann et al. 1996).

Assuming fracture lengths, positions (or density) and orientations independent entities, we can write the fracture model as

$$N_{2d}\left(L, l, \theta, \phi\right) = \alpha(\theta, \phi) L^{D_{2d}} l^{-a}, \qquad \text{for} \quad l \in [l_{min}, l_{max}] \tag{6.9}$$

where $\alpha(\theta, \phi)$ is the fracture density term, which depends on their orientations and positions. Note that the only intrinsic characteristic length scales in this model are the smallest l_{min} and the largest l_{max} fracture lengths. The exponents D_{2d} and a quantify the scaling aspects of the DFN (Lei & Wang 2016, Lei & Gao 2018): the former govern the fracture density, whereas the latter govern the length distributions. According to extensive outcrop data, D_{2d} typically varies between 1.5 and 2.0, whereas a ranges between 1.2 and 3.5 (Bonnet et al. 2001). In this preliminary investigation, we assume that fractures are uniformly distributed within the region of interest $L \times L$[2] (with random locations and orientations). This assumption implies that the fractal dimension D_{2d} equals the Euclidean dimension, i.e. $D_{2d} = 2$ (homogenous and isotropic case).

---

[2] Note that this assumption may not reflect most of the real cases, in which discrete set of joints with given orientations are observed. However, it can be easily relaxed to account for more complex configurations

By removing the system-size effect, the density distribution mode reduces to

$$n_{2d}(l,\theta,\phi)=\frac{N_{2d}(L,l,\theta,\phi)}{L^{D_{2d}}},\qquad \text{for}\quad l\in[l_{min},l_{max}] \tag{6.10}$$

which can be scaled by $\dfrac{l_{min}^{1-\alpha}\alpha}{-1+a}$ to obtain the probability density function (pdf)

$$f_{2d}(l)=\frac{-1+a}{l_{min}^{1-a}}l^{-a},\qquad \text{for}\quad l\in[l_{min},l_{max}] \tag{6.11}$$

This probability density function represents the scaling law for fracture lengths for a given DFN. Typically, this law must be spanned at least for two orders of magnitude.

Another important aspect that plays a role in the hydraulic stimulation of discrete fracture networks is the percolation parameter, which assesses the geometrical connectivity of the fracture network. This parameter (commonly denoted as p) will be denoted as $\bar{p}$ here (in order not to confuse it with the pore pressure p). For a given distribution of fractures orientation and position, its expression is (Lei & Gao 2018)

$$\bar{p}(l,L)=\int_{A_L}\frac{N_{2d}(L,l)l'^2}{L^2}\mathrm{d}l, \tag{6.12}$$

where l' denotes the fracture length included in the domain of area $A_L=L^2$. The larger $\bar{p}$ is, the more connected is the system and thus the more homogenous will be the fluid diffusion inside the DFN. Typically, a DFN is statistically connected if $\bar{p}$ is greater than a percolation threshold $\bar{p}_c$, with $\bar{p}_c\sim 5.8$ for 2D networks (Bour & Davy 1997).

In order to generate the set of pre-existing fractures, we use ADFNE, an open source library (written in Matlab) for DFN generation (Alghalandis 2017). We have replaced the original exponential distribution for fracture length with a power law distribution (6.11). For a given set of DFN properties, initial and end coordinates of each fracture are obtained. A pre-processing script in Mathematica is then used to mesh all the generated fractures, with the possibility of i) controlling the mesh element size per fracture, ii) inserting automatically a mesh node at each fracture intersection and finally iii) set a minimum number of finite straight segments per fracture.

6.3.1 Scaling & dimensionless governing parameters

Assuming neutral frictional conditions for the pre-existing fractures with zero cohesion, the scaling analysis analysis of the governing equations (elasticity equations (6.2) and fluid mass conservation equation (6.3)) is similar to the one proposed by Bhattacharya & Viesca (2019). However, in the case of a Discrete Fracture Network, the fluid flow is not known analytically. It is obtained numerically using the flow solver previously described for a fixed constant over-pressure as boundary condition. It is obviously strongly function of the percolation number of the DFN. Therefore, instead of having only one governing dimensionless parameter, the problem is now governed by i) the normalized injection over-pressure at the fracture in which fluid is injected into, ii) the stress criticality ratio function of the effective stress anisotropy ratio and local fracture orientation, and iii) the percolation number of the DFN.

In order to demonstrate this, we qualitative describe the scaling analysis. We scale all the spatial variables with $L/2$, which is the minimum distance that the fluid front can travel before reaching the boundary of the region of interest (supposing that fluid is injected at $(L/2; L/2)$) and the time t with the characteristic fluid diffusion timescale $L^2/(16\alpha)$. The characteristic scales for fluid over-pressure $\Delta p = (p - p_o)$ and effective tractions t'_i are respectively the in-situ effective normal traction $t^{\prime,k_{inj}}_{n,o}$ and the peak shear strength $t^{k_{inj}}_{s,p} = f \cdot t^{\prime,k_{inj}}_{n,o}$ of the fracture in which fluid is injected into (here denoted with the superscript ${}^{k_{inj}}$), while shear slip is scaled using the characteristic scale $d_{s,w} = \dfrac{t^{k_{inj}}_{s,p}}{E'}\dfrac{L}{2}$ that derives from elasticity. Upon scaling the governing equations with the previous characteristic scales, the solution given by $(p - p_p)/t^{\prime,k_{inj}}_{n,o}$, $t'_i/t^{k_{inj}}_{s,p}$, $d_s/d_{s,w}$ is function of (besides the geometry of the pre-existing fractures network) two dimensionless parameters: i) a stress criticality ratio

$$\Lambda = \frac{(\kappa - 1)}{f}\frac{\mathrm{Cot}(\theta)}{(\kappa \mathrm{Cot}(\theta)^2 + 1)}, \tag{6.13}$$

which is function of effective stress anisotropy ratio $\kappa = \dfrac{\sigma'^{o}_{xx}}{\sigma'^{o}_{yy}}$, friction coefficient f and local fracture orientation θ with respect to the minimum principal direction, and ii) normalized injection over-pressure at fracture k_{inj} in which fluid is injected into

$$\Pi = \frac{\Delta P}{t^{\prime,k_{inj}}_{n,o}}, \tag{6.14}$$

where $t^{\prime,k_{inj}}_{n,o}$ is the uniform ambient effective normal stress along the fracture k_{inj}. In Figure 6.3, we can see the variation of stress criticality Λ as function of fracture orientation θ (expressed in radians) and increasing effective stress anisotropy κ (denoted by the arrow), for a given value of friction coefficient f (specifically $f = 0.6$). As expected, for the limiting value of $\kappa = 1$ all the fractures in the DFN are far from being critically stressed: their criticality is null regardless their orientation with respect to the far field stress. For increasing value of κ, the critical fracture orientation θ_c (value at which the stress criticality is maximum) migrates from $\theta = \pi/4$ to $\theta = \pi/4 + \frac{\phi}{2}$ (see grey vertical line), where $\phi = \arctan(f)$ is the internal friction angle.

It is interesting to note that if we combine together the two dimensionless parameters (6.13) and (6.14), we can recover a similar expression than the one introduced by Bhattacharya

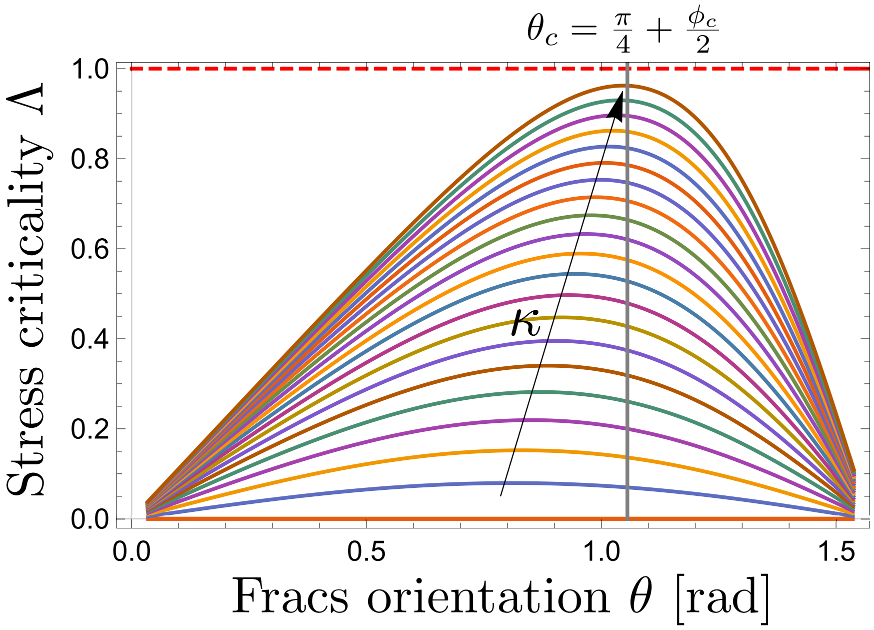

Figure 6.3 – Stress criticality evolution as a function of fracture orientation θ and increasing values of effective stress anisotropy ratio κ, for a fixed value of friction coefficient $f = 0.6$ (or critical internal friction angle $\phi_c \simeq 0.54$ radiants). The grey vertical line corresponds to the critical fracture orientation $\theta_c = \pi/4 + \dfrac{\phi_c}{2}$.

& Viesca (2019) (see Section 6.2)

$$T = (1 - \Lambda)\frac{1}{\Pi} \tag{6.15}$$

In the case of a DFN the dimensionless T parameter includes a family of solutions (due to the fracture orientation dependency on the stress criticality Λ). We would thus expect that a critically stressed DFN (large Λ or low T) subjected to fluid injection exhibits fast aseismic slip regardless the percolation value that characterize its fluid inter-connectivity as well as the value of injection over-pressure (as long as it is sufficient to activate slip). This is because the main driving force for the slipping patch propagation is the stress-interactions between fractures. On the other hand, the scenario may change for marginally pressurized or slightly critically stressed DFN characterized by low/moderate Λ or large/moderate T. The aseismic slip propagation in this case is directly affected by pore pressure diffusion inside the DFN and as a result the corresponding percolation parameter plays an important role. Low percolation values may lead to fluid localization and possibly very restricted aseismic slipping patch.

In the next two sections, we report two illustrative examples of fluid injection into a DFN. We generate 251 randomly oriented fractures with a power-law distribution for length with an exponent $a = 2.5$ in between a minimum and maximum cutoff of $0.01L$ and

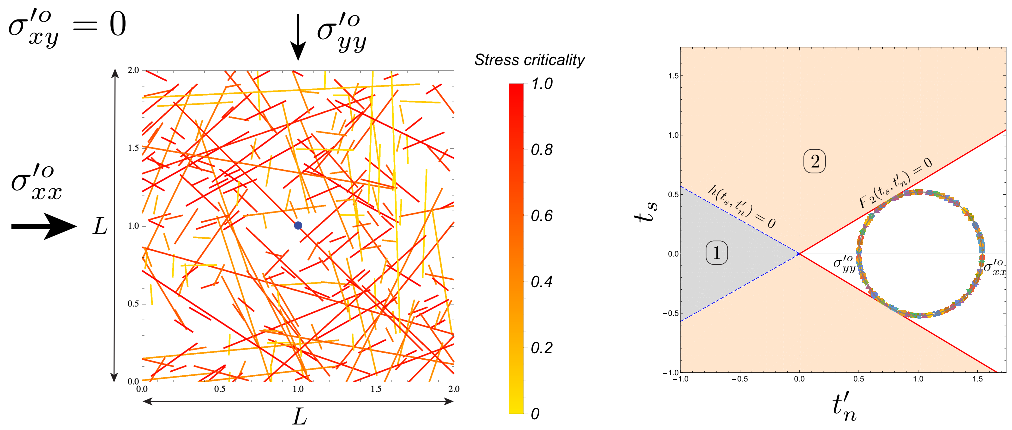

Figure 6.4 – Left: critically stressed discrete fracture network. The color of each fracture denotes the stress criticality Λ at ambient condition. Right: initial effective stress state in the Mohr-Coulomb plane for the critically stressed discrete fracture network. Along the circle, which is identified by the two principal effective stresses σ'^{o}_{xx} and σ'^{o}_{yy}, all the uniform stress states of each pre-existing fracture are reported. Since all the pre-existing fractures are randomly oriented within the region $L \times L$, the whole circle is uniformly "covered" by the fractures' initial stress states.

$0.9L$ respectively, where L is the simulation box. Upon discretization with 11376 straight segments (mean mesh size of $0.004L$), the total number of unknowns (displacement discontinuity and traction) is $\sim 9.1 \times 10^4$.

For a given constant value of friction coefficient $f = 0.6$ and a given value of normalized injection over-pressure $\Delta P / t'^{,k_{inj}}_{n,o} = 0.5$, we vary the stress anisotropy parameter κ such that the pre-existing fractures at ambient conditions are either critically stressed (large κ) or marginally pressurized (relatively low κ), depending on their orientations with respect to the far field stress.

6.3.2 Critically stressed condition

We first present the case of a hydraulic stimulation of a fractured rock mass, subjected to a compressive far-field stress state with an effective principal components denoted by σ'^{o}_{xx} and σ'^{o}_{yy} (with $\sigma'^{o}_{xx} > \sigma'^{o}_{yy}$) and a relatively large effective stress anisotropy ratio, i.e. $\kappa = 3$. In this example, failure can localize only along a set of 251 randomly oriented pre-existing fractures, which are uniformly located within the region of interest $L \times L$ (see Figure 6.4-left). Due to the relative large value of κ, all the pre-existing fractures oriented along the critical angle $\theta_c = \pi/4 + \phi/2$ are thus critically stressed, i.e. they are prompt to fail with little pressurization (see Figure 6.4-right).

The fluid is injected at $(L/2; L/2)$ under a constant injection over-pressure ΔP such

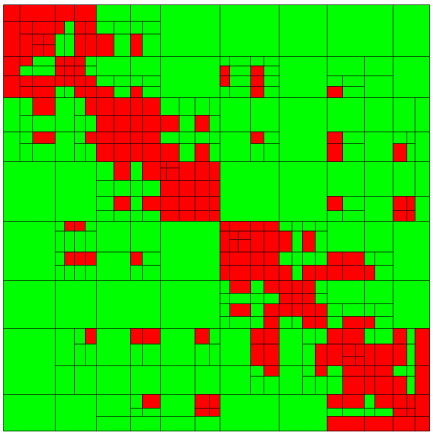

Figure 6.5 – Hiearchical matrix pattern upon compression (with $\eta = 5, \quad \epsilon_{ACA} = 10^{-6}$ and $n_{leaf} = 10^3$) with low-rank blocks in green.

that it always remain below the minimum principal effective normal stress (to avoid tensile opening of any fractures). We assume that the hydraulic diffusivity of all fractures are equal. The fluid flow is solved via a finite volume solver - uncoupled here to the mechanical deformations. The evolution of mechanical slip is solved using the boundary element based numerical solver for localized inelastic deformations described in Chapter 5.

Due to the large number of unknowns, we use a hierarchical approximation of the elasticity matrix using $\eta = 5, \quad \epsilon_{ACA} = 10^{-6}, \quad n_{leaf} = 10^3$ resulting in a a compression ratio of $c_r = 0.253$, sufficient to be able to run the simulation with a 2.9 GHz Intel Core i5 laptop with 8 GB memory (see the pattern of hierarchical matrix in Figure 6.5).

As one can see from Figure 6.6 that displays the normalized over-pressure and shear rupture evolution in function of normalized time/fluid front position, right after fluid injection the slipping patch evolves rapidly, much faster than fluid diffusion front. As the slipping patch propagates, the stress state changes within the elementary area, activating other fractures. At a normalized time $\dfrac{\sqrt{4\alpha t}}{L/2} \simeq 0.37$, the pressurized zone is still confined to the surrounding of the injection point, while the slipping patch is significantly larger. The slipping patch evolution is thus mainly driven by stress interaction between active fractures. From these numerical results, we can also conclude that the numerical solver proposed in Chapter 5 captures well the yielding evolution driven by fluid flow and elastic stress interactions between activated pre-existing fractures. That example with $\sim 10^5$ degrees of freedom demonstrates the robustness of the preconditioning developed in Section 5.3. The number of iterations (scaled by the number of unknowns) for the GMRES iterative solver remains below 1.5% for all time steps as can be seen in Figure 6.7.

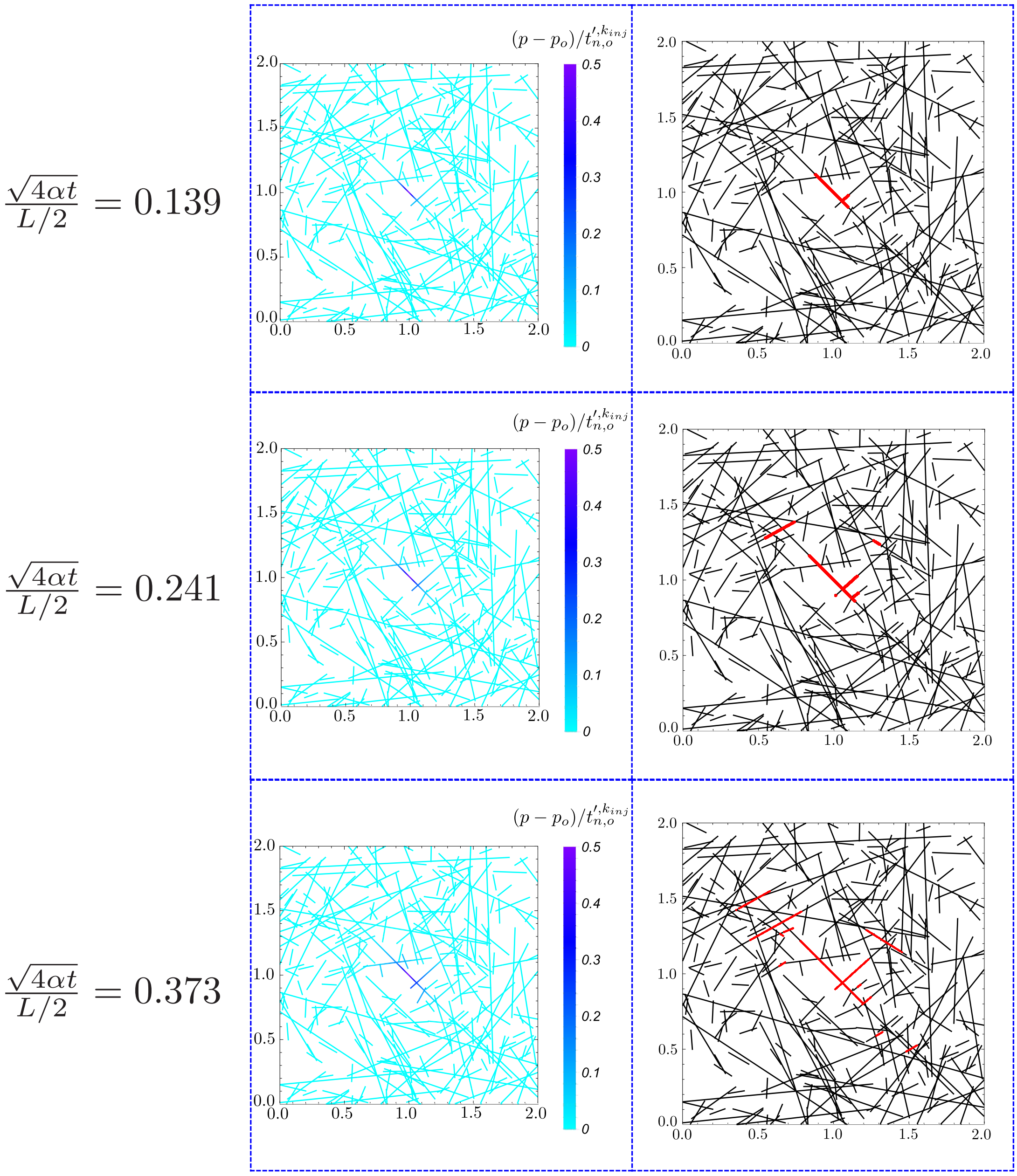

Figure 6.6 – Evolution of normalized over-pressure (left column) and plasticity localization (shear deformations - right column) along the pre-existing critically stressed fracture network in function of normalized time/fluid front position $\frac{\sqrt{4\alpha t}}{L/2}$. Fluid is injected at moderate over-pressure $\Delta P/t_{n,o}^{\prime,k_{inj}} = 0.5$ into one fracture that intersect the injection point located at $(1, 1)$.

6.3.3 Marginally pressurized condition

We finally present the case of fluid injection in a marginally pressurized fractured rock mass. Specifically, we consider the same Discrete Fracture Network presented in Section

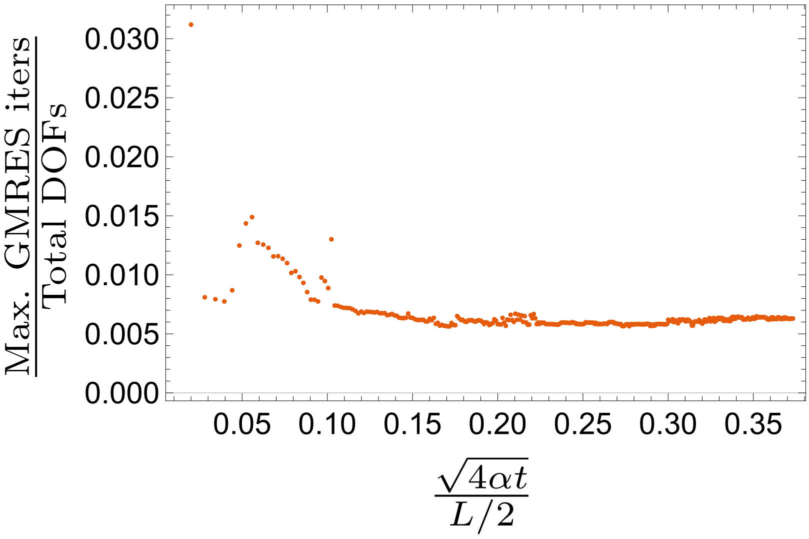

Figure 6.7 – Maximum number of GMRES iterations required to solve the mechanical problem at each time step. A convergence tolerance $tol = 10^{-6}$ was used for the GMRES iterative solver.

6.3.2, with the same loading conditions and the same location of injection point. The only difference in this example is the level of far field compressive effective stress, notably the stress anisotropy ratio that now is $\kappa = 2$. Each pre-existing fracture within the region of interest $L \times L$ is characterised by a relatively low stress criticality Λ. As one can see in Figure 6.8-right, indeed, the effective stress state in the Morh-Coulomb plot prior fluid injection, which is represented by a circle whose diameter is equal to the difference between the two principal effective stress at ambient conditions, is relatively far from the yielding failure line that here is represented by the Mohr-Coulomb criterion without cohesion (i.e. $\mathcal{F}_2(t_s, t_n') = 0$). All the pre-existing fractures that are randomly oriented and uniformly distributed within the region $L \times L$ are thus characterised by a relatively low stress criticality (see Figure 6.8-right).

Upon fluid injection at $\left(\frac{L}{2}, \frac{L}{2}\right)$, the slipping patch starts to expand paced by fluid flow. Because of the relatively low stress criticality, the aseismic slipping patch is located well inside the pressurized region. This can be clearly grasped from Figure 6.9 in which the pressurized region is compared to the shear rupture extent at different normalized time snapshots. At $\frac{\sqrt{4\alpha t}}{L/2} = 2.391$ the normalised fluid overpressure has nearly reached the external boundaries of the region $L \times L$, while the slipping patch is confined near the injection point. The fluid diffusion front is thus much faster than the slipping patch. Their relative position is, therefore, reversed with respect to the case of a critically stressed DFN.

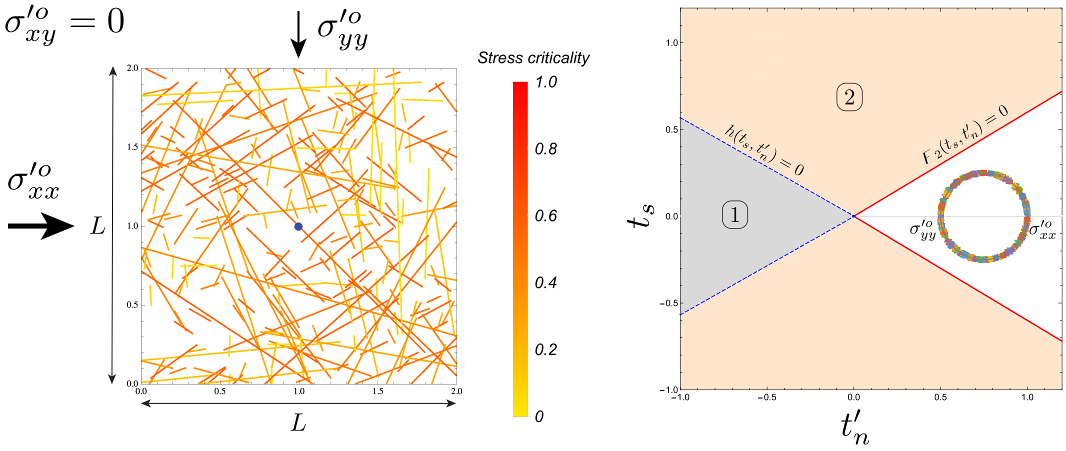

Figure 6.8 – Left: marginally pressurized discrete fracture network. The color of each fracture denotes the stress criticality λ at ambient condition. Right: initial effective stress state in the Mohr-Coulomb plane for the marginally pressurized discrete fracture network. Along the circle, which is identified by the two principal effective stresses σ'^{o}_{xx} and σ'^{o}_{yy}, all the uniform stress states of each pre-existing fracture are reported. Since all the pre-existing fractures are randomly oriented within the region $L \times L$, the whole circle is uniformly "covered" by the fractures' initial stress states.

6.4 Discussion and conclusions

From these numerical results we can observe that an aseismic slipping patch propagate much faster than fluid diffusion inside a pre-existing fracture network under critically stressed conditions. Although these results have been obtained for a single type of DFN (with a given percolation number, fractures orientations and positions etc.), in principle they can explain the reason why the inferred permeabilities from the evolution of (micro-)seismicity over-estimate values obtained from pumping tests. The explanation lies in the fact that for critically stressed DFN, the driving and triggering force of (micro-)seismic events corresponds to the fast aseismic slipping patch propagation and not the pore-pressure front.

Although the modelling approach is relative simple (constant friction and constant fractures permeability), it allowed us to investigate important physical mechanisms that occur at depth during hydraulic stimulation of fractured rock masses. Obviously, the parametric space defined by the governing dimensionless parameters must be spanned more widely with additional simulations. This is an on-going work. Other interesting scenarios that could also be investigated: i) change type of injection to a constant rate (with a stopping when the pressure approaches the minimum principal effective normal stress at depth - else a fully coupled hydro-mechanical solver is needed), ii) variation of the DFN parameters, notably the percolation parameter that govern fluid diffusion into the pre-existing fractures at macroscopic scale, iii) allow for a frictional weakening type of friction coefficient (which allows to have nucleation of dynamic ruptures) or iv) adding

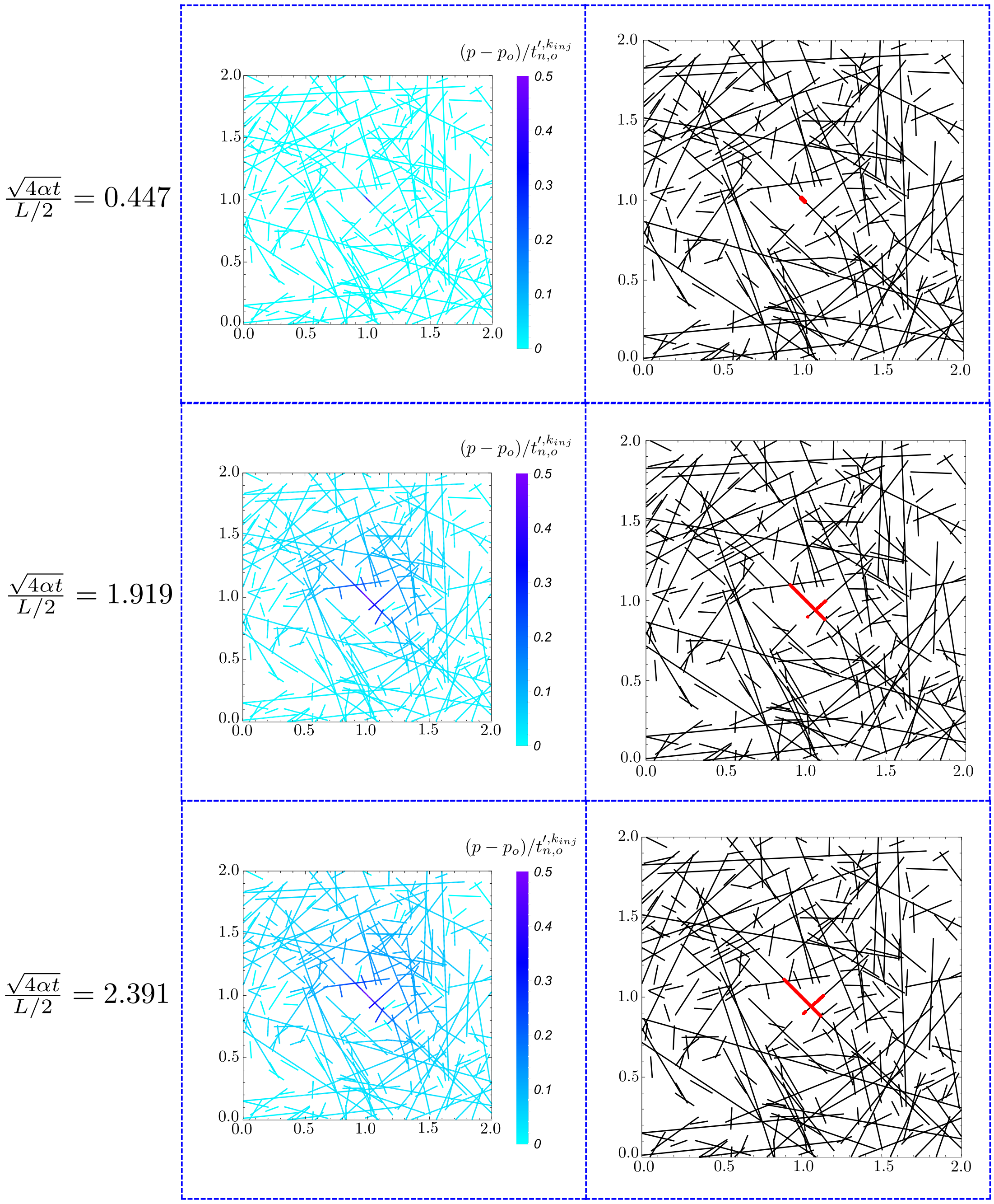

Figure 6.9 – Evolution of normalized over-pressure (left column) and plasticity localization (shear deformations - right column) along the pre-existing marginally pressurized ($\kappa = 2$) fracture network in function of normalized time/fluid front position $\frac{\sqrt{4\alpha t}}{L/2}$. Fluid is injected at moderate over-pressure $\Delta P/t_{n,o}^{\prime,k_{inj}} = 0.5$ into one fracture that intersect the injection point located at $(1, 1)$.

heterogeneous friction properties and/or fracture hydraulic properties (function of stress criticality).

7 Conclusions

Summary

This thesis aimed at investigating quasi-static fluid driven crack(s) propagation along pre-existing discontinuities within impermeable linearly elastic materials. This has been achieved by developing specific numerical algorithms that have been extensively verified against existing analytical and semi-analytical solutions. The devised numerical solvers have been used to get insights into some important physical mechanisms that occur at depth during hydraulic stimulation of fractured rock masses.

Although the numerical models proposed are in their constituents relatively simple, they were intentionally devised to be a simplification of reality rather than an imitation of reality. The intention was not to model all the geological complexity, but rather to address specific questions and capture important mechanisms with simplified, accurate and reliable models. This approach is of great importance as rock mechanics modelling fall into the class of "data-limited problems" and as such have to be used cautiously and thoughtfully (Starfield & Cundall 1988).

As a direct extension of the contribution of Garagash & Germanovich (2012), Chapter 4 investigated in details the effect of dilatancy on fluid driven shear crack propagation along a planar fault with frictional weakening properties. A planar bidimensional model was developed, together with a fully coupled hydro-mechanical solver which allowed to span all the parametric space identified by a dimensional analysis. Thanks to the combination of theoretical and numerical investigations, the results revealed that the mechanism of shear-induced dilatancy can stabilize an otherwise unstable fault. Although counter-intuitive, this is valid only for sufficiently large values of injection pressures such that residual friction is reached over a small length scale near the shear crack tip. By using linear elastic fracture mechanics (LEFM) under small scale yielding approximation, it could also be possible to show that there exist a critical value of dilatancy above which an unabated dynamic rupture is totally suppressed. This theoretical estimate has been confirmed by numerous simulations. Further numerical investigations showed that permeability increases with shear crack propagation lead to faster aseismic growth but do not impact the stabilizing effect of dilatancy. These results are important in the context of induced seismicity associated with engineering operations in deep fractured reservoirs.

The numerical solver developed for the frictional weakening dilatant fault can solve planar shear crack propagation (mode II) driven by fluid flow. In Chapter 5, a new boundary element based plasticity solver for mixed mode fracture propagation and shear bands was described. Although this hydro-mechanical solver is only one-way coupled, which means that flow influences the mechanical response but not vice-versa, it allows to investigate large scale problems defined over finite or infinite domains. This is efficiently achieved thanks to the use of a hierarchical approximation of the elasticity matrix combined with an ad-hoc preconditioner that improve the spectral properties of the final non-linear system of equations. The solver has been validated against several analytical and numerical solutions, showing good accuracy and efficiency even for large compression values of the elasticity matrix. Unlike existing numerical solvers based on local plasticity theory and softening constitutive relations, the numerical scheme proposed in Chapter 5 does not show any mesh dependency if the plastic evolution is localized along the exact (theoretical) failure plane and the softening material length scale is properly captured with a relatively large number of finite elements. This numerical solver was used to address various geo-mechanical problems, such as tensile wellbore failure due to wellbore pressurization and the well-known case of rigid retaining wall under active lateral Earth pressure. For all the problems addressed a good match between numerical and analytical results (when available) was obtained.

Finally preliminary numerical investigations on the interplay between aseismic slipping patch and fluid front position in a Discrete Fracture Network have been carried out. A scaling analysis has allowed to highlight the governing dimensionless parameters. As expected, the results revealed that the aseismic slipping patch propagates must faster than fluid diffusion on a critically stressed DFN, while the opposite scenario occur on a marginally pressurized DFN. Further investigations, however, must be carried out in order to span all the parametric space defined by the governing parameters.

Future perspectives

This Ph.D. work provides specific numerical algorithms that can be used mainly in the context of hydraulic stimulation of deep fractured reservoirs. However, there are several aspects that have been neglected.

In particular, the following physical phenomena should be further investigated:

- Full coupling between fluid flow within pre-existing discontinuities and elastic deformations in the numerical solver for localized inelastic deformations described in Chapter 5. This is of great importance when modelling hydraulic fracturing as well as hydro-shearing stimulation, in which the coupling between elasticity and fluid flow is very stiff (highly non-linear permeability evolution). Although the algorithm's architecture would remain similar, the sparsity pattern of the final system of equations (5.25) will change and with that its spectral properties. For this reason, a new ad-hoc preconditioner would have to be developed.

- In order to address problems that involve fluid driven fracture(s) propagation in intact rocks, the numerical solver presented in Chapter 5 should be extended to add elements on the fly when, for instance, when a stress criterion is locally reached. In its current version, fluid driven crack(s) propagation is restricted to occur only along pre-existing fractures or faults (i.e. pre-existing discontinuities) that must be pre-meshed with finite segments before fluid injection. This modelling approach is valid until the cracks reach the end of the computational mesh, after which the potential creation of new fracture surfaces is expected. Furthermore, for interior problems that involve plastic localization into shear bands whose location is not known a priori, having the possibility of adding segments on the fly in the current (exact) direction of plastic flow would avoid the mesh dependency problem that occurs otherwise. This extension opens another physical aspect: the coalescence between propagating fractures in intact rocks. Although this problem has already been investigated in the literature (Bobet & Einstein 1998*a*,*b*), it represents a non trivial numerical challenge, which would benefit from a local adaptive mesh refinement.

- In the model developed for fluid injection into a frictional weakening planar fault (see Chapter 4), only a simple linear friction weakening law has been used. The extension to more sophisticated friction laws can be done, using for instance well accepted phenomenological rate & state friction laws (Dublanchet 2019).

- Furthermore, the model of planar dilatant fault is built on the underlaying hypothesis that fluid flow is only occuring within the fault without leak-off in the surrounding rock mass. This hypothesis has an important (stabilising) effect during the undrained fault response at high slip rates. A possible extension of the model would include the leak of fluid from the fault plane to the surrounding medium, using for instance a Carter leak-off approximation (Howard & Fast 1957, Lecampion et al. 2018) or a pressure-dependent leak-off model. This will modify the conclusions with respect to the stabilizing effect of shear-induced dilatancy, since the leak of fluid will surely reduce the pore pressure drop during undrained conditions.

- A last extension of the fault model would be to include others weakening effects that typically take place during dynamic propagation of shear crack, such as flash heating and/or thermal pressurization. It would be interesting, indeed, to investigate whether the stabilizing effect of dilatancy is still valid when theses dynamic effects are accounted.

In parallel, a number of computational improvements could also allow a speed up of the computations:

- Parallelization onto multi-threads of the hierarchical matrix-vector dot product. This operation, in fact, represents the computational bottleneck (hot spot) of the numerical solver introduced in Chapter 5, and is way more computationally expensive than the others sparse matrix-vector dot products required to solve the final system of equations (5.25). Since it is located in the most "inner" part of the algorithm (for each yielding iteration and for each fixed point iteration, the $\mathcal{H}$-matrix-vector product is adopted during GMRES iterations), its computation with multi-threading would lead to a tremendous speed up, especially for numerical problems characterised by a large number of degrees of freedom, say $\mathcal{O}(n^6)$. This can be done using Intel Threading Building Blocks (TBB) library, for instance, which allows recursive parallelism (Reinders 2007).
- Another possible solution is to rewrite the fully implicit hydro-mechanical solvers presented in Chapters 4 and 5 using a combination of implicit and explicit time integration. This would be beneficial during slow aseismic slip propagation for which an implicit version would be used (without having any restrictions on the time stepping), while a fully explicit scheme would be used accelerated growth and nucleation / propagation of dynamic ruptures (where small time-steps are required to capture the system response anyway).

A Stress kernels of boundary integral equations for plane elasticity

The stress components σ^s_{ij} and σ^n_{ij} at a generic point x_i due to a shear and normal displacement discontinuity applied on the reference element can be obtained by evaluating analytically the 12 integrals in equation (2.59), which for the relations (2.49) and (2.50) can be rewritten as

$$\begin{aligned}\sigma^s_{ij}(x'_1,x'_2) &= -\underbrace{\int_{-1}^{+1}\frac{\partial s_{ij1}}{\partial\xi}N_1(\xi)\mathrm{d}\xi}_{\sigma^{s,1}_{ij}}\times d^1_s-\underbrace{\int_{-1}^{+1}\frac{\partial s_{ij1}}{\partial\xi}N_2(\xi)\mathrm{d}\xi}_{\sigma^{s,2}_{ij}}\times d^2_s\\ \sigma^n_{ij}(x'_1,x'_2) &= \underbrace{\int_{-1}^{+1}\frac{\partial s_{ij2}}{\partial\xi}N_1(\xi)\mathrm{d}\xi}_{\sigma^{n,1}_{ij}}\times d^1_n-\underbrace{\int_{-1}^{+1}\frac{\partial s_{ij2}}{\partial\xi}N_2(\xi)\mathrm{d}\xi}_{\sigma^{n,2}_{ij}}\times d^2_n\end{aligned} \tag{A.1}$$

Let us consider one integral in equation (A.1), say the stresses $\sigma^{s,1}_{ij}$ due to a unit shear displacement discontinuity interpolated only with the shape function $N_1(\xi)$ (unit value at the left node of the reference element). Upon integration by parts, this integral can be rewritten as

$$\sigma^{s,1}_{ij}\times\frac{\pi(\kappa+1)}{2G}=\left[h_{ij1}N_1(\xi)\right]^{\xi=+1}_{\xi=-1}-\int_{-1}^{+1}h_{ij1}\frac{\partial N_1(\xi)}{\partial\xi}\mathrm{d}\xi, \tag{A.2}$$

which can be easily solved analytically using Mathematica for instance (knowing that the h_{ijk} components are given by (2.47)).
By doing the same for all the integrals, which they reduce to 8 integrals due to the symmetry of h_{ijk}, one gets the following analytical expressions for the stress kernels:

$$\sigma^{n,1}_{22}\times\tfrac{\pi(\kappa+1)}{2G}=\tfrac{2x_1x_2^2}{x_1^4+2\left(x_2^2-1\right)x_1^2+\left(x_2^2+1\right)^2}-\tfrac{(x_1+1)\left((x_1+1)^2+3x_2^2\right)}{\left((x_1+1)^2+x_2^2\right)^2}+\tfrac{1}{2}\tanh^{-1}\left(\tfrac{2x_1}{x_1^2+x_2^2+1}\right)$$

$$\sigma^{n,2}_{22}\times\tfrac{\pi(\kappa+1)}{2G}=-\tfrac{2x_1x_2^2}{x_1^4+2\left(x_2^2-1\right)x_1^2+\left(x_2^2+1\right)^2}+\tfrac{(x_1-1)\left((x_1-1)^2+3x_2^2\right)}{\left((x_1-1)^2+x_2^2\right)^2}-\tfrac{1}{2}\tanh^{-1}\left(\tfrac{2x_1}{x_1^2+x_2^2+1}\right)$$

$$\sigma_{22}^{s,1} \times \frac{\pi(\kappa+1)}{2G} = \sigma_{12}^{n,1} \times \frac{\pi(\kappa+1)}{2G} = \frac{2(x_1-1)(x_1+1)^2 x_2 - 2(3x_1+1)x_2^3}{\left((x_1-1)^2+x_2^2\right)\left((x_1+1)^2+x_2^2\right)^2}$$

$$\sigma_{22}^{s,2} \times \frac{\pi(\kappa+1)}{2G} = \sigma_{12}^{n,2} \times \frac{\pi(\kappa+1)}{2G} = \frac{(2-6x_1)x_2^3+2(x_1-1)^2(x_1+1)x_2}{\left((x_1-1)^2+x_2^2\right)^2\left((x_1+1)^2+x_2^2\right)}$$

$$\sigma_{11}^{n,1} \times \frac{\pi(\kappa+1)}{2G} = \sigma_{12}^{s,1} \times \frac{\pi(\kappa+1)}{2G} = -\frac{2x_1x_2^2}{x_1^4+2\left(x_2^2-1\right)x_1^2+\left(x_2^2+1\right)^2} + \frac{(x_1+1)x_2^2-(x_1+1)^3}{\left((x_1+1)^2+x_2^2\right)^2} + \frac{1}{2}\tanh^{-1}\left(\frac{2x_1}{x_1^2+x_2^2+1}\right)$$

$$\sigma_{11}^{n,2} \times \frac{\pi(\kappa+1)}{2G} = \sigma_{12}^{s,2} \times \frac{\pi(\kappa+1)}{2G} = \frac{2x_1x_2^2}{x_1^4+2\left(x_2^2-1\right)x_1^2+\left(x_2^2+1\right)^2} + \frac{(x_1-1)\left((x_1-1)^2-x_2^2\right)}{\left((x_1-1)^2+x_2^2\right)^2} - \frac{1}{2}\tanh^{-1}\left(\frac{2x_1}{x_1^2+x_2^2+1}\right)$$

$$\sigma_{11}^{s,1} \times \frac{\pi(\kappa+1)}{2G} = \begin{cases} \frac{2x_2\left(x_2^4+(x_1(2x_1+3)+3)x_2^2+(x_1-2)(x_1-1)(x_1+1)^2\right)}{\left((x_1-1)^2+x_2^2\right)\left((x_1+1)^2+x_2^2\right)^2} + \tan^{-1}\left(\frac{x_1-1}{x_2}\right) - \tan^{-1}\left(\frac{x_1+1}{x_2}\right) & x_2 \neq 0 \\ \frac{1}{2}\pi\left(\frac{x_1-1}{\sqrt{(x_1-1)^2}} - \frac{x_1+1}{\sqrt{(x_1+1)^2}}\right) & x_2 = 0 \end{cases}$$

$$\sigma_{11}^{s,1} \times \frac{\pi(\kappa+1)}{2G} = \begin{cases} \frac{-2x_2^5+\left(-4x_1^2+6x_1-6\right)x_2^3-2(x_1-1)^2(x_1+1)(x_1+2)x_2}{\left((x_1-1)^2+x_2^2\right)^2\left((x_1+1)^2+x_2^2\right)} + \tan^{-1}\left(\frac{1-x_1}{x_2}\right) + \tan^{-1}\left(\frac{x_1+1}{x_2}\right) & x_2 \neq 0 \\ \frac{1}{2}\pi\left(\frac{1-x_1}{\sqrt{(x_1-1)^2}} + \frac{x_1+1}{\sqrt{(x_1+1)^2}}\right) & x_2 = 0 \end{cases}$$

Note that the stresses are singular for $x_1 = \pm 1$ and $x_2 = 0$ (see Figure A.1). In addition to this, some stress components are singular for $x_1 = \xi$ and $x_2 = 0$, which requires the evaluation of the Principal Values and a limiting process after integration.

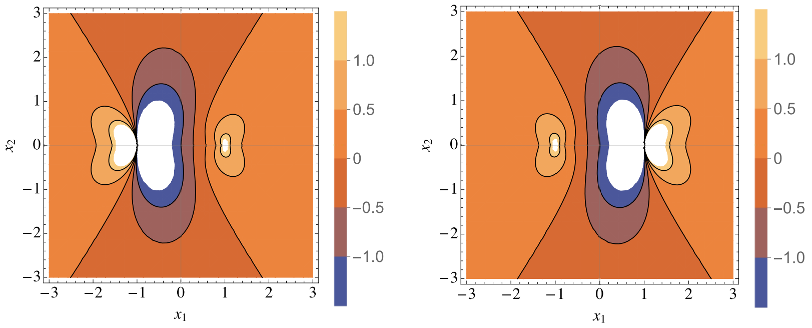

(a) $\sigma_{22}^{n,1} \times \frac{\pi(\kappa+1)}{2G}$.   (b) $\sigma_{22}^{n,2} \times \frac{\pi(\kappa+1)}{2G}$.

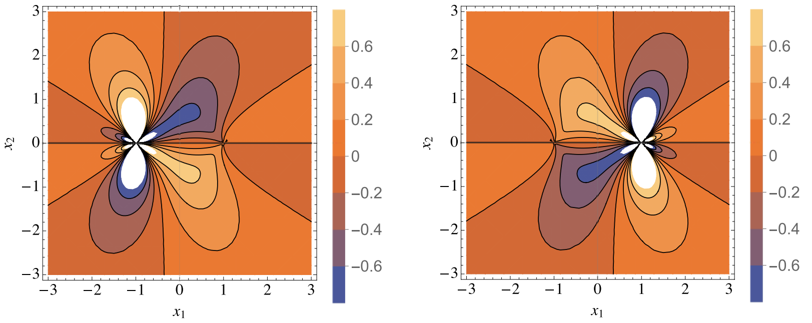

(c) $\sigma_{22}^{s,1} \times \frac{\pi(\kappa+1)}{2G} = \sigma_{12}^{n,1} \times \frac{\pi(\kappa+1)}{2G}$.   (d) $\sigma_{22}^{s,2} \times \frac{\pi(\kappa+1)}{2G} = \sigma_{12}^{n,2} \times \frac{\pi(\kappa+1)}{2G}$.

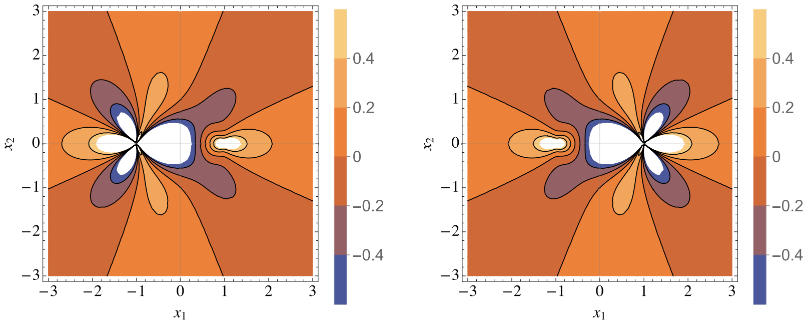

(e) $\sigma_{11}^{n,1} \times \frac{\pi(\kappa+1)}{2G} = \sigma_{12}^{s,1} \times \frac{\pi(\kappa+1)}{2G}$.   (f) $\sigma_{11}^{n,2} \times \frac{\pi(\kappa+1)}{2G} = \sigma_{12}^{s,2} \times \frac{\pi(\kappa+1)}{2G}$.

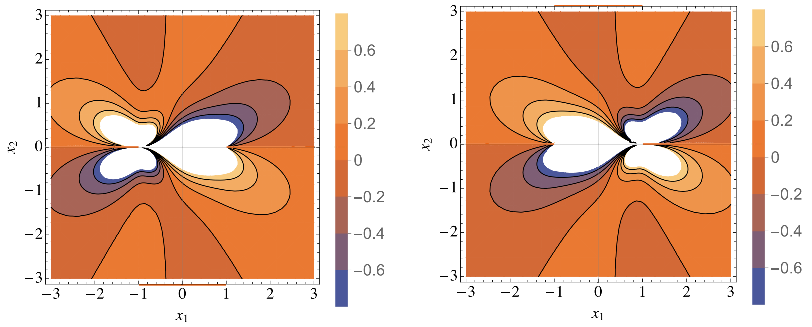

(g) $\sigma_{11}^{s,1} \times \frac{\pi(\kappa+1)}{2G}$.   (h) $\sigma_{11}^{s,2} \times \frac{\pi(\kappa+1)}{2G}$.

Figure A.1 – Normalized stress components due to unit linear displacement discontinuity acting on the reference element.

B Accelerated boundary element method via hierarchical matrix

Unlike domain discretization methods, such as finite element method or finite volume method, boundary element method reduces the problem dimension of one by building the approximate numerical solution only along the boundary of the problem. Although this achievement is particularly great for 3-D large scale problems, this numerical method leads to intrinsic bottlenecks that have pushed scientists in late nineties to find out alternative solutions.

Because of the non-local nature of the boundary integral operators (kernels) involved in the boundary element method, the resulting final elastic matrix is dense (i.e. fully populated, see Figure 2.8 for an example). The memory requirement to store such a matrix scales as $\mathcal{O}(n^2)$[1] for n degrees of freedom, which consequently set a strict constraint for current available laptops with 64-bit processors. Rather small size problems, in fact, can be addressed, notably all problems whose degrees of freedom range between $\mathcal{O}(n^4)$ and $\mathcal{O}(n^5)$. Furthermore, the computational cost required to solve the final elastic system may represent an additional bottleneck.

Generally, a linear system of equations can be solved either with *direct methods* or with *iterative methods*. The formers are usually appropriate for very small size problems as their computational complexity scales as $\mathcal{O}(n^3)$, whereas iterative methods are more attractive for slightly larger problems as their computational complexity scales as $\mathcal{O}(n^2)$ for each iteration k (and typically $k \ll n$). However, when boundary element method is used for large models (say $\mathcal{O}(n^6)$), even iterative methods are prohibitive and acceleration techniques must be used to speed up computations.

In the next sections, a quick overview of the main acceleration techniques for boundary element method is presented as well as an in-depth description of the hierarchical matrix technique combined with adaptive cross approximation (ACA), which is the acceleration technique used in this contribution.

---

[1] Note that also the computing time for the evaluation of the elastic matrix scales as $\mathcal{O}(n^2)$ since the effects of all the elements on themselves has to be calculated (which requires a double nested loop).

B.1 Overview & general idea

In the last decades of 20-th century, several numerical techniques have been introduced in order to speed up computations of non-local integral operators (Greengard 1994). Specifically, large research efforts have been devoted to the numerical evaluation of a generic integral (or its discretized version)

$$\mathcal{L}(\mathbf{x}) = \int K(\mathbf{x},\mathbf{y})u(\mathbf{y})\mathrm{d}\mathbf{y}, \tag{B.1}$$

in which the kernel $K(\mathbf{x},\mathbf{y})$ is non-local and decays in space. This particular integral operator is commonly involved in elliptic boundary value problems that can arise in many applications, such as problems in acoustics, electromagnetism, elasticity etc.

The first contributions in this respect started in 1981 when Hockney & Eastwood (1981) introduced a particle-mesh method in order to simulate large scale gravitational Coulombic systems. In the same period, Appel (1985) and others developed what is known as "tree code" in which pre-existing particles are clustered into groups based on the fact that the gravitational field decays in space and its far field is smooth. A cluster of particles is thus replaced by a simpler representation, which is used to compute the influence of the cluster at sufficiently great distances (Greengard 1994).

Following the same idea used in the "tree code" method, a couple of years later Rokhlin (1985) introduced the Fast Multipole Method in the context of classical potential theory. The main idea behind this method stems from the observation that far away from a collection of sources, the potential field can be expanded with an analytical series. Although this technique reduces the computational cost to evaluate (B.1) from $\mathcal{O}(n^2)$ to $\mathcal{O}(n \cdot \log(n))$, it requires complicated mathematical derivation of the integral operator.

Few years later, Hackbusch & Nowak (1989) introduced another acceleration technique for non-local integral operators: the panel clustering method. With this numerical technique, large problems can be addressed by using an expansion of the kernel function and decompositions of the spatial domain with "panels" (domain decomposition). It can be proved that the computational complexity of such algorithm is $\mathcal{O}(N\log^{d+2}N)$, where d is the dimension of the problem.

Recently, a new acceleration technique called hierarchical matrix ($\mathcal{H}$-matrix) technique has been developed by Hackbusch (2015*b*). This technique is purely based on an algebraic approach and it allows to approximate and consequently to speed up the usual matrix operations, such as addition, multiplication, inversion etc (Hackbusch 2015*b*, Bebendorf & Rjasanow 2003). In addition to this, this technique is kernel agnostic, i.e. it can be applied to any kind of integral operators if and only if they decay in space.

In the context of boundary element method, notably displacement discontinuity method, the integral operator for stress calculation decays as $\frac{1}{r^2}$ in 2-dimensional space (see Section 2). In Figure B.1, an example of stress decay in space is showed. A linear shear displacement discontinuity is applied on an element of size a, whose centre corresponds with the origin of the local reference system. This element is embedded in an infinite,

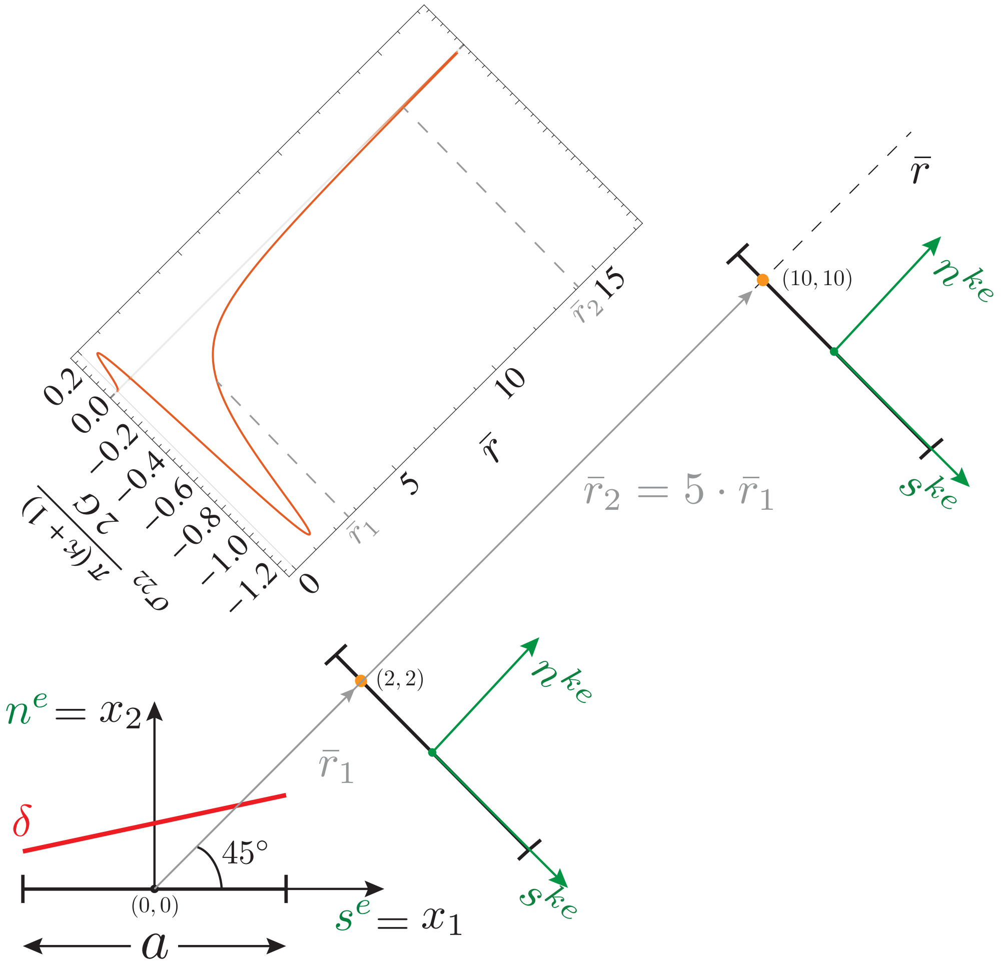
0.2
0.0
−0.2
−0.4
−0.6
−0.8
−1.0
−1.2
$\sigma_{22}\frac{\pi(\kappa+1)}{2G}$
0
5
10
15
$\bar{r}$
$\bar{r}_1$
$\bar{r}_2$
$\bar{r}$
(10, 10)
n^{ke}
s^{ke}
$\bar{r}_2 = 5 \cdot \bar{r}_1$
(2, 2)
n^{ke}
s^{ke}
$\bar{r}_1$
$n^e = x_2$
δ
45°
(0, 0)
$s^e = x_1$
a

Figure B.1 – Evolution of normalized σ_{22} stress along the normalized $\bar{r} = \frac{r}{a}$ -direction due to a linear shear displacement discontinuity acting on an element of length a. The stress evolution decays with normalized distance $\bar{r}$ due to the fast decay of the elastic displacement discontinuity kernel.

homogenous, linear elastic and isotropic medium, such that the stress distribution within the medium due to such a shear displacement jump can be calculated via the elastic boundary integral equation (2.34).

The normalized stress $\sigma_{22}\frac{\pi(\kappa+1)}{2G}$ is calculated along a pre-defined normalized direction $\bar{r} = \frac{r}{a}$, with inclination of 45° counter-clockwise with respect to x_1−axis (see Figure B.1). For a generic element k with a collocation point located at $\bar{r} = \bar{r}_1 = 2\sqrt{2}$, the corresponding normalized stress due to a linear shear displacement discontinuity is $\sigma_{22}\frac{\pi(\kappa+1)}{2G}\Big|_{\bar{r}=\bar{r}_1} \approx -0.3$ (see plot in Figure B.1), considerably larger in magnitude than the same normalized stress calculated on the same collocation point of the same element, upon shifting it along $\bar{r}$-direction of a distance $\bar{r}_2 = 5\bar{r}_1$. Specifically, $\sigma_{22}\frac{\pi(\kappa+1)}{2G}\Big|_{\bar{r}=\bar{r}_2}$ is $\sim 3.37\%$ of $\sigma_{22}\frac{\pi(\kappa+1)}{2G}\Big|_{\bar{r}=\bar{r}_1}$, denoting thus a fast decay of stress kernel with space.

Obviously, this can be generalized to the whole two dimensional space, leading thus to the conclusion that there is a closed area within the 2D elastic medium after which the stress induced by a shear displacement discontinuity become negligible.
Hierarchical matrix technique, therefore, makes use of this kernel property to approximate the far field contributions, i.e. those contributions that do not bring relevant information to the problem solution, in order to reduce memory requirements and, at the same time, speed up algebraic operations. In the next section, a description of this technique, combined with adaptive cross approximation, is reported.

B.2 $\mathcal{H}$-matrix and Adaptive Cross Approximation

$\mathcal{H}$-matrix technique uses a data-sparse representation to approximate dense matrices that result from discretization of non-local operators. Notably, the H-matrix technique makes use of low-rank[2] matrices and their approximation to represent dense matrices during their storage and their usage in arithmetic operations. Compared to general dense matrices, in fact, low rank matrices contain less independent information, reducing thus the storage requirements (Bebendorf 2008*a*).
Denoting as $\mathbb{C}_k^{m\times n}$ a group of matrices each characterised by at most k linearly independent rows or columns, an efficient representation of a generic matrix $A \in \mathbb{C}_k^{m\times n}$ is given by

$$A = UV^H, \tag{B.2}$$

where $U \in \mathbb{C}^{m\times k}$ and $V \in \mathbb{C}^{n\times k}$ are two auxiliary matrices that allow to change the entrywise representation of matrix A to outer-product form. Theoretically, this representation is always possible since only k columns or rows of matrix A are sufficient to represent the whole matrix. Hence, instead of saving in memory $m \cdot n$ entries, only $k\,(m+n)$ entries are stored, reducing thus the storage requirements when $k \ll n$ or $k \ll m$. Only under this conditions, the matrix A can be considered as low-rank matrix, i.e. a rank deficit matrix with $k(m+n) \ll m \cdot n$.
It can also be proven that the outer-product form of a low-rank matrix facilitates matrix-vector multiplications, i.e. it reduces the arithmetic operations from $2m\cdot n$ to $2k(m+n)-k$ operations (Bebendorf 2008*a*).

Since the final matrix that result from discretization of non-local operators are invertible and thus full rank (see for instance the final elastic matrix in Figure 2.8), the problem reduces to find an efficient numerical technique that allows to approximate the entrywise representation of such a matrix by low-rank matrices, within a given intrinsic error. This is certainly an approximation and it can not be avoided as the exact global representation of a dense matrix by a low-rank matrix is not feasible for modern laptops. The idea, therefore, is to decompose hierarchically the final dense matrix into sub-blocks, such that some of those can be approximated by low-rank matrices.

---

[2] The rank of a matrix $A \in \mathbb{C}^{m\times n}$ is the maximum number of linearly independent column or row vectors. When the rank of matrix A equals the minimum between m or n, then A is said to be full rank. Otherwise, A is said to be rank deficit.

B.2.1 Clustering and admissibility condition

Because of the non-local nature of elliptical integral operators along a computational mesh, a block domain decomposition of the problem is a powerful technique to cluster its degrees of freedom, such that constitutive indices of each cluster correspond to points interacting at close range (Chaillat et al. 2017). Although there are several algorithms for block domain decomposition, hierarchical matrix technique involves a hierarchical domain decomposition through a binary cluster tree, often called *cluster tree* $\mathcal{T}_{\mathcal{I}}$. As suggested by its name, this data structure is composed of

- a *root* $\mathcal{I}$ that contains the indices of all the degrees of freedom, such that $\mathcal{I} \times \mathcal{I}$ represents the whole matrix resulting from discretization of integral operator,
- *nodes* that are nothing else but the subsequent clusters $t, s \subset \mathcal{I}$ that result from recursive block domain decomposition and
- *leaves* that are nodes with cardinality equal to the minimum value n_{leaf}. In other words, leaves are blocks without sons.

Typically, the cluster tree is built recursively by splitting the computational domain via bounding boxes. During the first partitioning, for instance, the problem domain is fully enclosed in a bounding box, which is then split into two boxes through a separation plane. The two resulting boxes are in turn split into two others boxes respectively, and so on. Depending on the position of the separation plane at each recursive partitioning, two types of cluster tree can be built:

1. *balanced cluster tree*, for which each nodes are split into two clusters with approximately equal cardinality,
2. *geometric cluster tree*, for which the resulting bounding boxes after each partitioning have approximately equal volume.

It is worth mentioning that during the construction of the cluster tree, a renumbering of the degrees of freedom may occurs (Desiderio 2017).

In Figure B.2 an example of geometric clustering of the domain applied to a 2-dimensional discrete fracture network is reported. Notably, the problem domain is recursively decomposed into two equal-sized sub-boxes by means of a hyperplane (of dimension 1 in 2-dimensional space), using the algorithm introduced by Börm et al. (2003). This algorithm, in fact, allows to build a geometric cluster trees by calling recursively a splitting procedure (which has been coded up in Mathematica), until the cardinality of each node reaches n_{leaf} [3].
Each mesh node $x_i \in \mathbb{R}^2$ is associated to an index $i \in \mathbb{N}$ (i.e. mapping) such that all mesh nodes forms a set $\mathcal{I}$ of indices. The splitting procedure by bisection is then applied recursively to $\mathcal{I}$ in order to build the geometric cluster tree (starting from its root, until its leaves) and consequently in order to decompose the problem domain. The number of nodes created at each stage of partitioning p are thus

$$n = 2^p$$

In the specific example of Figure B.2, only three recursively splitting have been performed ($p = 3$), hence obtaining 8 nodes at the bottom of the tree. Due to the univocal mapping between the indices and the mesh nodes, the decomposed domain can be easily re-computed a posteriori (see Figure B.2).

A direct consequence of the domain decomposition via a cluster tree $\mathcal{T}_{\mathcal{I}}$ is that each node of the cluster can be used to define a matrix sub-block of the fully-populated matrix that results from discretization of (B.1). Indeed, the so called block cluster tree $\mathcal{T}_{\mathcal{I}\times\mathcal{I}}$ can be build recursively by running through all the nodes of the cluster tree, starting from its root up to its leaves.
Referring to the example of Figure B.2, the geometric cluster tree built for the 2-dimensional discrete fracture network would lead to the following matrix partitioning

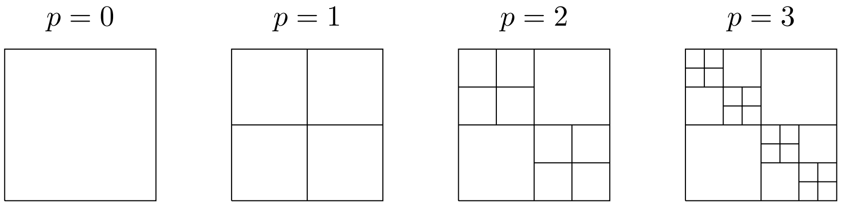

When $p = 0$, the root of the cluster tree $\mathcal{I}$ defines the entire matrix in the block cluster tree $\mathcal{T}_{\mathcal{I}\times\mathcal{I}}$.
If some sub-blocks of the partitioned matrix can be successfully approximated by low-rank matrices and thus stored as (B.2), then a considerably gain in terms of memory requirements and speed up of algebraic operations can be achieved. A condition is thus needed to establish whether a cluster pair $(t, s) \in \mathcal{T}_{\mathcal{I}\times\mathcal{I}}$ can be approximated or not.

---

[3] This parameter defines thus the depth of the tree.

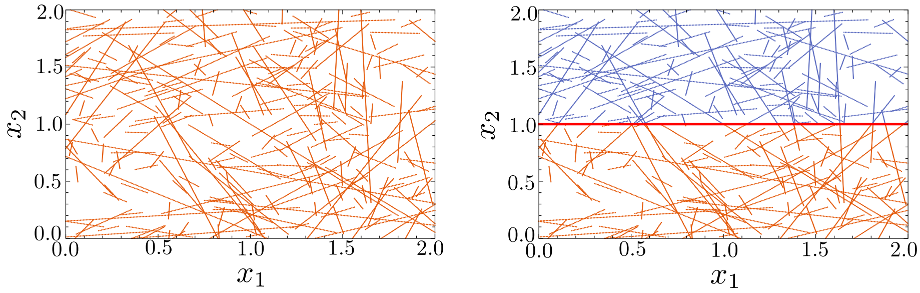

(a) $\mathcal{I}_1^{(0)} = \mathcal{I}$ (b) $\mathcal{I}_1^{(1)}$ (blue) and $\mathcal{I}_2^{(1)}$ (orange)

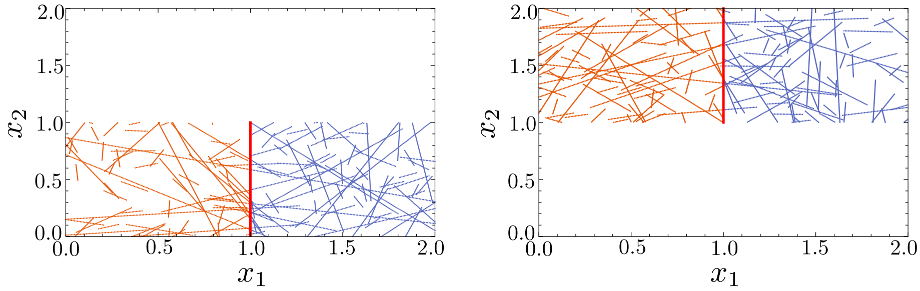

(c) $\mathcal{I}_1^{(2)}$ (blue) and $\mathcal{I}_2^{(2)}$ (orange) (d) $\mathcal{I}_3^{(2)}$ (blue) and $\mathcal{I}_4^{(2)}$ (orange)

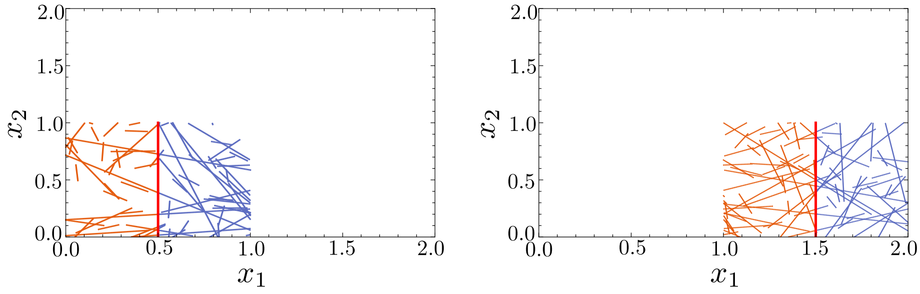

(e) $\mathcal{I}_1^{(3)}$ (blue) and $\mathcal{I}_2^{(3)}$ (orange) (f) $\mathcal{I}_3^{(3)}$ (blue) and $\mathcal{I}_4^{(3)}$ (orange)

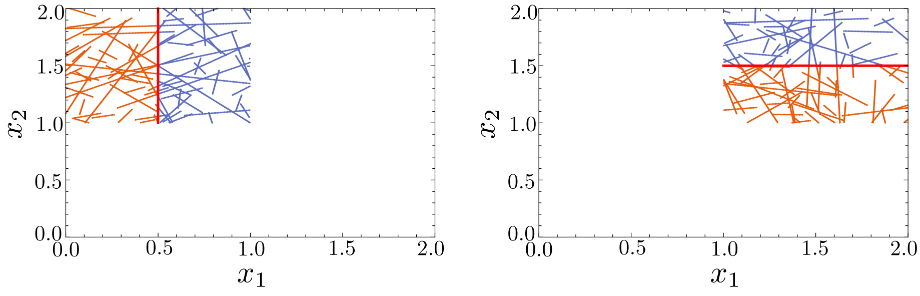

(g) $\mathcal{I}_5^{(3)}$ (blue) and $\mathcal{I}_6^{(3)}$ (orange) (h) $\mathcal{I}_7^{(3)}$ (blue) and $\mathcal{I}_8^{(3)}$ (orange)

Figure B.2 – Example of block domain decomposition of a discrete fracture network via geometric clustering algorithm introduced by Börm et al. (2003). Three recursive clusterings ($p = 3$) have been computed, thus obtaining 8 nodes of the geometric cluster tree.

For asymptotically smooth kernels [4], such as the one of displacement discontinuity method, the admissibility condition is given by

$$Adm(t,s) = \text{true} \iff \min\{\text{diam}(t), \text{diam}(s)\} \leq \eta \cdot \text{dist}(t,s), \tag{B.3}$$

where the diameter of a cluster $t \in \mathcal{T}_{\mathcal{I}}$ is defined as

$$\text{diam}(t) := \max_{i,j \in t} ||\mathbf{x_i} - \mathbf{x_j}|| \,, \tag{B.4}$$

and the distance between two clusters $t, s \in \mathcal{T}_{\mathcal{I}}$ is

$$\text{dist}(t,s) := \min_{i \in t, j \in s} ||\mathbf{x_i} - \mathbf{x_j}|| \tag{B.5}$$

Note that the computations of the diameter of each cluster as well as their relative distance are too expansive, so these quantities are commonly replaced by bounding boxes. This admissibility condition depends only on one parameter η, which govern the severity of the sub-blocks partitioning. Basically, it states that if two clusters are geometrically located far away between each others, then the generic contribution of one of them onto the other is small enough (due to the smooth decay of the kernel) such that the resulting sub-block matrix can be approximated with low-rank matrix format. By applying this admissibility condition to all the pair-nodes composing the block cluster tree $\mathcal{T}_{\mathcal{I} \times \mathcal{I}}$ in a hierarchical way, one can get a partitioning of the final dense matrix (arising from the full problem discretization) into admissible and inadmissible blocks (see Figure B.3 for a real example). Hence, admissible blocks are approximated with low-rank matrices, whereas inadmissible blocks are stored and treated as dense matrices (full rank representation). It is straightforward to understand that sub-blocks located along the main diagonal of the final dense matrix are always inadmissible since the self-effects' contributions are always the most relevant.

B.2.2 Low-rank approximation using ACA

All admissible cluster pairs $(t,s) \in \mathcal{T}_{\mathcal{I} \times \mathcal{I}}$ that arise from hierarchical clustering of a dense matrix $\mathcal{A}$ can be approximated with low-rank matrices and stored in outer-product form (B.2). The resulting matrix is a hierarchical representation $\mathcal{A}_{\mathcal{H}}$ of matrix $\mathcal{A}$.
Although the Eckart-Young theorem states that the best low rank approximation of a matrix A in $\mathbb{C}_k^{m \times n}$ is given by its truncated Singular Value Decomposition (Bebendorf

---

[4] A kernel function $K(\cdot,\cdot)$ is called *asymptotically smooth* if there constants $C_{as1}, C_{as2} \in \mathbb{R}_{>0}$ satisfying

$$\left|\partial_x^\alpha \partial_y^\beta K(x,y)\right| \leq C_{as1} \left(C_{as2} \, ||x-y||\right)^{-|\alpha|-|\beta|} \alpha + \beta \, |g(x,y)|,$$

for all multi-indices $\alpha, \beta \in \mathbb{N}_0^d$ and all $x, y \in \mathbb{R}^d$ with $x \neq y$ [X].

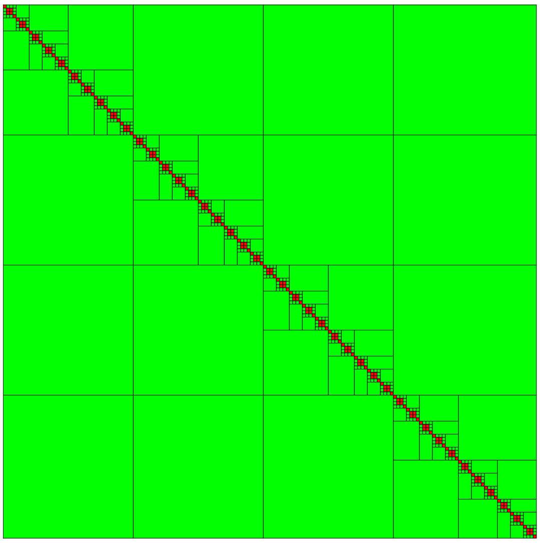

Figure B.3 – Example of block hierarchical partitioning of a dense matrix resulting from discretization of non-local elastic operator. Based on the admissibility condition (B.3), the matrix is subdivided into admissible blocks (green), for which low-rank approximation is applied, and inadmissible blocks (red). Note that all the sub-blocks located along the main diagonal are inadmissible (self-effects).

2008*a*)

$$A_r = \sum_{l=1}^{r} \mathbf{u}_l \mathbf{s}_l \mathbf{v}_l^H = USV^H \qquad \text{with } \text{r<k}, \tag{B.6}$$

the computational cost required to perform a truncated SVD is too high for modern laptops. For this reason, in the context of $\mathcal{H}$-matrix, several others techniques have been introduced for low-rank approximation of admissible blocks.

Partially-pivoted adaptive cross approximation is one of them. Basically, it is a numerical technique that aims at the constructions of low-rank approximants from few of the original entries of the discrete integral operator, instead of approximating its kernel function (Bebendorf 2008*a*). It can be proved that the application of $\mathcal{H}$-matrix combined with partially-pivoted adaptive cross approximation reduces the computational complexity of relevant matrix operations to

$$\mathcal{O}(n^\alpha) \to \mathcal{O}(n \cdot \log(n)^\alpha),$$

where n is the number of degrees of freedom of the problem and α is a parameter that depends on the type of operation, e.g $\alpha = 1$ for the storage requirement or matrix-vector multiplication and $\alpha = 2$ for matrix-matrix multiplication.

The aim of this thesis is not to enter into details of adaptive cross approximation technique. The reader, therefore, is invited to see Hackbusch (2015*b*), Bebendorf (2008*a*)

for full details. It is worth mentioning, however, that this technique relies only on parameter $\epsilon_{ACA} > 0$ that govern the stopping criterion for the approximation and thus the compression of each admissible block.
Upon construction of a hierarchical matrix $\mathcal{A}_{\mathcal{H}}$ with adaptive cross approximation, it is sometimes useful to quantify the total compression with respect to the initial dense matrix $\mathcal{A}$. This parameter is called *compression ratio* and it is defined as

$$c_r(\mathcal{A}_{\mathcal{H}}) := \frac{1}{n^2}\left(\sum_{(t,s)\in\mathrm{Leaf}^+(\mathcal{T}_{\mathcal{I}\times\mathcal{I}})} r(|t|+|s|) + \sum_{(t,s)\in\mathrm{Leaf}^-(\mathcal{T}_{\mathcal{I}\times\mathcal{I}})} |t|\cdot|s|\right), \tag{B.7}$$

where $(t,s) \in \mathrm{Leaf}^+(\mathcal{T}_{\mathcal{I}\times\mathcal{I}})$ and $(t,s) \in \mathrm{Leaf}^-(\mathcal{T}_{\mathcal{I}\times\mathcal{I}})$ are respectively admissible and non-admissible cluster pairs.

Among all the open source libraries for $\mathcal{H}$-matrix and adaptive cross approximation available in literature (written almost in any kind of programming language), in this contribution the C++ Hierarchical matrix library developed by InsideLoop in collaboration with S. Chaillat-Loseille (ENSTA) is used. This library is integral operator independent (kernel agnostic) and it is suited for both bi-dimensional and tri-dimensional problems. More importantly, it has been devised for both scalar and vectorial problems, such us elastic problems arising continuum mechanics. In the context of this thesis, this library allows to approximate boundary element matrices by a hierarchical approximation based on a mesh tree structure and low rank approximants of admissible blocks. It also contains a special direct solver based on a hierarchical LU decomposition algorithm, originally developed by Chaillat et al. (2017) for oscillatory kernels, and a matrix-free Generalized Minimal Residual Method for iterative solution of system of equations that can embed a Hierarchical matrix (with a right-preconditioned implementation based on (Saad 1992)). For further details about this library, the reader is invited to have a look at the online repository https://github.com/InsideLoop/HMatrix.

C HFPx2D: an open-source code for 2D fluid driven crack(s) propagation

This appendix describes the current state of the open-source code HFPx2D that is under development at Geo-energy Laboratory, Gaznat-Chair on Geo-Energy (GEL), at École Polytechnique Fédérale de Lausanne. This is the result of nearly four years of joint work between three members of GEL laboratory: Prof. B. Lecampion, Dr. D. Nikolskiy and F. Ciardo. Although the code is still under development for further extensions and improvements, its current version has reached a mature stage (at least from a code architecture point of view).

Authors' contributions: B.L. coded up the elasticity, i.e. the boundary integral elasticity equations discretized with a boundary element method suited for fracture problems (for full details see Chapter 2), while F.C. coded up fluid mass conservation equation using the finite volume scheme described in Chapter 3. This represent the numerical framework for all the hydro-mechanical solvers included in HFPx2D.
B.L. contributed actively in the development of *ElasticSolver* for static elastic benchmarks with and without hierarchical matrix as well as in the development of *MultiFracsSolver* together with D.N. This latter, however, is the main developer of *MultiFracsSolver*, which is a pseudo 3D multi-stage fracturing simulator for height constrained fractures. Indeed, D.N. developed the fully coupled hydro-mechanical solver that includes the coupling between fluid flow in fractures and elastic deformations (fractures opening) and the one between fluid flow in the wellbore and hydraulic fractures propagation.
F.C. devised the code architecture of HFPx2D. He also developed a fully coupled hydro-mechanical solver for fluid injection in a planar fault exhibiting frictional weakening properties (*PlanarFault*) as well as *MixedCohesiveFracsSolver*, which is a one-way coupled boundary element based solver for localized inelastic deformations that can be used to address various geo-mechanical/geo-technical problems.
In the following, more details about HFPx2D and its numerical solvers are reported.

C.1 Conception and current capabilities

HFPx2D is an open source C++ code for simulating hydraulic stimulation[1] of naturally fractured tight rock masses. Although this code can only address bi-dimensional problems (or pseudo 3D problems with one specific solver), it can be very useful for scientist or engineers to get insight into the physical phenomena that occur at depth upon fluid injection and activation of pre-existing fractures. Among other applications, HFPx2D can be used to simulate nucleation of shear dynamic ruptures (earthquakes) due to fluid injection in a planar fault or it can be used to simulate multi-stage hydraulic fracturing. It is capable of capturing all the non-linearities arising at crack tips due to dissipative processes (friction weakening, cohesion softening etc.) as well as the one arising from coupling fluid flow with elasticity. Therefore, its applicabilities can vary from hydro-shearing stimulation of deep geothermal systems to hydro-fracturing of unconventional reservoirs for oil and gas extraction.

The numerical framework behind HFPx2D is the one introduced in Chapters 2 and 3, i.e. elasticity is discretized with displacement discontinuity method (with piecewise linear displacement discontinuities), whereas a finite volume scheme is used for fluid flow. Some solvers of this code includes also the possibility of using the $\mathcal{H}$-matrix technique, combined with adaptive cross approximation introduced in Appendix B.

Currently, HFPx2D includes 4 solvers. Each of them addresses different problems. A generic user can choose one solver rather than another by providing its name in the configuration file[2]. In order to show all the main capabilities of this numerical code, a quick qualitative description of each solver is reported.

ElasticSolver As suggested by its name, this solver is a purely mechanical solver (no fluid flow). It has been devised to benchmark static elastic problems with piecewise linear displacement discontinuity elements (such us the Griffith crack under uniform pressure, arc crack subjected to a remote compressive state etc.), as well as to test the $\mathcal{H}$-matrix technique, combined with adaptive cross approximation. A generic user can decide to solve an elastic problem with fully populated elasticity matrix or with its hierarchical representation, via direct method (direct inversion or H-LU decomposition in case of $\mathcal{H}$-matrix) or via iterative method (GMRES with or without pre-conditioner). This solver provides also a simple numerical tool for testing the influence of $\mathcal{H}$-matrix parameters on the approximation of the numerical solution with respect to the analytical solution (if available).

---

[1] Although HFPx2D has been devised mainly to model hydraulic stimulation of deep reservoirs, it can be used also to address others geo-mechanical applications.

[2] HFPx2D requires a configuration file in .json format as a program argument. This file contains the geometry of the problem under investigation as well as all the input data.

PlanarFault This solver simulates the shear crack propagation paced by pore pressure expansion within a pre-existing planar fault. Upon fluid injection into the fault, a shear crack is activated and starts to propagate along the fault driven by fluid flow expansion. During its propagation, the frictional properties of the fault weakens with deformations along with a progressive crack opening in response of shear-induced dilatancy (up to a maximum value for large shear deformations).
This problem is fully coupled as pore pressure evolution perturbs elasticity through the Terzaghi's principle of effective stress and, vice-versa, elasticity affects pore pressure through dilatancy. Because of the weakening nature of the friction coefficient and dilatant fault behaviour, this problem is also highly non-linear.
A fully implicit algorithm has been devised to solve numerically this particular problem. The numerical results have been benchmarked against the semi-analytical ones of Garagash & Germanovich (2012), valid for a frictional weakening non-dilatant fault. The reader is invited to see Chapter 4 for full details about this problem and its numerical resolution.

MultiFracsSolver This solver represents a multi-stage fracturing simulator for height constrained fractures (see Figure C.1 for an example). Although the problem is three-dimensional in its nature, the solver uses a simplified 3D kernel with fixed fracture height introduced by Wu & Olson (2015) to reduce the problem to be bi-dimensional (basically, a plan view of the 3-dimensional problem is considered). It accounts for fully hydro-mechanical coupling between i) fluid flow in fracture and elasticity (fractures opening) and between ii) fluid flow in wellbore and hydraulic fractures propagation via fracture entry perforation friction. An ILSA scheme with universal tip asymptote is used for fractures propagation.
This solver has been validated against several analytical solutions, under different regimes of propagation. For full details about this numerical solver, see Nikolskly & Lecampion (2019).

MixedCohesiveFracsSolver This solver is an accelerated BEM based localized plasticity solver for fractures and shear bands. Plastic deformations localize along potential planes of deformations when yielding criteria are locally violated. Specifically, the constitutive relations for displacement discontinuity locus are composed of a Mohr-Coulomb criterion and a tensile vertical cut-off, with the possibility of softening or hardening of material's strength parameters (see Chapter 5 for full details). Although this solver is only one-way coupled, i.e. the mechanical problem is coupled to fluid flow problem through Terzaghi's principle of effective stress but the way around is not valid, mixed mode fluid driven crack(s) propagation along pre-existing cohesive interfaces can be investigated with this solver. Hydraulic stimulation can be performed either controlling the pressure history at injection point or controlling the injection rate history. In case of loading and unloading scenario during hydraulic-fracturing operations, for instance due to injection followed by a shut-in, this solver is capable of capturing the contact condition by enforcing

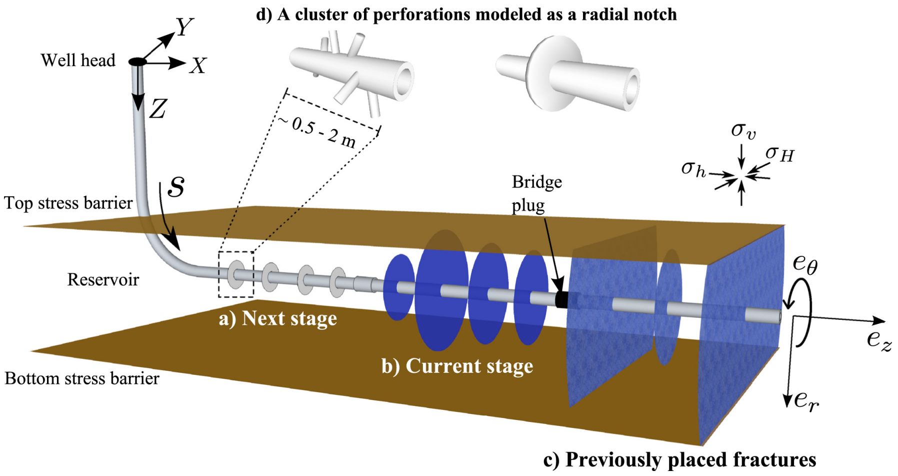
d) A cluster of perforations modeled as a radial notch
Well head
Y
X
Z
$\sim 0.5 - 2\,m$
S
Top stress barrier
Reservoir
Bridge plug
σ_v
σ_H
σ_h
e_θ
e_z
e_r
a) Next stage
b) Current stage
Bottom stress barrier
c) Previously placed fractures

Figure C.1 – Sketch of multi-staged fracturing operation in a contained reservoir. The wellbore is drilled in the direction of the minimum horizontal in situ stress σ_h. At each pumping operation, multiple fractures propagate in the direction of the maximum horizontal in situ stress σ_H. This picture is taken from Lecampion & Desroches (2015).

an inter-penetrability constraint. Large scale simulations can be carried out in modern laptops or workstations thanks to the possibility of using $\mathcal{H}$-matrix combined with ACA in the mechanical solver. Hydraulic stimulation of large scale Discrete Fracture Networks is one application this solver is capable of addressing.

In addition to this, the numerical scheme devised for this solver allows also to investigate geo-mechanical problems of finite domain, whose boundary conditions are represented by either prescribed tractions or prescribed displacements (see Chapter 5 for some illustrative examples).

C.2 External dependencies

HFPx2D has been intentionally devised to rely on the least number of external libraries or dependencies. This is to simplify the compilation of the code and ultimately its execution, while keeping the cross-platform feature.

HFPx2D can be compiled and executed in Unix/Linux or Win32 operating systems (using either clang, gcc or icc/icpc compilers). Before its compilation, some external libraries have to be linked to the program and thus installed in the OS.

Within the mathematical framework, a generic user must install one among the following two open-source libraries:

- Intel Math Kernel Library (MKL)
- OpenBLAS library

MKL is an open source library of optimised math routines, engineering and financial applications, for Intel-based systems. Its core math functions include Basic Linear Algebra SubPrograms (BLAS), LAPACK, ScaLAPACK, vector math, sparse solvers and fast Fourier transforms. Similarly, OpenBLAS is an opmitised version of BLAS library, commonly used under Win32 operating systems. Upon their installation on a local machine, a generic user can use one library or the other by changing a specific flag in the Cmake[3] file.

In addition to this, HFPx2D relies on another open-source library developed for high performance scientific applications: InsideLoop library (IO) (https://github.com/InsideLoop/InsideLoop). Although this library has been intentionally developed to be free library dependent for an easy integration in free softwares or commercial products, it can be easily linked to MKL or BLAS library. This library has been already included in the HFPx2D source folder, so that everyone can get it upon cloning locally the source code from the remote repository https://c4science.ch/diffusion/7687/repository/master/.

Finally, Boost library must be included and linked to the executable file (https://www.boost.org/). This library provides advanced mathematical formula that are missing in the Standard library of C++.

Beside the mathematical dependencies, HFPx2D uses H-Matrix library developed by InsideLoop to build hierarchical representation of elasticity matrix (as already mentioned in Appendix B) and Nlohmann/json library to parse Json type of format (see its remote repository in https://github.com/nlohmann/json). The latter is required from the program to read all the input data that the user has included in the configuration file (that must be written in .json format).

Like the IO library, these two libraries are part of the HFPx2D project. A clone of the code from the remote repository would thus involve the downloading of these libraries.

C.3 Code architecture

Before developing a numerical code, it is good practice to design its architecture. Although this key aspect is sometimes underestimated, it can make the difference in long-term developing projects.

Generally, a program has to meet various requirements in order to be released and ultimately used by people (Kleppmann 2017). *Functional requirements* are surely the most important. A program has to do what it is supposed to do. Data have to be store, retrieved, searched and processed by the program correctly. If a program can not fulfil these requirements, then it can not be used by people. Albeit these program requirements are crucial for its correct execution, they do not affect the code architecture or, in other words, these requirements can be met in any code architecture.

In addition to this, a program has to meet also *nonfunctional requirements* such as reliability, scalability, maintainability and performance. Commercial programs, in fact, have to work even when faults occur; they have to be fast even for large scale problems and last but not least they have to be easy to maintain. Unlike the case of functional requirements, non-functional requirements are highly affected by the choice of the code architecture. It is of great importance, therefore, to design a good code architecture prior developing a program (although there is not a unique optimal solution).

---

[3] CMake is an open-source, cross-platform family of tools designed to build, test and package software.

The code architecture of HFPx2D has been designed with the purpose of fulfilling the aforementioned requirements, without going into deep abstraction solutions (mainly for a better readability). Classes and interfaces have been designed in a way to make the code easier to maintain and at the same time easier to generalise and to understand. Inheritance of classes combined with run-time polymorphisms[4] helps a lot in this respect. Thanks to the combination of these features, a generic user can decide prior executing the program to use a specific friction law rather than another or to use a fully populated elasticity matrix rather than its hierarchical approximation, to cite few examples. This can be easily done by changing the respective keyword in the configuration file, without modifying any line of the source code.
In order to better understand and visualise its architecture, the reader is invited to look at the class diagrams of the routines composing the 'core' of HFPx2D in Figures C.2-C.4. As suggested by its name, the 'core' of HFPx2D is a sub-folder of the project that includes all the most important classes and routines of HFPx2D code. The class diagrams have been generated with PlantUML language (see http://plantuml.com/guide for full details about the language and the symbols involved). Classes are thus represented by yellow boxes, whose identifier green capital letter specifies their type (either simple class C or abstract class A). Classes can or can not be connected between each others based on their dependencies. Aggregation, composition or extension are the possible relations for class dependency.
As one can see from Figure C.3, all the softening/hardening variables composing the constitutive relations for displacement discontinuities locus are embedded in a class hierarchy type of architecture. Each mother class represents an interface (abstract class) for its daughter classes. A run time-polymorphism allows the generic user to use a specific softening/hardening laws rather than another one, without modifying the source code. If the desired softening/hardening law is not present, then the user has only to implement it as a derived class and add its call in the polymorphism. Similarly, the solution class (which is a class that provide a solution object containing the numerical solution of the problem under investigation at each time step) is split into daughter classes in order to keep flexibility among different solvers and at the same time to avoid the storing of unnecessary variables in memory (as different solvers typically need different variables). Each daughter class of the solution class is thus calibrated to each solver. If a user wants to develop another solver, what has to be done is nothing else but deriving another

---

[4] One of the key features of class inheritance is that a pointer to a derived class is type-compatible with a pointer to its base class. Polymorphism is the art of taking advantage of this simple but powerful and versatile feature.

daughter class from the base solution class (which provides the variables and methods that are surely necessary for all the solvers).

This architecture provides an organised but flexible framework for developers and users.

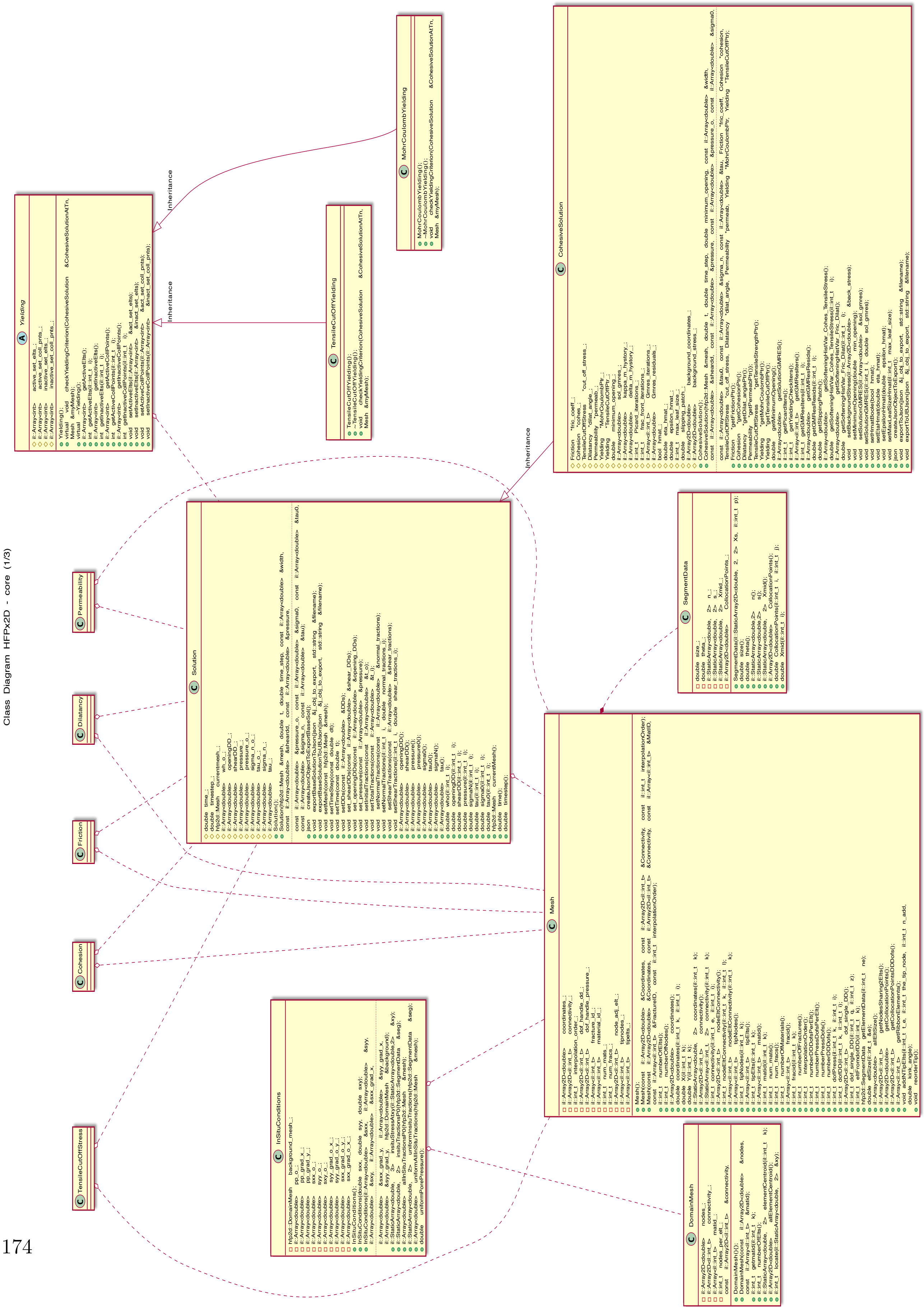
Class Diagram HFPx2D - core (1/3)
Yielding
MohrCoulombYielding
TensileCutOffYielding
CohesiveSolution
Inheritance
Inheritance
Inheritance
Permeability
Dilatancy
Friction
Cohesion
TensileCutOffStress
Solution
SegmentData
Mesh
InSituConditions
DomainMesh

Figure C.2 – Part 1 of class diagram of HFPx2D core.

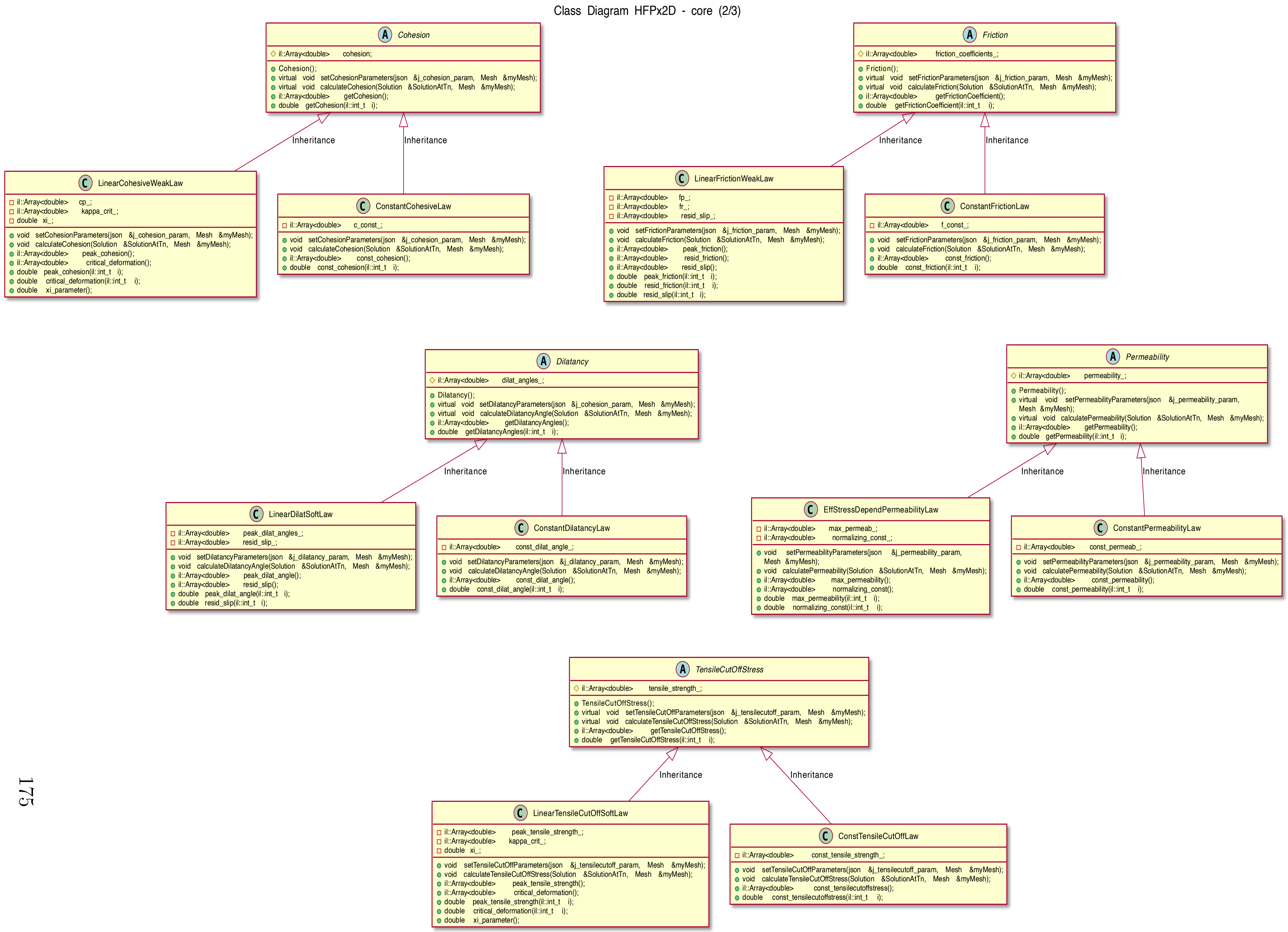
Class Diagram HFPx2D - core (2/3)
A Cohesion
◇ il::Array<double> cohesion;
● Cohesion();
● virtual void setCohesionParameters(json &j_cohesion_param, Mesh &myMesh);
● virtual void calculateCohesion(Solution &SolutionAtTn, Mesh &myMesh);
● il::Array<double> getCohesion();
● double getCohesion(il::int_t i);
Inheritance
Inheritance
C LinearCohesiveWeakLaw
□ il::Array<double> cp_;
□ il::Array<double> kappa_crit_;
□ double xi_;
● void setCohesionParameters(json &j_cohesion_param, Mesh &myMesh);
● void calculateCohesion(Solution &SolutionAtTn, Mesh &myMesh);
● il::Array<double> peak_cohesion();
● il::Array<double> critical_deformation();
● double peak_cohesion(il::int_t i);
● double critical_deformation(il::int_t i);
● double xi_parameter();
C ConstantCohesiveLaw
□ il::Array<double> c_const_;
● void setCohesionParameters(json &j_cohesion_param, Mesh &myMesh);
● void calculateCohesion(Solution &SolutionAtTn, Mesh &myMesh);
● il::Array<double> const_cohesion();
● double const_cohesion(il::int_t i);
A Friction
◇ il::Array<double> friction_coefficients_;
● Friction();
● virtual void setFrictionParameters(json &j_friction_param, Mesh &myMesh);
● virtual void calculateFriction(Solution &SolutionAtTn, Mesh &myMesh);
● il::Array<double> getFrictionCoefficient();
● double getFrictionCoefficient(il::int_t i);
Inheritance
Inheritance
C LinearFrictionWeakLaw
□ il::Array<double> fp_;
□ il::Array<double> fr_;
□ il::Array<double> resid_slip_;
● void setFrictionParameters(json &j_friction_param, Mesh &myMesh);
● void calculateFriction(Solution &SolutionAtTn, Mesh &myMesh);
● il::Array<double> peak_friction();
● il::Array<double> resid_friction();
● il::Array<double> resid_slip();
● double peak_friction(il::int_t i);
● double resid_friction(il::int_t i);
● double resid_slip(il::int_t i);
C ConstantFrictionLaw
□ il::Array<double> f_const_;
● void setFrictionParameters(json &j_friction_param, Mesh &myMesh);
● void calculateFriction(Solution &SolutionAtTn, Mesh &myMesh);
● il::Array<double> const_friction();
● double const_friction(il::int_t i);
A Dilatancy
◇ il::Array<double> dilat_angles_;
● Dilatancy();
● virtual void setDilatancyParameters(json &j_cohesion_param, Mesh &myMesh);
● virtual void calculateDilatancyAngle(Solution &SolutionAtTn, Mesh &myMesh);
● il::Array<double> getDilatancyAngles();
● double getDilatancyAngles(il::int_t i);
Inheritance
Inheritance
C LinearDilatSoftLaw
□ il::Array<double> peak_dilat_angles_;
□ il::Array<double> resid_slip_;
● void setDilatancyParameters(json &j_dilatancy_param, Mesh &myMesh);
● void calculateDilatancyAngle(Solution &SolutionAtTn, Mesh &myMesh);
● il::Array<double> peak_dilat_angle();
● il::Array<double> resid_slip();
● double peak_dilat_angle(il::int_t i);
● double resid_slip(il::int_t i);
C ConstantDilatancyLaw
□ il::Array<double> const_dilat_angle_;
● void setDilatancyParameters(json &j_dilatancy_param, Mesh &myMesh);
● void calculateDilatancyAngle(Solution &SolutionAtTn, Mesh &myMesh);
● il::Array<double> const_dilat_angle();
● double const_dilat_angle(il::int_t i);
A Permeability
◇ il::Array<double> permeability_;
● Permeability();
● virtual void setPermeabilityParameters(json &j_permeability_param, Mesh &myMesh);
● virtual void calculatePermeability(Solution &SolutionAtTn, Mesh &myMesh);
● il::Array<double> getPermeability();
● double getPermeability(il::int_t i);
Inheritance
Inheritance
C EffStressDependPermeabilityLaw
□ il::Array<double> max_permeab_;
□ il::Array<double> normalizing_const_;
● void setPermeabilityParameters(json &j_permeability_param, Mesh &myMesh);
● void calculatePermeability(Solution &SolutionAtTn, Mesh &myMesh);
● il::Array<double> max_permeability();
● il::Array<double> normalizing_const();
● double max_permeability(il::int_t i);
● double normalizing_const(il::int_t i);
C ConstantPermeabilityLaw
□ il::Array<double> const_permeab_;
● void setPermeabilityParameters(json &j_permeability_param, Mesh &myMesh);
● void calculatePermeability(Solution &SolutionAtTn, Mesh &myMesh);
● il::Array<double> const_permeability();
● double const_permeability(il::int_t i);
A TensileCutOffStress
◇ il::Array<double> tensile_strength_;
● TensileCutOffStress();
● virtual void setTensileCutOffParameters(json &j_tensilecutoff_param, Mesh &myMesh);
● virtual void calculateTensileCutOffStress(Solution &SolutionAtTn, Mesh &myMesh);
● il::Array<double> getTensileCutOffStress();
● double getTensileCutOffStress(il::int_t i);
Inheritance
Inheritance
C LinearTensileCutOffSoftLaw
□ il::Array<double> peak_tensile_strength_;
□ il::Array<double> kappa_crit_;
□ double xi_;
● void setTensileCutOffParameters(json &j_tensilecutoff_param, Mesh &myMesh);
● void calculateTensileCutOffStress(Solution &SolutionAtTn, Mesh &myMesh);
● il::Array<double> peak_tensile_strength();
● il::Array<double> critical_deformation();
● double peak_tensile_strength(il::int_t i);
● double critical_deformation(il::int_t i);
● double xi_parameter();
C ConstTensileCutOffLaw
□ il::Array<double> const_tensile_strength_;
● void setTensileCutOffParameters(json &j_tensilecutoff_param, Mesh &myMesh);
● void calculateTensileCutOffStress(Solution &SolutionAtTn, Mesh &myMesh);
● il::Array<double> const_tensilecutoffstress();
● double const_tensilecutoffstress(il::int_t i);

Figure C.3 – Part 2 of class diagram of HFPx2D core.

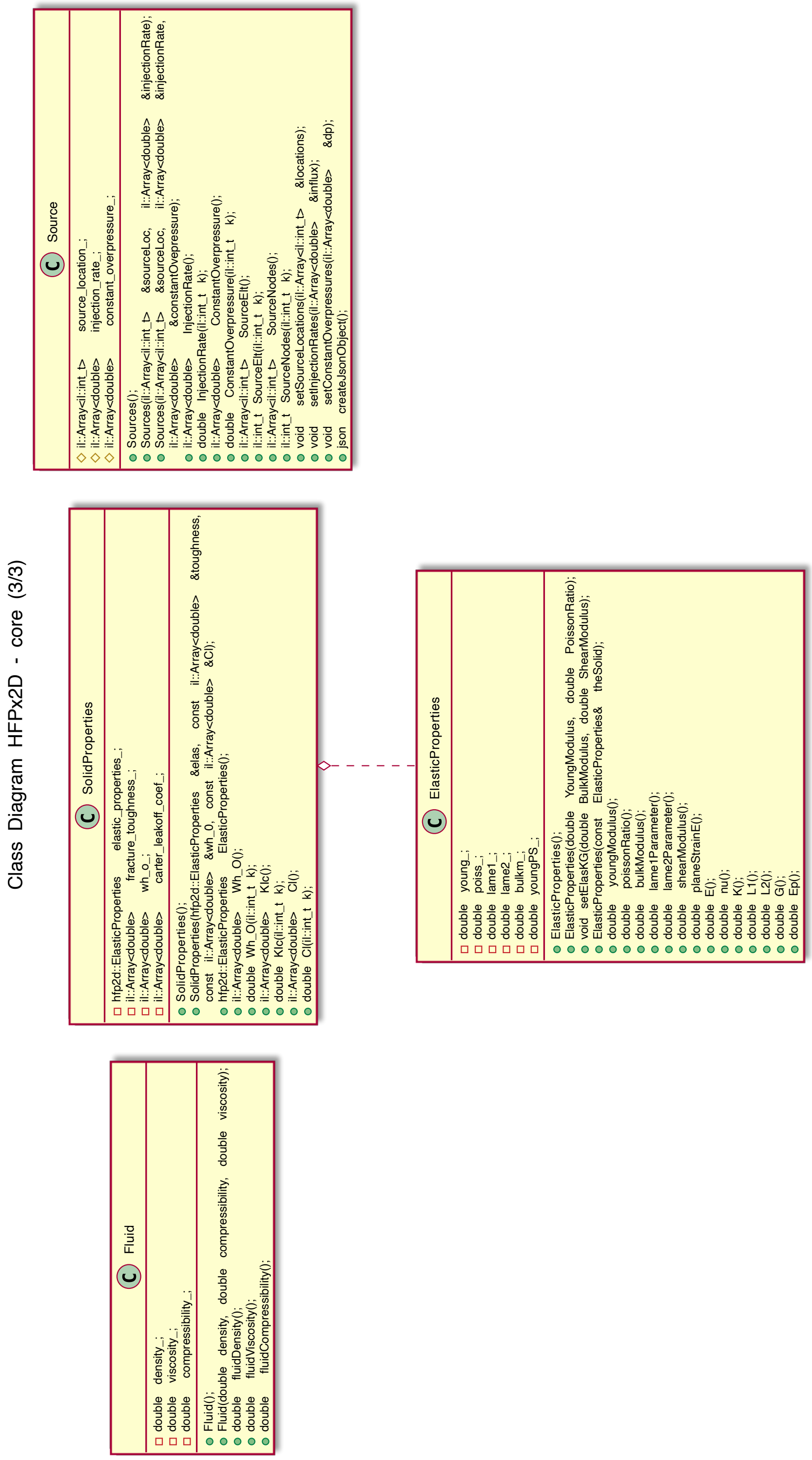
Class Diagram HFPx2D - core (3/3)
C Source
◇ il::Array<il::int_t> source_location_;
◇ il::Array<double> injection_rate_;
◇ il::Array<double> constant_overpressure_;
● Sources();
● Sources(il::Array<il::int_t> &sourceLoc, il::Array<double> &injectionRate);
● Sources(il::Array<il::int_t> &sourceLoc, il::Array<double> &injectionRate, il::Array<double> &constantOvepressure);
● il::Array<double> InjectionRate();
● double InjectionRate(il::int_t k);
● il::Array<double> ConstantOverpressure();
● double ConstantOverpressure(il::int_t k);
● il::Array<il::int_t> SourceElt();
● il::int_t SourceElt(il::int_t k);
● il::Array<il::int_t> SourceNodes();
● il::int_t SourceNodes(il::int_t k);
● void setSourceLocations(il::Array<il::int_t> &locations);
● void setInjectionRates(il::Array<double> &influx);
● void setConstantOverpressures(il::Array<double> &dp);
● json createJsonObject();
C SolidProperties
□ hfp2d::ElasticProperties elastic_properties_;
□ il::Array<double> fracture_toughness_;
□ il::Array<double> wh_o_;
□ il::Array<double> carter_leakoff_coef_;
● SolidProperties();
● SolidProperties(hfp2d::ElasticProperties &elas, const il::Array<double> &toughness, const il::Array<double> &wh_0, const il::Array<double> &Cl);
● hfp2d::ElasticProperties ElasticProperties();
● il::Array<double> Wh_O();
● double Wh_O(il::int_t k);
● il::Array<double> KIc();
● double KIc(il::int_t k);
● il::Array<double> Cl();
● double Cl(il::int_t k);
C ElasticProperties
□ double young_;
□ double poiss_;
□ double lame1_;
□ double lame2_;
□ double bulkm_;
□ double youngPS_;
● ElasticProperties();
● ElasticProperties(double YoungModulus, double PoissonRatio);
● void setElasKG(double BulkModulus, double ShearModulus);
● ElasticProperties(const ElasticProperties& theSolid);
● double youngModulus();
● double poissonRatio();
● double bulkModulus();
● double lame1Parameter();
● double lame2Parameter();
● double shearModulus();
● double planeStrainE();
● double E();
● double nu();
● double K();
● double L1();
● double L2();
● double G();
● double Ep();
C Fluid
□ double density_;
□ double viscosity_;
□ double compressibility_;
● Fluid();
● Fluid(double density, double compressibility, double viscosity);
● double fluidDensity();
● double fluidViscosity();
● double fluidCompressibility();

Figure C.4 – Part 3 of class diagram of HFPx2D core.

Bibliography

Albaric, J., Oye, V., Langet, N., Hasting, M., Lecomte, I., Iranpour, K., Messeiller, M. & Reid, P. (2014), 'Monitoring of induced seismicity during the first geothermal reservoir stimulation at Paralana, Australia', *Geothermics* **52**, 120–131.

Alghalandis, Y. F. (2017), 'ADFNE: Open source software for discrete fracture network engineering, two and three dimensional applications', *Computers & Geosciences* **102**, 1–11.

Anders, M. H. & Wiltschko, D. V. (1994), 'Microfracturing, paleostress and the growth of faults', *Journal of Structural Geology* **16**(6), 795–815.

Appel, A. W. (1985), 'An efficient program for many-body simulation', *SIAM J. Scien. Stat. Comp.* **6**(1).

Armero, F. & Garikipati, K. (1996), 'An analysis of strong discontinuities in mutiplicative finite strain plasticity simulation of strain localization in solids', *Int. J. Solids Structures* **33**(20-22), 2863–2885.

Armstead, H. C. H. (1983), *Geothermal energy*, London: E. & F. N. Spon.

Asanuma, H., Nozaki, H., Niitsuma, H. & Wyborn, D. (2005), 'Interpretation of Microseismic Events with Larger Magnitude Collected at Cooper Basin, Australia', *GRC Transactions* **29**.

Audigane, P., Gaus, I., Czernichowski-Lauriol, I., Pruess, K. & Xu, T. (2007), 'Two-dimensional reactive transport modeling of CO_2 injection in a saline aquifer at the Sleipner site, North Sea', *American journal of science* **307**, 974–1008.

Baisch, S., Koch, C. & Muntendam-Bos, A. (2019), 'Traffic Light Systems: To What Extent Can Induced Seismicity Be Controlled?', *Seismological Research Letters* **90**(3).

Bandis, S., Lumsden, A. C. & Barton, N. R. (1981), 'Experimental Studies of Scale Effects on the Shear Behavior of Rock Joints', *Int. J. Rock Mech. Min. Sci. & Geom. Abstr.* **18**(1-21).

Bao, X. & Eaton, D. W. (2016*a*), 'Fault activation by hydraulic fracturing in western Canada', *Science* p. aag2583.

Bao, X. & Eaton, D. W. (2016*b*), ‘Fault activation by hydraulic fracturing in western Canada’, *Science* .

Baria, R., Baumgärtner, J., Gérard, A., Jung, R. & Garnish, J. (1999), ‘European HDR research programme at Soultz-sous-forêts (France) 1987-1996’, *Geothermics* **28**, 655–669.

Barton, N., Bandis, S. & Bakhtar, K. (1985), ‘Strength, Deformation and Conductivity Coupling of Rock Joints’, *Int. J. Rock. Mech. Min. Sci. & Geomech. Abstr.* **22**(3), 121–140.

Batchelor, A. S. (1985), Hot dry rock reservoir stimulation in the UK an extended summary, *in* ‘International seminar on the results of EC geothermal energy research. 3’, European Commission, München, pp. 681–711.

Bawden, W. F., Curran, J. H. & Roegiers, J.-C. (1980), ‘Influence of Fracture Deformation on Secondary - A Numerical Approach’, *Int. J. Rock Mech. Min. Sci. & Geom. Abstr.* **17**, 265–279.

Bebendorf, M. (2008*a*), *Hierarchical matrices*, Springer.

Bebendorf, M. (2008*b*), *Hierarchical matrices: A Means to Efficiently Solve Elliptic Boundary Value Problems*, Springer.

Bebendorf, M. & Rjasanow, S. (2003), ‘Adaptive low-rank approximation of collocation matrices’, *Computing* **70**(1), 1–24.

Beltrami, H., Wang, J. & Bras, R. L. (2000), ‘Energy balance at the Earth’s surface: Heat flux history in Eastern Canada’, *Geophysical Research Letters* **27**(20), 3385–3388.

Belytschko, T., Fish, J. & Engelmann, B. E. (1988), ‘A finite element with embedded localization zones’, *Computer methods in applied mechanics and engineering* **70**, 59–89.

Benallal, A., Botta, A. & Venturini, W. S. (2006), ‘On the description of localization and failure phenomena by the boundary element method’, *Computer methods in applied mechanics and engineering* **195**, 5833–5856.

Benallal, A., Fudoli, C. A. & Venturini, W. S. (2002), ‘An implicit BEM formulation for gradient plasticity and localization phenomena’, *Internatioan journal for numerical methods in engineering* **53**, 1853–1869.

Benzi, M., Golub, G. H. & Liesen, J. (2005), ‘Numerical solution of saddle point problems’, *Acta Numerica* pp. 1–37.

Bernabé, Y., Mok, U. & Evans, B. (2003), ‘Permeability-porosity relationships in rocks subjected to various evolution processes’, *Pure and Applied Geophysics* **160**(5-6), 937–960.

Bertani, R. (2015), Geothermal power generation in the world 2010-2014 update report, *in* ‘Proceedings World Geothermal Congress’.

Bhattacharya, P. & Viesca, R. C. (2019), ‘Fluid-induced aseismic fault slip outpaces pore-fluid migration’, *Science* **364**(6439), 464–468.

Bigoni, D. & Capuani, D. (2002), ‘Green’s function for incremental nonlinear elasticity: shear bands and boundary integral formulation’, *Journal of the Mechanics and Physics of Solids* **50**, 471–500.

Bobet, A. & Einstein, H. H. (1998*a*), ‘Fracture coalescence in rock-type materials under uniaxial and biaxial compression’, *International Journal of Rock Mechanics and Mining Sciences* **35**(7), 863–888.

Bobet, A. & Einstein, H. H. (1998*b*), ‘Numerical modeling of fracture coalescence in a model rock material’, *International Journal of Fracture* **92**(3), 221–252.

Bommer, J. J., Oates, S., Cepeda, J. M., Lindholm, C., Bird, J., Torres, R., Marroquín, G. & Rivas, J. (2006), ‘Control of hazard due to seismicity induced by a hot fractured rock geothermal project’, *Engineering geology* **83**, 287–306.

Bonnet, E., Bour, O., Odling, N. E., Davy, P., Main, I., Cowie, P. & Berkowitz, B. (2001), ‘Scaling of fracture systems in geological media’, *Rewiews of Geophysics* **39**, 347–383.

Bonnet, M. (1995), *Boundary Integral Equation Methods for Solids and Fluids*, John Wiley and Sons Ltd.

Bonnet, M. (1999*a*), *Boundary integral equation methods for solids and fluids*, John Wiley & Sons.

Bonnet, M. (1999*b*), *Boundary Integral Equation Methods for Solids and Fluids*, John Wiley & Sons.

Bonnet, M., Maier, G. & Polizzotto, C. (1998), ‘Symmetric Galerkin boundary element methods’, *Applied Mechanics Reviews* **51**, 669–704.

Börm, S., Grasedyck, L. & Hackbusch, W. (2003), ‘Introduction to hierarchical matrices with applications’, *Engineering analysis with boundary elements* **27**(5), 405–422.

Bour, O. & Davy, P. (1997), ‘Connectivity of random fault networks following a power law fault length distribution’, *Water resources research* **33**(7), 1567–1583.

Bourouis, S. & Bernard, P. (2007), ‘Evidence for coupled seismic and aseismic fault slip during water injection in the geothermal site of Soultz (France), and implications for seismogenic transients’, *Geophys. J. Int.* **169**, 723–732.

Brantut, N. & Viesca, R. C. (2015), ‘Earthquake nucleation in intact or healed rocks’, *Journal of Geophysical Research: Solid Earth* **120**, 191–209.

Bruel, D. (1995), ‘Heat extraction modelling from forced fluid flow through stimulated fractured rock masses: application to the Rosemanowes hot dry rock reservoir’, *Geothermics* **24**(3), 361–374.

Brum, M., Bigoni, D. & Capuani, D. (2003), ‘A boundary element technique for incremental, non-linear elasticity - Part II: Bifurcation and shear bands’, *Computer methods in applied mechanics and engineering* **192**, 2481–2499.

Camacho, G. T. & Ortiz, M. (1996), ‘Computational modelling of impact damage in brittle materials’, *Int. J. Solids Structures* **33**(20-22), 2899–2938.

Cao, Z.-H. (2008), ‘Augmentation block preconditioners for saddle point-type matrices with singular (1,1) blocks’, *Numerical linear algebra with applications* **15**, 515–533.

Cao, Z.-H. (2009), ‘Constraint Schur complement preconditioners for nonsymmetric saddle point problems’, *Applied Numerical Mathematics* **59**, 151–169.

Cappa, F. & Rutqvist, J. (2011), ‘Impact of CO_2 geological sequestration on the nucleation of earthquakes’, *Geophys. Res. Lett.* **38**.

Carnec, C. & Delacourt, C. (1999), ‘Three years of mining subsidence monitored by SAR interferometry, near Gardanne, France’, *Journal of Applied Geophysics* **43**, 43–54.

Carslaw, H. S. & Jaeger, J. C. (1959), *Conduction of heat in solids*, Oxford Univ Press.

Chaillat, S., Desiderio, L. & Ciarlet, P. (2017), ‘Theory and implementation of H-matrix based iterative and direct solvers for Helmholtz and elastodynamic oscillatory kernels’, *Journal of Computational Physics* **351**, 165–186.

Chan, A. W. & Zoback, M. D. (2006), ‘The role of hydrocarbon production on land subsidence and fault reactivation in the louisiana coastal zone’, *Journal of Coastal Research* **23**, 771–786.

Ciardo, F. & Lecampion, B. (2019), ‘Effect of dilatancy on the transition from aseismic to seismic slip due to fluid injection in a fault’, *Journal of Geophysical Research: Solid Earth* **124**, 3724–3743.

Cooke, M. L. & Pollard, D. D. (1997), ‘Bedding-plane slip in initial stages of fault-related folding’, *Journal of Structural Geology* **19**(3-4), 567–581.

Cornet, F. E. (2015*a*), *Elements of Crustal Geomechanics*, Cambridge University Press.

Cornet, F. H. (2015*b*), *Elements of Crustal Geomechanics*, Cambridge University Press.

Cornet, F. H. (2016), ‘Seismic and aseismic motions generated by fluid injections’, *Geomechanics for Energy and the Environment* **5**, 42–54.

Cornet, F. H., Helm, J., Poitrenaud, H. & Etchecopar, A. (1997*a*), 'Seismic and Aseismic Slips Induced by Large-scale Fluid Injections', *Pure and Applied Geophysics* **150**, 563–583.

Cornet, F. H., Helm, J., Poitrenaud, H. & Etchecopar, A. (1997*b*), 'Seismic and Aseismic Slips Induced by Large-scale Fluid Injections', *Pure Appl. Geophys.* **150**, 563–583.

Crawford, A. & Curran, J. (1982), 'Higher-order functional variation displacement discontinuity elements', *International Journal of Rock Mechanics and Mining Science & Geomechanics Abstracts* **19**(3), 143–148.

Crouch, S. L. & Starfield, A. M. (1983), *Boundary Element Methods in Solid Mechanics*, George Allen and Unwin.

Davy, P., Bour, O. & De Dreuzy, J.-R. (2006), Discrete fracture network for the Forsmark site, Technical report, Itasca Consulting Group.

De Barros, L., Guglielmi, Y., Rivet, D., Cappa, F. & Duboeuf, L. (2018), 'Seismicity and fault aseismic deformation caused by fluid injection in decametric in-situ experiments', *Comptes Rendus Geoscience* .

De Borst, R. (1991), 'Simulation of strain localisation: a reappraisal of the Cosserat continuum', *Engineering computations* **8**, 317–332.

De Borst, R. & Mühlhaus, H.-B. (1992), 'Gradient-dependent plasticity: formulation and algorithm aspects', *Internatioan journal for numerical methods in engineering* **35**, 521–539.

Deep Geothermal Energy - R&D Roadmap for Switzerland, 2014 (2014), Technical report, SCCER-SoE.

Deichmann, N. & Giardini, D. (2009), 'Earthquakes Induced by the Stimulation of an Enhanced Geothermal System below Basel (Switzerland)', *Seismological Research Letters* **80**, 784–798.

Desiderio, L. (2017), H-matrix based Solvers for 3D Elastodynamic Boundary Integral Equations, PhD thesis, Univesité Paris-Saclay.

Dublanchet, P. (2019), 'Fluid driven shear cracks on a strengthening rate-and-state frictional fault', *Journal of the Mechanics and Physics of Solids* **132**.

Duboeuf, L., De Barros, L., Cappa, F., Guglielmini, Y., Deschamps, A. & Seguy, S. (2017), 'Aseismic motions drive a sparse seismicity during fluid injections into a fractured zone in a carbonate reservoir', *Journal of Geophysical Research: Solid Earth* **122**, 8285–8304.

Economides, M. J. & Nolte, K. G. (2000), *Reservoir Stimulation*, John Wiley & Sons.

Ellsworth, W. L. (2013), 'Injection-induced earthquakes', *Science* **341**.

Erisman, A. M. & Tinney, W. F. (1975), 'On computing certain elements of the inverse of a sparse matrix', *Numerical mathematics* .

Evans, K. F., Genter, A. & Sausse, J. (2005), 'Permeability creation and damage due to massive fluid injections into granite at 3.5 km at soultz: 1. borehole observations', *Journal of Geophysical Research: Solid Earth* **110**(4), 1–19.

Evans, K. F., Moriya, H., Niitsuma, H., Jones, R., Phillips, W. S., Genter, A., Sausse, J., Jung, R. & Baria, R. (2005), 'Microseismicity and permeability enhancement of hydrogeologic structures during massive fluid injections into granite at 3 km depth at the soultz hdr site', *Geophysical Journal International* **160**(1), 388–412.

Fehler, M. C. (1989), 'Stress Control of Seismicity Patterns Observed During Hydraulic Fracturing Experiments at the Fenton Hill Hot Dry Rock Geothermal Energy Site, New Mexico', *Int. J. Rock Mech. Min. Sci. & Geomech.* **26**(34), 211–219.

Finsterle, S. (2007), *iTOUGH2*, Lawrence Berkeley National Laboratory (LBLN).

Garagash, D. I. & Germanovich, L. N. (2012), 'Nucleation and arrest of dynamic slip on a pressurized fault', *Journal of Geophysical Research* **117**(B10310).

Garagash, D. I. & Rudnicki, J. W. (2003), 'Shear heating of a fluid-saturated slip-weakening dilatant fault zone, 1, limiting regimes', *J. Geophys. Res.* **108**(B2).

Gebbia, M. (1891), 'Formule fondamentali della statica dei corpi elastici', *Rend. Circ. Mat. di Palermo* **5**, 320–323.

Giardini, D. (2009), 'Geothermal quake risks must be faced', *Nature* **462**, 848–849.

Greengard, L. (1994), 'Fast Algorithm for Classical Physics', *Science* **265**(5174), 909–914.

Grigoli, F., Cesca, S., Rinaldi, A. P., Mnconi, A., López-Comino, J. A., Clinton, J. F., Westaway, R., Cauzzi, C., Dahm, T. & Wiemer, S. (2018), 'The November 2017 Mw 5.5 Pohang earthquake: A possible case of induced seismicity in South Korea', *Science* **360**, 1003–1006.

Guglielmini, Y., Cappa, F., Avouac, J.-P., Henry, P. & Elsworth, D. (2015), 'Seismicity triggered by fluid injection-induced aseismic slip', *Science* **348**.

Hackbusch, W. (1999), 'A Sparse Matrix Arithmetic Based on $\mathcal{H}$-Matrices. part i: Introduction to $\mathcal{H}$-Matrices.', *Computing* **62**, 89–108.

Hackbusch, W. (2015*a*), *Hierarchical matrices: algorithm and analysis*, Vol. 49, Springer.

Hackbusch, W. (2015*b*), *Hierarchical matrices: algorithms and analysis*, Vol. 49, Springer.

Hackbusch, W. & Nowak, Z. P. (1989), 'On the fast matrix multiplication in the boundary element method by panel clustering', *Numerische Mathematik* **54**(4), 463–491.

Hamilton, D. H. & Meehan, R. L. (1971), ‘Ground rupture in the Baldwin Hills’, *Science* **172**(3981), 333–344.

Hatton, C. G., Main, I. G. & Meredith, P. G. (1994), ‘Non-universal scaling of fracture length and opening displacement’, *Nature* **367**.

Healy, J. H., Rubey, W. W., Griggs, D. T. & Raleigh, C. B. (1968), ‘The Denver earthquakeS’, *Science* **161**(3848), 1301–1310.

Hill, D. A., Kelly, P. A., Dai, D. N. & Korsunsky, A. M. (1996), *Solution of Crack Problems: the Distributed Dislocation Technique*, Kluwer Academic Publishers.

Hirschberg, S., Wiemer, S. & Burgherr, P. (2015), Energy from the Earth - Deep Geothermal as a Resource for the Future?, Technical report, Centre for Technology Assessment.

Hockney, R. W. & Eastwood, J. W. (1981), *Computer Simulation Using Particles*, McGraw-Hill.

Howard, G. C. & Fast, C. R. (1957), ‘Optimum fluid characteristics for fracture extension’, *Drilling and Production Practice* pp. 261–270.

Ida, Y. (1972), ‘Cohesive force across the tip of a longitudinal-shear crack and griffith’s specific surface energy’, *Journal of Geophysical Research* **77**(20), 3796–3805.

IEA 2019 (2019), ‘World energy balances’.
URL: *https://doi.org/10.1787/data-00512-en*

Itasca Consulting Group (2010), Flac Constitutive models, Technical report, Itasca Consulting Group.

Itasca Consulting Group, Inc. (2017) Minneapolis: Itasca. (2017), ‘Flac3d – fast lagrangian analysis of continua in three-dimensions, ver. 6.0.’.

Jeffrey, R. G., Zhang, X. & Jung, R. (2015), Reassessing Stimulation for EGS Reservoirs, *in* ‘Proceedings World Geothermal Congress’.

Kirsch, G. (1898), *Die Theorie der Elastizität und die Bedürfnisse der Festigkeitslehre.*

Kleppmann, M. (2017), *Designing Data-Intensive Applications*, O’Reilly.

Kranz, R. L. (1983), ‘Microcracks in rocks: a review’, *Tectonophysics* **100**, 449–480.

Kranz, R. L., Frankel, A. D., Engelder, T. & Scholz, C. H. (1979), ‘The permeability of the whole and jointed Barre granite’, *Int. J. Rock Mech. Min. Sci. & Geom. Abstr.* **16**, 225–234.

Lecampion, B. (2012), ‘Modeling size effects associated with tensile fracture initiation from a wellbore’, *International Journal of Rock Mechanics and Mining Science* **56**, 67–76.

Lecampion, B., Bunger, A. P. & Zhang, X. (2018), ‘Numerical methods for hydraulic fracture propagation: A review of recent trends’, *Journal of Natural Gas Science and Engineering* **49**, 66–83.

Lecampion, B. & Desroches, J. (2015), ‘Simultaneous initiation and growth of multiple radial hydraulic fractures from a horizontal wellbore’, *Journal of the Mechanics and Physics of Solids* **82**, 235–258.

Lee, H. S. & Cho, T. F. (2002), ‘Hydraulic characteristics of rough fractures in linear flow under normal and shear load’, *Rock Mechanics and Rock Engineering* **35**(4), 299–318.

Leeman, J. R., Saffer, D. M., Scuderi, M. M. & Marone, C. (2016), ‘Laboratory observations of slow earthquakes and the spectrum of tectonic fault slip modes’, *Nature communications* **7**.

Leguillon, D., Quesada, D., Putot, C. & Martin, E. (2007), ‘Prediction of crack initiation at blunt notches and cavities: size effects’, *Eng. Frac. Mech.* **74**(15), 2420–2436.

Lei, Q. & Gao, K. (2018), ‘Correlation between fracture network properties and stress variability in geological media’, *Geophysical Research Letters* **45**.

Lei, Q., Latham, J.-P. & Tsang, C.-F. (2017), ‘The use of discrete fracture networks for modelling coupled geomechanical and hydrological behaviour of fractured rocks’, *Computers and Geotechnics* **85**, 151–176.

Lei, Q. & Wang, X. (2016), ‘Tectonic interpretation of the connectivity of a multiscale fracture system in limestone’, *Geophysical Research Letters* **43**, 1551–1558.

Li, B., Jiang, Y., Koyama, T., Jing, L. & Tanabashi, Y. (2008), ‘Experimental study of the hydro-mechanical behavior of rock joints using a parallel-plate model containing contact areas and artificial fractures’, *International Journal of Rock Mechanics and Mining Sciences* **45**(3), 362–375.

Li, J.-L., Huang, T.-Z. & Li, L. (2010), ‘The spectral properties of the preconditioned matrix for nonsymmetric saddle point problems’, *Journal of Computational and Applied Mathematics* **235**, 270–285.

Li, S., Ahmed, S., Klimeck, G. & Darve, E. (2008), ‘Computing entries of the inverse of a sparse matrix using the FIND algorithm’, *Journal of Computational Physics* **227**, 9408–9427.

Liu, Y., Wang, G., Yue, G., Zhang, W., Zhu, X. & Zhang, Q. (2019), ‘Comparison of enhanced geothermal system with water and CO_2 as working study: A case study in Zhacanggou, Northeastern Tibet, China’, *Energy exploration & exploitation* **37**(2), 736–755.

Lockner, D. A. & Byerlee, J. D. (1994), ‘Dilatancy in hydraulically isolated faults and the suppression of instability’, *Geophysical Research Letters* **21**(22), 2353–2356.

Lockner, D.and Naka, H., Tanaka, H., Ito, H. & Ikeda, R. (1999), Permeability and Strength of core samples from the Nojima fault of the 1995 Kobe earthquake, *in* 'Int. workshop on the Nojima fault core and borehole data analysis'.

Lubliner, J. (2005), *Plasticity Theory*, Dover.

Maerten, F., Maerten, L. & Cooke, M. (2010), 'Solving 3D boundary element problems using constrained iterative approach', *Computational Geoscience* **14**, 551–564.

Maier, G., Novati, G. & Chen, Z. (1993), 'Symmetric Galerkin boundary element method for quasi-brittle-fracture and frictional contact problems', *Computational Mechanics* **13**, 74–89.

Majer, E. L., Baria, R., Stark, M., Oates, S., Bommer, J., Smith, B. & Asanuma, H. (2007), 'Induced seismicity associated with enhanced geothermal systems', *Geothermics* **36**(3), 185–222.

Makurat, A., Neuman, S. P. & Simpson, E. S. (1985), 'The effect of shear displacement on the permeability of natural rough joints', *Hydrogeology of rocks of low permeability: International Association of Hydrogeologists Memoir* **17**, 99–106.

Marone, C., Raleigh, C. B. & Scholz, C. H. (1990), 'Frictional behavior and constitutive modeling of simulated fault gouge', *Journal of Geophysical Research: Solid Earth* **95**(B5), 7007–7025.

Matsuki, K., Kimura, Y., Sakaguchi, K., Kizaki, A. & Giwelli, A. A. (2010), 'Effect of shear displacement on the hydraulic conductivity of a fracture', *International Journal of Rock Mechanics and Mining Sciences* **47**(3), 436–449.

McClure, M. W. & Horne, R. N. (2013), *Discrete Fracture Network Modeling of Hydraulic Stimulation: Coupling Flow and Geomechanics*, Springer Briefs in Earth Sciences, Springer, New York.

McClure, M. W. & Horne, R. N. (2014), 'An investigation of stimulation mechanisms in Enhanced Geothermal Systems', *Int. J. Rock Mech. Min. Sci.* **72**, 242–260.

McKittrick, A., Abrahams, L., Clavin, C., Rozansky, R. & Bernstein, D. (2019), FORGE - Frontier Observatory for Research in Geothermal Energy: a roadmap, Technical report, IDA - science and technology policy institute.

Mignan, A., Broccardo, M. & Giardini, D. (2017), 'Induced seismicity closed-form traffic light system for actuarial decision-making during deep fluid injections', *Nature - Scientific reports* **7**.

Mogilevskaya, S. G. (2014*a*), 'Lost in translation: Crack problems in different languages', *International Journal of Solids and Structures* **51**(25), 4492–4503.

Mogilevskaya, S. G. (2014*b*), 'Lost in traslation: Crack problems in different languages', *International Journal of Solids and Structures* **51**, 4492–4503.

Mogilevskaya, S. G. & Nikolskiy, D. V. (2014), 'The use of complex integral representations for analytical evaluation of three-dimensional bem integrals—potential and elasticity problems', *The Quarterly Journal of Mechanics and Applied Mathematics* **67**(3), 505–523.

Mühlhaus, H.-B. & Aifantis, E. C. (1991), 'A variational principle for gradient plasticity', *Int. J. Solids Structures* **28**(7), 845–857.

Murphy, H. D., Keppler, H. & Dash, Z. V. (1983), Does hydraulic fracturing theory work in jointed rock masses?, Technical report, Los Alamos National Laboratory.

Needleman, A. (1972), 'A numerical study of necking in circular cylindrical bars', *J. Mech. Phys. Solids* **20**, 111–127.

Needleman, A. (1988), 'Material rate dependence and mesh sensitivity in localization problems', *Computer methods in applied mechanics and engineering* **67**, 69–85.

Needleman, A. & Tvergaard, V. (1977), 'Necking of biaxially stretched elastic-plastic circular plates', *J. Mech. Phys. Solids* **25**, 159–183.

Nguyen, T. S. & Selvadurai, A. P. S. (1998), 'A model for coupled mechanical and hydraulic behaviour of a rock joint', *International Journal for Numerical and Analytical Methods in Geomechanics* **22**(1), 29–48.

Nikolskly, D. & Lecampion, B. (2019), 'Modeling of simultaneous propagation of multiple blade-like hydraulic fractures from a horizontal well', *Rock Mechanics and Rock Engineering* .

Noël, C., Passelègue, F. X., Giorgetti, C. & Violay, M. (2019), 'Fault reactivation during fluid pressure oscillations: transition from stable to unstable slip', *Journal of Geophysical Research: Solid Earth* **124**.

Norbeck, J. H., McClure, M. W., Lo, J. W. & Horne, R. N. (2016), 'An embedded fracture modeling framework for simulation of hydraulic fracturing and shear stimulation', *Computational Geosciences* **20**, 1–18.

Ortiz, M., Leroy, Y. & Needleman, A. (1987), 'A finite element method for localized failure analysis', *Computer methods in applied mechanics and engineering* **61**, 189–214.

Ortiz, M. & Pandolfi, A. (1999), 'Finite-deformation irreversible cohesive elememts for three-dimensional crack-propagation analysis', *International journal for numerical methods in engineering* **44**, 1267–1282.

Palmer, A. C. & Rice, J. R. (1973), The growth of slip surfaces in the progressive failure of over-consolidated clay, *in* 'Proceedings of the Royal Society of London A: Mathematical, Physical and Engineering Sciences', Vol. 332, The Royal Society, pp. 527–548.

Pandolfi, A. & Ortiz, M. (2002), 'An efficient adaptive procedure for three-dimensional fragmentation simulations', *Engineering with computers* **18**, 148–159.

Patir, N. & Cheng, H. (1978), 'An average flow model for determining effects of three-dimensional roughness on partial hydrodynamic lubrication', *Journal of Tribology* **100**(1), 12–17.

Peirce, A. P., Spottiswoode, S. & Napier, J. A. L. (1992), 'The Spectral Boundary Element Method: a New Window on Boundary Elements in Rock Mechanics', *Int. J. Rock Mech. Min. Sci. & Geom. Abstr.* **29**(4), 379–400.

Phan, A.-V., Napier, J. A. L., Gray, L. J. & Kaplan, T. (2003), 'Symmetric-Galerkin BEM simulation of fracture with frictional contact', *International journal for numerical methods in engineering* **57**, 835–851.

Piva, A. (1982), 'A crack along a circular interface between dissimilar media', *Meccanica* **17**(2), 85–90.

Quarteroni, A., Sacco, R. & Saleri, F. (2000*a*), *Numerical Mathematics*, Texts in applied mathematics, Springer.

Quarteroni, A., Sacco, R. & Saleri, F. (2000*b*), *Numerical mathematics*, Springer.

Rahman, M., Hossain, M. & Rahman, S. (2002), 'A shear-dilation-based model for evaluation of hydraulically stimulated naturally fractured reservoirs', *International Journal for Numerical and Analytical Methods in Geomechanics* **26**(5), 469–497.

Reinders, J. (2007), *Intel Threading Building Blocks*, O'Reilly.

Renshaw, C. E. (1995), 'On the relationship between mechanical and hydraulic apertures in rough-walled fractures', *Journal of Geophysical Research: Solid Earth (1978–2012)* **100**(B12), 24629–24636.

Rice, J. (1976), 'The localization of plastic deformation', *Theoretical and Applied Mechanics (Proceeding of the 14th Internation Congress on Theoretical and Applied Mechanics, Delft, 1976, ed. W. T. Koiter)* **1**, 207–220.

Rice, J. R. (1968), *Mathematical analysis in the mechanics of fracture*, Vol. 2, Academic Press, chapter Fracture: An Advanced Treatise, pp. 191–311.

Rice, J. R. (1975), 'On the stability of dilatant hardening for saturated rock masses', *Journal of Geophysical Research* **80**(11).

Rice, J. R. (1977), The localization of plastic deformation, *in* W. Koiter, ed., '14^{th} International Congress on Theoretical and Applied Mechanics', North-Holland, Amsterdam, pp. 207–220.

Rice, J. R. (1992*a*), 'Fault stress states, pore pressure distributions, and the weakeness of the san andreas fault', *International Geophysics* **51**(Fault Mechanics and Transport Properties of Rock: A Festschrift in Honor of W. F. Brace), 475–503.

Rice, J. R. (1992*b*), 'Fault Stress States, Pore Pressure Distributions, and the Weakness of the San Andreas Fault', *International Geophysics* **51**, 475–503.

Rice, J. R. (1993), 'Spatio-temporal complexity of slip on a fault', *Journal of Geophysical Research* **98**(B6), 9885–9907.

Rice, J. R. (2006), 'Heating and weakening on faults during earthquake slip', *J. Geophys. Res* **111**(B05311).

Rinaldi, A., Vilarrasa, V., Rutqvist, J. & Cappa, F. (2015), 'Fault reactivation during CO_2 sequestration: Effects of well orientation on seismicity and leakage', *Greenhouse Gas Sci Technol.* **5**, 645–656.

Rokhlin, V. (1985), 'Rapid solution of integral equations of classical potential theory', *Journal of computational physics* **60**(2), 187–207.

Rudnicki, J. W. (1979), 'The stabilization of slip on a narrow weakening fault zone by coupled deformation-pore fluid diffusion', *Bull. Seism. Soc. Am.* **69**(4), 1011–1026.

Rudnicki, J. W. & Chen, C.-H. (1988), 'Stabilization of rapid frictional slip on a weakening fault by dilatant hardening', *Journal of Geophysical Research: Solid Earth* **93**(B5), 4745–4757.

Rudnicki, J. W. & Rice, J. R. (1975), 'Conditions for the localization of deformation in pressure-sensitive dilatant materials', *J. Mech. Phys. Solids* **23**, 371–394.

Rutqvist, J. & Stephansson, O. (2003), 'The role of hydrochemical coupling in fractured rock engineering', *Hydrogeology Journal* **11**(1), 7–40.

Saad, Y. (1992), 'A Flexible Inner-Outer Preconditioned GMRES Algorithm', *SIAM J. Sci. Comput.* **14**(2), 461–469.

Samuelson, J., Elsworth, D. & Marone, C. (2009), 'Shear-induced dilatancy of fluid-saturated faults: Experiment and theory', *Journal of Geophysical Research: Solid Earth* **114**(B12).

Schäfer, M. (2006), *Computational Engineering - Introduction to Numerical Methods*, Springer.

Scotti, O. & Cornet, F. H. (1994), ‘In Situ Evidence for Fluid-Induced Aseismic Slip Events Along Fault Zones’, *Int. J. Rock Mech. Min. Sci. & Geom. Abstr.* **31**(4), 347–358.

Segall, P. & Rice, J. R. (1995), ‘Dilatancy, compaction, and slip instability of a fluid-infiltrated fault’, *Journal of Geophysical Research: Solid Earth* **100**(B11), 22155–22171.

Segall, P. & Rice, J. R. (2006), ‘Does shear heating of pore fluid contribute to earthquake nucleation?’, *Journal of Geophysical Research: Solid Earth* **111**(B9).

Segall, P., Rubin, A. M., Bradley, A. M. & Rice, J. R. (2010), ‘Dilatant strengthening as a mechanism for slow slip events’, *Journal of Geophysical Research: Solid Earth* **115**(B12).

Seront, B., Wong, T.-F., Caine, J., Forster, C., Bruhn, R. & Fredrich, J. (1998), ‘Laboratory characterization of hydromechanical properties of a seismogenic normal fault system’, *Journal of Structural Geology* **20**(7), 865–881.

Shao, H., Hein, P., Sachse, A. & Kolditz, O. (2016), *Geoenergy Modeling II - Shallow Geothermal Systems*, SpringerBriefs in Energy.

Shapiro, S. A., Huenges, E. & Borm, G. (1997), ‘Estimating the crust permeability from fluid-injection-induced seismic emission at the KTB site’, *Geophys. J. Int.* **131**, F15–F18.

Shapiro, S. A., Kummerow, J., Dinske, C., Asch, G., Rothert, E., Erzinger, J., Kumpel, H.-J. & Kind, R. (2006), ‘Fluid induced seismicity guided by a continental fault: Injection experiment of 2004/2005 at the German Deep Drilling Site (KTB)’, *Journal of Geophysical Research* **33**.

Shapiro, S. A., Rothert, E., Rath, V. & Rindschwentner, J. (2002), ‘Characterization of fluid transport properties of reservoirs using induced seismicity’, *Geophysics* **67**(1), 212–220.

Shibazaki, B. (2005), ‘Nucleation process with dilatant hardening on a fluid-infiltrated strike-slip fault model using a rate- and state-dependent friction law’, *Journal of Geophysical Research* **110**(B11308).

Simo, J. C. & Hughes, T. (1997), *Computational Inelasticity*, Vol. 7, Springer.

Skoumal, R. J., Brudzinski, M. R. & Currie, B. S. (2015), ‘Earthquakes induced by hydraulic fracturing in Poland Township, Ohio’, *Bulletin of the Seismological Society of America* **105**(1), 189–197.

Snozzi, L. & Molinari, J.-F. (2013), ‘A cohesive element model for mixed mode loading with frictional contact capability’, *International journal for numerical methods in engineering* **93**, 510–526.

Sornette, A., Davy, P. & Sornette, D. (1993), 'Fault growth in brittle-ductile experiments and the Mechanics of continental collisions', *Journal of Geophysical Research* **98**(N7), 12111–12139.

Starfield, A. M. & Cundall, P. A. (1988), 'Towards a methodology for rock mechanics modelling', *International Journal of Rock Mechanics and Mining Sciences & Geomechanics Abstracts* **25**(3), 99–106.

Stober, I. & Bucher, K. (2013), *Geothermal Energy*, Springer.

Stupkiewicz, S. & Mróz, Z. (2001), 'Modelling of friction and dilatancy effects at brittle interfaces for monotonic and cyclic loading', *Journal of theoretical and applied mechanics* **3**(39).

Tada, H., C., P. P. & Irwin, G. R. (2000), *The Stress Analysis of Cracks Handbook*, 3rd edn.

Terzaghi, K. (1943), *Thoretical soil mechanics*, John Wiley & Sons.

Townend, J. & Zoback, M. D. (2000), 'How faulting keeps the crust strong', *Geology* **28**(5), 399–402.

Tvergaard, V., Needleman, A. & Lo, K. K. (1981), 'Flow localization in the plane strain tensile test', *J. Mech. Phys. Solids* **29**(2), 15–142.

Ucar, E., Berre, I. & Keilegavlen, E. (2018), 'Three-Dimensional Numerical Modeling of Shear Stimulation of Fractured Reservoirs', *Journal of Geophysical Research* **123**, 3891–3908.

Uenishi, K. & Rice, J. R. (2003), 'Universal nucleation length for slip-weakening rupture instability under nonuniform fault loading', *Journal of Geophysical Research: Solid Earth* **108**(B1).

Van der Giessen, E. & Needleman, A. (1995), 'Discrete dislocation plasticity: a simple planar model', *Modelling and Simulation in Materials Science and Engineering* **3**, 689–735.

Vasterling, M., Wegler, U., Becker, J., Brüstle, A. & Bischoff, M. (2017), 'Real-time envelope cross-correlation detector: application to induced seismicity in the Insheim and Landau deepgeothermal reservoirs', *J. Seismol* **21**, 193–208.

Viesca, R. C. (2016*a*), 'Self-similar slip instability on interfaces with rate-and state-dependent friction', *Proc. Roy. Soc. Lond. A* **472**(2192), 20160254.

Viesca, R. C. (2016*b*), 'Stable and unstable development of an interfacial sliding instability', *Physical Review E* **93**(6), 060202.

Viesca, R. & Rice, J. R. (2012), 'Nucleation of slip-weakening rupture instability in landslides by localized increase of pore pressure', *Journal of Geophysical Research* **117**(B03104).

Viola, E. (2003), *Lezioni di Scienza delle Costruzioni*, Pitagora Editrice Bologna.

Walmann, T., Malthe-Sørenssen, A., Feder, J., Jøssang, T. & Maekin, P. (1996), 'Scaling relations for the Lenghts and Widths of Fractures', *Phys. Rev. Letters* **77**(27).

Wei, S., Avouac, J.-P., Hudnut, K. W., Donnellan, A., Parker, J. W., Graves, R. W., Helmberger, D., Fielding, E., Liu, Z., Cappa, F. & Eneva, M. (2015), 'The 2012 Brawley swarm triggering by fluid-induced aseismic slip', *Earth and Planetary Science Letters* **442**, 115–125.

White, M., Fu, P., McClure, M., Danko, G., Elsworth, D., Sonnenthal, E., Kelkar, S. & Podgorney, R. (2017), 'A suite of benchmark and challenge problems for enhanced geothermal systems', *Geomechanics and Geophysics for Geo-Energy and Geo-Resources* pp. 1–39.

Willis-Richards, J., Watanabe, K. & Takahashi, H. (1996), 'Progress toward a stochastic rock mechanics model of engineerred geothermal systems', *J. Geophys. Res* **101**(B8), 17,481–17,496.

Witherspoon, P. A. (1980), 'Validity of cubic law for fluid flow in a deformable rock fracture', *Water Resources Res.* **16**(6), 1016–1024.

Wu, K. & Olson, J. E. (2015), 'A simplified three-dimensional displacement discontinuity method for multiple fracture simulations', *International Journal of Fracture* **193**(2), 191–204.

Xu, T. & Pruess, K. (2001), 'On fluid flow and mineral alteration in fractured caprock of magmatic hydrothermal system', *Journal of Geophysical Research* **106**(B2), 2121–2138.

Xu, X.-P. & Needleman, A. (1994), 'Numerical simulations of fast crack growth in brittle solids', *Journal of the Mechanics and Physics of Solids* **42**(9), 1397–1434.

Zhang, X., Jeffrey, R. G. & Llanos, E. M. (2005), 'On plane-strain fluid-driven shear fracture propagation in elastic solids', *Geophys. J. Int.* **163**, 419–430.

Zhou, F. & Molinari, J.-F. (2004), 'Dynamic crack propagation with cohesive elements: a methodology to address mesh dependency', *International journal for numerical methods in engineering* **59**, 1–24.

Zhou, F., Molinari, J.-F. & Shioya, T. (2005), 'A rate-dependent cohesive model for simulating dynamic crack propagation in brittle materials', *Engineering Fracture Mechanics* pp. 1383–1410.

Zimmerman, R. W. & Bodvarsson, G. S. (1996), 'Hydraulic Conductivity of Rock Fractures', *Transport in Porous Media* **23**, 1–30.

Federico Ciardo

Rue du Maupas 36B – 1004 Lausanne – Switzerland

☎ +41 76 778 60 21 • ✉ federico.ciardo2@gmail.com
Italian Citizen – 18.02.1991 – Single – Swiss B permit

Education

École Polytechnique Fédérale de Lausanne (EPFL) **Lausanne, Switzerland**
PhD in Mechanics *02.2016 – 01.2020*
Geo-Energy Laboratory - Gaznat chair on Geo-Energy
Title: Hydraulic stimulation of pre-existing discontinuities in tight rocks
Support: Swiss Federal Office of Energy (SFOE) & Swiss National Science Foundation (SNF)

University of Bologna **Bologna, Italy**
Bsc & Master in Civil engineering, Summa Cum Laude *0.9.2010 – 07.2015*
Major in Structural engineering with focus on computational mechanics

Liceo scientifico E. Ferrari **Cesenatico, Italy**
Mathematics & Informatics *09.2005 – 07.2010*

Professional Experience

École Polytechnique Fédérale de Lausanne (EPFL) **Lausanne, Switzerland**
Teaching assistant *2016 – 2020*
Courses: Ouvrages Géotechnique & Reservoir geo-mechanics engineering
Supervisions of exercise sessions and students' projects

Languages

Italian: Mothertongue	
English: Fluent	*C2 level*
French: Intermediate	*B1/B2 level*
Portuguese: Beginner	*A2 level*

Scientific publications

PhD thesis

- F. Ciardo, *Hydraulic stimulation of pre-existing discontinuities in tight rocks*. EPFL, 2020. Supervisor: Prof. B. Lecampion. Jury members: Prof. J. F. Molinari, Prof. H. Bhat, Dr. G. Siddiqi and Prof. M. Violay

Journal articles

- F. Ciardo, B. Lecampion. Effect of dilatancy on the transition from aseismic to seismic slip due to fluid injection in a fault. *Journal of Geophysical Research: Solid Earth*, 124, 3724-3743. https://doi.org/10.1029/2018JB016636
- F. Ciardo, B. Lecampion and F. Fayard. A boundary element based solver for localized inelastic deformations. Under review for *International journal for Numerical Methods in Engineering*.

Awards

- Fellowship from Swiss Seismological Service (SED) for being one of the best student among the partecipants of 2nd Schatzalp workshop on induced seismicity (Davos, 2017).

Professional & PhD Courses

- *Hands-on Intel Software Developer Workshop for Technical Computing and Artificial Intelligence*, by Intel
- *Advanced in Contact Mechanics*, by Prof. J. F. Molinari - EPFL
- *Scientific programming for engineers*, by Prof. A. Guillaume - EPFL
- *Similarity and Transort Phenomena in Fluid Dynamics*, by Prof. C. Ancey - EPFL
- *Information Science in Engineering*, by Prof. S. Ian - EPFL
- *Communication for Research Engineers*, by Prof. S. Ian - EPFL
- *Python for computational science*, by Cineca, Bologna

Personal skills

Computer skills

Prototyping programming: Mathematica (preferred), Python, Matlab

Developing programming languages: C++ (preferred), C, Fortran, VBA, Julia

IDE: CLion (preferred), Xcode

Operating Systems: Unix/Linux (preferred), Windows

Version Control Systems: Git (Github, C4science)

Cross-platforms build system generator: CMake

Other skills

Finite Element softwares: Abaqus, Ansys, Straus7, FreeFem++, Code Aster

Civil engineering softwares: SimaPro 8.0, abc, Epanet, Rhinoceros, Autocad 2D/3D, Paraview, EnExSys, SWMM, Solema-Meca, SimaPro

Organizational: Solid experience in project management, problem solving

Graphics softwares: Adobe Illustrator (preferred), Photoshop, GIMP

Typesetting systems: LaTeX(preferred), Microsoft Office package

Relational: Teaching, presentations and public speaking, communication

Interests

Travel: Discover new cultures to enrich my life

Football: I was a professional player at that time…

Skiing: (Free-)skier since I was 7 y/o

Reading: Mainly newspapers to keep up with World's evolution

References

- **Prof. Brice Lecampion**, thesis supervisor
  EPFL, Switzerland
  brice.lecampion@epfl.ch
  Tel: +41 (0) 21 693 27 07
  https://www.epfl.ch/labs/gel/
- **Dr. Gunter Siddiqi**, member of PhD jury
  Swiss Federal Office of Energy (SFOE), Suisse
  gunter.siddiqi@bfe.admin.ch
  Tel: +41 (0) 58 462 56 11
  www.bfe.admin.ch

Last updated: February 11, 2020